UNIVERSITÀ
DEGLI STUDI
FIRENZE

DOCTORAL PROGRAMME IN INDUSTRIAL
ENGINEERING
DOTTORATO DI RICERCA IN INGEGNERIA
INDUSTRIALE

XXXII

RE&AM-based methods and tools for biomedical engineering

ING/IND-15

Doctoral Candidate	**Supervisors**
Michaela Servi	Prof. Monica Carfagni

External Referees	**Dean of the Doctoral Programme**
Prof. Francesco Bianconi	Prof. Maurizio De Lucia

Prof. Roberto Meneghello

Years 2016/2019

Dedicated to my family

Summary

In line with recent approaches to personalized medicine, where 3D technologies are rapidly becoming a new concept of treatment based on the ability to model patient-specific devices, this work aims to analyze the life cycle of a customized device in order to achieve a related systematic production. The common approach for the realization of these devices involves the digitization of the affected anatomy, followed by the modeling of the device and when needed, the production through additive manufacturing. The literature in these cases does not offer a unified framework that directly allows the clinical staff to acquire independently and easily the anatomy of the patient and then design the printable 3D model of the medical device, without the help of an expert CAD modeler.

In the effort to provide tools that can be introduced into clinical practice and used directly by hospital staff, the life cycle of a generic customized medical device has been analyzed. The idea is to formulate a framework describing the phases of implementation of a personalized treatment system. The objective of the framework is to be used for each new production system of devices dedicated to a specific anatomy.

This work has been conducted in collaboration with the Meyer Children's Hospital medical staff within a joint laboratory with the Department of Industrial Engineering of the University of Florence. The chosen pilot cases are: 1) the systematic production of orthoses for children for the treatment of bone fractures of the upper limbs; 2) the development of tools for the treatment of chest malformations.

The implementation of the two pilot cases was carried out following the phases defined in the framework and using common design and implementation tools.

With regard to the first case, an innovative system has been devised, which would make it possible to envisage a new scenario in which, upon the arrival of the injured patient, the hospital staff would be able, autonomously and quickly, to scan the broken arm , to create the CAD model of the orthosis, to send the file to the production and to applicate the corrective device.

The defined framework was also applied to the second pilot case, the treatment of chest malformations, following the identified phases. In this second case, as well, the idea was to create an advanced system that would allow to have an easy to use outpatient instrument that would facilitate the hospital staff in making new (non-invasive) measurements and that would allow to produce a customized medical device without the intervention of CAD experts.

Table of Contents

1. Introduction

In recent years, discoveries in the field of Reverse engineering (RE) and Additive manufacturing (AM) techniques have led to the development of innovative solutions for personalized medicine. 3D technologies are rapidly becoming a new treatment concept based on the ability to model patient-specific devices. Using reverse engineering and additive manufacturing techniques, it is possible to conceive an innovative and personalized treatment that can be more effective as it is adapted to each patient. Customized medicine, in fact, has been revolutionized by these technologies, as they can be effectively applied in the medical field to: i) acquire information about the patient's anatomy; ii) design CAD models based on specific anatomical references; iii) produce parts with sufficient precision for different medical applications. Ultimately, reverse engineering and additive manufacturing techniques provide physicians with the ability to adapt each treatment to the specific needs of the patient: modeling and manufacturing of specific instruments, development of medical training simulators for complex surgical operations and production of medical implants modeled directly on the anatomy of patients are some examples of possible applications.

Focusing on the pediatric field, it can be said that medical devices for children (implantable and non-implantable) often have to follow all stages of development related to the growth of the patient and not always the best size is available. The current manufacturing scenario, in fact, makes it difficult for device manufacturers to produce small batches necessary to meet the variety of sizes and anatomical variations for infants. In this context, the use of production systems tailored onto the patient, i.e. where the device is made from the specific anatomy, can ensure better functionality and, among other benefits, easier installation. By leveraging the flexibility that modern 3D printing systems provide, new opportunities can be opened in the technological landscape of pediatric medicine. By introducing 3D technologies such as CAD processing, scanning and printing, in clinical practice, it is possible to lay the foundations for the standardization of procedures for the construction of customized medical devices in line with the philosophy of personalized medicine, where each patient is unique, and the solution is built around him.

This work aims to exploit these technologies to introduce into clinical practice systems and tools that can be used directly by hospital staff to create customized medical devices. The idea is to provide comprehensive tools that can allow the creation of devices for each patient's anatomy without the help of expert CAD modelers, designers or engineers.

In this direction, the collaboration between the Department of Industrial Engineering of the University of Florence and the Meyer Children's Hospital in Florence has led to the creation of a joint laboratory called T3Ddy, in which doctors and engineers collaborate with

the aim of introducing innovative and customized 3D technologies in the clinical practice. Within the T3Ddy program, two pilot cases have been identified, representative of the possible applications for the achievement of the objective described above: 1) systematic production of children's orthoses for the treatment of upper limb bone fractures (external conservative orthoses); 2) development of tools for the treatment of thoracic malformations.

The first pilot case concerns the realization of an acquisition system of the hand-wrist-arm district and the modeling of immobilizing devices that can replace the common plaster cast providing benefits of breathability, lightness, washability and comfort. It is intended to initially treat "buckle" type fractures that, as we will see below, occur only in children and are very common. An important aspect is the acquisition system that must be able to scan the entire district in a very short time since body movements would invalidate the acquisition. This aspect is emphasized by the pediatric context, for which it is even more difficult for a child to maintain a stable position for a long time. The medical device produced should take into account a number of medical specifications such as the need not to compress predetermined areas and should respect the strengths necessary to properly immobilize the limb.

In the second pilot case, the focus will be on two types of thoracic malformations: Pectus Excavatum (PE) and Pectus Carinatum (PC). The first is a structural deformation of the anterior thoracic wall in which the sternum and thoracic cage have a hollow or recessed shape. PE can be present at birth or develop after puberty and can affect cardiac and respiratory function and can cause chest and back pain. Pectus Carinatum, also called pigeon chest, is a malformation of the chest characterized by a protrusion of the sternum and ribs. People suffering from these conditions may experience severe negative psychosocial effects and avoid activities that expose the chest. Surgery is used to treat these diseases or external corrective orthoses can be used. As far as PE is concerned, the corrective medical device is called Vacuum Bell, and works by air suction to lift the chest. The PC, on the other hand, is corrected with a compression brace. In this work it has been studied the possibility of producing personalized Vacuum Bell, adapted to the patient's chest, in order to increase comfort and effectiveness. For both the chest malformations, it also aims to develop outpatient support tools that can help in diagnosis by providing objective metrics to assess the disease.

The thesis is structured as follows: in chapter 2 is briefly presented the state of the art regarding the use of 3D modeling tools in the medical field; in chapter 3 is analyzed the process leading to the implementation of systems to create custom medical devices; in chapter 4 and 5 are analyzed in detail the two pilot cases; finally conclusions are drafted in chapter 6.

Before proceeding with the chapters describing the development of the work it is necessary to introduce the concepts of point cloud, mesh and ply format.

Point Cloud

A point cloud (Figure 1-1) is a collection of data points defined by a given coordinates system. In a 3D coordinates system, for example, a point cloud may define the shape of some real or created physical system. In a 3D Cartesian coordinates system, a point is identified by three coordinates that, taken together, correlate to a precise point in space relative to a point of origin. X, y and z axes extend in two directions and the coordinates identify the distance of the point from the intersection of the axes (0) and the direction of divergence, expressed as + or -.

Point clouds are used to create 3D meshes and other models used in 3D modeling for various fields including medical imaging, architecture, 3D printing, manufacturing, 3D gaming and various virtual reality (VR) applications.
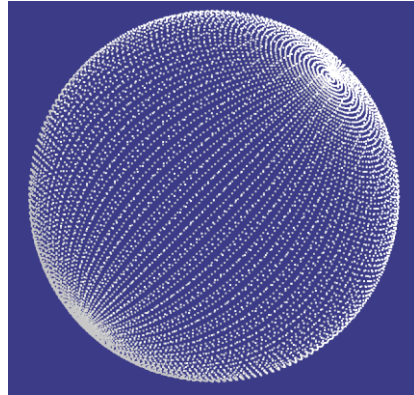
Figure 1-1 Example of a point cloud representing a sphere.

3D Mesh

A 3D mesh (Figure 1-2) is the structural build of a 3D model consisting of polygons. 3D meshes use reference points in X, Y and Z axes to define shapes with height, width and depth. While it can take large numbers of polygons to make a 3D mesh approach photorealism, these relatively simple shapes allow for faster processing than other techniques. The polygons used are typically quadrangles or triangles; these geometric shapes can be further broken down into vertices in X, Y, Z coordinates and lines.
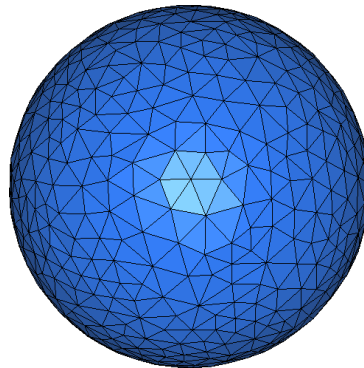
Figure 1-2 Example of a mesh representing a sphere.

PLY - Polygon File Format

The PLY file format describes a 3D object as a collection of vertices, faces and other elements, along with properties such as color and normal direction that can be referred to these elements. The data storage format supports a relatively simple description of a single object as a list of nominally flat polygons. There are two versions of the file format, one in ASCII, the other in binary. Files are organized as a header, that specifies the elements of a mesh and their types, followed by the list of elements itself. The elements are usually vertices and faces, but may include other entities such as edges, samples of range maps, and triangle strips. The header of both ASCII and binary files is ASCII text. Only the numerical data that follows the header

is different between the two versions. A basic PLY object definition is simply a list of (x,y,z) triples for vertices and a list of faces that are described by indices into the list of vertices.

2. RE&AM in medicine

The application of Reverse Engineering (RE) and Additive Manufacturing (AM) techniques to clinical practice allows the creation of highly customized medical devices, modeled directly on the anatomy of the patient. The versatility of these techniques makes them suitable to be used on a wide range of applications, for example for the realization of anatomical models, surgical implants, surgical cutting templates, external supports such as prostheses and orthoses, or even the realization of bio-fabrics. In recent years, research is constantly increasing, to give an idea of this increase consider that in 2004 three articles have been published in the field of medical applications of AM, which have risen to 426 in 2016 [1]. The intention of this section is therefore not to provide a complete review of the literature, but to give an overview of the use of these techniques.

The study of the state of the art has shown that most of the use of 3D printing in the clinical setting has been limited to unconventional surgery and isolated patient cases. These cases demonstrate the effectiveness of a personalized approach to the problem, which allowed the production of appropriate medical devices, where traditional techniques could not be used.

The application of 3D printing to pathological conditions of the head and neck has been one of the first uses and to date remains the most common [2, 3]. Although there are fewer reports on the use of 3D printing from chest images, a 2-month-old baby with tracheomalacia has successfully received a specially printed airway support [4].

Three-dimensional printing has bridged the visualization gap in the planning of cardiovascular interventions, with vascular models, becoming the second most popular method after bone models.

A retrospective feasibility study of 12 patients showed that 3D printing models are superior to magnetic resonance imaging to identify the best candidates for implantation of a percutaneous pulmonary valve [5]. Several authors suggested routine use of 3D printing for demanding cardiac decisions [6, 7], particularly as an important strategy for obtaining cardiovascular images of children.

3D printing can also positively influence the presentation of medical-legal data [8] and used post-mortem [9, 10] in order to fabricate e.g. 3D models of fetuses to study intrauterine diagnostic opportunities.

As mentioned in the introductory section, this work focuses on two medical applications, fracture orthoses in the forearm-pulse-hand district and devices for the treatment of thoracic malformations. Below it is briefly reported the state of the art concerning these two fields.

RE&AM for upper limbs orthopedics devices

The realization of personalized corrective orthoses for fractures of the upper limbs is composed of two important phases: first, it is necessary to reproduce the anatomy of the patient's arm, then the device is modeled from the 3D data and the CAD model is generated, which can be realized with additive techniques.

There are several scanning systems on the market dedicated to the acquisition of the arm, from which the prototype of the orthosis can then be made. The two most relevant ones

are: acquisition device coupled with a tablet [11], scanning device designed by the company Holey srl [12].

The first scanning system works by placing the arm in a sufficiently stable position, for example leaning with the elbow on a table, so that the operator making the acquisition is able to capture the entire limb. However, the resulting acquisitions can be very coarse, due to the mutual movement between the acquiring user and the patient.

The second scanning system consists of positioning the scanner on the edge of a table, and an "L" shaped arm on which the acquisition device is mounted rotates around the arm. The procedure in this case is to place the arm in correspondence with the axis of rotation of the scanner. Once activated, the scanner performs a 360° overview of the arm. Compared to the previous case, it requires a fixed distance between the camera and the axis of rotation of the acquisition system. The position taken by the arm represents, compared to the previous case, a greater problem since it is more difficult to keep the arm stationary while it is suspended.

We can therefore state that state of the art technologies to scan the whole hand-wrist-arm (HWA) district for the 3D reconstruction of the patient's anatomy are either too expensive [13] or too slow [11, 12], requiring the patient to stay still for an extended period (at least 30 seconds). The speed of the acquisition process is, nonetheless, a fundamental characteristic to minimize artefacts due to subject movement.

A number of studies concern the development of CAD models of the orthosis to be fabricated. Shaping of the cast model (starting from the acquired data) is mostly carried out by aesthetic designers, such as by Cortex [14] and Osteoid [15]. Although they are aesthetically pleasing, these works have not been subjected to a clinical trial or to the approval of an ethics committee, therefore, their procedure lacks clinical application and approval [16]. Moreover, the development of such casts requires the presence of an expert CAD modeler to be completed; hence, clinicians are hindered from using the procedure on a regular basis. With the aim of simplifying the modelling process by shortening it in terms of time, Huhn Kim et al. [17] proposed a hybrid method with the basic concept of separating the orthosis in two components, consisting of an inner structure, which perfectly fits the patient anatomy, that is fastened to a standardized outer cover. Their approach, although interesting, still requires a CAD expert to generate the models of the orthosis. Palousek et al. [18] proposed a partial solution to the problem of simplifying the manufacturing process by scanning only one side of the arm and generating a splint, thus gaining some advantages such as ventilation, cleanability and lightness, but resulting in a limited protection for the patient.

Although literature offers different methodologies that allow the development of customized orthoses through 3D Scanning and Additive Manufacturing techniques, however, none of the proposed technologies has yet been tested and validated within the common hospital clinical practice. The search for a robust and reliable procedure, capable of effectively replacing the traditional plaster cast, for wrist fracture treatments, is still, in many respects, an open question.

Much of the work found in the literature refers to prototypes of orthoses developed using the classic strategy of manual reverse engineering. This means long modeling times that are not compatible with hospital applications and technical expertise that medical personnel do not have.

Few studies provide for a semi-automatic procedure, which can be used in a simple and intuitive way. Among these stands out a recent study by Lin et al. [16], where an intelligent system to make the orthosis process manageable by the medical staff is presented. The authors designed a procedure that starts with the computation of the central line of the arm and can automatically find the right pattern for ventilation that corresponds to a robust structure.

Although promising, this procedure only addresses the reconstruction of the arm and does not consider the hand region. The same authors [19] recently tested the orthoses generated with the above-mentioned procedure in a medical trial.

Another work that aims to semi-automate the process is presented in [20], where a semi-automatic procedure is generated for the creation of a splint that allows the supervision of the process. In this work, however, the position of the hand and the shape of the splint do not comply with the clinical specifications of this project, as will be explained below, and the generation of the 3D model of the arm is also done using a hand handled 3D scanner.

RE&AM for thoracic malformations
Since thoracic malformations are likely to be asymptomatic with the possibility of worsening during growth, it is essential for the proper treatment of patients with PE and PC to monitor the progression of the disease over time and estimate their severity. To this end, over the years, so-called severity indices or chest indices have been introduced, both for PE and PC measurement.

A chest index is a formula used to qualify or quantify the chest deformity [21, 22]. Severity indices can be used to assess the gravity of the defect, define the treatment and eventually determine its conclusion; they can also be used to quantify post-operative changes. Severity indices can be divided into four main categories: Clinical, Chest X-ray, Chest CT/MRI scan and Optical.

Clinical indexes [21] are manually evaluated by the physician during the examination. Although easily applicable and low-cost, the indices in this class may be subject to errors and are not fully repeatable, as it is not possible to consider the patient's body mass and changes in age and height [23]. For this purpose, indexes referring to the patient's bone and internal cartilage can be calculated on X-rays, CT or MRI. Despite these indices are more repeatable and reliable, there is a great deal of variability in their interpretation, and they may also depend on the variation in age, sex or thoracic shape of the patient, as well as on the respiratory phase with which the tomographic image is acquired.

In recent years, so-called optical indices, calculated on external optical scans of the patient's chest [24–26], have been gaining ground. The reason for their popularity is that external optical scanning is faster to apply and prevents the patient from being exposed to radiation. In addition, they allow the accuracy of the measurement, which can be automated (and therefore not manually carried out) as in the case of clinical indices. Optical indices, however, may also suffer from variations in weight and shape of the individual patient

The detailed description of the measurement methods of thoracic indexes of the clinical, X-ray, and CT/MRI type is not here reported for reasons of space and relevance, however, below are illustrated the techniques proposed at the state of the art as concerns the optical indexes for the measurement of Pectus Excavatum and Pectus Carinatum. Lain et al. [27] presented a 3D external scanning technique as a new, non-invasive imaging methodology to assess chest wall deformations, making it easier to follow the evolution of the deformity. A 3D reconstruction of the thoracic cage is created by processing the images acquired by using a 3D scanner.

These indices were found to be able to evaluate changes over time and to compare the state of the deformity before and after surgery.

Unfortunately, the work proposed by Lain et al. has some drawbacks, which limits a straightforward application of their method on the clinical practice. First, the method is landmark based since it requires the application of a number of anatomical landmarks placed in the front and in the back of the trunk. Furthermore, the acquisition of the patient anatomy,

performed using a commercial body scanner, takes a very long time thus requiring the patient to stay as still as possible for about half a minute. Then, to perform the 3D model reconstruction, used to derive the PE and PC related indices, a series of additional data processing tasks, carried out by expert users, are required (e.g. erasing of upper and lower parts of the torso).

Ponchet et al. in [28] also developed an optical measurement system to prevent the patient from being exposed to radiation and compared the extracted measurements with the analogous ones calculated on CT scans. Professional scanners are used here, too, and the calculation of the indices is based on landmarks and is therefore not automated and not easily usable and reproducible. In other similar works [29, 30] professional optical scanners are used which require the patient to maintain his position for a long time and the measurements are calculated manually and correlated with the measurements computed on tomographic images.

3. Methods and tools for personalized medical devices

When a process of realization and validation of a medical device is undertaken, the first thing to be defined is the design life cycle, that is, the steps leading, starting from the specification of the requirements, to the realization of such equipment. The design life cycle consists of several phases in which the output elements of a phase represent the input elements of the immediately following phase and on which it is possible to carry out the relative controls and the relative validation checks.

In this work, three main steps of the life cycle have been identified: the clinical specifications of the device to be manufactured; the technical scheme underlying the construction, and the clinical applications. The definition of these three phases is examined below, investigating in detail the two case studies treated, which are the creation of custom orthotics for fractures involving the hand-wrist-arm district and the construction of devices for the treatment of chest malformations.

3.1. Clinical specifications

The first phases of the design life cycle are the most delicate of the process because they define the requirements of the medical device that will affect all subsequent steps.

The peculiarity of the production cycle of a customized device is that it mainly involves dialogue and collaboration between engineers and medical personnel. Moreover, the characteristic of this specific project is that it is not limited to the realization of the medical device but aims to provide the hospital with a tool that can allow the realization of the same medical devices without the intervention of a technician.

The first important step within the operating cycle is the definition of clinical specifications: technologies experts and health care professionals, must co-operate at this stage in order to define a common language aiming at the proper interpretation of clinical requirements to be translated in functional technical specification.

The medical staff identifies the scenario in which a custom device could bring advantages and proposes its realization specifying the medical conditions that the device will help to treat and its clinical purpose, as well as the needs of users and patients to whom the device will be dedicated. In this phase, it is the responsibility of engineers to identify the system requirements that can be the operational response to clinical needs. Among the requirements of the device are specified technical details such as the size, the material (defined according to the type of stiffness that is to be obtained) and other characteristics that vary depending on the problem under consideration. So, to define the requirements of the device, the interdisciplinary team is asked a few questions: What is the purpose of the device? What types of patients is it intended for? In which cases will it be used? Which important attributes or characteristics should it possess? For what kind of procedures will the device be used? With which other HW / SW products will the device interact? Who will use the device? How will the user interact with the device? What level of education, competence and training do they

need to have? Will the user be able to operate alone, or will the intervention of a specialized technician be necessary?

The definition of the requirements does not stop with those relating to the medical device. Since, as mentioned, the objective is to create a tool that allows the systematic production of custom devices in the hospital environment, the requirements of the system, i.e. the tools with which users will interface, are also included.

Once the needs and requests of the device and the system have been defined, the project level is reached where these requests must be transformed into real functions. The defined requirements are divided into explicit and implicit requirements. The first are those actively established in the first design phase according to the requests and needs identified. The second are second level requirements which, although not directly expressed in the definition phase, are essential to obtain full efficiency of the equipment and compliance with the security and privacy regulations.

In the following, the technical specifications for the two pilot cases are described; they will be further discussed in paragraphs 4.1, with regard to the creation of corrective orthoses for the upper limbs and 5.1 for the problem of thoracic malformations.

Upper limb orthosis - clinical specifications

The first pilot case concerns, as mentioned above, the realization of corrective orthoses for fractures of the upper limbs. The aim is to create a device that can replace the current plaster cast and bring advantages of lightness, comfort and washability.

To date, the treatment of fractures of the upper limbs consists of a plaster cast tailored to the patient. The procedure is rather economical and provides an effective immobilization but has some drawbacks: the correction device is typically heavy, can cause skin rashes and does not allow ventilation of the treated area [31]. As a result, serious medical complications may occur, such as compartmental syndrome, ischaemia, heat lesions, bedsores and skin breaks [32].

The purpose is to realize, with RE and AM techniques, an orthopaedic device with mechanical properties similar to the plaster cast (such as rigidity), but with certain advantages: 1) the new device must be more comfortable as it is built on the particular anatomy of the individual patient; 2) it must be designed so as to be light and removable; 3) it must be designed with a reticulated structure that ensures beneficial access of water and air to the treated arm. Taking these three points into account, the specifications of the device in terms of shape and sizing with respect to the limb will be defined in paragraph 4.1.

With regard to the requirements of the system, in order to be fully exploited in the hospital environment, the infrastructure created must meet two main requirements: (i) the preliminary phase of collecting the 3D anatomy of the patient must be fast and manageable and (ii) the procedure that builds the CAD model of the orthosis must not require the user neither CAD technical skills nor significant time for model generation.

As far as the first requirement is concerned, state-of-the-art professional scanning systems are very expensive and/or have long acquisition times that are not suitable for hospital use, let alone paediatric use. In fact, each movement creates artifacts in the scan by invalidating it and on the other hand it is very difficult for a child to maintain a fixed position for long periods of time (meaning for more than a few seconds).

As far as the second requirement is concerned, it is important to consider the competence gap between the two disciplines in order to create an instrument that is really usable by hospital staff and therefore suitable for the clinical practice.

Thoracic malformations - clinical specifications

The second pilot case concerns the treatment of congenital thoracic malformations leading to sinking of the sternum in the case of Pectus Excavatum or raising of the sternum in the case of Pectus Carinatum.

Unlike Pectus Carinatum, for which the treatment consists in the use of compression corsets whose effectiveness has been validated over the years [33], to date the external corrective treatment for the pathology of Pectus Excavatum consists of a device called Vacuum Bell [34]. It is a suction cup consisting of a deformable body, made of silicone, which is placed over the area to be treated and which, using a depression created by a manual pump, is able to lift the patient's sternum upwards. The Vacuum Bell is available on the market in various types and sizes in order to adapt as much as possible to the thoracic conformation of the patient. In the case of female patients there are Vacuum Bell shaped so as not to interfere too much with the breast. Despite the fact that, as said, different sizes and shapes are available on the market, some important problems can be highlighted. The shape of the Vacuum Bell is, with the exception of the female ones, of the "elliptical" type, allowing to treat always the same area or the central part of the thorax. If there are asymmetrical malformations, the treatment is obviously not very effective. Moreover, the part that gets in contact with the chest is flat and therefore in some cases it may not adhere perfectly to the chest.

The purpose is therefore to create, with RE and AM techniques, a personalized Vacuum Bell, that follows the shape of the patient's chest, with the aim of obtaining a better adherence and a better final result, and having a shape that is not elliptical but different from patient to patient, chosen by the specialist himself, to also treat particular cases of asymmetry of the malformation. The specifications of the device in terms of shape and sizing with respect to the patient's thoracic wall will be further defined in paragraph 5.1. The aim is therefore to create a system that allows hospital staff to easily acquire the reference anatomy and give guidelines for the creation of the personalized device.

In order to evaluate the progress of the disease of patients affected by PE and PC and thus also evaluate the effectiveness of the treatment, additional system requirements have been defined involving the development of semi-automatic measurement procedures of severity indices. The calculation must be intuitive for the clinical staff and the extrapolated measurements must accurately describe the deformation.

3.2. Technical framework

Once the clinical/medical requirements and necessities are collected, the next step is the development phase where clinical specifications take shape and, through a series of implementation phases, the acquisition tools and the CAD model of the customized device are created.

In general, as already mentioned, to build a medical device that can be 3D printed, using reverse engineering techniques for modeling and additive manufacturing for production, three main phases must be considered: i) the collection of the patient's anatomy in the form of 3D data using a 3D scanner; ii) the modeling of the customized device in a CAD environment; iii) the printing of the device.

i. For the 3D data collection phase, the most suitable acquisition device on the market must initially be selected. A key factor is the number and arrangement of devices needed to efficiently and accurately acquire the anatomy under consideration. The design must take into account and contain as much as possible the costs and time of acquisition. To allow non-

specialized personnel to interact autonomously with the acquisition tool, it is also necessary to develop a simple and intuitive user interface for the handling of the acquisition. The software development must be based on a series of use cases that define the interaction between the user and the program.

ii. After collecting the 3D data, the second phase consists in the modeling and generation of the personalized medical device, realized through CAD operations starting from the patient's anatomy with a dedicated software. The CAD procedure must be defined paying particular attention to the repeatability and robustness of the entire procedure and focusing on a number of anatomical features that can be extracted from the acquisition, which are necessary to make the procedure automatic as we will see when implementing details will be introduced. This operation, if it is not simplified with special tools, results complex for hospital staff. This phase is therefore usually carried out by experts, but the purpose of the work is precisely to allow a non-specialist user to interact with it and we will see how the procedure will be automated.

iii. Finally, for the actual production of the device it will be necessary to choose, among the available technologies, the most suitable one for the specific case, considering the mechanical properties required and the appropriate production times.

A brief overview of how to configure the system development for the two pilot cases is given below; each step will then be further developed in paragraphs 4.2, as regards the creation of corrective orthoses for the upper limbs and 5.2 for the problem of chest malformations.

Upper limbs orthopedic devices - technical framework
   i.   Anatomy collection
The most common design for creating custom 3D printed plasters begins with capturing arm geometry using 3D scanning technologies. As is well known, these technologies can be classified into professional 3D scanners (e.g. Romer Absolute Arm, Konica Minolta Range7, Aicon 3D System StereoScan) and low-cost devices (e.g. RGB-D cameras, e.g. Kinect, Intel RealSense, Occipital Structure and flight time cameras (ToF), e.g. Kinect v2). Due to the high cost of professional technologies, several state-of-the-art 3D modeling applications use low-cost devices [11, 12]. Unfortunately, to date, hand-wrist-arm district scanners (integrating professional or low-cost technologies) require the patient to remain static for an extended period (at least 30 seconds). As explained above, the speed of the acquisition process is still a key feature to minimize artifacts due to the movement of the subject. As a first step, therefore, we proceed to the choice of a sufficiently compact and accurate low-cost acquisition device. The compactness of the device will allow to position the cameras in such a way as to obtain a 360° coverage of the limb. The ergonomics of the scanner will also be considered, in order to accommodate the patient's arm in the most comfortable way possible, avoiding movements that could invalidate the scan.

ii.   Device modeling

Two main strategies for creating a CAD model of an orthosis can be identified at the state of the art: a) the adaptation of a predefined model to the scanned geometry [35–37] or b) a manual procedure performed in a CAD environment [14–19]. Most of the methodologies described in the literature do not guarantee the achievement of a medically valid result [16, 19] nor do they allow an easily usable and scalable framework for application in clinical practice. In particular, these latter objectives would be achieved by implementing a fully automated procedure that: 1) does not require the user to have technical CAD skills; 2) does not require significant time for the generation of the CAD model; 3) is validated with respect to a set of clinical studies. To achieve such an ambitious and challenging result, an important first step is to create a systematic procedure to produce a consistent orthotic model using common CAD tools. The procedure identified can then be automated, in whole or in part.

iii.   Device production

The orthosis can be made using Additive Manufacturing techniques, which represent the perfect solution given the complex and variable shape of the orthopaedic device due to the specific anatomy of the patient. Paragraph 4.2 provides more details about the printing techniques and materials chosen.

Thoracic malformations - technical framework

i.   Anatomy collection

The second pilot case, as said, has not yet been analysed at the state of the art. Also in this case we intend to realize a low cost and accurate scanner. The idea is to acquire the chest of the patient from lying down and, to increase the comfort and accuracy of the result, the speed of acquisition is a fundamental requirement. As a first step, therefore, we proceed to choose a sufficiently accurate low-cost acquisition device. The portability of the scanner will also be considered, to be able to move and position the system easily.

ii.   Device modeling

As already introduced for the case of arm orthoses, if we intend to allow clinical staff to model the device without the need for expert intervention, it is necessary to implement a procedure that does not require CAD technical skills and does not require significant time for the generation of the model. To achieve this, a first step is to create a systematic procedure to produce a consistent orthotic model using common CAD tools. The procedure identified can then be automated, either fully or in part.

iii.   Device production

Unlike the first pilot case, for which additive manufacturing techniques represent the most suitable scenario, given the conformation and stiffness characteristics of the device, in this second case the creation of the personalized Vacuum Bell will take place through the casting of silicones into moulds specially made with additive techniques. This difference lies in the fact that the body of the Vacuum Bell must be adaptable to the chest and deformable.

3.3. Clinical applications

Verification and validation

Once the process of creating the tool for the serial production of custom medical devices has been completed, intended both as an acquisition device and as the implementation of the procedures for creating the CAD model, it is necessary to validate the entire system. It is therefore necessary to define checks and controls that are useful to assess, under various aspects, the degree of compliance and adherence of the system specifications to what emerged

in the phase of defining the needs. The intention is to check the product and check whether the medical device has been designed correctly, whether it meets the specifications and is therefore correct. Other checks may include completeness, i.e. whether all requirements have been taken into account, and safety, i.e. the confidentiality of the data processed and regulatory compliance.

After verification of the device, validation is required, a phase in which it is checked whether the right device has been designed for the intended purpose. The device produced should be checked by the physician to ensure that each item meets the appropriate specifications and standards. Validation is therefore a control activity that occurs at the end of the product development process. It is designed to confirm not only proper technical functioning, but also proper usability and ability of the object to perform the functions for which it was designed, i.e. to ensure clinical effectiveness and benefit to the patient against a proper assessment of the associated risk. The validation must provide confirmation that the products manufactured in the production environment, with all the criteria that the production will adopt and with the direct contribution of the production staff, meet expectations

Clinical trial

Once the instrument has been verified and validated, we proceed with the clinical trial. A clinical trial is a type of research conducted to collect data on the safety and efficacy of new drugs or devices. These trials can only be conducted after sufficient information on product characteristics and preclinical safety has been collected.

The protocol of a clinical trial describes the scientific basis, objectives, design, methodology, statistical considerations, and organization of the trial planning.

An essential component to start a clinical trial is to enrol subjects for the study, following a procedure that consists of signing a document called "informed consent". Informed consent is a process defined as legally directed at a person who is told the key factors of a clinical trial, before deciding whether to participate or not. The researchers provide a document for informed consent that includes the clinical trials, as well as its purpose, duration, required procedures, risks, potential benefits. The participant then decides whether or not to sign the document. Informed consent is not an immutable contract, participants may withdraw at any time.

All studies involving medical or therapeutic intervention on a patient must be supervised by an ethics committee before permission is given to proceed with the clinical trial.

 In the clinial trial phase it will therefore be necessary to choose the duration of the trial and the number of patients to be enrolled with the aim of obtaining a statistically significant result. It is also important to define the criteria for inclusion and exclusion from the study, as well as the criteria for stopping the trial.

Usability

Another important step is the evaluation of the usability of the software produced. According to the ISO 9126 series of standards, the largest software quality model developed to date [38], usability is interpreted as "the extent to which a product can be used by specific users to achieve certain goals with effectiveness, efficiency and satisfaction in a given context of use. Usability can be expressed as the ability of the software product to be understood, learned, used and attractive to the user, and is a combination of factors including: intuitive design, ease of learning, efficiency of use, memorability, frequency and severity of errors, subjective satisfaction. Evaluating usability is a fundamental step for the User-Centered Design (UCD) framework for software development, defined in ISO-13407 [39]. Consequently, the

evaluation of usability must take place within the project lifecycle and the results of the evaluation must be translated into any changes to the project.

3.4. Definition of a generic pipeline

The above can be summarized in a framework applicable every time it is intended to approach the implementation of a custom medical device, with the idea of having a low-cost acquisition system and simple tools for implementation.

The defined workflow, shown in Figure 3-1Figure 3-1 Diagram outlined to achieve the systematic realization of customized medical devices, is composed of the following steps:
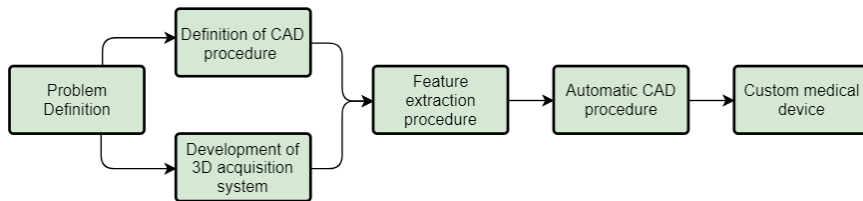
Figure 3-1 Diagram outlined to achieve the systematic realization of customized medical devices.

Problem definition: in this first phase engineers and doctors together define the final purpose, the main aspects of the system and of the medical device.

Definition of CAD procedure: in this phase we proceed to define the operations leading to the creation of the CAD model of the customized device in view of the future automatization of the entire process, choosing repeatable operations and highlighting the main steps.

Development of a dedicated 3D acquisition system: this phase can be launched in parallel with the one described above and refers to the creation of an ad-hoc acquisition system for the problem under examination. Specifically, it will be composed of several main steps such as the choice of the type of acquisition device and the number of devices required, as well as their reciprocal position and with respect to the anatomy to be acquired. This phase also foresees the development of a control program of the acquisition devices to make the collection of the anatomy simple and effective.

Feature extraction procedure: in this phase the two previous phases are combined. In fact, according to the specific CAD procedure defined in phase two, the acquisition system will have to extract some characteristics from the 3D anatomy, as transparent as possible to the user. In some cases it is possible that the extraction of these characteristics requires the intervention of the physician, in which case the program must be able to provide a simple interaction with the 3D model.

Automatic CAD procedure: by providing the characteristics extracted in the previous step, the CAD procedure can be automated or semi-automated to make the creation of the printable model simple and intuitive, eliminating the need for an expert modeler for the creation of each new device.

Custom medical device: the production of the device with additive techniques will be followed by a phase of verification and testing of the device itself within the hospital.

It is therefore expected that this workflow can be applied generally whenever the problem of developing personalised medical devices is to be addressed. In the following

chapters the framework will be applied separately to the two pilot cases. Specifically, the following chapter will refer to the problem of custom orthoses and the next to chest malformations and the development of corrective devices.

4. RE&AM methods and tool for personalized orthosis

The following are realization phases of the acquisition system of the hand-wrist-arm district and the consequent realization of the personalized orthosis. As explained above, the clinical specifications were initially defined, followed by the implementation of the acquisition system and the semi-automatic procedure for the realization of the orthosis. Finally, the system has been clinically tested.

4.1. Clinical specifications
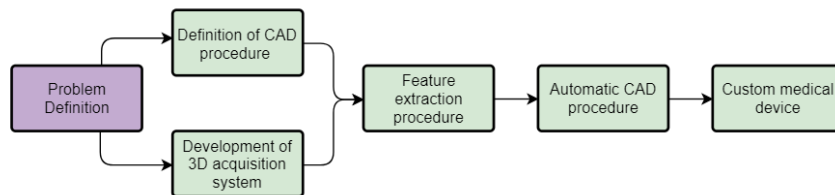
Figure 4-1 Diagram outlined to achieve the systematic realization of customized medical devices

In this first phase, the treated types of fractures and the main characteristics of the external corrective device, the orthosis, were defined in collaboration with the orthopaedists.

The device has been design considering "buckle" fractures, also known as "torus". A buckle fracture occurs when a bone "buckles", or slightly crushes in on itself. The most common type of buckle fracture in children occurs in the forearm, near the wrist, usually after a child falls onto an outstretched arm. The injury affects mostly the radius bone. The radius runs from the elbow to the hand. It makes up the forearm along with the ulna, the bone that runs alongside it. The 'distal' part of the radius is the part furthest away from the centre of the body, in other words, nearest the wrist. Buckle fractures occur only in children and are very common. Children's bones are softer than adult bones and able to bend and compress without fully breaking. Although the bone does not fully break, the fracture can still cause pain.

The age range is the main constraint for the design of the scanner as this data is defined as the majority of design choices. The age range indicated for the required device is between 3 and 14 years old, in this range the region to be acquired is subject to a large change in size. The most complete document about the variation that the part of the arm can assume in the considered age is dated 1975 [40], in which are reported the quantities about the anthropometric characteristics of children, both male and female, of the U.S. contained in the document are divided by 5°, 50°, 90° percentile; for this study it was chosen to use the data referring to the 50° percentile, as it represents the dimensions assumed by the greatest number of children. The data of interest, present in the design document and shown in Figure 4-2 , are:

- The length of the forearm, considered as the distance between the elbow and the tip of the middle finger;
- The length of the hand, defined as the distance between the wrist and the tip of the middle finger;
- The width of the hand, defined as the distance between the index finger and the little finger;
- Finger length, defined as the distance between the knuckles and the middle fingertip;
- The circumference of the forearm, defined as the circumference near the elbow;
- The circumference of the hand, defined as the circumference measured near the knuckles;
- The inner diameter of the hand grip.

Lunghezza Avambraccio

Età	
3	24.9
4	26.3
5	28.2
6	29.8
7	31.4
8	32.7
9	34.4
10	35.5
11	37.6
12	39.1
13	40
14	40.6

Lunghezza Mano

Età	
3	10.6
4	11.1
5	11.8
6	12.5
7	13
8	13.6
9	14.1
10	14.5
11	15.4
12	15.6
13	16
14	16.4

Larghezza Mano

Età	
3	5
4	5.2
5	5.5
6	5.8
7	6
8	5.2
9	6.5
10	6.6
11	6.9
12	7.2
13	7.3
14	7.5

Lunghezza Dita

Età	
3	4,4
4	4,6
5	4,9
6	5,2
7	5,5
8	5,7
9	6
10	6,1
11	6,5
12	6,5
13	6.8
14	7

Circonferenza Avambraccio

Età	
3	15,1
4	15,5
5	15,9
6	16,4
7	17
8	17,4
9	18,2
10	18,6
11	19,8
12	20,6
13	20.8
14	21.2

Circonferenza Mano

Età	
3	4,24
4	4,37
5	4,57
6	4,72
7	4,92
8	4,99
9	5,14
10	5,31
11	5,55
12	5,74
13	5,84
14	5,94

Diametro Interno Impugnatura

Età	
3	2,81
4	2,93
5	3,15
6	3,33
7	3,51
8	3,67
9	3,83
10	3,99
11	4,24
12	4,38
13	4.5
14	4,61

Figure 4-2 Anthropometric characteristics of children regarding the lengths of interest.

These values have been used for the realization of a 3D CAD model of the arm that will be used for the definition of the position of the cameras through simulations and to define the arm support type and dimension, as we will see in the next section.

As far as the disposition of the limb is concerned, there is another constraint: the interested zone, the hand-wrist-arm district, must be placed in a horizontal position (Figure 4-3). While no constraints are defined, neither on the distance that this region must assume from the torso, nor on the height with respect to the shoulder.

Figure 4-3 Position of the articulation to be acquired.

In collaboration with orthopaedics, the 3D printed cast is designed (see Figure 4-4) as two separate halves, one resting on the back of the hand and the other on the internal side, to ensure an easy fit. The two halves are joined together by a three-zip closure system. The connectors are held in place by a designated housing system.
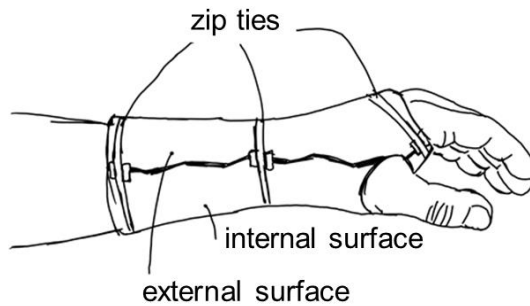

Figure 4-4 Prototype concept of custom orthosis.

According to the common medical practice [31], the effective treatment of a wrist fracture requires the application of a restrictive device, which, regardless of its production technology, assures the compliance with the fundamental requirements described below. The hand-wrist-arm district needs to be rigidly constrained during the entire treatment, which usually requires four weeks for healing. During this period, the arm position needs to be in a resting configuration, with the hand defining an angle of 10°-20° with the arm [32], as shown in Figure 4-5a.
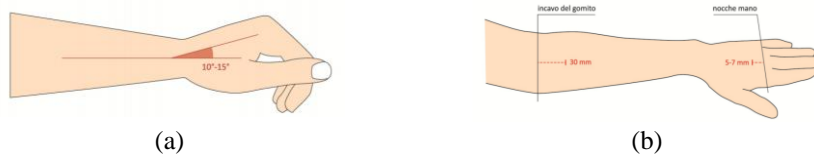
(a)   (b)

Figure 4-5 a) Hand/arm angle in resting position; b) reference lines representing the limit of the orthosis.

Considering the principal direction of the arm (Figure 4-5b), the device must begin within ~3cm from the elbow recess and must end few millimetres below the knuckles, to ensure mobility of the fingers. The hole for the thumb must be positioned to allow mobility to the proximal and digital phalanges and to prevent discomfort. Moreover, the device must have a good adhesion to the arm surface in order to hinder articulation movements as well as rigid movements between the arm and the device itself.

Some basic characteristics that a personalized orthosis must guarantee have been outlined: complete customization (the internal surface of the brace must perfectly follow the surface of the limb); particular attention must be paid to the bone protrusions, where pressure fields could be generated causing pain and skin irritation to the patient; skin transpiration through the creation of holes of suitable shape; biocompatibility of the material in extended contact with the skin; possibility of opening the orthosis for dressings and periodic checks by medical personnel.

As far as the specifications of the acquisition system are concerned, in addition to the scanning speed, which is necessary to avoid introducing errors to the model, the system must be compact, low-cost and have a sufficiently safe and resistant structure. In addition, all necessary precautions must be taken at the design stage to prevent accidental impacts from causing structural failure or tipping over of the device. In addition to these basic features, the system must be easy for hospital personnel to use and must be able to provide procedures and tools for making the CAD model of the device.

4.2. Technical framework

The creation of a dedicated acquisition system, with low cost and adequate precision characteristics, is composed of a number of successive choices, as already introduced in paragraph 3.2. In the first instance, among the low-cost devices available on the market, the one most suited to the needs of the specific case was chosen. The choice of the device was supported by the metrological characterization and the evaluation of the performance of the device itself and the comparison with other similar devices to validate its feasibility. The number and position of the cameras were then chosen to best acquire the hand-wrist-arm district. The software was then developed to allow the collaboration of the devices for the creation of the final 3D model, which can be used to model the orthosis.

In the following phase, a CAD procedure with robustness and repeatability characteristics was developed. The software was then updated to extract the features needed to automate the procedure, the execution of which is then made fully automatic in the CAD environment.

In the following paragraphs each step, which can be associated with a macroblock of the pipeline defined in 3.4, is described in detail.
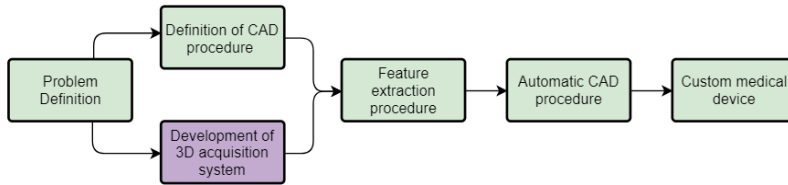
4.2.1. **Choice of 3D acquisition sensor**

Figure 4-6 Diagram outlined to achieve the systematic realization of customized medical devices.

Human oriented 3D scanners pose new challenges in the panorama of existing optical measurement systems; in fact, the agile and deformable human nature, imposes the acquisition to be specifically fast to avoid movement artefacts. Nowadays very good results are possible with the existing body scanners (both professionals and consumer devices) however, focusing on relative complex shape of some body details, the results still lack precision and acceptable accuracy. This is particularly true when the human body (of some of its parts) is acquired by using low-cost devices such as, for instance, the Microsoft® KinectTM [41] and the Intel® Realsense [42] i.e. camera systems able to provide both color and dense depth image. These sensors have been recently applied in a huge number of industrial and biomedical applications. Compared with traditional 3D scanners, these sensors can capture depth and RGB data at video rate. Despite both the RGB quality and the depth resolution are limited, the major benefit comes from the overall acquisition speed and the near IR pattern that allows the acquisition in poor lighting conditions as well as on dark surfaces. Consequently, the use of such devices rapidly grew especially regarding the human motion analysis [43] but also for creating low-cost body scanners. An early publication dealing with the use of Kinect™ as a 3D body scanner was performed in 2012 demonstrating the effectiveness of approaches based on the use of low-cost device for this kind of application [44, 45]. Unfortunately, several drawbacks remain in developing full body scanners based on RGB-D sensors. First, the depth data captured is of extreme low quality (low X/Y resolution and depth accuracy) especially when dealing with non-static bodies (like living human bodies are) that should be measured instantaneously [46]. Furthermore, RGB-D sensors require relatively long computational time to reconstruct a complete model from the scan data (and the obtained model is often unreliable). Eventually, to increase the resolution of the acquired body/body part requires the contemporary use of multiple devices with several problems related to registration, superimposition of projected IR patterns, data flow management etc. Such critical drawback remains unsolved also when dealing with the instantaneous acquisition of the hand-wrist-arm anatomy. Required in a variety of applications related to robotics, medical devices (cast and orthosis), tailor made jewelry as well as sport and fashion apparel, the peculiar geometry of human HWA remains one of the most challenging part to measure.

As mentioned a number of 3D scanners are available in the market, roughly divided into two main categories: professional 3D scanners (e.g. Romer Absolute Arm [47], Konica Minolta Range7 [48], Aicon 3D System StereoScan [49]) and low-cost devices such as, for instance RGB-D cameras (e.g. Kinect [41], Intel RealSense [42], Occipital Structure [11]). Even if this last typology of devices was specifically conceived to address topics related to face analytics and tracking, scene segmentation, hand and fingers tracking, gaming and

Augmented Reality [50–52], they prove to have the potential to be used as a low-cost 3D scanner [45, 53]. For this reason, together with the need of scalability of the proposed system, among commercial 3D scanners, it emerged in terms of performances and versatility the new Intel RealSense SR300 frontal camera. SR300 is a short-range camera that uses coded light 3D imaging system.

Intel® SR300 depth camera

The SR300 is the second generation of front-facing Intel® RealSense™ cameras. It is a subassembly camera product that implements a short range (SR), coded light, 3D imaging system (Figure 4-7).
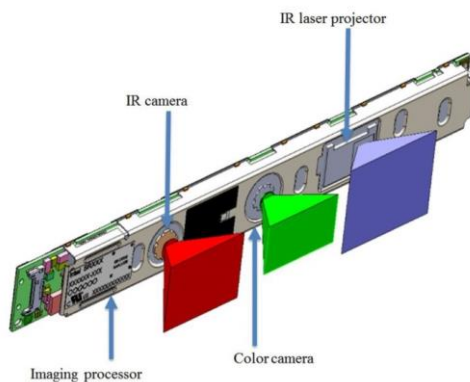
Figure 4-7 Components location inside the camera.

Along with an infrared laser projector, the subassembly includes a Fast VGA infrared camera and a 2-Mpixel RGB color camera with an integrated image signal processor. Fast VGA depth mode reduces exposure time and allows dynamic motion up to 2 m/s. This new feature leads to a less-noisy result when the scene is not static, as can be qualitatively seen in Figure 4-8 where a moving hand, captured respectively with a F200 and SR300 camera, is shown.

Figure 4-8 A single depth frame of a moving hand captures with F200 depth camera (left) and SR300 depth camera (right).

The SR300 also provides synchronized color, depth, and IR video streaming to the client system. The effective range of depth is optimized from 0.2 m to 1.5 m for use indoors. The dimensions of the device are approximately 110 mm x 12.6 mm x 3.8–4.1 mm; its weight is 9.4 g, which makes it very compact and well-suited for a wide range of 3D imaging

applications.

The manufacturer overall technical specifications of Intel® RealSense SR300 are summarized in Table 4-1. Although the overall camera range is 20-150 cm, the range for using the sensor as a pure 3D scan is suggested to stay within 70 cm.

Table 4-1 Technical specifications of Intel RealSense SR300.

Technology	Coded Light, Fast VGA 60 fps
Colour Camera	Up to 1080p 30 fps, 720p 60 fps
Indoor Range	20-150 cm
Depth FOV (DxWxH)	88+/- 3°x71.5+/- 2°x55 +/- 2°
Depth fps	30/60
IR fps	30-300

Beyond such a distance, the accuracy of the camera drastically decreases, as shown in Figure 4-9 in which a plane wall portion is captured at incremental distance from the camera, starting from 20 cm up to 150 cm with a step of 10 cm approximately.

The horizontal resolution (usually named "point density") of a 3D optical scanner is defined as the spatial sampling frequency of the area framed in the orthogonal position with respect to the sensor. This area will increase with increasing distance of the sensor from the surface, producing a decrement of the point density. Intel® SR300, having a depth camera resolution of 640x480 pixel and a depth field of view of diagonal 88°x width 71.5°x height 55°, makes no exception as demonstrated in Table 4-2 where point density measured at increasing distances of the sensor from the scene is listed.
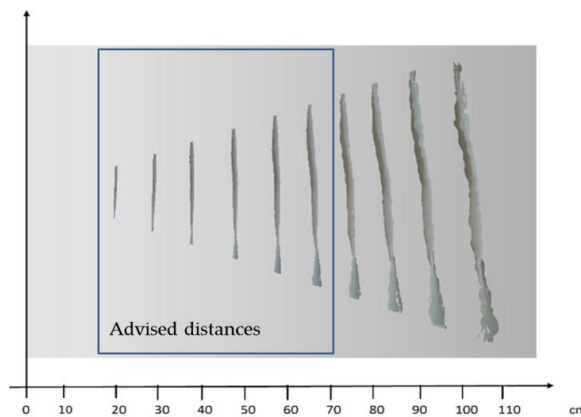

Figure 4-9 Qualitative evaluation of the error introduced in measuring a flat surface. Over 70 cm the acquisition degrades considerably, thus restricting the use of the sensor as a 3D scanner to such distance.

The table has been populated computing the scale factor as follows in which the scale factor of the depth image at different distance is given by the following relation:

$$scale\ factor = \frac{sen(\beta)*(d)}{sen(\delta)*\#pixels} \tag{1}$$

where d is the camera-subject distance, β is half of the opening angle and δ the angle of incidence of the camera.

Table 4-2 Technical specifications of Intel® RealSense SR300.

Distance	Scale factor	X	Y	Framed area	Point density
[mm]	%	[mm]	[mm]	[mm2]	[Points/ mm2]
200	0.4	256	192	49152	6.25
450	1	640	480	307200	1.00
600	1.3	832	624	519168	0.59
800	1.8	1152	864	995328	0.31
1000	2.3	1472	1104	1625088	0.19

The overall performance of a depth camera system is highly influenced by the used pattern projector illuminator. The Intel® RealSense cameras partially overcomes the limitation of temporal multiplexing [54] illuminators (i.e. unreliable in case of fast moving scenes), by leveraging the innovative MEMS mirror technology [55] to speed up the pattern frames projection time. This is possible thanks to the use of a miniaturized projector made of three tiny components: an IR laser, a line lens and a resonant micro mirror. The line lens takes the point of light from the IR laser and turns it into a flat horizontal line. This is subsequently bounced off the resonant micro mirror, which is twisted by an electrical signal. This micro mirror is moved by a torsional drive system, where an electrostatic signal twists the mirror, which is manufactured in a single piece. The combination of lens and rapidly moving mirrors creates a pattern of light that is projected, and the reflection is detected by the IR camera on the other side of the module, which is used to acquire the scene.

The new RealSense camera provide a rich SDK library that allows to configure the camera with a number of internal settings, such as Accuracy, Filter Option, Laser Power and so on: some of them are post-processing settings, others are acquisition settings; furthermore, a set of default configurations are possible. Such versatility allows users to arrange the best possible setup for the task under study.

SR300 - metrological and critical characterization
In the first instance, given the potential of this device, it was decided to characterize and provide metrological considerations on the Intel® RealSense™ SR300 depth sensor when it is used as a 3D scanner. To this end, the device sensor performances in terms of accuracy of indication of size and form, are firstly assessed by applying the VDI/VDE normative (i.e. the international standard for characterization of measuring devices) to a set of raw captured depth data. Limiting the analysis to the raw data extracted only by the depth sensor allows to discard possible signal processing of the many filters available on the released cross-platform camera capture for Intel® RealSense™. In other words, the analyzed sensor data are processed using

the normative without optimizing it so as to detect the worst possible conditions a user might incur in using the SR300 device.

Further assessment of the device performances is carried out by using "real life" setting (i.e. selecting an optimized profile for the use as a 3D scanner) and by applying best practices proposed in literature.

Additionally, the performance of the device is critically compared against the performance of latest short-range devices.

The main issue related to the performance assessment of the above-mentioned devices, is related to the lack of a comprehensive internationally-recognized standard (or a guideline) helpful in defining a common language between users and manufacturers.

As such, the inadequacy of standard characterization methods from trusted sources make it difficult for a user to select a device among others, based on the specification sheet provided by the manufacturer. This is particularly true for close range systems where the gap in the existing documentary and physical standards is more evident. Examples of this gap are related to the lack of methods for performance assessment on free-form surfaces, for accuracy of 3D moving cameras acquiring static objects, or for the accuracy of 3D static cameras acquiring moving reference [56].

According to the considerations made above, international standards can be only partially applied to assess the performance of the Intel® SR300 depth camera, resulting inadequate to discover all its potential. Therefore, standard procedures commonly used for measuring devices are here complemented with practices proposed in scientific literature.

The measurement range in close range applications may vary from few centimeters to one meter. The trustworthiness of depth camera systems is crucial to determine whether the acquired data fits the specific application requirements. The purpose specifications are also important in defining test methods that highlights impartial weaknesses and strengths of the systems. To fairly quantify the overall accuracy of the 3D optical imaging system, appropriate physical standards, together with related tests procedures, are needed. The goal of a standard is to provide a way to evaluate product performance for a specific need. Close range, structured light based scanners, need to be verified over their close-range volume and often, over multiple registered 3D images representing a 360 degrees' object surface.

VDI/VDE Normative
The only available short-range 3D imaging standard today is the German standard VDI/VDE 2634 [57]. The specific guidelines for the acceptance and reverification of optical based 3D scanning systems cover the following issues:

    Part 1: "Imaging systems with point-by-point probing";
    Part 2: "Optical systems based on area scanning";
    Part 3: "Multiple view systems based on area scanning";

Since The VDI/VDE 2634 is derived from coordinate measuring machines (CMM), it naturally considers measurements at close range.

A comprehensive report on standards developments of 3D imaging systems is reported in [56]. VDI/VDE guideline defines a method of measuring a reference object (sphere, plane), which is typically used to define some basic feature of the analyzed optical system. To assure traceability of 3D measurements of a specific device, acceptance test and re-verification are

univocally defined.

Acceptance test involves the measurement of a calibrated artefact; the test is accepted if the error lies inside the limits specified by the manufacturer, while the re-verification test is a repetition of the acceptance test over time.

The VDI/VDE 2634 also recommends the artefacts, the procedure and the method to calculate the results, and the interpretation of the results. VDI/VDE defines three types of standard object: a sphere, a ball bar and a plane; some examples of calibration standards are shown in Figure 4-10 and the recommended arbitrary positions are illustrated in Figure 4-11.

The guidelines propose to use diffuse reflecting test objects materials, certified with a known level of accuracy and uncertainty (4-5 times better than the device under test).

Figure 4-10 Examples of 3D calibration standards for probing error and flatness error calculation according to VDI/VDE 2634.
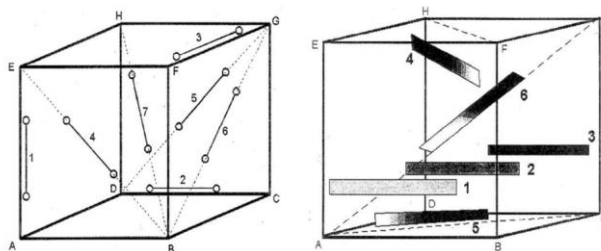
Figure 4-11 Recommended arbitrary positions within the systems field of view covering the working volume.

The considered operations are performed on a single point cloud or on a multi-view registered point cloud, as described below; the normative also allows the measured values to be filtered and pre-processed only if they are part of the boundary conditions for the characteristic test, or it is a routine event in the operation of the system.

Being L0, the main diagonal length of the scanning volume, the sphere diameter must be between 0.1 and 0.2 times L0. The characteristic estimated with such a sphere is the Probing

Error P that describes the characteristic error of the system within a small portion of the measuring volume attempting to evaluate the intrinsic properties of the 3D imaging sensor. The form probing error is the range of radial distance between the real measured points and a best-fit sphere evaluated according to the least-squares method. The size probing error is the difference between the estimated (as the best fit sphere) and the "true" diameter of the sphere. The guidelines recommend to survey at least ten uniformly-distributed positions of the artefact within the operative volume.

The ball-bar is a bar connecting two spheres. The distance among the ball centres is Lp and must be larger or equal to $0.3 \cdot L0$. The characteristic estimated with this artefact is the Sphere Spacing Error SD that proves the capability of the system in measuring lengths. SD is the difference between the acquired distance and the "true" distance between the centres of the two spheres (estimated from the point cloud of data using a best-fit sphere-fitting); the guidelines recommend to survey at least seven positions within the operative volume.

The plane is a rectangular parallelepiped wide at least 50 mm and long not less than $0.5 \cdot L0$. The characteristic estimated with this artefact is the Flatness Measurement Error F that is the range of the signed distances of the measured points from the best-fit plane; the guidelines recommend to measure at least six different orientations of the artefact.

  The normative indicates that only 0.3% of the worst data can be rejected for such test. However, no indication about the number of points needed for the test is reported. Therefore, the results cannot be compared fairly between different types of scanners or other types of measurement instruments.

The more recent part of the VDI/VDE 2634 (Part 3) is dedicated to the most common scenario found in many applications: the multiple 3D views. The 3D views are commonly aligned each other in the same coordinate system through an ICP algorithm [58]. The probing error is affected by two influence factors: the errors of a single 3D image (as found per Part 2 tests) and the errors due to the transformation of the different 3D images in a unique coordinate system. As for the Part 2, both form and size describe the quality parameter. The sphere artefact is suggested to be surveyed in at least three arbitrary positions within the operative volume, and for each of them, the artefact must be measured from at least five sensor positions to fully capture the surface.

The sphere-spacing error is used to test the capability of the complex system of performing length measurements. The error is computed using ball bars, ball beams, gauge blocks, step gauges or ball plates. The actual procedure requires a reference artefact that is fully characterised, i.e., the calibration certificate must contain both the spacing and the form of all probing elements and the roughness of the surfaces should be negligibly small. The reference artefact is measured in seven different positions.

Other approaches provided in literature

The scientific community has been working worldwide on possible characterization protocols to assess the devices performances and comparing each other in many operating fields: new parameters has been investigated, new standard artefacts proposed as well as new procedures devised. Gonzalez-Jorgea et al [59] proposed a metrological comparison between Kinect v1 and Kinect v2 by using a certified standard artefact developed at University of Vigo based on 5 spheres and 7 cubes. The accuracy and precision tests are done for different ranges and changing the inclination angle between each sensor and the artefact. Wasenmuller et al. [60] investigated the accuracy and precision of the Kinect v1 and v2 for their usage in the context

of 3D reconstruction, SLAM or visual odometry. They based the accuracy and precision of the devices on a ground truth (a planar wall) detected through the pose estimation of a checkerboard on the wall. They tested the devices performances in terms of varying temperature, camera distance and object color.

Zennaro et al [61], compared the depth data that can be obtained using two depth camera sensors, pointing out the devices performance in terms of accuracy and robustness to artificial illumination and sunlight. The same result of range depending accuracy is found by Khoshelham et al [62] where, to investigate the systematic errors in Kinect data, a comparison is accomplished with a point cloud (the ground truth) obtained by a high-end laser scanner. The first generation of Microsoft device is also investigated by T. Dutta [63] to determine whether the hardware sensing components were sensitive enough to be used as a portable 3D motion capture system for workplace ergonomic assessments. Dutta compares the acquisition of four cubes obtained with both Kinect v1 and a Vicon motion capture system (considered as the ground truth). Menna et al. in [64] evaluate the Kinect accuracy in modelling indoor environments by measuring a special rigid test-field with a calibrated reference scale bar.

The suitability and accuracy of RGB-D cameras for close range 3D modelling was investigated by Lachat et al [65]; their study highlights errors arising from the environment and the properties of the captured scene and reflectivity of the items. A model automatically obtained using an appositely devised tool is compared to a ground truth model. Breuer et al [66] also provided an analysis of measurement noise, accuracy and other error sources with the Kinect v2, pointing out a significant distance dependent error and that the device is capable of better resolving fine structures in certain scenarios although the image resolution of the depth camera has been decreased. Guidi et al. [67] proposed a simple yet effective method for estimate the systematic error that once modelled can be eliminated through a proper calibration. The 3D digitizer is considered as a "black box" system whose behavior influence the 3D cloud differently at different spatial frequencies. Given that the system uncertainty is given by random and systematic errors, they model the global random contribution of each range image of a reference plane as Additive White Gaussian Noise (AWGN) that is associated to high spatial frequency. By means of a smoothing filter they filter out the random errors thus estimating the systematic error.

Experimental results

Data acquisition for the sensor characterization was carried out using a dedicated software, developed by means of the open source library "Librealsense" [68], which is a cross-platform library that allow access to the Intel® Realsense device. The point clouds have been acquired after the first 30 frames to allow an initial camera stabilization.

In the following paragraphs, a description on how the Intel® SR300 overall accuracy has been assessed by following both applicable rules stated in the VDI/VDE standard and literature methods to assess other camera features relevant for close range applications.

As mentioned, the experimental results obtained by applying the VDI/VDE normative are firstly performed by decoupling the contribution coming from the sensor raw data from the contribution of the processing of the many filters available on the released cross-platform camera capture for Intel® RealSense™. Consequently, the analysed sensor data are processed without optimizing it thus allowing to understand which the worst performances of the device are when used as a 3D scanner. After this preliminary analysis, the VDI/VDE standard has been applied with reference to optimized camera setting, but still taking into account only the

data coming from depth sensor (information from RGB sensor have not been considered). Then, systematic errors affecting the device (with optimized setting) during 3D acquisition are analysed with the help of a Coordinate Measuring Machine. Finally, a multiple-view acquisition of two objects is carried out to qualitatively assess the overall performance of (optimized) device.

VDI/VDE-based performance test using raw data

Inspired by the VDI/VDE 2634 Part 2 recommendations, the device performance test has been carried out first by identifying the auxiliary parameter L0 defined as the body diagonal of the measuring volume. As mentioned above, this parameter is needed for sizing the spheres, the bar and the plane for the performance evaluation test.

The normative suggests a sphere diameter between 0.1 and 0.2 times L0; this translates in the present case, in a diameter between 9.5 and 19 cm. The distance between the spheres in the ball-bar should be larger than 0.3* L0, i.e. in the present case larger than 28.6 cm. The plane should wide at least 0.5 cm and long at least 0.5* L0 thus resulting ranging from 0.5 cm and 47.6 cm. Accordingly, selected target to be acquired are: 1) a single sphere with diameter of 14 cm; 2) a ball-bar composed of two spheres with diameter equal to 14 cm fixed at 39.2 cm from one another and 3) a plane iron bar of dimension 5 cm x 50 cm (see Figure 4-12).

The balls material is polystyrene which proves to have optimal diffusive infrared reflection proprieties, even though not certified as suggested by the normative.

(a)

(b)

(c)
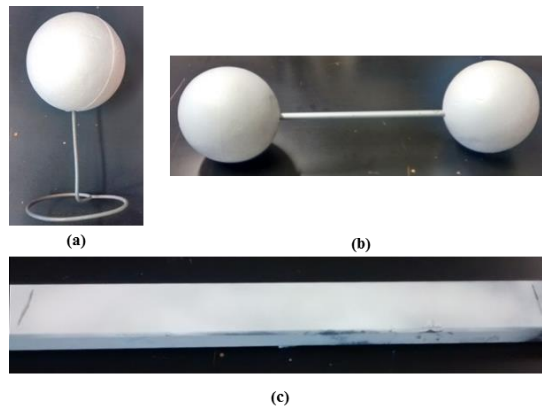
Figure 4-12 Artefacts proposed to measure the quality parameters inspired by the VDI/VDE normative; (a) single sphere having diameter of 14 cm; (b) ball-bar composed of two spheres with radius of 7 cm fixed at 39.2 cm from one another; (c) iron bar of dimensions 5x50 cm.

To deal with the lack of a certification for the target artefacts, these have been acquired by using a high precision laser scanner, the Romer Absolute Arm 7520 SI/SE that has an overall accuracy of ±0.063 mm, therefore allowing to obtain a sufficiently reliable "reference measure". In other words, the 3D scanned data obtained with the Romer scanner are considered the ground truth for testing the SR300 device.

The camera is mounted on a stable tripod in front at the cuboid at 20 cm from its smallest face. Not to leave any blind area when choosing the reference working volume, for close range 3D acquisitions evaluation, a truncated pyramid having diagonal equal to 953 mm

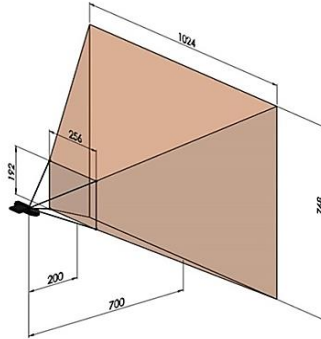(see Figure 4-13) has been considered as the device actual working volume.

Figure 4-13 Truncated pyramid delimitating the working volume boundaries.

VDI/VDE-based tests have been repeated 4 times using two samples of SR300 devices to avoid the possibility of testing a defective device. Since the maximum percentage difference, in absolute terms, between two couple of parameters (see below) acquired using the two devices is within 3%, tests can be considered reliable.

1) Probing error evaluation

The first test consists of evaluating the probing error both in terms of form and size. Accordingly, the target sphere has been positioned in 10 sequential arbitrary locations (as indicated in the normative) within the working volume (see Figure 4-14a). The form probing error (PFi) is defined for each acquisition, as the range of radial deviations of the measured spheres points and the best-fit sphere:

$$P_{Fi} = R_{imax} - R_{imin} \qquad (2)$$

Where R_{imax} and R_{imin} are, respectively, the maximal and minimal distance of the measured surface points of the ith sphere from the centre of the compensating element (i.e. the best-fit sphere).
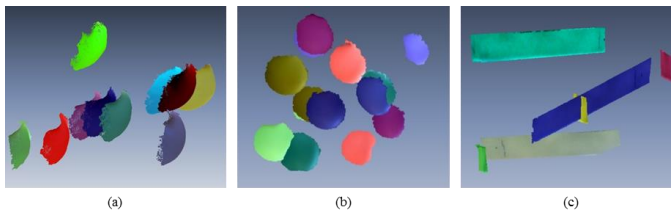
Figure 4-14 (a) 3D recording of the single sphere captured in 10 arbitrary positions homogeneously distributed within the working volume. (b) 3D points of the ball-bar captured in 7 positions within the working volume (the same sphere colour corresponds to the same bar). (c) 3D points of the plane captured in 6 positions within the working volume.

The size probing error (P_{Si}) describes for each acquisition, the difference between the estimated diameter (D_{mi}) and the "true" diameter (D_c) of the sphere:

$$P_{Si} = D_{mi} - D_c \quad (3)$$

The estimated diameters are assessed through a best sphere fit process, implemented by the least square method; the "true" diameter, is defined as the one measured on the target spheres using the Romer Absolute Arm 7520 SI/SE, i.e. is the diameter of the ground truth.

From the above defined probing errors, testing form and size of the 10 spheres (repeated 4 times as previously mentioned), it is possible to evaluate the average value of both kind of errors, namely: P_F (average form error) and P_S (average size error). The absolute values of these errors are listed in Table 4-3 (second row).

Table 4-3 Results of the probing error test (size and form), Sphere-spacing and Flatness obtained using raw data and data acquired with optimized parameters.

Device	P_F [mm]	P_S [mm]	SS [mm]	F [mm]
SR300 raw data	13.93	4.57	5.11	19.33
SR 300 filtered data	8.30	1.91	6.05	6.88

2) Sphere-spacing error evaluation

The sphere-spacing error Δl_i is measured by using the balls-bar target. Such an error is defined as the difference between the acquired distance l_{m_i} and the "true" distance l_k (i.e. the one measured with the Romer Absolute Arm 7520 SI/SE) between the centres of the two spheres.

$$\Delta l_i = l_{m_i} - l_k \quad (4)$$

The target sphere has been positioned, in 7 sequential arbitrary locations (as indicated in the normative) within the working volume (see Figure 4-14b).

In Table 4-3 the averaged value of sphere-spacing and flatness errors are reported.

3) Flatness error evaluation

The flatness (or planarity) error (F_i), is computed as the minimum distance between two parallel planes comprising the ith scanned point cloud.

To measure this parameter, the plane has been sequentially uniformly-placed, in arbitrary positions inspired by the VDI/VDE normative, within the working volume as shown in Figure 4-14c.

VDI/VDE-based performance test using optimized data

As mentioned, the objective is to assess the performance of the SR300 device when this is used as a 3D scanner. Accordingly, it is worth to repeat the VDI/VDE tests using optimized parameters (as officially distributed Intel library [69] for 3D scanning). The parameters are: the finest accuracy, e.g. accuracy parameter value equal to 1, and the default filter option value, corresponding to filter number 5. Overall results of the repeated test are in Table 4-3.

Results show that the available signal processing algorithms, can greatly improve the overall accuracy of the system except the sphere-spacing error, representing the traceability of the experiment [56].

Systematic errors

One of the most common systematic errors for RGB-D close-range devices is the so called "distance inhomogeneity" i.e. the set of possible errors coming out from acquisitions at different distances from the sensor.

To study such systematic errors, the camera, set with optimized parameters, is positioned parallel to a white planar wall at different well-known distances to 1) acquire such plane with the 3D device and 2) compare the acquired data with the planar wall. The systematic distance measurement error evaluation has been approached in literature [65, 67, 70] through custom made set up by manually positioning the camera on tripods "parallel" to a wall then moving the tripod.

In this study the perpendicular alignment with the optical axis direction and the acquisition of the planar target (with certified flatness of 3 μm) at increasing distances is performed by mounting the device on a Coordinate Measuring Machine (CMM) (

Figure 4-15).

After securing the device to the CMM, the optical axis direction was detected with the help of a marker placed on the centre of the IR image, by assuring that during the vertical translation of the camera the optical centre remains aligned with the marker (see

Figure 4-16).

(a)   (b)
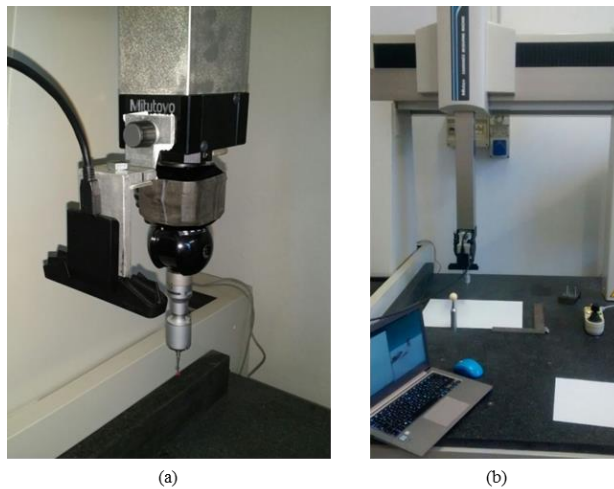
Figure 4-15 The SR300 device mounted on the CMM on the left. The experimental setup on the right.

(a)

(b)
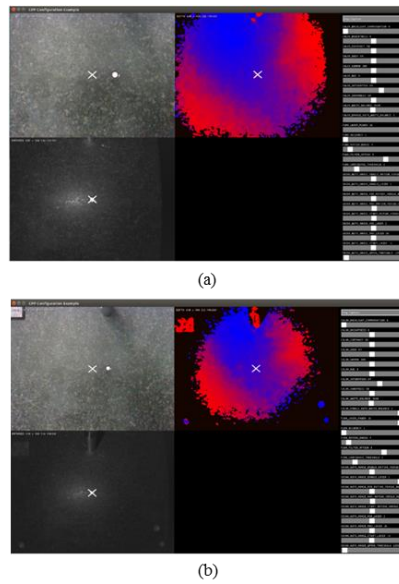
Figure 4-16 The calibration of the optical axis of the camera has been assessed by framing the planar surface of the CMM table and verifying that the IR image centre (the superimposed white cross) corresponds to the depth map centre: (a) close distance (20 cm); (b) far distance (40 cm).

The calibration of the optical axis of the camera has been assessed by framing the planar surface of the CMM table and verifying that the IR image centre (the superimposed white cross) corresponds to the depth map centre.

The acquisition step was performed exploiting the ability of the high precision machine to move arbitrarily along a single axis, incrementing of 5 cm each step, relatively to the CMM coordinate system. The systematic distance inhomogeneity brings two main systematic error components increasing with the distance: the non-planarity and the depth offset, as summarized in Figure 4-17.
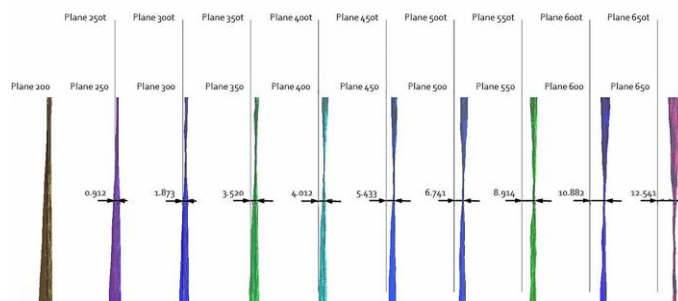
Figure 4-17 The systematic distance inhomogeneity brings two main systematic error components increasing with the distance: the non-planarity and the depth offset.

1) Systematic non-planarity error assessment

To decouple the random error from the systematic one, two approaches are described in literature. One foresees to get more acquisitions for each chosen camera position and averaging them [65]. The other, proposed by Guidi et al [67], consists in filtering out the random error (that it is supposed to occupy the low frequencies) through a smoothing filter.

Inspired by the procedure proposed in [70], the systematic error is evaluated by relying on a precise ground truth to assess the planarity of the reference i.e. by precisely vertically moving the device with respect to the plane. In Figure 4-18 the flatness error for the 10 point clouds acquired by moving vertically the sensor is depicted.
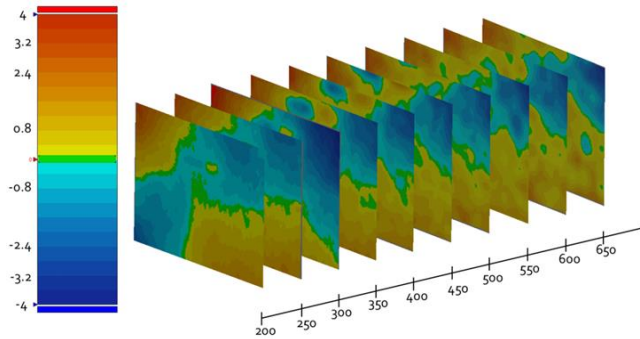
Figure 4-18 Error map between the target white plane and the 10 point clouds acquired using the SR300 device with increasing distance from the plane itself.

2) Systematic depth offset assessment

As reported in [54] the configuration of structured light system is "flexible" this meaning that either a single camera (as in the case of PrimeSense products and the Intel® F200 and SR300) or two cameras (as in the case of the Intel® R200) can be used to acquire the scene. However, all devices can be considered as different members of the same family in the unified framework proposed in [71] by which a system with a single camera and an illuminator is equivalent to a system with two rectified cameras and an illuminator.

As such, to determine the theoretical depth estimation error of the SR300 camera we can consider a scenario with two cameras with focal length f separated by distance b. Let d be the difference in x coordinates, called disparity, of two corresponding pixels. The depth z of the triangulated point is given by $z = \frac{bf}{d}$. The depth error can be rewritten in terms of the disparity error ε_d (when ε_d is small as the pixel size, the approximation holds):

$$\varepsilon_z = \frac{bf}{d} - \frac{bf}{d+\varepsilon_d} = \frac{z^2\varepsilon_d}{bf+z\varepsilon_d} \approx \frac{z^2}{bf} \cdot \varepsilon_d \qquad (5)$$

The final step is obtained by taking the first order Taylor series approximation about $\varepsilon_d \approx 0$. The experimental data shown in

Figure **4-19** confirms the expected error model in which ε_z has a quadratic trend in the z direction. The graph, showing how far off the camera measurements are from the average distance, demonstrate that the depth error values for increasing distances can be approximated by a parabolic function with a high coefficient of determination ($R^2 = 0.9962$).
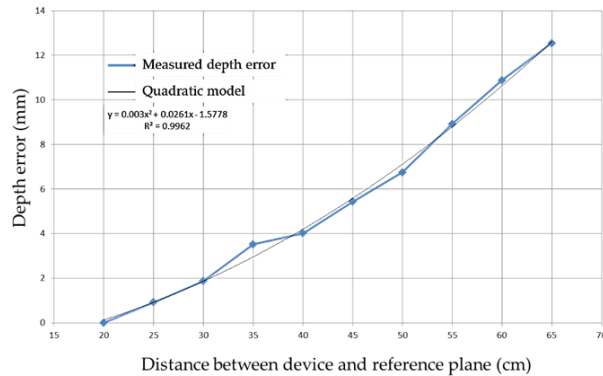

Figure 4-19 The depth sensor precision by varying the distance. A quadratic relationship between the distance to the depth camera and the standard deviation of depth values is found.

Error assessment removing the boundary edges of the acquired data

Optical depth sensors acquisitions are often prone to a border's degradation, depending on the underlying camera technology; in fact, when the optical ray is tangent with respect to the object to be measured, a little variation of a pixel on the sensor leads to a considerable difference in the detected pixel coordinates. For this reason, in proximity of an edge these devices show strong deformations and cannot be considered fully reliable. As such, and for the sake of completeness, the performances of the camera after excluding the object contours are here further investigated. For this test, a polystyrene sphere having a diameter of 18 mm, acquired at about 50 cm from the camera, is considered. Figure 4-20 shows the obtained results by considering all data (left), and by removing 8% of the borders from the acquisition (right).
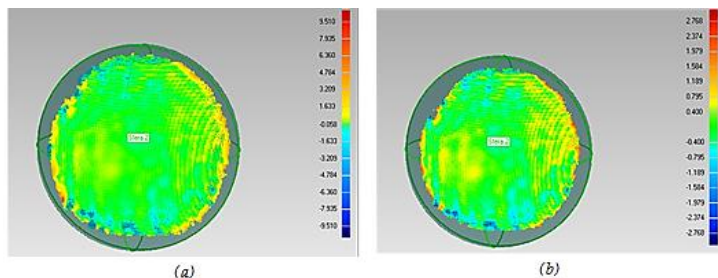
Figure 4-20 Example of radial distance computed between the captured sphere and best-fitted sphere: (a) without deleting noisy boundaries; (b) after boundary elimination.

Discarding the borders, the span of radial distance decreases remarkably: from 19 mm to 5.5 mm. However, such results can be noticed on the P_{Fi} and F_i errors by considering not only the error span of each acquisition, but also the averaged mean and the corresponding standard deviation.

The systematic non-planarity error represented in Figure 4-21 shows a constant behaviour of the scanner in the central part of the field of view with a maximum deviation from the best fit plane of ±4 mm.

Such an error obviously increases when considering the whole scanned area (at a 650-mm distance), as shown in Figure 4-21, presenting a maximum deviation of ±11 mm.
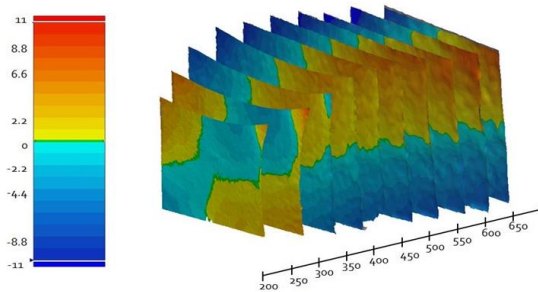
Figure 4-21 Error map between the target white plane and the 10 point clouds acquired using the SR300 device with increasing distance from the plane itself, using the whole framed area.

Multiple views performances

Even if a sub-millimetric precision can be offered by high end laser scanner or photogrammetry techniques for 3D reconstruction of small objects, depth cameras used as a multiple views 3D camera, offer an excellent trade-off between cost and scanning result. To assess the performances of a realistic 3D mesh acquisition, multiple 3D views of the same object to be measured have been generated by positioning the sensor around it.

Finding inspiration by the VDI/VDE Part 3 guidelines on Multiview acquisition - which recommends 5 devices placed at a distance from one another such as to contain the working volume introduced above - in the multiple views experiment, 5 images for each object have been acquired, rotating it with respect to a stable camera, placed 0.40 m far from it.

The SR300 camera multi-views performances have been surveyed over two meaningful objects: 1) a freeform smooth object (0.20 m height and ~0.07 m wide) and 2) a 3D Tangram object (bounding box with dimensions 0.15 m height and 0.15 m wide). To obtain two reference models for assessing the device performance, the Romer Absolute Arm 7520 SI/SE has been used (see Figure 4-22).

(a)   (b)
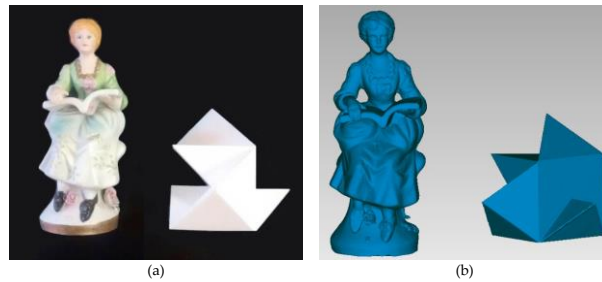
Figure 4-22 (a) Test objects for multiple-view reconstruction: a freeform statue and a 3D tangram; (b) reference 3D models for multiple-view reconstruction, obtained starting from the Romer Absolute Arm acquisition (accuracy of +- 0.063 mm).

The meshes, obtained using Geomagic® Studio software package (3D Systems, Rock Hill, South Carolina, USA) starting from the point cloud acquired with the SR300 camera, and the reference 3D model have been globally registered using the ICP algorithm.

The Euclidean distances between them are shown in Figure 4-23 and Figure 4-24; to increase the quality of the mesh reconstruction, 5% borders have been removed prior to perform the alignment. The comparison between the ground truth and the acquired data is limited to the target portion obtained with the multiple-view acquisition; grey areas in Figure 4-23 and Figure 4-24 are not, therefore, considered.
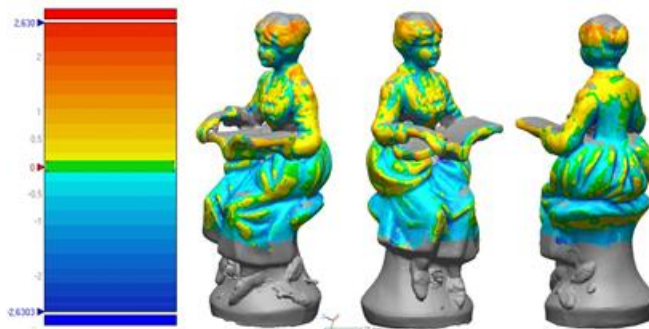
Figure 4-23 3D comparison between the statue ground truth and the SR300 acquired data (mesh). Errors are in mm.
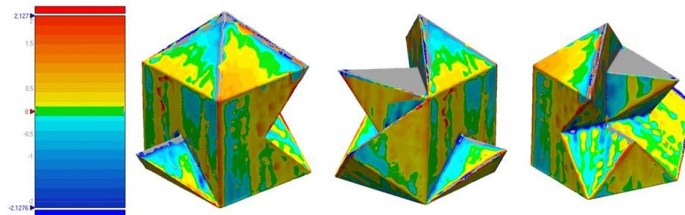
Figure 4-24 3D comparison between the tangram ground truth and the SR300 acquired data (mesh). Errors are in mm.

From the results of experimental assessment, the Intel® RealSense SR300 close range camera, when used as a 3D scanner, presents a significant alteration of the captured real-world 3D coordinates when the whole scanning volume is considered. However, its performances should be compared with the ones of other RGB-D devices to understand if SR300 is in line with competitor cameras. To this purpose, the results from the analyzed device are compared with those from Primesense Carmine 1.09 and with the Kinect v2. Such a comparison is carried out with reference to the VDI/VDE standards.

Moreover, since a number of 3D scanners have been characterized by using the mentioned normative, it is possible to partially compare the SR300 also with other devices such as, for instance, Smartscan, DPI7 and Structure Sensor. Finally, the multi-view acquisition performed using the tested device is compared with analogous acquisitions carried out by other researchers by using the Kinect v2.

VDI/VDE-based comparison

To provide a direct comparison between the 3D scanning performance of the inspected device and widely known competitor cameras such as the Primesense Carmine 1.09 and the Kinect v2, the same experimental test setup carried out as described above is repeated for such competitors. Depth data, acquired with respectively the OpenNI2 library [72] and the Libfreenect2 library [73], are used for evaluating VDI/VDA-based parameters. Results of this test are presented in Table IV where the SR300 with filtered data (i.e. 3D scanning setting for the camera) are used as the reference for comparing the performance. In particular for each of the parameters assessed using the VDI/VDE standard a parameter Δ is evaluated as the difference between any normative-based error measured for the SR300 and the same error measured for competitor cameras.

Referring to probing errors P_F and P_S, both Primesense and Kinect v2 present higher errors with respect to the SR300 device thus proving that this device performed better in this test (particularly when compared with Kinect v2). Higher performance of SR300 is even more evident when dealing with sphere-spacing error **SS**; in fact, the Δ_{SS} is considerably high for both the competitor cameras. Quite the reverse, the performance in terms of flatness error **F** is almost the same for the three devices with a slightly better performance provided by Primesense Carmine 1.09. Interestingly, even using the raw data, the SR300 proves to perform better than Kinect v2 in all tests except for flatness assessment.

Table 4-4 Comparison between SR300, Primesense Carmine 1.09 and Kinect v2 in terms of VDI/VDE error assessment

Device	SR 300 filtered data (reference)	Kinect v2	Carmine 1.09	SR300 (raw data)
P_F [mm]	8.3	20.13	9.32	13.93
Δ_{PF} [mm]	-	11.83	1.02	5.63
P_S [mm]	1.91	15.26	10.57	4.57
Δ_{PS} [mm]	-	13.35	8.66	2.66
SS [mm]	6.05	19.7	26.08	5.11
Δ_{SS}	-	13.65	20.03	-0.94
F [mm]	6.88	12.58	6.71	19.33
Δ_F	-	5.7	-0.17	12.45

To partially extend the comparison to other similar devices, some results from scientific literature can be used. Referring to probing errors, for instance, the SR300 performance can be compared also to the ones provided in [74] and [75]. In both such contributions, authors evaluate the performance of the sensors by testing more cameras of the same model. In Figure 4-25 the probing errors (PS / PF) of several depth cameras, evaluated in [74] are shown.
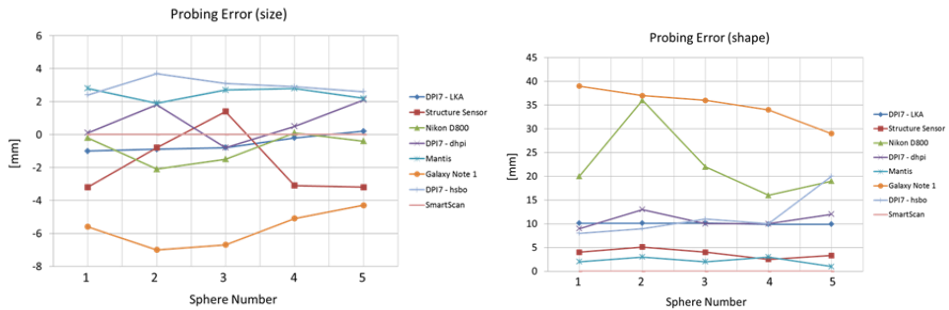

Figure 4-25 Results of probing error (PS / PF) equivalent to VDI/VDE 2634, part 2 as reported in Fig. 3 of [74]**.**

It must be noticed that among the variety of devices inspected in [75] (spanning from different technologies, products and models) the most relevant competitor for the SR300 camera the Occipital® Structure Sensor device which basically exploit analogous technology for 3D acquisition.

The performance in terms of probing error (form and size) results similar to the one of Structure Sensor as demonstrated in Figure 4-25; in particular, the form error presents an average value of 8.3 mm for the Intel® SR300 filtered data and an average value of 13.93 for raw data, comparable to the ~10 mm average value measured using the Occipital® sensor. The size error is 1.9 mm for the filtered data and 4.57 mm for the raw data, compared with ~2.2 mm.

Referring to sphere spacing error, it is possible to see, in Figure 4-26, the deviations observed in [74] and referred to the sphere spacing measurement using the Asus Xtion Pro camera are reported. Such errors, spanning from -8 to 2 mm, are in line with the SR300 performances providing (see Table 4-4) an average SS error in the range 5-6 mm.
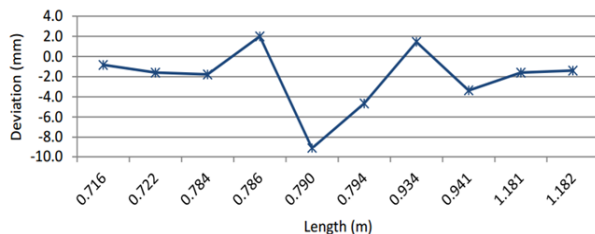
Figure 4-26 Results of the deviations in the sphere spacing measurements of the Asus Xtion Pro camera as reported in Fig. 8 of the paper [74]**.**

Also, flatness error can be compared with the one provided in literature [75] and referred to a number of devices (see Figure 4-27).

The average performance of SR300 camera (with optimized setting) in terms of flatness, listed in Tab. IV, is lower but "comparable" to the performance of DPI7 3D scanners and is considerably better than the one reported for the Structure Sensor device. Quite the reverse, referring to raw data, SR300 performance is comparable only with the one assessed in literature for the Structure Sensor.
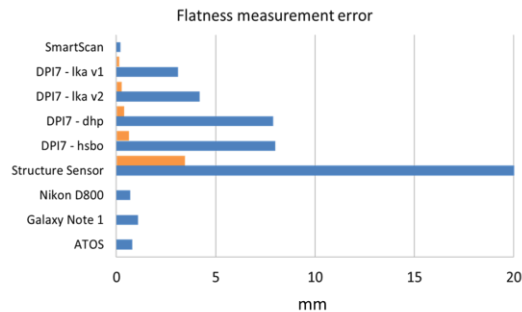
Figure 4-27 Results of flatness measurement. Blue - flatness measurement error, orange - standard deviation as reported in Fig. 5 of [75]**.**

VDI/VDE-based comparison

The multi-views acquisition test for the full 3D reconstruction proves (see Figure 4-23 and Figure 4-24) that the prismatic shape (tangram 3D) is slightly better measured than the free form shape (statue). The error range computed with the latter varies more than the range of the tangram object.

For both the acquired objects the reconstruction results appear to achieve a better precision with respect to the Kinect 2 device tested in [65] for which the error range span in an interval of 27 mm (as shown in Figure 12b of [65]) compared to the worst case here presented (the free form statue) showing a maximum error lower than 2.5 mm.

Concluding, test addressed to the Intel® SR300 shows that this device allows to acquire 3D scenes (i.e. to work as a 3D scanner) with a performance comparable to most competitor cameras, or even better for close range applications, despite its miniaturized dimensions especially when the camera settings are properly optimized. As a consequence, despite the device is born for addressing applications such as tracking, gaming or gesture recognition, it could also be satisfactorily employed as a 3D scanner i.e. could be referred as a low-cost device for a number of 3D scanning applications dealing also with medical applications.

The work continued in two directions after choosing the acquisition device: on the one hand, the choice of the number of cameras and the implementation of the scanner structure, and on the other hand, the implementation of the system control software. These aspects are presented in the following chapters.
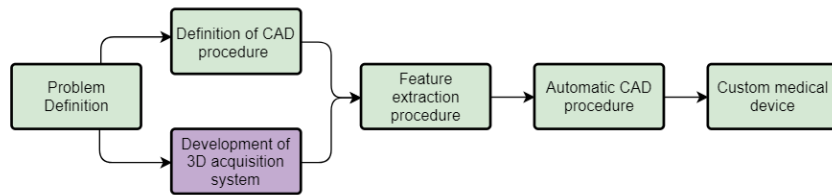
4.2.2. **Hardware setup**

Figure 4-28 Diagram outlined to achieve the systematic realization of customized medical devices.

With the aim of building an accurate HWA scanner a crucial step is to state the correct number and position of cameras needed to acquire the entire 3D geometry while preserving the hardware complexity of the whole scanner.

Following the tests shown in the previous paragraph, the acquisition is more accurate the closer the object is to the minimum acquisition distance, i.e. 200 mm. Fixed as reference the axis of the forearm, the camera is placed at a distance of 250 mm, so that, being the radius of the forearm between 25-35 mm, it is acquired with a distance from the arm close to the minimum value of the acquisition range (Figure 4-29). This choice also allows to reduce the overall dimensions.
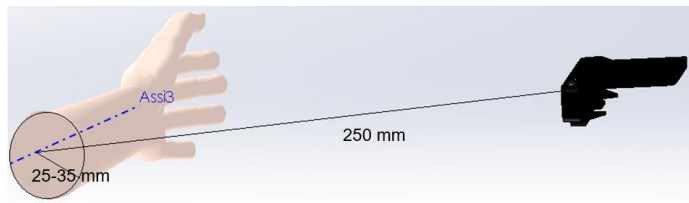
Figure 4-29 Distance between the camera and forearm axis.

Once the distance had been fixed, in order to evaluate how many cameras were needed to cover the entire length of the arm, acquisition simulations were carried out using Blender 3D modelling software [76]. The software allows to simulate the visual field of the device and color the framed scene.

The dimensions of the limb considered are those of the 3-year-old child and those of the 14-year-old child, i.e. the extremes of the acquisition range.

From Figure 4-30 it can be seen how the acquisition carried out with a camera perpendicular to the axis of the forearm (red colour) can be sufficient for the arm of the 3 year old child, but not for the 14 year old child as the regions near the elbow and the hand are not acquired (black in the image).

In the light of this test, it was decided to use two groups of cameras to safely acquire the arms of older children. In particular, the reciprocal position of the cameras is shown.
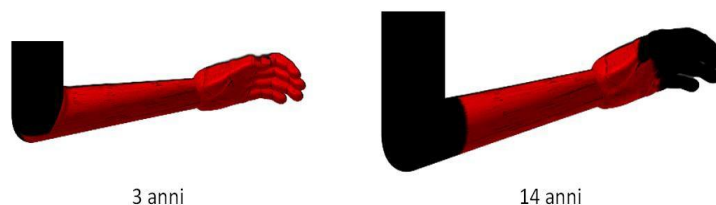
3 anni   14 anni

Figure 4-30 Simulation of single camera acquisition.

A ring support for the rooms has been adopted for a circular rig configuration allows an easy scalability of the system: if a camera's repositioning is requested, or one or more devices are needed to expand the 3D scanner, additional supports can be placed over the ring, maintaining a constant distance between adjacent supports. This circular disposition in fact allows to choose the observing angle keeping the camera-subject distance constant.
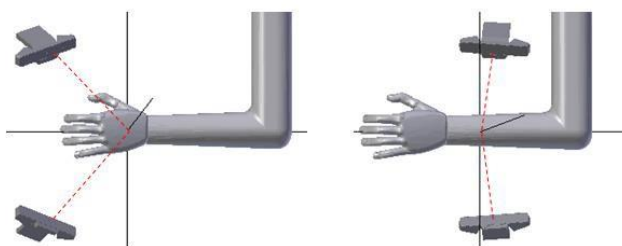
Figure 4-31 Position of the cameras in the two groups.

The cameras are then divided into two groups, one for hand acquisition and one for forearm acquisition. Based on the above, simulations of the camera's view were carried out, also using Blender. The number and position of the scanners have been defined in order to obtain a 3D model of the limb at 360°.

Trying to maximize the overlaps between adjacent acquisitions and at the same time acquire the whole arm with the least number of devices possible, the first attempt to arrange the cameras was made with three devices for each group of cameras, thus assuming to be able to acquire the whole arm with 6 cameras. These devices are arranged at 120° one from the other (Figure 4-32). This configuration has been designed to minimize the cost of the scanners and reduce the acquisition time as much as possible.
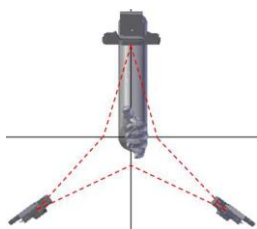

Figure 4-32 Position of the cameras in the first simulation.

Defining with the colours red, green and blue the areas seen from a single camera, with the colours purple, blue and yellow the areas where the pattern is superimposed and with

black the regions that are not seen from any camera, it is possible to see from Figure 4-33 how this configuration is not correct. It turns out, in fact, that the acquisition of the 8 and 14 year old limb is not complete in the first-second finger region and even the overlaps between the acquisitions are limited. For these reasons, it was decided to add a camera to each group to obtain a better result.
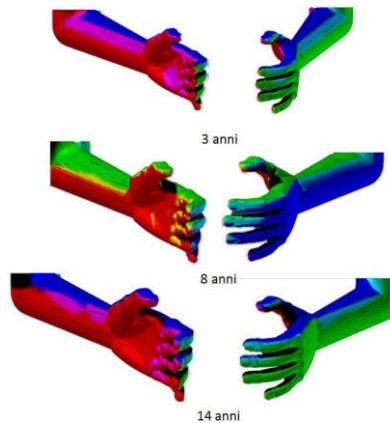

Figure 4-33 Simulation carried out with three cameras per group.

The solution with eight devices is therefore adopted, four per group. The two rings are fixed at a distance of 95mm, according to the idea that it would be impossible for smaller patients to insert the arm comfortably into the scanner, as we can see in figure xx in which an alternative configuration was tested by moving the two rings away.

Figure 4-34 Example of incorrect positioning of the arm when the rings are too far apart.
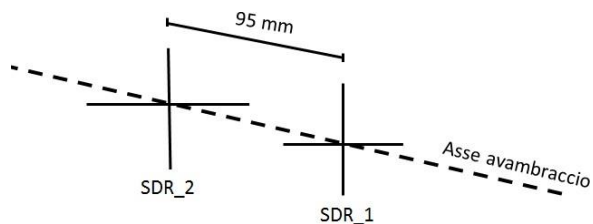
Figure 4-35 Position of the forearm reference system with respect to the palm reference system.

Once the distance between the two rings had been fixed, with the idea of simplifying the design and therefore the realization of the supports for the cameras, it was decided to orientate all the devices towards the axis of the forearm (i.e. the axis of the rings) with an angle of 70°. To validate this orientation of the camera, another simulation was carried out with the Blender software, for arms of children aged 3, 8 and 14 years. By defining the individual scans with the colours blue and green, and the pattern superimpositions with the light blue, it is possible to see how the regions of interest are completely acquired and there is a wide overlap (Figure 4-36). In Figure 4-37 the final configuration of the cameras is shown.
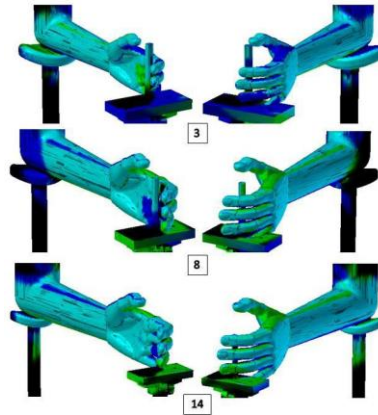
Figure 4-36 Acquisition with new camera disposition.

Figure 4-37 Camera support assembly.

To accommodate the patient's arm, the scanner provides two supports, one for the hand, located between the two rings, and one for the elbow, located on a linear slide that allows to support arms of different sizes (Figure 4-38-Figure 4-39).

Figure 4-38 Example of correct arm positioning in patients of 3 and 14 years old.

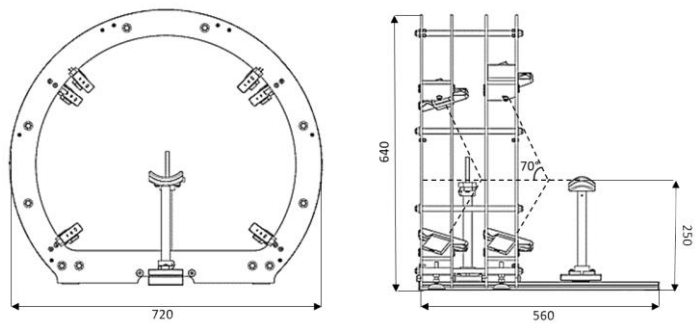**Figure 4-39 Hand-wrist-arm scanner structure.**

Figure 4-40 Specifics of the designed hardware.

The cost for the purchase of all the necessary parts to realize the scanner is about 2300€ (including the cost of the devices).

To sum up, with the aim of obtaining a wide field of view which can cover the range of sizes variation of growing children, the arm scanner is designed as composed of two rings and a moving support for the elbow; the support can easily slide towards the centre of the scanner to accommodate smallest arms or move away for bigger anatomies. This allows to acquire anatomies with length varying from 200 mm up to 410 mm. Each ring structure reaches a diameter of 720 mm (Figure 4-40), the support for the hand is positioned between the two rings and each camera is place at approximately 245-255 mm from it.

This configuration allows to have enough over imposition between the acquired point clouds, yet maintaining a compact and low-cost device, which is modular and can adapt to significantly different anatomies.

The material used for the support rings is PMMA, with a thickness of 5mm. The choice of PMMA allows to reduce the weight of the device.

The structure has been verified with Abaqus 6.14-5 to simulate a minor accidental impact. A load of 42N is imposed at the weakest point of the structure, i.e. where there are no reinforcements (spacers or camera support plates). The assembly is bound at the base.

Figure 4-41 and Figure 4-42 show the model used with the respective global reference system. Figure 4-42 shows the point of application and the direction of the forces applied.

To estimate the risk of the device tipping over, an additional simulation was performed with the SolidWorks Motion software, to replicate the behavior of the assembly, considered as a rigid body, at an imposed rotation.

The results of the simulations, shown in Figure 4-43 and Figure 4-44, indicate that the structure is perfectly capable of withstanding accidental shocks of even greater magnitude than those actually foreseeable. Moreover, the risk of tipping over in the event of foreseeable adverse events is very low or zero.

Structural Analysis

The magnitude of the forces is chosen in order to simulate the accidental impact of an uncooperative patient. The older ages are not considered for the study of the applicable force, because it is remote the possibility that an older child is uncooperative in the very short period necessary for acquisition. The point and direction of application of the stress are chosen specifically because they represent the most critical condition verifiable, both for the stress on the structural element and for the risk of rollover. The weight is considered not as a concentrated force, but by adding the acceleration of gravity in the model.
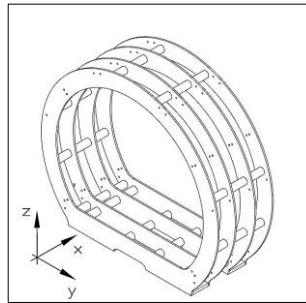
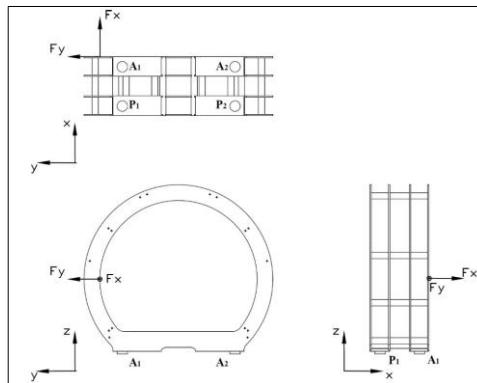**Figure 4-41 Positioning of forces for structural analysis.**

Figure 4-42 Positioning of forces for structural analysis.

Table 4-5 Strengths and Constraints imposed in the simulation.

Forces	
Fx	30N
Fy	30N
Peso	87N
Constraints	
A1	Lock in A e P
A2	Lock in A e P
P1	Lock in A e P
P2	Lock in A e P

As shown in Figure 4-43 and Figure 4-44, stresses and deformations in PMMA following impact are negligible.
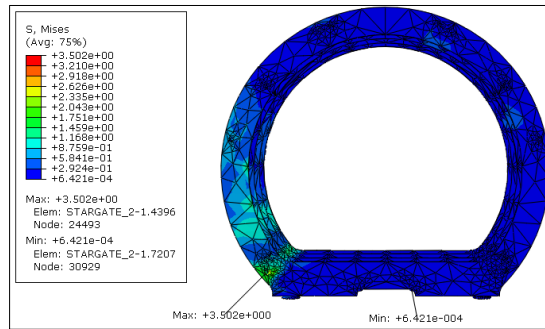
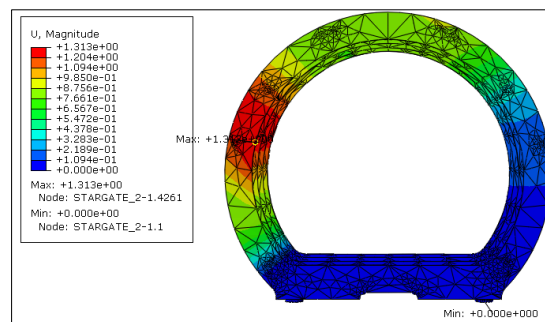**Figure 4-43 stresses and deformations in PMMA as a result of impact.**

Figure 4-44 stresses and deformations in PMMA as a result of impact.

Tipping risk

To evaluate the risk of the device tipping over, in particular to verify that the possible displacement of the centre of gravity following the impact does not cause instability, a second simulation was carried out (Table 4-6) to study the evolution in time of the assembly following a rotation imposed equal to 10° (Figure 4-45).

Table 4-6 Strengths and Constraints imposed in the simulation.

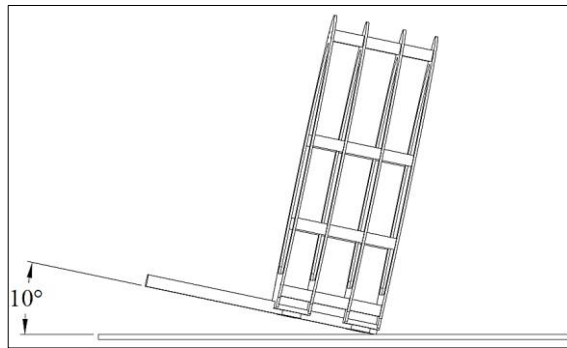| Set Rotation	
Around Y	10°
Weight	87N
Constraints	
A1	Surface support in A e P
A2	Surface support in A e P
P1	Surface support in A e P
P2	Surface support in A e P

Figure 4-45 Tipping test result.

The results obtained are shown in Figure 4-46: note that, even if a rotation of 10° is imposed (Figure 4-45), the device returns to the correct position without tipping over.
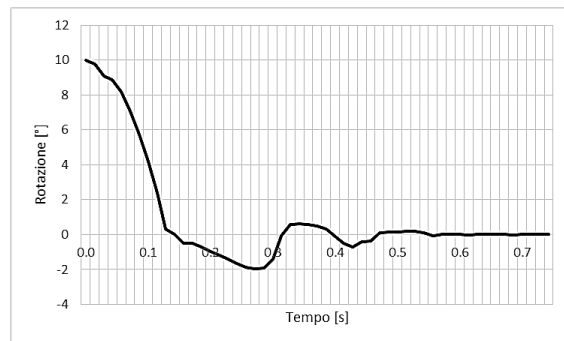

Figure 4-46 Tipping test result for greater accidental impacts.

The results of the simulations, shown in Figure 4-46, indicate that the structure is perfectly capable of to withstand accidental shocks of even greater magnitude than those actually foreseeable.

Moreover, the risk of tipping over in the event of foreseeable adverse events is very low or zero.

Multicamera system calibration

The acquisition system described above acquires the hand-wrist-arm district from 8 different points of view. Each device stores a point cloud with respect to its reference system, with origin in the optical center of the camera. It is necessary, in order to obtain a 360° model of the arm, to orient all point clouds in a common reference system. This procedure requires the calculation of eight rototranslation matrices, one for each device, which moves the point cloud, in the global reference system (an example is depicted in Figure 4-47).
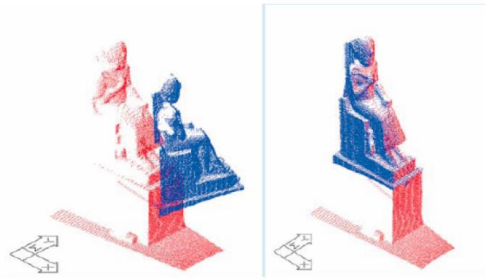
Figure 4-47 Example of point cloud rigid alignment.

In this work, a manual alignment strategy was initially implemented, which was subsequently made automatic, thereby releasing the user from the task of manually selecting correspondences. Let's now see these two strategies in detail; their implementation is presented in the next paragraph.

        1)   Manual calibration with a target object

This first strategy is based on the rigid alignment of corresponding points in space. This means that we want to estimate the roto-translation that brings two sets of points to coincide. Specifically, we want to bring all the reference systems of the eight cameras to coincide on a single global reference system. For this purpose, a target object has been defined, consisting of several planes and edges in different directions, in order to define characteristics of robustness and efficiency. The target was realized with additive techniques and then scanned with a high precision scanner (the Romer Absolute Arm with RS1 probe) to create the reference model.

        The idea is to show the user the target object scanned by the camera and the reference model in a 3D viewer. The user can select three or more point matches in the two models and the program can, starting from the selected matches, find the rototranslation matrix that leads to overlap these points.
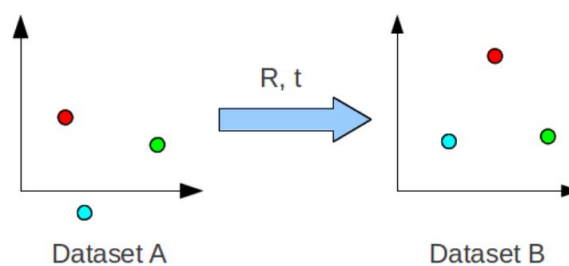

Figure 4-48 Example of point set transformation with R and t matrices.

The aim is therefore to find the R and t components of the rototranslation matrix, shown in Figure 4-48. This transformation is sometimes called the Euclidean or rigid transformation, because it preserves its shape and size. In general, the problem is solved:

$$B = R*A + t \qquad (6)$$

Where R and t are the transformations applied to dataset A to align it with dataset B, in the best possible way. The procedure for finding the optimal rigid transformation matrix can be divided into the following successive steps: find the centroids of both datasets; bring both datasets to the origin and find the optimal rotation (matrix R); find the translation t.

The centroids are the midpoint and can be calculated as follows:

$$P = \begin{bmatrix} x \\ y \\ z \end{bmatrix} \qquad (7)$$

$$centroidA = \frac{1}{N}\sum_{i=1}^{N} PA^i \qquad (8)$$

$$centroidB = \frac{1}{N}\sum_{i=1}^{N} PB^i \qquad (9)$$

Here, P_A and P_B are points in data set A and B respectively.

There are several ways to find the optimal rotations between points. The easiest way is to use Singular Value Decomposition (SVD), as it is a function widely available in many programming languages. Without going into detail on how it works, SVD calculates the decomposition/factorization of a matrix (called E), in three other matrices, so that:

$$[U, S, V] = SVD(E) \qquad (10)$$

$$E = USV^T \qquad (11)$$

If E is a square matrix, U, S and V are also the same size.

To find the optimal rotation, first of all we have to re-center both data sets so that both centroids are at the origin, as shown in Figure 4-49.
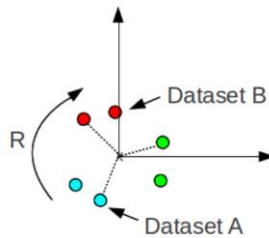

Figure 4-49 Rotation of pointset A to be aligned with pointset B.

This removes the translation component, leaving only the rotation to be addressed. The next step is to accumulate a matrix, called H, and use SVD to find the rotation as follows:

$$H = \sum_{i=1}^{N} (PA^i - centroidA)(PB^i - centroidB)^T \qquad (12)$$

$$[U, S, V] = SVD(H) \qquad (13)$$

$$R = VU^T \qquad (14)$$

H is the covariance matrix. The translation is

$$t = -R \; x \; centroidA + centroidB \qquad (15)$$

The centroids are column vectors 3×1.

Figure 4-50 shows the target realized for the calibration and an example of correspondence selection (the software will be explained in detail below). The target has the origin in its center of gravity placed on the flat face.
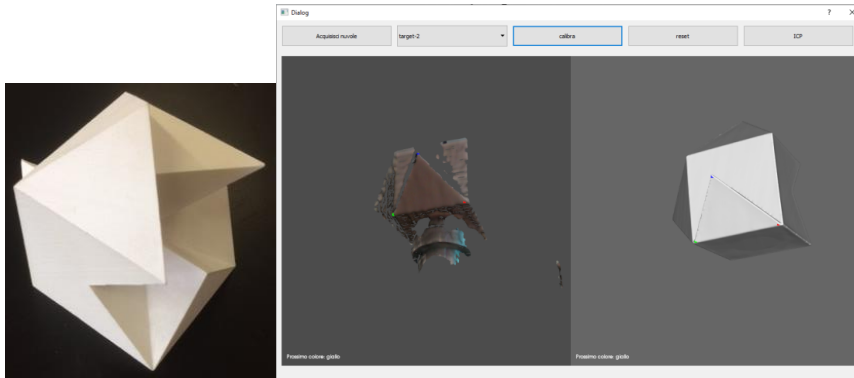

Figure 4-50 Target realized for the calibration (left) and an example of correspondence selection (right).
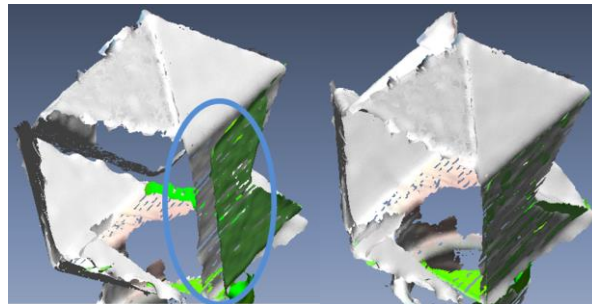

Figure 4-51 Example of alignment error due to poor accuracy of the manual selection (left) and alignment using ICP in addition to manual selection (right).

As can be seen Figure 4-51, the alignment based on the selection of matches can lead to alignment errors as manual selection is very prone to errors. For this reason, after calculating the coarse roto-translation matrix, the cloud is finely registered with ICP to the target model.
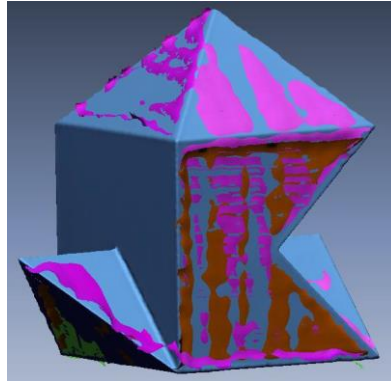
Figure 4-52 Fine registration of the target.

In this strategy the process of manual selection and alignment must be repeated for the eight point clouds.

  2) Automatic calibration with a target object and ArUco markers

To automatically calibrate the position of each camera with respect to a global reference system, a strategy based on ArUco targets has been subsequently devised. ArUco targets [77–79] are one of the most popular approaches for pose estimation in computer vision [80, 81]. The main benefit of these markers is that a single marker provides enough correspondences (its four corners) to obtain the camera pose. Also, the inner binary codification makes their identification especially robust. Therefore, an appositely devised target object was equipped with two ArUco markers (8X8cm) anchored on two planar faces that formed an angle of 60 degrees (see Figure 4-53). The target object was designed to be embedded in the scanner by placing it on the moving bracket after removing the elbow support (Figure 4-53c).

  Four cameras can see the marker on the left face, and the remaining four cameras can see the marker on the right face. A global reference system was defined as shown in Figure 4-53b, where the origin was set on the barycentre of the pyramid formed by the two faces. With such a reference system, the Z-axis roughly corresponded to the principal axis of the arm to be acquired. Since the target was not sealed to the rest of the structure, its position may vary slightly from one calibration to another. It is therefore important to manually arrange the object such that the pyramid tip (which defines the Z-axis) was approximately aligned with the axis of the two rings. Even if this manual positioning did not assure collinearity with the rings axis, a small variation of the target position along this axis would not influence the final result, as the following chapters will explain.
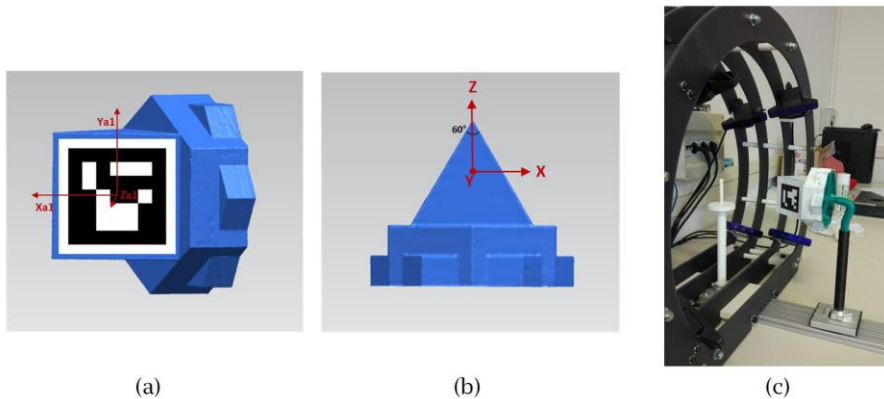
Figure 4-53 The designed target object for the automatic calibration process: a) lateral view of the left face containing the ArUco marker; b) top view of the target with the origin positioned on the barycentre of the pyramid formed by the two planar faces and c) the 3D printed target object positioned on the support for the calibration procedure

To determine the roto-translation matrix that moves the acquired point cloud from the camera view point to the global reference system, an image of the target is acquired by each camera (using the embedded RGB sensor of the device). Using the ArUco library [82], it is possible to detect the target and evaluate the camera position with respect to the acquired ArUco reference system (see Figure 4-53a). Since the position of the two ArUco with respect to the global reference system is known a priori, it is possible to determine the position of each camera with respect to the global reference system.

Actually, the use of so-calculated roto-translation matrices allows a rough registration that needs to be refined. For this purpose, a finer registration is carried out by using the ICP algorithm. In particular, the raw registered model is aligned with a reference model obtained by using a high precision scanner (in this work, the Romer Absolute Arm with RS1 probe) and virtually placed in the same global reference system. It has to be noticed that, in order to "help" the ICP algorithm in finding the best possible alignment, the target is manufactured with sharp edges around the two faces.
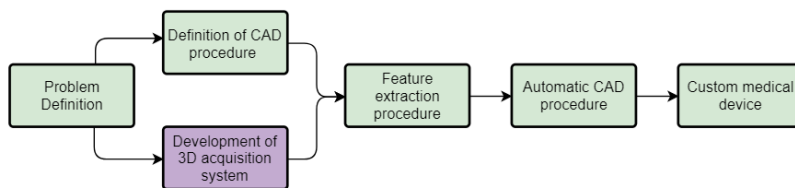
4.2.3. Initial software design

Figure 4-54 Diagram outlined to achieve the systematic realization of customized medical devices.

The structure of the control software developed to manage the multi-camera configuration, is presented below. The idea is to create a user interface that can allow hospital staff to generate the main structure of the orthosis independently, without the need to be supervised by an

expert in 3D acquisition and modeling. The software must therefore manage the interaction between the user and the cameras and provide the modeling options.

The software is designed according to the requirements defined by the use cases; in software and systems engineering, a use case is a list of actions or event steps typically defining the interactions between a role (an actor which can be a human or other external system) and a system to achieve a goal.

In this chapter are shown the use cases related to the scanning of the arm and the calibration of the scanner. These use cases will be extended in the next chapters, introducing the features for the orthosis modelling.
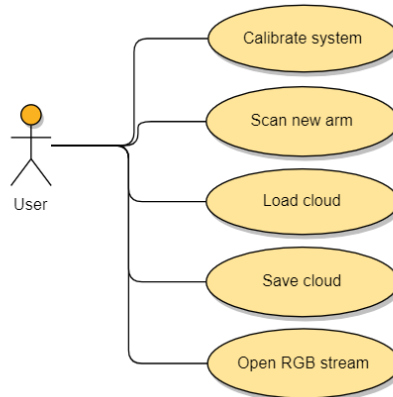

Figure 4-55 Initial use cases for the first pilot case.

Figure 4-55 shows the five initial use cases of the system: the actor must be able to calibrate the system, to capture the 3D anatomy of the patient, to store and load the 3D image and open the video stream to help the positioning of the patient's arm.

The software was designed accordingly, following the Model View Controller (MVC) design pattern (Figure 4-56). MVC is an architectural pattern commonly used for developing user interfaces that divides an application into three interconnected parts. This is done to separate internal representations of information from the way information is presented to and accepted from the user [83]. The MVC design pattern decouples these major components allowing for code reuse and parallel development.
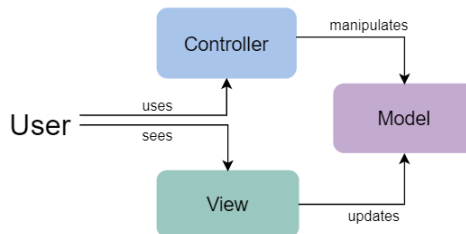

Figure 4-56. Model View Controller scheme.

The Model is the central component of the pattern. It is the application's dynamic data structure, independent of the user interface [84]. It directly manages the data, logic and rules of the application. The View is any representation of information such as a chart, diagram or table. The Controller accepts input and converts it to commands for the model or view. In addition to dividing the application into these components, the MVC design defines the interactions between them: the model is responsible for managing the data of the application, it receives user input from the controller. The view means presentation of the model in a particular format and the controller responds to the user input and performs interactions on the data model objects. The controller receives the input, optionally validates it and then passes the input to the model. Because MVC decouples the various components of an application, it is possible to work in parallel on different components without affecting or blocking one another.

Figure 4-57 shows the class diagram created for the control software, following the MVC model. There is the Controller class, and the Viewer class, both initialized by the class that manages the interface. The model, then the manipulated data (in the form of point clouds, meshes and images), and the cameras are managed by the *MulticameraController* class, which activates the eight cameras and acquires the relative point clouds and RGB images.

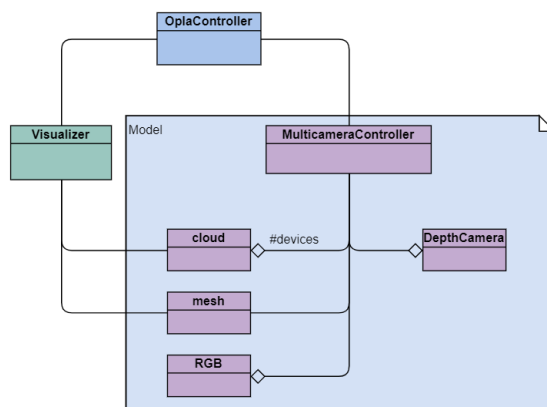Below we see how the individual classes interact to realize the use cases.

Figure 4-57 Class diagram of the control software.

The class structure has been designed in such a way as to create a modular structure. This means that each segment communicates with the others but remains, if necessary, replaceable. This guarantees the scalability of the system, in case, for example, it is necessary to replace the acquisition device, it will be sufficient to replace the *DepthCamera* class.

Sequence diagrams and main steps
Each use case is now described in detail with a sequence diagram. A sequence diagram shows object interactions arranged in time sequence. It depicts the objects and classes involved in the scenario and the sequence of messages exchanged between the objects needed to carry out the functionality of the scenario.

For each use case, the sequence diagram is reported, and the main steps are described. In this work the user interface was handled using Qt framework [85], a free and open-source widget toolkit for creating graphical user interfaces and cross-platform applications. The

management and processing of point clouds has been implemented for the most part through the open-source library PCL (Point Cloud Library) [86] and the open-source library VTK (VisualizationToolkit) [87] is used for mesh management. The interaction with the depth cameras is managed by the librealsense [68] library, developed by Intel.

The minimum requirements are: 6th generation Intel Core processor, 64-bit Windows 10 operating system, 8Gb disk memory, 4Gb RAM, 2x PCIe expansion card with 4 USB 3.0 ports.

The times indicated are related to a machine that mounts windows 10, Intel Core i7 processor, 16 GB of RAM.
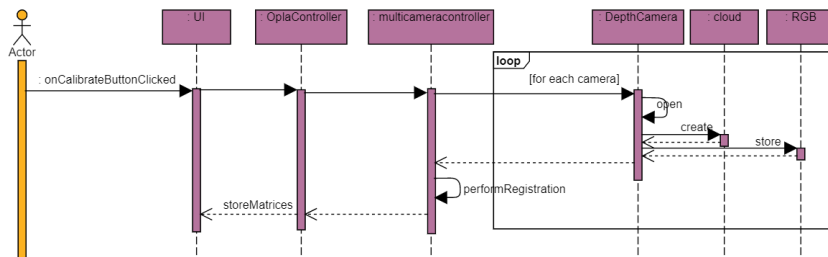
Calibration system

Figure 4-58 Sequence diagram of the Calibrate operation.

After placing the calibration target containing the ArUco markers approximately in the center of the system, the user presses the "Calibration" button. When the process starts, the cameras are switched on in sequence, saving both a depth and an RGB frame for each one. Each camera is then turned off and the program continues to work in the background. In the "performRegistration" function, the ArUco marker is identified in each saved image using the appropriate functions of the OpenCV library [88]. The detection of the markers makes it possible to recognize the position of each camera with respect to the center of the system, which, as mentioned above, is positioned in the center of gravity of the pyramid. This step determines a first roto-translation matrix. In a second calibration phase the program uses the saved point clouds to refine the recording with the ICP algorithm, using the high resolution scan of the target saved in the system. ICP parameters have been empirically chosen as a trade-off between calculation time and result reliability.

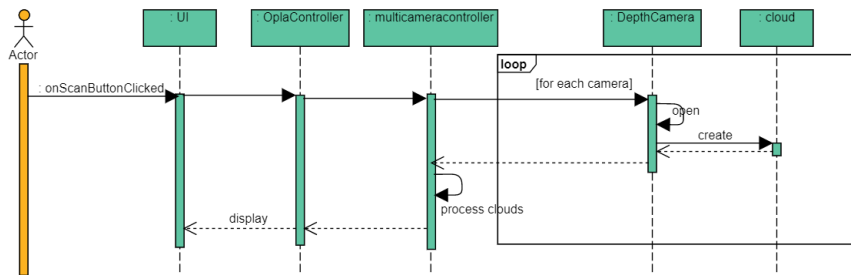The program performs the calibration in about 80 seconds.

Scan new patient

Figure 4-59 Sequence diagram of the Scan operation.

Once the patient's arm has been placed inside the scanner, the "Scan" button is pressed to acquire the scanner's geometry and the cameras are switched on at the same time.

The multi-camera configuration, however, can lead to interferences when all cameras are facing the same scene. The interferences are due to the structured light nature of the selected depth camera, which works by projecting an infrared pattern and reconstructing the 3D image by triangulation [54]. When two or more cameras share the same field of view, the patterns are projected together, thus compromising the 3D reconstruction. For this reason, the devices cannot be operated to acquire the scene simultaneously. On the other hand, the latency of the acquisition process would be unacceptable envisaging a sequential activation of the cameras since the overall acquisition time would be too high for the intended application. A viable solution was found by turning on all cameras at the beginning of the scanning process but keeping the laser projectors off. Each laser is subsequently powered in sequence and a single image is acquired for each camera. When the laser is turned on fifteen frames are captured for each camera to give autoexposure, after which the last acquired frame is saved before switching to the next camera. This operation requires ~0.25 s at a frame rate of 60 fps. The switch from a camera to another had a computational cost of about 0.06 s. With this solution, the scene is acquired in about 2.5 seconds for the eight-cameras configuration.

After being saved each cloud is cleaned with smoothing, spatial filtering and Statistical Outlier Removal (SOR) to remove the noise. The parameters identified with an experimental campaign for these filters are: smoothing radius equal to 1.5 mm, number of points for SOR analysis equal to 350 with standard deviation multiplier equal to 0.08.

For each cloud the normal are then calculated and saved and the roto-translation matrices saved in the calibration step are applied. The normal vectors computation is necessary in order not to create errors in the construction of the mesh (as an example of wrong mesh construction see Figure 4-61), the meshing step will be clarified later. Finally, a new finer alignment is made, between each point cloud and all the others. This second alignment is intended to compensate for any involuntary movements of the patient during the scan. The parameters for the fine alignment step are: maximum correspondence distance equal to 8 mm, number of iteration equal to 500.

The total time required for the full scan of filtering and alignment (see an example in Figure 4-60) is about 2 minutes.
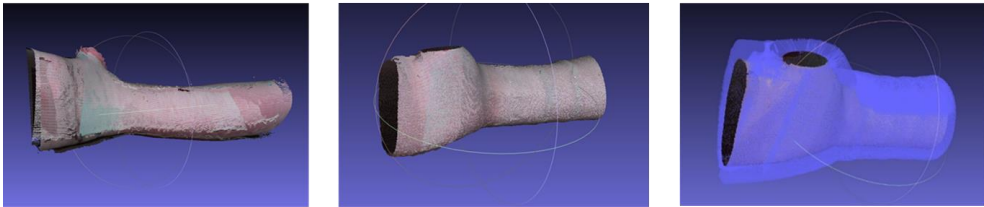
Figure 4-60 Example of point cloud elaboration.
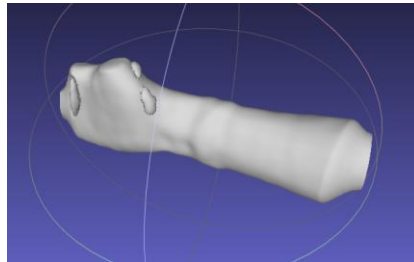
Figure 4-61 Example of meshing error due to wrong cloud normals.

It is important to underline that, as you can see from Figure 4-62, the acquisition of the hand-wrist-arm district is very imprecise if we want to acquire skin naked. It is therefore necessary to cover the limb with a bandage that does not invalidate the acquisition.

Figure 4-62 Example of bad acquisition of bare skin.

Following a discussion with doctors, it was decided to use an elastic gauze that fits perfectly to the geometry of the arm and its thickness (about 1 mm) does not interfere with the correct acquisition of the arm.

Load old scan
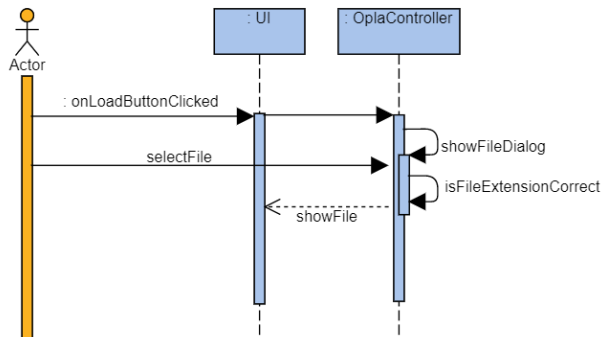
Figure 4-63 Sequence diagram of the Load operation.
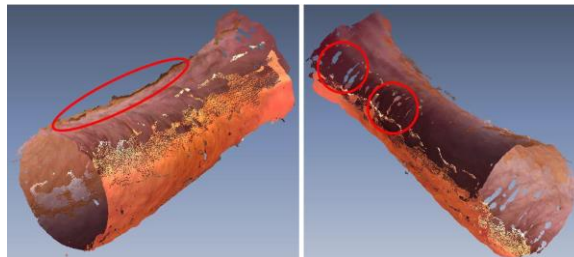
When the user clicks the "Load" button the program shows on the screen the file navigation dialog. In this dialog, if the user selects a previously saved point cloud, the program checks that the file extension is correct and, if so, loads the selected model and displays it in the 3D viewer.

Save scan
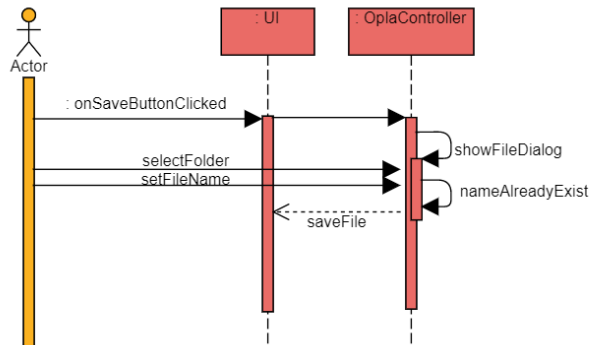
Figure 4-64 Sequence diagram of the Save operation.

When the user presses the "Save" button the program shows a dialog to choose destination and file name, if the name is not already existing in the selected folder the file is saved in ply format.
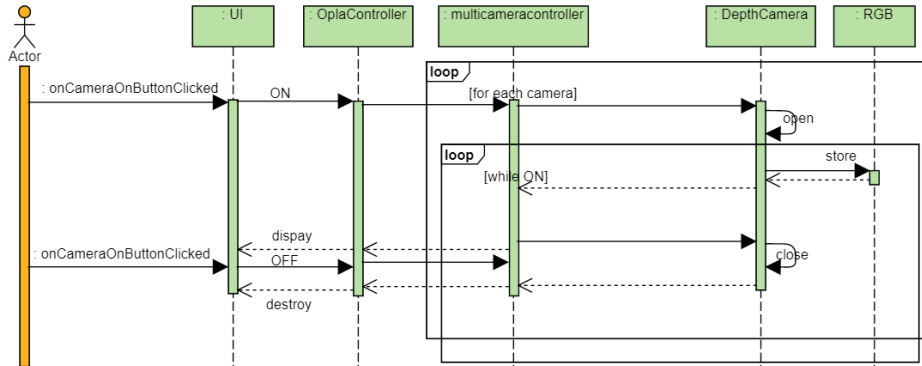
Open RGB stream

Figure 4-65 Sequence diagram of the Open RGB Stream operation.

When the user presses the button to open the devices, each camera is opened and the RGB stream is generated and shown on the screen until the user presses the button again.

The user interface programmed to provide the tasks described above is depicted in Figure 4-66 and Figure 4-67. It is composed of a toolbar containing the described actions and a three-dimensional object viewer. In addition to these features, a form for saving patient information has been included.
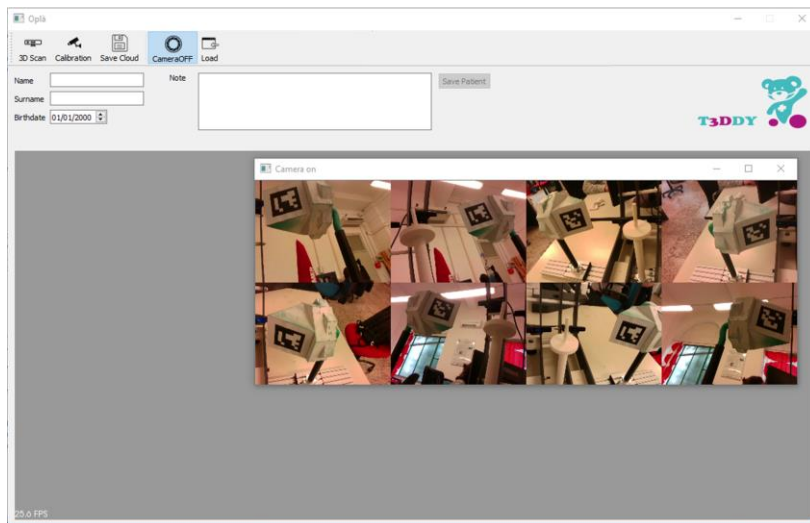
Figure 4-66 Scanner control software with RGB stream opened.
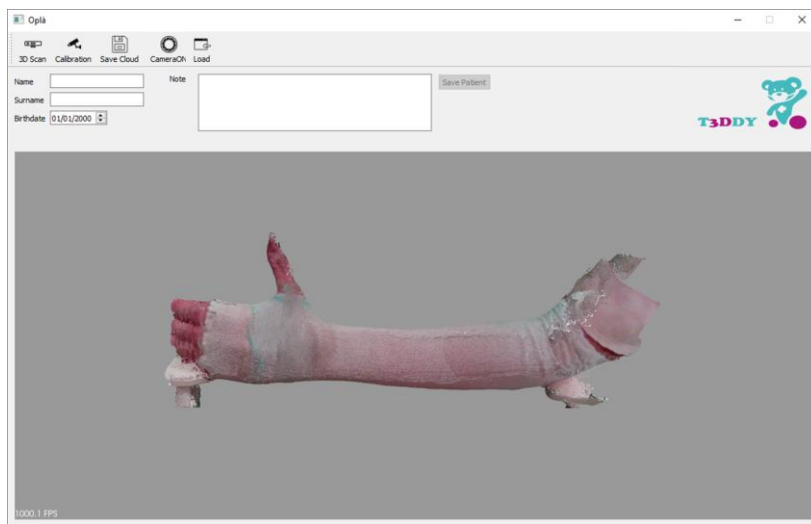
Figure 4-67 Example of final result of arm acquisition.

4.2.4. **CAD modelling**
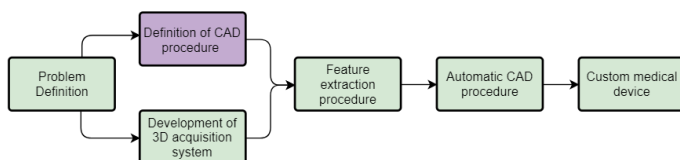
Figure 4-68 Diagram outlined to achieve the systematic realization of customized medical devices.

The procedure for designing the CAD model of the orthosis, defined in view of the future automation of the entire process, is here presented.

In general, two principal strategies can be identified at the state of the art to create the CAD model: i) the adaptation of a pre-defined template to the scanned geometry [36]; ii) a manual procedure performed within a CAD environment [14–16, 18, 19]. Most methodologies described in literature neither guarantee the achievement of a valid result from a medical perspective [16, 19] nor allow an easily usable and scalable framework for the application in clinical practice. Specifically, these last goals would be reached by implementing a fully automatized procedure that: i) does not require CAD technical skills to the user; ii) does not needs significant time for the generation of the CAD model; iii) are validated against a set of clinical trials. To reach such result, a first important step consists of creating a systematic procedure, which would allow to produce a consistent orthosis model using common CAD tools. Considering medical guidelines, the procedure is conceived to be easily automatized, thus reducing as much as possible the human interaction.

A valid and reliable orthosis reconstruction procedure in fact needs to be sound – i.e. a correct model reconstruction should be obtained independently from the acquired arm geometry. This

means that it should allow the reconstruction of all possible arm anatomies (e.g. adults/children, male/female, etc.).

As said, in order to assure the wearability of the AM-produced device, the orthosis is designed as composed by two separate shells: one rests on the back of the hand, and one on the internal side. The two halves are joined together by means of a closing system based on zip-ties; the connectors are kept in place thanks to a specifically designed housing system. The classic approach used in the field of Reverse Engineering to model an object, which does not derive from industrial design and therefore cannot be described by means of elementary geometric features, is called Fitting Surface Modeling. This allows to adapt surface patches, i.e. freeform surfaces, on the optimized mesh in order to create a surface body. Such a methodology cannot be adopted in this case, since the CAD functions used are very sensitive to the mesh conformation and often tend to generate errors, especially in areas of the mesh with high curvature. Moreover, the adoption of the Fitting Surface Modeling strategy would involve a subsequent modeling approach, i.e. the use of various CAD tools in order to "adjust and correct" the model, without following a pre-established sequence of functions. Considering, therefore, the need to develop a code that can allow the automation of the entire process of CAD construction of the orthosis, the aforementioned strategy can not be used in the considered case study. Modeling must necessarily be done using a Parametric Feature Modeling approach, i.e. using a sequence of parametric CAD functions, starting from a sampling of the arm's 3D mesh data. The strategy studied must include the development of a single sequence of functions that can be the same for each orthosis, allowing its construction for each patient.

Accordingly, the systematic procedure proposed for designing 3D printable arm-wrist-hand cast consists of 5 phases as depicted in Figure 4-69.
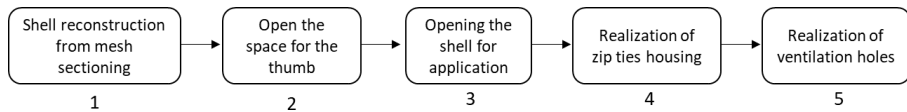

Figure 4-69 Modeling macroblocks of the procedure for the generation of a personalized cast.

The starting point of the procedure is the 3D reference data of the arm that is acquired by means of the 3D scanner based on RGB-D cameras, described above. The output data produced by the scanner is pre-oriented so that the z-axis is aligned with the arm principal direction; the origin corresponds to the barycenter of the obtained mesh (computed by triangulating the resulting arm point cloud), the y-axis is oriented towards the upper side of the hand and the x-axis is consequently oriented (see Figure 4-70). After the 3D reference data is properly aligned, a solid shell is built upon the arm anatomy (Step 1). In Step 2, the solid shell is perforated to create an opening for the thumb finger. Subsequently, the shell is cut in half to create two wearable parts (Step 3) and zip-ties housing features are built on the external surface of the orthosis (Step 4). Finally, in Step 5, ventilation holes are generated on the two halves of the orthosis. The result of the procedure consists of the CAD model of the cast, ready to be manufactured using AM.

The reconstruction approach makes use of a number of 2D sections obtained by intersecting the 3D scan data with properly chosen planes. Two issues related to the generation of such mesh sections have to be confronted with: i) the position and the orientation of cutting planes with respect to the reference system; ii) the number of sectional planes and their reciprocal distance to assure a good resolution during the loft operation. Cutting planes are generated as locally orthogonal to a guide curve obtained by intersecting the mesh with the

XZ-plane (see Figure 4-70a) and selecting (between the two resulting curves) the one corresponding to the external part of the arm.

Referring to the number and spacing of cutting planes, convenient values are identified for both the arm and the hand regions; searching for a compromise value between required accuracy and the weight of the procedure as well as the smoothness of the generated surface, such values are set at 10mm for the arm and 5mm for the hand. This choice was confirmed during a series of preliminary tests, as it well adapts to the reconstruction of arms characterized by significant differences in shape and proportion (e.g. children vs. adults).

The polylines obtained by intersecting the 3D scan data with the sectional planes are used to generate 2D sketches (i.e. closed spline curves) of sectional profiles of the arm district so as to reconstruct the arm model by using a single loft operation. The most challenging geometric feature to reconstruct, following this strategy, is represented by the thumb area. In order to avoid the generation of irregular section profiles, which lead to reconstruction errors during the loft operation (see Figure 4-70b) and to provide the bases for the generation of a suitable hole for the thumb, the original mesh must be edited. Specifically, the thumb area is "segmented" in the original mesh and deleted, leaving a hole which is subsequently filled with a curvature-based automatic patch (Figure 4-70c). The edited surface is suitable for a reconstruction based on a single loft operation.

| (a) | (b) | (c) |
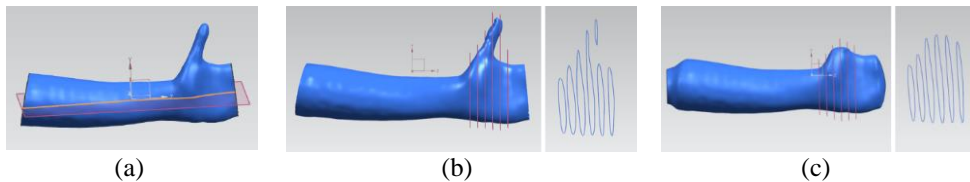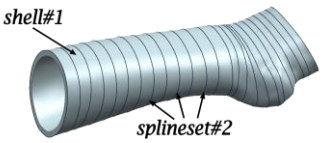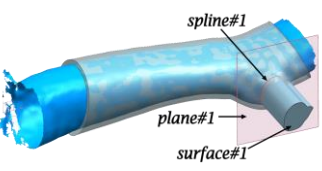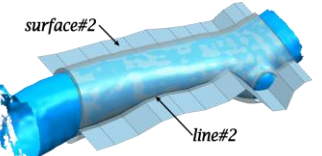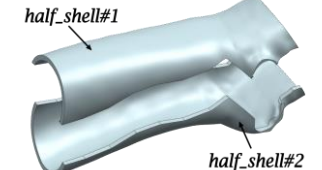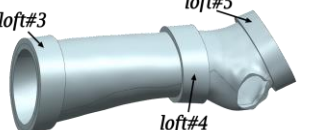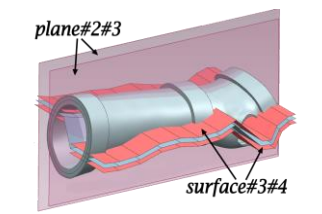
Figure 4-70 a) Generation of the guide curve for section extraction; b) irregular sectional profiles of the original mesh; c) regular sectional profiles of the edited mesh.

The CAD modelling procedure is detailed in Table 4-7 where each task is numbered according to the steps of Figure 4-69. All the steps have been carried out within Siemens NX modelling environment [89].

Table 4-7 Evolution phases of an applying example of the devised procedure.

	1a. the mesh representing the arm geometry obtained from the acquisition system is imported (blue in the figure); 1b. the guide curve (*line#1*) representing the back profile of the arm-wrist-hand district is extracted by intersecting the mesh with the *XZ-plane*; 1c. consecutive sections (*sectionset#1*) of the mesh are extracted with a sheaf of plane locally orthogonal to *line#1*;
	1d. from each section of *sectionset#1* a set of 20 points uniformly distributed (*pointset#1*) is extracted and a spline is built (*splineset#1*); the number of points has been empirically determined as sufficient to describe the arm geometry. 1e. a solid loft (*solid#1*) is performed on *splineset#1*;

	1f. each spline of *splineset#1* is offset of 4mm (*splineset#2)* and a second external solid loft (*solid#2*) is performed on *splineset#2*. The thickness value is chosen as a compromise to allow orthoses strength and reasonable time for the AM process. 1g. a Boolean subtraction operation between *solid#2* and *solid#1* is performed to obtain the principal shell of the orthosis (*shell#1*);
	2a. a plane parallel to the XZ-plane intersecting the mesh in the thumb area is created (*plane#1*). The position of *plane#1* is determined by a distance of 4mm from the vertex of the mesh characterized by the maximum Y value; 2b. a spline curve (*spline#1*) is fitted on the polyline resulting from the intersection of *plane#1* and the mesh; 2c. from *spline#1* is created an extruded surface in the Y direction (*surface#1*) which is used to delimitate *shell#1* and create the hole for the thumb;
	3a. *line#2* is defined as the broken line which interpolates for each curve of *splineset#1* the point characterized by the maximum value in the Y coordinate among the 20 points extracted in step 1d; 3b. *line#2* is extruded in the Y direction to create *surface#2*
	3c. *shell#1* is trimmed with surface#2 to generate *half_shell#1* and *half_shell#2*
	4a. three section pairs within *splineset#2* (placed in elbow, wrist and hand areas) are offset of 3mm; 4b. three lofts are generated from each section pair to create the housing space for zip ties (*loft#3#4#5*);
	4c. *surface#2* is offset of 4mm and -4mm (*surface#3#4*) in the X direction to delimitate *loft#3#4#5*, discarding the areas of *loft#3#4#5* that are not contained between *surface#3* and *surface#4*; 4d. the XZ-plane is offset of 4mm and -4mm (*plane#2#3*) in the Y direction to delimitate *loft#3#4#5*, discarding the areas of loft#3#4#5 that are not contained between *plane#2* and *plane#3*;
	4e. rectangular openings (4 mm width) are generated in the centre of *loft#3#4#5* following the curvature of *shell#1* to create the guides for the zip ties.

	5a. a set of equally distributed points *pointset#2* is generated on the external surfaces of *halfshell#1* and *halfshell#2*. Such pattern is generated leaving a margin of 5mm from the surfaces edges and using a pitch distance of 20 mm. 5b. holes with a diameter of 12 mm are generated on each point of *pointset#2*, using local normal directions extracted from *halfshell#1* and *halfshell#2* as cutting directions.

The last step, i.e. the realization of ventilation holes, is fundamental to reduce weight and to allow both inspection and ventilation of the treated area. The proposed solution is based on a hole pattern obtained starting from a set of randomly generated points equally distributed on the entire surface, except for the perimeter of the two halves and the zip ties housing locations.

The devised procedure has been tested in the generation of orthoses for six people, three children (1 male and 2 female) and three adults (2 male and 1 female). The composition of the panel group has allowed the validation of the modelling process on significantly different arm-wrist-hand anatomies (Table 4-8). For each case, the procedure has been applied following the framework described in the previous section. All the orthoses models were correctly generated without major complications, enabling the generation of six valid medical devices ready to be manufactured.

Table 4-8 Composition of the panel group.

	Patient information				
	Gender	*Age*	*Weight*	*Arm* ***Length*** (elbow to knuckles line)	*Arm* ***Diameter*** (elbow)
Patient #1	*M*	*11*	*40kg*	*31cm*	7
Patient #2	*M*	*50*	*73kg*	*38cm*	8
Patient #3	*M*	*45*	*87kg*	*40cm*	9
Patient #4	*F*	*6*	*25kg*	*19cm*	4.5
Patient #5	*F*	*7*	*26kg*	*22cm*	5.5
Patient #6	*F*	*30*	*48kg*	*31cm*	6

In order to evaluate the effectiveness of the produced results in terms of practical usability such as the reliability of the closing system, the adherence to the scanned arm, and their restraining properties compared with traditional plaster casts, all the generated models were manufactured. All devices were FDM-produced, specifically using the Stratasys F370 machine [90]. ABS-M30 material [91], a z-resolution of 0.178 mm and a horizontal orientation of the device on the build plate were chosen to maximize the orthosis strength. All the remaining settings are automatically handled by the software provided with the F370. The machine of choice is capable of printing soluble support material; as a result, minimal post processing efforts are required to clean the produced parts. Figure 4-71 shows an example of the resulting orthosis manufactured. Most important factors that brought to the choice of FDM are: i) it is a "clean" process – no dust is generated – and, therefore, it can be used also in medical environments; ii) the mechanical performances of the printed parts are generally

compliant with the application requirements; iii) FDM-printed orthoses (in ABS) have already been proposed and approved for medical applications.

Figure 4-71 Custom-made orthosis manufactured with FDM technology.

Each subject tested his/her orthosis by wearing it for a limited amount of time (~1 hour) in order to highlight possible major flaws. Even in this limited timespan, comfort/discomfort related issues can be highlighted. Subjects were asked to fill an appositely devised questionnaire, designed, based on published studies [17, 19], to investigate ergonomics, comfort and user satisfaction; the questionnaire is presented in Table 4-9. For each question, each subject assigned a score from 1 (very unsatisfying) to 5 (highly satisfying).

Table 4-9 Satisfaction questionnaire.

Question	*Scores*				
	1	*2*	*3*	*4*	*5*
Q1. Is the cast comfortable?	Want it removed	Irritating	Fairly comfortable, occasional irritation	Comfortable	Very comfortable
Q2. Would you prefer the new cast over traditional one?	Non-willing	Accepted reluctantly	Minor doubt	Positively	Strong willingness to try new cast
Q3. How do you consider the cast weight?	Heavy cast. Difficult to use arm	Moderately heavy. Limited multiple activities	Mildly heavy. Limited several activities	Fairly light	Light cast. Won't interfere with activities
Q4. Is the restricting effect stable?	Non-satisfying reduction requiring further procedure	Reinforced same cast	Slight shift	Marginal shift but no need for re-manipulation	No loss of reduction

Results of the questionnaire for the six patients are in Table 4-10.

Table 4-10 Results of the questionnaire.

	Scores				
	Q1	*Q2*	*Q3*	*Q4*	*Total Score*
Patient #1	*3*	*4*	*5*	*4*	*16*
Patient #2	*2*	*3*	*4*	*5*	*14*
Patient #3	*4*	*4*	*5*	*5*	*18*
Patient #4	*3*	*4*	*5*	*4*	*16*
Patient #5	*3*	*4*	*5*	*4*	*16*
Patient #6	*3*	*3*	*4*	*5*	*15*
Average	*3.0*	*3.7*	*4.7*	*4.5*	

Three subjects out of six scored 16 out of 20, one subject scored 18 and no subject scored fewer than 14. With an average score of 3, the comfort of the device (Q1) represents the lowest score. From a further verbal investigation this discomfort resulted mainly caused by the contact of the 3D printed cast on the ulnar styloid process. Consequently, for a future development of AM-based casts, an appositely shaped hole in the correspondent region of the cast needs to be created. Accordingly, this aspect will affect the strategy adopted for generating ventilation holes.

On the other hand, the overall assessments of both hand-wrist-arm district restricting effect and weigh of the device were assigned high marks (4 to 5) thus proving that the new device is highly effective in these terms.

Moreover, in order to assess the mechanical performance of the so-generated device, a Finite Elements Analysis (FEA) has been performed on a simulated worst-case scenario representing the orthosis for a 95th percentile 14 y.o. male arm [40]. Accordingly, an orthosis of length ~400 mm and maximum diameter of ~90 mm, has been used for this analysis; five alternative design solutions have been 3D modelled, changing the random configuration of scattered points on the surface, and analysed. A cantilever load case has been simulated.

Load has been imposed as a vertical concentrated force (100N) applied on the side of the hand, while the opposite side has been modelled as fixed geometry. This load condition is perfect to test the resistance of the most critical section of the arm (i.e. wrist section); moreover, it simulates a possible load condition typically characterizing the HWA district.

In the absence of specific strength requirements for immobilization devices, the entity of the vertical load has been estimated referring to similar studies in literature [92]. The resulting stress distribution is similar in all analysed cases, as reported in Table 4-11. In particular, the maximum value of the Von Mises stress is around 13MPa, with a maximum total displacement of around 2,5 mm. Figure 4-72 reports two of the tested configurations.
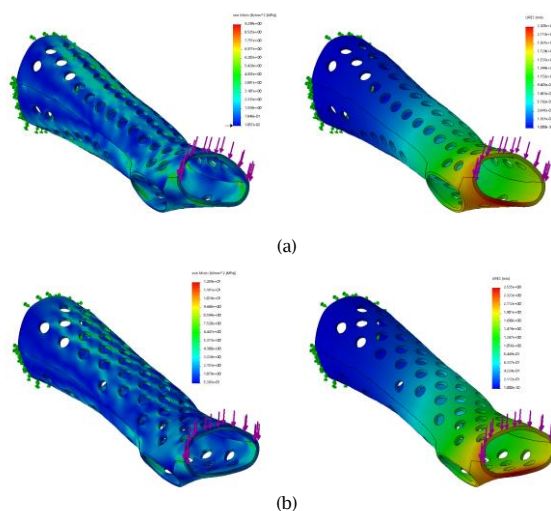

(a)

(b)

Figure 4-72 Results of the FEM analysis for two random configurations of ventilation holes, on the left the Von Mises stress distribution, on the right the corresponding total displacement.

Table 4-11 Results of the FEM analysis conducted on five different models, reporting five different configurations of the ventilation pattern.

#simulation	*Maximum Von Mises Stress (MPa)*	*Max Total Displacement (mm)*
1	9.60	2.34
2	9.29	2.31
3	10.33	2.42
4	11.19	2.49
5	12.89	2.54
mean	**10.66**	**2.42**
std.dev.	**1.45**	**0.097**

Since, as mentioned above, the standard deviation value characterizing the maximum stress observed in all the simulations is negligible for the considered application, the adoption of a random procedure to generate the pattern of ventilation holes is not prone to introduce an unexpected stress peak or an atypical tension distribution that could compromise the safety of the device (i.e. all generated models are topologically equivalent). In fact, the material used to produce the orthoses is the Stratasys ABS M-30 which has a tensile yield strength equal to at least 26 MPa (along Z axis of the 3D printer, as reported in [91]); this value is two times higher than the maximum stress condition observed in the simulations (12.89 MPa). In other words, the compliance of the orthoses w.r.t. the load conditions imposed is assured with a safety factor equal to about 2.

4.2.5. **Software adjustment – feature extraction**
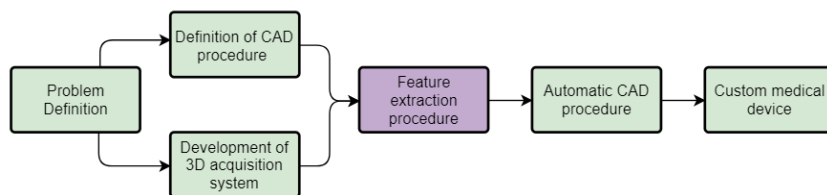
Figure 4-73 Diagram outlined to achieve the systematic realization of customized medical devices.

In order to automate the operations that perform the CAD model of the orthosis, shown in the previous paragraph, the software has been updated as shown below.

The feature extraction is carried out directly within the above-mentioned user interface due to a series of custom-built user-guided tools and consists of evaluating the following geometric features:

a. internal and external profiles of the mesh (that will be used to build the principal shell of the orthosis);

b. the bounding box of the orthopaedic device and the definition of zip ties positioning areas;

c. the shape and position of the opening space to accommodate the thumb finger;

d. the shape and position of a set of lines used to separate the orthosis into two halves (this allows the application on the patient arm) and for final positioning of the zip ties housings.

Except for the thumb finger opening region and the bounding box of the orthosis, which must be chosen by orthopaedics on each single case to ensure the conformity of the produced device to medical requirements, the remaining features are automatically computed as described below.

a) Extraction of internal and external profiles of the mesh

As said, one of the strategies to automatically generate a parametric surface that accurately describes the entire patient's anatomy is to use a loft operation guided by properly selected profiles, i.e. a series of set of points where each one defines a contour. The most intuitive strategy for defining such profiles consists of choosing a direction locally orthogonal to the line defining the external profile of the arm (Figure 4-74a). However, considering the imposed position of the hand-wrist-arm district, this strategy can be difficult to automate since a high sample density can lead to intersecting sections (Figure 4-74b). On the other hand, a lower sample density can leave large areas uncovered near the wrist (Figure 4-74c).

A solution to avoid these issues is to cut the mesh with a parallel sheaf of planes orthogonal to the dorsal profile of the hand (Figure 4-74d). This direction will be used to cut the surface at a distal extremity, thus preserving the correct orientation of the device.
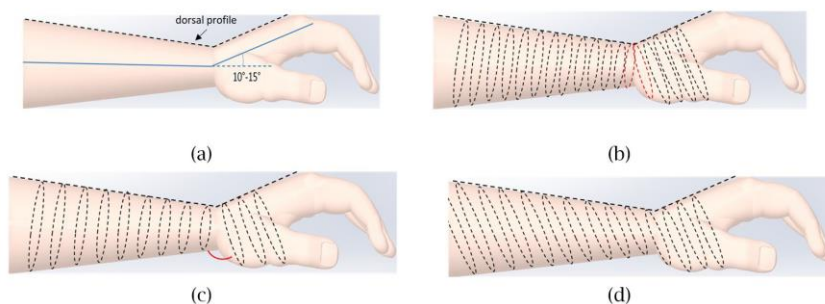
Figure 4-74 a) Indication of the angle defined by the arm and the hand in the resting position, and of the considered external profile of the arm; b) example of intersecting sections due to high density sampling; c) example of large open areas due to low density sampling and d) example of sectioning with a parallel sheaf of planes which follows the growing direction of the hand.

The cut direction is computed with an automatic process by initially intersecting the reference mesh with a sheaf of planes parallel to the Z-axis and considering the pointset composed by the barycenter of each obtained intersection. This pointset is then processed with the Douglas–Peucker algorithm [93] to find the two principal directions, d1 and d2 respectively corresponding to the arm and the hand directions (see Figure 4-75a). Between these, the one describing the hand orientation is chosen to extract the so-called internal profile for the loft operation (Figure 4-75b), i.e. the set of points used to model the internal surface of the cast.

The sample density for these profiles was set to 4 mm between each section, in an effort to optimize the value between required accuracy and the weight of the procedure, as well as the smoothness of the generated surface. In addition to internal profiles, a correspondent external profile (see Figure 4-75c) is also computed for each section. Through the offset profiles, a second loft operation is applied in the modelling process to obtain the external surface of the cast. These profiles are created at a distance of 4 mm. Such a value is crucial for the final design of the orthosis since it corresponds to the final thickness of the personalized cast. The selected value is a good compromise to allow both orthoses strength and a reasonable time for the manufacturing process. Both the internal and external profiles point coordinates are stored in an excel file to be used for modelling procedure.

b) *Definition of the bounding box of the orthopaedic device and of zip ties positioning areas*

To define the boundaries of the orthosis among all generated sections, two points, at distal and proximal extremities, needs to be manually selected by the user. A plane orthogonal to the Z-axis and passing through the selected proximal point is defined. Moreover, on the distal extremity, a plane orthogonal to the direction used to define the internal profiles and passing through the distal point is generated. This procedure will design a well-built model for the knuckle area, i.e. to have the right orientation, while keeping the correct structure over the elbow recess.

Moreover, the first four and the last four external profiles are externally offset with a 4 mm value (see Figure 4-75c) to generate zip tie housing profiles that will be used for the construction of the closing system. In addition, since a third zip is recommended to assure the correctness of the closing system, a further set of four external profiles roughly positioned in correspondence of the midpoint of the line d1 are offset using the same 4 mm value. Both the distal and proximal planes coefficients and the zip ties housing profiles are stored into an excel file.

c) *Definition of the opening space for the thumb finger*

The opening space for the thumb finger is generated by manually selecting the portion of points defining the profile of the thumb base from the point cloud data (Figure 4-75b-Figure 4-75c in red). These points are automatically projected onto their best fit plane and a close 2D NURBS curve (whose points are stored in an excel file) is fitted to extract the boundaries of the hole. Dimension and shape of the thumb opening were determined according to the standards used for the typical plaster cast treatment.
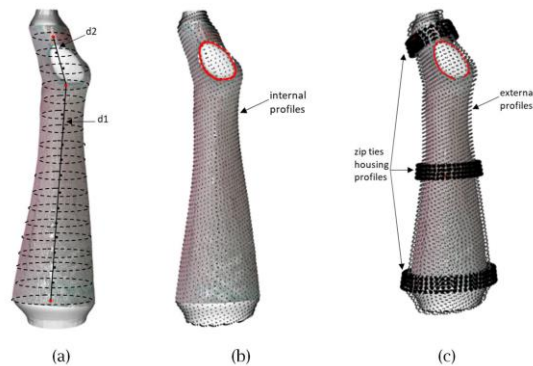
Figure 4-75 a) Example of cutting direction automated computation procedure with the Douglas–Peucker algorithm; b) example of automatic extraction of internal profiles and c) example of automatic extraction of external profiles, along with information relative to shape and position of zip-tie housing spaces and to the opening space for the thumb finger (in red).

d) Definition of lines for dividing cast and for final positioning of the zip ties housings

The modelling procedure also requires additional geometrical information to generate the two separate halves of the orthosis as well as to model the closing mechanism. In order to achieve these goals, three lines are automatically extracted by the system (Figure 4-76 in orange). Line 1 and Line 2 define the profile of the two halves of the cast, marking the future separation line. These curves are defined by a series of points extracted from the internal profiles generated as described in section above. Specifically, the points characterized by a maximum and minimum value along the Y direction are selected from each section. The line intersecting the thumb area (Line 1) is modified to "regularize" the cut of the thumb hole. This change is performed by adding to Line 1 the points with a minimum and maximum Z value for the closed curve that defines the thumb opening and discarding the points of Line 1 that fall between these two points. Without this adjustment, the principal shell could be erroneously cut in two difficult-to-wear halves. Line 1 also defines the position of the zip tie housings in correspondence of the separation between the two halves.

Line 3 defines the position of dorsal and palmar zip ties housings and is computed as passing through the points of each section with maximum value in the X direction (Line 3 in Figure 4-76). All the points defining Lines1, 2 and 3 are stored in an excel file.
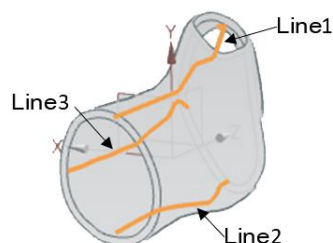
Figure 4-76 Example of the lines defining the cut for the medical device application (Lines 1 and 2) and the reference to build zip ties housing (Lines 1,2 and 3) automatically computed from the software.
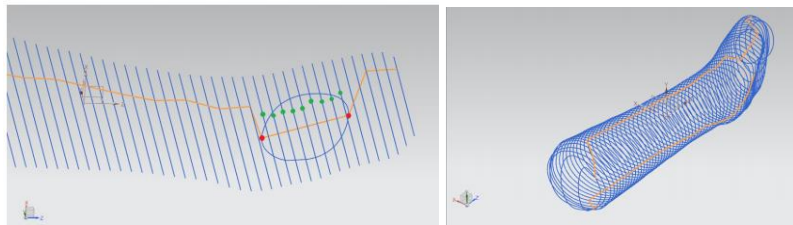
Figure 4-77 Example of correction of Line 1 with thumb points.

According to the above, the software has been updated to calculate the features necessary for the CAD modeling of the device; some are extracted automatically and some are provided under user input. The changes have been implemented according to the new use cases defined by the modeling choices. The five new use cases are shown in Figure 4-78 following the sequence of operations needed to extract all the features. The dotted arrows indicate the dependence from the operation indicated by the arrow. Each new function therefore corresponds to a new key on the toolbar.
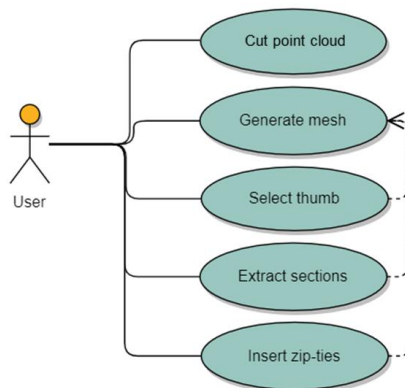
Figure 4-78 Additional use cases for the orthosis realization.

      Cut point cloud
When the 360° 3D image of the arm is ready, by pressing the buttons "select area" and "delete", the user can select and cut all those portions of points which will not be part of the orthosis, therefore, in most cases, the anatomy is cut approximately 3 cm before the elbow recess, and slightly under the knuckles [94], also the thumb finger is removed to create an opening space for application (Fig. 5a). To ease this process, visual references can be manually drawn onto the gauze before the 3D image is acquired. As shown in fig.x. The rubber band selection has been implemented using the PCL library.

      Generate mesh
When the model of the orthosis is ready the button "Triangulate" computes the Poisson surface [95] of the arm. The calculation of the Poisson surface (shown in Figure 4-79) is based on the orientation of the points, if the cloud contains points whose normal are not correct, there will

be an error in the reconstruction of the mesh. For this reason, during the scanning phase we proceed immediately to the calculation of the normals before applying to the cloud the matrices of rototranslation, because the calculation is easier if the direction of acquisition is known.
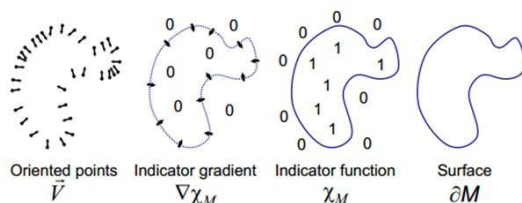
Figure 4-79 Example of Poisson surface computation.

The choice to use this type of surface derives from the fact that is a smooth and detailed mesh, and which automatically close the hole produced by removing the thumb finger. As explained above, this hole needs to be closed in order to extract the mesh sections as shown below. The best parameters identified for mesh reconstruction are: maximum tree depth for surface reconstruction equal to 10 and sample per node equal to 10.

Select thumb

Before triangulation the user must select the portion of points defining the opening space for the thumb (Figure 4-80a). These points are elaborated by the program which automatically project them onto the best fit plane and fit a close 2D NURBS curve to extract the geometry of the hole. These operations are also performed with PCL library.

(a)   (b)
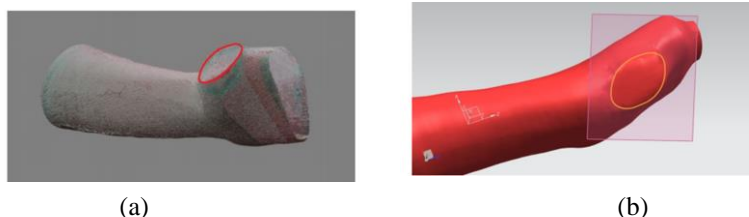
Figure 4-80 (a) Thumb point manual selected (in red); (b) best fit plane computed on the selected points.

Extract sections

Pressing the button Sections, the mesh is automatically sectioned with a sheaf of planes parallel to the reference line with a gap of 4 mm between each section. This operation is performed with the VTK library. Once the program has calculated the intersections with the sheaf of planes, each section is reorganized and sampled with 100 equidistant points. These points are then sorted in polar order with center of gravity in the section barycentre. Sorting the points of each section is a fundamental step to avoid errors in the reconstruction of the main shell during the loft operation. In this way the sections will all be oriented in the same direction and with the first point coinciding with the highest point in y of the section, and will not create the hourglass effect. If the hand is particularly angled with respect to the rest of the arm, however, the loft may still be slightly bent because the polar order will not follow the

axes of inertia of the section. Figure 4-81 shows an example of this problem. If on the other hand all the sections are ordered according to the axes of inertia, it is highly probable that the arm area presents problems in the loft operation because it has an irregular shape.
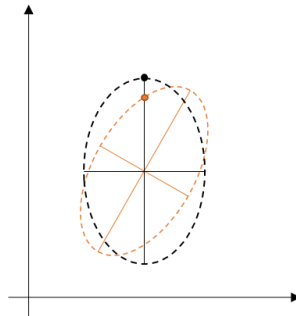
Figure 4-81 Example of rotated section (orange) and regular section (black).

For each section is also automatically computed the parallel, or offset, curve as depicted in Figure 4-82.
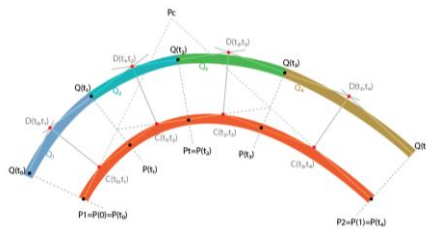
Figure 4-82 Offset section computation.
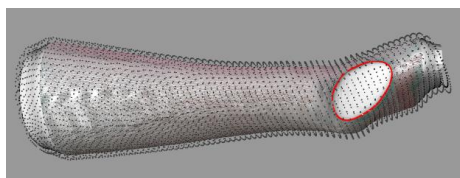
Figure 4-83 Example of offset sections automatically computed.

Insert zip-ties

Since the Poisson surface will not precisely respect the scanning limits and sections of the entire mesh are extracted, it will be necessary to select the distal and proximal limits of the device. By pressing "Insert zip-ties" three points can be manually selected, the first point is in correspondence with the elbow recess and when selected it defines a cut automatically parallel to the Z-axis (i.e. the growing direction of the arm) such to obtain a comfortable and effective device; the second point is in correspondence of the knuckles and when selected it defines a plane automatically parallel to the direction used to extract the sectional profiles of the reference mesh (Figure 4-75c). This choice allows the model to be well-built on the knuckles

area, i.e. to have the right angulation, while keeping the correct structure over the elbow recess.

When the user selects these points the program also automatically generates the offsets of four sections at a distance of 3 mm from the offset curve, which will be used for the automatic construction of the closing system. Finally, a third point more or less in the middle of the cast is selected under the styloid process of the ulna that defines the central band. For this band, sections parallel to the Z axis are extracted, as for the band near the elbow.

Additional Info – computed in background

The program also automatically compute and store in a file the information about the points defining three lines, that will be used in the modelling process (Figure 4-76 in orange): the two lines which describes where the orthosis will be cut in half for application (line 1 and 2 in Figure), defined respectively by the points of each section with the maximum and minimum value along the Y-coordinate, where the line that runs through the thumb area (line 1) is modified such to regularly cut the hole in half. This alteration is performed by interpolating the line with the extremities (in the Z-coordinate) of the closed curve that defines the thumb opening and discarding the section's points that fall between these values; without this adjustment the principal shell could be erroneously cut in two difficult to wear halves. The third line is computed as passing through the points of each section with maximum value in the X-coordinate (line 3 in Figure); this line will be use as reference to build the lateral closing system; its necessity will be clarified later in the modelling procedure. Points are exported to a text file. Computation of directions with the Douglas-Peucker algorithm may fail if the arm is particularly straight, in this case the possibility to enter the direction manually is provided.

Figure 4-84 shows the result of all these steps, the red dots represent the area of the thumb selected by the user and the green dots are the guide points to create the cutting lines extracted from the sections.
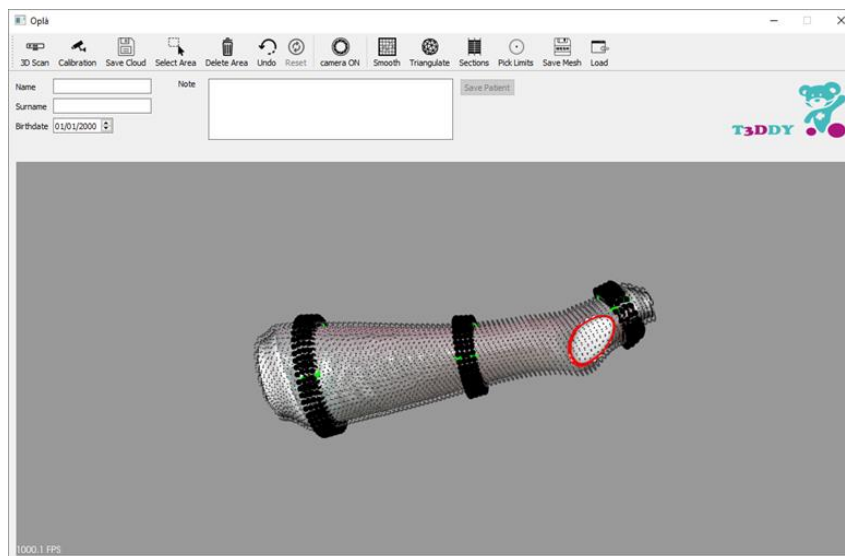
Figure 4-84 Final stage of the feature extraction phase.

4.2.6. **Automatic CAD procedure**
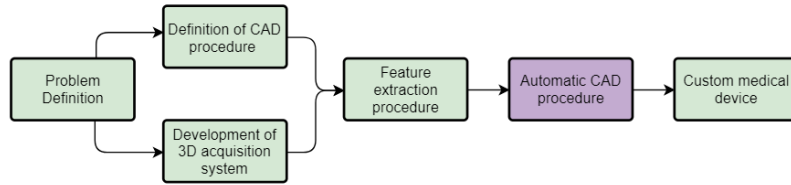
Figure 4-85 Diagram outlined to achieve the systematic realization of customized medical devices.

Starting from the features extracted using the above-mentioned strategy, an appositely devised tool (developed by using NX Open Application Programming Interface (API) toolkit [96]), was implemented to allow the automatic modelling of the personalized cast. In detail, the devised procedure is based on the workflow depicted in Table 4-12.

Table 4-12 Evolution phases of an applying example of the automatic procedure.

	The program starts by reading the file containing the points of each internal and external profile and builds two sets of spline curves: the internal curve for the internal profile and the external curve for the external profile.
	Two solid lofts, guided by the internal and external spline curves, are built. One is defined as an inner loft and is guided by mesh internal curves; the other is the outer loft and is guided by the external curves. The inner loft is then subtracted from the outer, realizing the principal cast shell.
	The two planes defining the boundaries of the orthosis are computed by exploiting the information extracted in the feature extraction phase; then, a trimming operation on the solid shell guided by these planes is performed.
	A set of spline curves is fitted on the zip ties housing profiles, thus defining a set of zip tie curves. Then, multiple solid loft operations are performed on such generated curves to model the zip housing. The inner loft is again subtracted from each of the obtained solids.
	To realize the opening space for the thumb finger, the points of the spline surrounding the thumb area are used to build a close spline curve. A solid cut extrusion of the spline is performed to obtain the hole.
	The lines defining the opening profile (Line 1 and Line 2 of Figure 4-76) are imported; a polyline is fitted on each set of points and extruded orthogonally to the XZ-plane. The principal shell is trimmed with the two so generated surfaces.

	A second-degree spline is fitted on each set of points corresponding to Line 1 and Line 3; the generated lines are extruded orthogonally to the XZ-plane and to the YZ-plane, respectively. The extruded surfaces are offset in both directions of 4 mm to define the boundaries of the zip ties housing. Zip ties supports are then cut with the so generated surfaces.
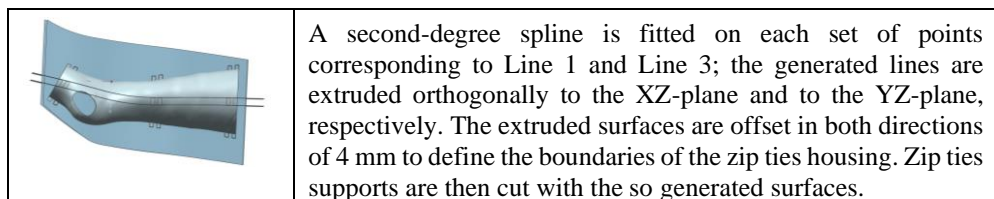
The result of the devised procedure is shown in Figure 4-86, where two wearable parts (external and internal half shells) were generated, along with the closing system.
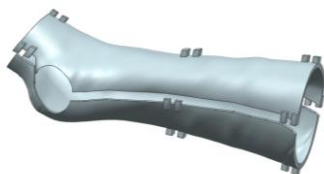
Figure 4-86 Result of the automated NX procedure.

All the modelling steps are handled with a macro procedure that was made available to the user through a customized toolbar button within the NX 10 toolbar (Figure 4-87). The procedure is completely automatic, exploiting the information stored in the previous step of feature extraction, hence it does not need any intervention from the user. The program usually takes approximately 60 seconds to generate a new cast model starting from the hand-wrist-arm district mesh.
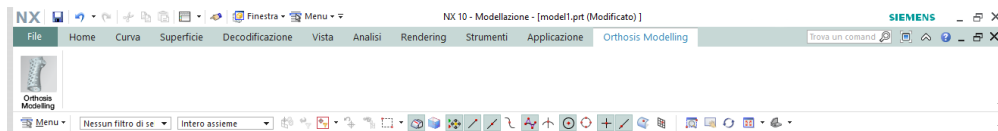
Figure 4-87 Customized button for orthosis modelling added to the Siemens NX 10 toolbar.

> *Generation of ventilation holes – first attempt*

A fundamental aspect that can be pursued by 3D printed casts is transpiration and the possibility of a regular inspection of the injury site. As oppose to traditional plaster casts, additive manufactured casts can be perforated to increase ventilation of the treated area, reducing the risk of irritation [31] and the overall device weight. A correct ventilation pattern, while being as light as possible, must preserve the mechanical properties of the device, assuring the correct stiffness and mechanical resistance to external loads for the entire treatment.

To overcome this issue, two automatic strategies were initially devised to generate the ventilation holes. The first strategy consists of generating a set of equally distributed control points using a pitch distance of 20 mm. This can be done directly using an embedded command in Siemens NX (i.e. pattern feature command). Circular holes that have a centre on such points and a diameter of 12 mm were then generated using local normal directions for cutting. The generation of control points, moreover, reserved a margin of 5 mm along the edges to prevent damage to the functional surfaces of the orthosis (i.e. zip tie closing system and mating surfaces of the two orthosis halves as shown in Figure 4-88a).

Such values were selected since they empirically demonstrated a good compromise between lightness and structural strength. A Finite Element Analysis (FEA) was performed on a synthetic worst-case scenario representing the orthosis for a 95th percentile 14-year-old male arm [40]. Accordingly, an orthosis of length ~400 mm and maximum diameter of ~90 mm, was used for this analysis. Five alternative design solutions were 3D modelled, changing the random configuration of scattered points on the surface, and then analysed. A cantilever load case was simulated. The load was imposed as a vertical concentrated force (100N) applied on the side of the hand, while the opposite side was modelled as fixed geometry. This load condition was perfect to test the resistance of the most critical section of the arm (i.e. wrist section). Moreover, it simulated a possible load condition typically characterizing the hand-wrist-arm district. In the absence of specific strength requirements for immobilization devices, the entity of the vertical load was estimated referring to similar studies in literature [97]. The resulting stress distribution was similar in all analysed cases with a maximum value of the Von Mises stress around 7MPa and a maximum total displacement of around 2 mm. This value is about three times higher than the maximum stress condition observed in the simulations since the material that is expected to be used to produce the orthoses is ABS characterized by a tensile yield strength equal to at least 20 MPa.

(a)   (b)
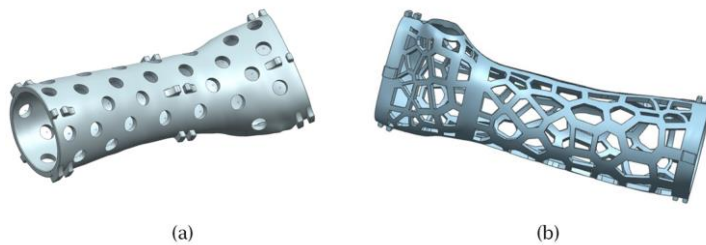
Figure 4-88 Example of the result of the two perforating strategies: a) strategy carried out in the NX 10 environment based on the generation of a random set of control points; b) Voronoi perforating pattern, applied within the grasshopper environment.

This first strategy is based on a uniform distribution of control points and generates a fully perforated cast. However, it does not take into account areas subjected to possible collision risks. In other words, the wrist area, which is the most sensitive region of the HWA district (and the most likely to receive collisions), could be considered to be too weak in the final model.

In the light of these considerations, a second strategy was devised within the Rhinoceros/Grasshopper environment [98]. The idea was to create an adaptive Voronoi perforating pattern specifically tailored for the orthosis topology. To accomplish this, the hole-generation algorithm must preserve the following: i) the areas supporting the zip ties holding mechanism, ii) the mating surfaces of the two halves of the orthosis, and iii) the wrist region (specifically, a bend of 20 mm in correspondence of the wrist as shown in Figure13(b)). The result obtained with this strategy was entirely automated and used a combination of existing Grasshopper libraries and is shown in Figure 4-88b. A FEA, conducted in accordance with the first strategy, proved the effectiveness of this strategy.

While being both reliable and automatic, the two above strategies were not optimized for topology. Hence, a third strategy was devised based on a topological optimization (TO) analysis [99] of the cast.

The goal was to determine a generic topology of the ventilation holes that guarantees the required mechanical performance of the device and adapts to each specific case.

Considering that the structural problems faced by each specific orthosis are generally equivalent (assuming they are subjected to similar load/stress configurations), the idea was to replicate an optimized generic pattern evaluated for the previously defined worst-case scenario. To this end, the worst-scenario model obtained at the end of Phase II was imported into a TO dedicated software, Inspire SolidThinking [100], to extract the optimized pattern for the ventilation holes.

The TO algorithm determined a generic distribution of the holes ensuring the desired stiffness and resistance of the device, while lightening the orthosis in the most beneficial way. This distribution can then be adapted to each patient-specific geometry of the orthosis, by means of scaling/morphing operations. This strategy avoids the computational costs that would be introduced in the procedure by performing a specific TO analysis for every new cast model. The validity of this approach was guaranteed by the safety margins adopted in the initial simulation phase, which considered the variability introduced by the loads, the geometry of the orthosis and the uncertainties of the scaling/morphing operations.

With reference to Von Mises stress, a safety factor of three was used to run the simulation. The thickness of the ribs and bands that characterize the final result (Figure 4-89) were determined, verifying its compliance with respect to the safety factor.
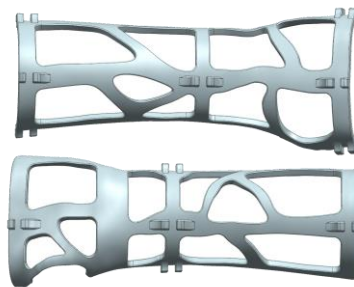
Figure 4-89 Example of the result obtained after the scaling/morphing of the generic TO-generated pattern for the ventilation holes on a specific case (two halves of the orthosis).

At this stage time, the adaptation of the ventilation pattern on each specific orthosis needs to be carried out by means of manual operations (scaling/morphing) performed in the NX CAD environment. In the following the procedure for creating the holes has been fully automated.

3D printing

As previously mentioned, the cast is subjected to mechanical stresses compatible with fabrication with a plastic material. This choice of using additive manufacturing techniques guarantee the comfort and lightness requirements that are sought in this application. Among the AM technologies available on the market capable of producing plastic parts, FFF (Fused Filament Fabrication), commonly known as FDM (Fused Deposition Modelling), represents the most suitable choice considering both the costs and the fabrication time required.

Accordingly, a suitable material for the fabrication can be the Stratasys ABS M-30 [91], which has a tensile yield strength equal to 26 MPa (along ZX axis of the 3D printer). Such a material satisfies the standards required in terms of biocompatibility, namely cytotoxicity, for medical applications and orthopaedic devices.

Indeed, time is an essential element that needs to be considered in the development of the entire procedure, specifically for the fabrication step, to guarantee the applicability and efficacy of the treatment. Moreover, the orthosis costs should be reduced as much as possible. Therefore, a series of tests were carried out in order to estimate time and costs associated with the FDM fabrication of personalized orthoses. Table 4-13 shows the results from simulating the manufacturing a representative sample of patient geometries in terms of cost and printing time. The simulation was carried out considering the Stratasys F370 FDM machine [90]. The costs reported in Table 4-13 considered the material required, hourly machine costs and labour. It is important to note that the fabrication time can be reduced by at least a factor of two if a parallel production process is used for the two orthosis halves. Evidently, this solution considers the availability of two FDM machines. The F370 machine was chosen because it is able to use a material for the generation of support structures (always required by the FDM technology for the fabrication of the orthoses models) that is water-soluble. This strongly improves the efficiency and quality of the process, removing the need for mechanical post-processes to clean the printed parts.

Table 4-13 Fabrication times and costs.

Arm	Length	Diameter of the arm at the elbow recess	Approximate Cost (€)	Printing Time
Male Adult	360 mm	100 mm	180	18h 6min
Female Adult	320 mm	80 mm	146	15h 54min
Child	200 mm	55 mm	84	7h 21min

Results

The semi-automatic method for the generation of a personalized casts for the HWA district was tested for five case studies. The entire procedure (with the exception of the generation of ventilation holes) was carried out, in all cases, by clinicians who regularly perform the traditional plaster cast treatment in day hospital. The anatomies chosen for this preliminary study significantly differed in size and local geometry. The results obtained were evaluated considering both the adherence of the generated casts to the medical requirements and the times required to accomplish the entire procedure (see Table 4-14).

In each case, the geometry of the HWA district was acquired using the hardware described in Section 1 without any major issue. The use of gauze was necessary to allow the correct acquisition of the HWA district and can be used by the medical staff to introduce visual reference elements prior to the acquisition phase. The clinicians can use the gauze to draw anatomical landmarks with a marker. This information can be acquired by the RGB cameras of the 3D scanner and later used to guide the user in the feature extraction phase. Although not essential, the marking of the knuckle line, the elbow recess and the thumb finger base eases the execution of the feature extraction step. Another sensible aspect that emerged during the tests is the positioning of the patient during the acquisition. Specifically, the thumb finger must be oriented vertically to remove shadowing effects on the surface of the hand palm. Accordingly, the operator needs to carefully place the patient hand in the correct pose.

Table 4-14 Average times required by each procedure's phase.

Phase	Time required
Acquisition	~5 minutes
Feature extraction	~5 minutes
Automatic modelling	~2 minutes
Generation of ventilation holes	~40 minutes

The feature extraction step proved to be the most challenging phase to be carried out by a non-expert user. Even in the case its execution is performed by following the above-mentioned visual landmarks particular care must be taken in the generation of the thumb opening. The most common human errors in the selection of the points defining the profile of the thumb base can lead to either the failure of the automatic procedure or the creation of an anatomically incorrect opening. A typical example, with respect to the last occurrence, was the generation of a too-restrictive aperture for the thumb, which hindered the full mobility of the patient and caused discomfort.

The automatic modelling phase was successfully executed in all cases. Indeed, all minor errors observed in the tests were ascribable to poor input provided by the previous feature extraction phase.

The generation of ventilation holes was the most time-consuming step, as reported in Table 4-14, since it is manually performed by an expert CAD modeler. In this respect, the use of spline modelling tools and other 3D modelling functions is required to adapt the curves defining the pattern of ventilation holes to the specific orthosis.

Finally, the orthoses were manufactured using the F370 Stratasys machine. In all cases, their compliance to medical requirements were approved by orthopaedics. The closing system for the orthoses, based on the application of zip ties, proved reliable and valid, as it guarantees the safety of the injured arm while maintaining the possibility of access to the region of interest for inspection. The orthoses modelled and manufactured using the proposed procedure are depicted in Figure 4-90.

Figure 4-90 Orthoses fabricated in ABS in the five case studies, wear on the scanned arms.

4.2.7. **Ventilation pattern – automatic strategy**

Various solutions have been tested to achieve a robust and reliable automatic hole making procedure. Below are the considerations and tests carried out before reaching the final procedure.

In detail, three procedures were investigated and tested in three different development environments:

    i.   transfer of the ventilation pattern through texture mapping techniques, tested in a python environment;

    ii.   adaptation of the ventilation pattern with surface morphing techniques, tested in Rhinoceros environment;

    iii.   creation of holes using known feature of reference geometry, tested in Siemens NX environment.

The methods (i) and (ii) are briefly described below, followed by the method (iii), which is the methodology chosen for the final prototype.

i) transfer of the ventilation pattern through texture mapping techniques

The idea behind this method is to create a pattern of perforations on a flat surface, create an associated image and apply it to each new orthosis with texture mapping techniques [101] and then derive the curves by analyzing the colors of the points.

To test this technique, the entire procedure for the realization of the orthosis has been reimplemented in python, using the CAD library pythonOCC [102]. For the re-implementation of the procedure some minor changes were necessary but the workflow, composed of the steps described above in Table 4-12, has remained unchanged.

In Figure 4-91 is depicted the orthosis realized with the python procedure.
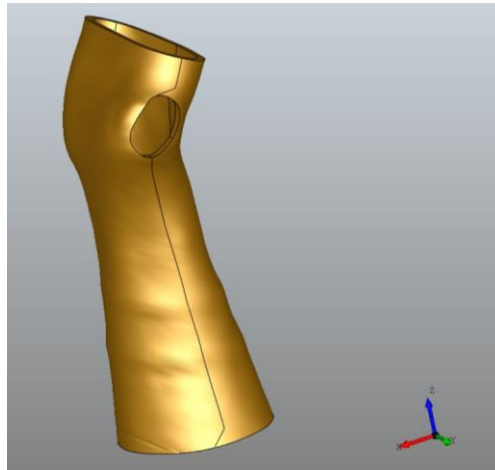
Figure 4-91 Resulting orthosis of the python automatic procedure.

Once the CAD model of the orthosis has been created, the texture image has been mapped, the result is shown in Figure 4-92.

Figure 4-92 Result of the texture mapping operation.

Analyzing this methodology some issues are observed:

1) the processing time to create the CAD model is considerably longer than the procedure implemented on NX. Specifically, boolean operations can take up to 10 minutes, for example to empty the main shell.

2) Secondly, with texture mapping we are not able to control well the arrangement of the holes because these techniques are based on the development of UV planar model and then map the texture image, but, since the model created is not developable, there may be very different mappings between the different orthoses and also it is difficult to manage the positioning of the holes.

ii) adaptation of the ventilation pattern with surface morphing techniques
This second method is based on the adaptation of planar curves on arbitrary surfaces. The idea is to create a planar surface containing the holes in the form of curves and map these curves to a certain portion of the orthosis. To test this strategy it was chosen to use the tools provided by the modeling software Rhinoceros. The automatic CAD model construction procedure was implemented with the Rhino API in python language and, as in the previous case, some minor changes were necessary but the workflow, consisting of the steps described in Table 4-12, has remained unchanged.
            The result of the procedure is shown in Figure 4-93.
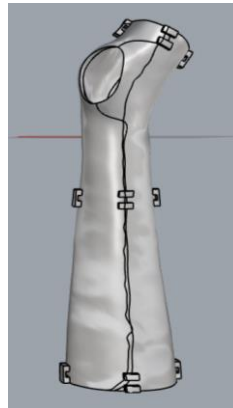
Figure 4-93 Resulting orthosis of the Rhinoceros automatic procedure.

The procedure identified for the application of the holes follows the following steps:

1) The interested portion of the orthosis is developed on the two-dimensional plane with the function *createUVcrv* (Figure 4-94b)
2) Two flat surfaces are created in the areas of interest. These surfaces define the spaces on which the pattern will be mapped (blue in Figure 4-94b).
3) With the *ApplyCrv* function, the curves of the holes (Figure 4-94a) are remapped on the surfaces created in step 2.
4) *RebuildUV* is made on the starting surface in order to apply the mapped curves.
5) With the *ApplyCrv* function, the holes are transferred to the reconstructed surface.
6) With the MakeHole function the solid is drilled with the mapped curves (Figure 4-94c).
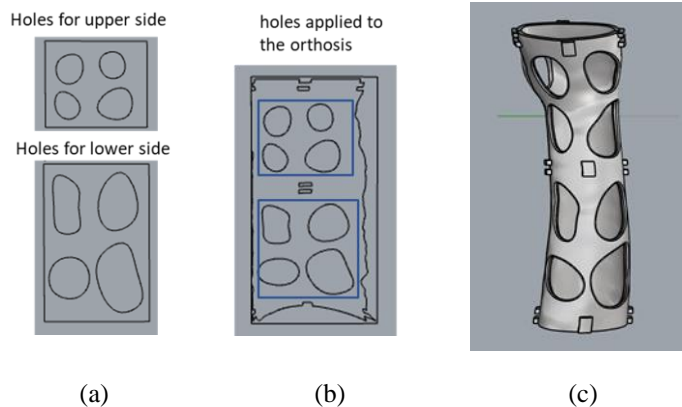
(a)　　　　　(b)　　　　　(c)

Figure 4-94 Hole mapping steps.

The analysis of this second technique also reveals some problems:

1) The construction procedure of the orthosis is not as robust as the one carried out with Siemens NX and sometimes generates errors. For example, it is necessary to perform some checks on the normal surfaces, which can be reversed and thus generate errors that lead to the failure of the procedure.

2) Secondly, even in this case, it is not possible to control the arrangement of the holes inside the area selected for mapping. There may be cases where too fine nerves are made which could lead to device ruptures, or too large, resulting in material waste and device heaviness.

iii) creation of holes using known feature of reference geometry

The third technique is based on the idea that, given known points of the geometry of the model, it is possible to map a ventilation pattern correctly by making some geometric considerations. Specifically if a valid ventilation pattern is available, this can be taken as a reference and adapted to new orthoses by identifying the different areas of the device.

The procedure for making the final ventilation holes was carried out in two phases: the definition of the reference pattern and the definition of the adaptation strategy. As will be seen, the reference pattern is initially identified following the topological optimization of the device and simplified to be able to be reproduced in a robust way on each new orthosis. In the adaptation procedure the pattern will be further simplified in order to identify reference points that can be extracted automatically with the management software presented above. These are the steps in detail.

Definition of the reference pattern: medical and structural considerations

The reference pattern has been determined through a process of synthesis of various aspects, discussed in the following. The pattern should be clinically sound: it should maximize the quality of the treatment, patient's comfort and reduce typical cast-related problems – e.g. rashes and compartment syndrome. Moreover, areas sensitive to rubbing and compression should be left uncovered. Regions that require particular attention (see Figure 4-95) are:

  i) styloid process of the ulna – this area should be left open to prevent cutaneous lesions and severe discomfort;

  ii) the internal wrist area – this area needs to be protected the most in case of wrist fractures;

  iii) center line of both internal and external halves - a surface portion along the centerline that should be left solid to preserve a continuous ribbing structure.
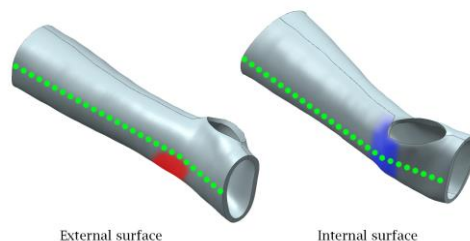
Figure 4-95 Relevant arm areas. Red – styloid process of the ulna. Blue – Internal wrist area. Green – center line.

The holes should evenly cover the surface of the cast to allow proper ventilation, possibility to wash and to scratch the arm, which are perceived as primary concerns by end users. Therefore, a minimum holes area of ~1cm2 should be granted. Moreover, the pattern should guarantee the integrity of the device and its compliance w.r.t. the loads induced by regular use. Other structural aspects that need to be considered are the preservation of a minimum thickness in every direction and the removal of stress concentrations points, which results in the generation of a smooth set of curves for the generation of holes, characterized by large fillet radiuses. Since in the present work the final orthosis will be 3D printed by using a Fused Deposition Modeling (FDM) process, the minimum thickness is stated equal to 4 mm. Finally, an additional functional aspect needs to be considered in case the orthoses are generated using the approach provided in [103]. In fact, three zip ties are applied near the knuckles, the elbow, and in a central region, to keep the two halves of the orthosis together. Such areas need to be left untouched by the hole pattern in order to avoid possible complications. The integration of thermal comfort analyses as a parameter in the definition of the reference pattern is another requirement that could be considered; however, in this work, such aspect has not been included yet.

As previously mentioned, TO can help in the identification of a general pattern maximizing the structural response of the device. In this study, a TO performed within Solidthinking Inspire has been used to obtain a starting solution for the generation of the reference pattern on an orthosis modeled on a 50th percentile 10-years-old male arm (Total Arm length of 643mm [104]). Load conditions used for the TO are in Figure 4-96.

Due to the unpredictability of possible external and accidental loads, this study takes into consideration only the loads that can be traced back to the patient itself. Considering the wrist joint, four movements can be identified (see Figure 4-97): flexion-extension and radial-ulnar deviations. Following the approach proposed in [105], literature values have been used to estimate maximum torques that healthy people usually produce. Four different load conditions, one for each wrist movement, were considered. Wrist torques, due to wrist joint movements (depicted in Figure 4-97) have been expressed as forces applied on the front face of the orthosis (different areas depending on the direction – see Figure 4-96 where a value of 0.1m has been used as distance).
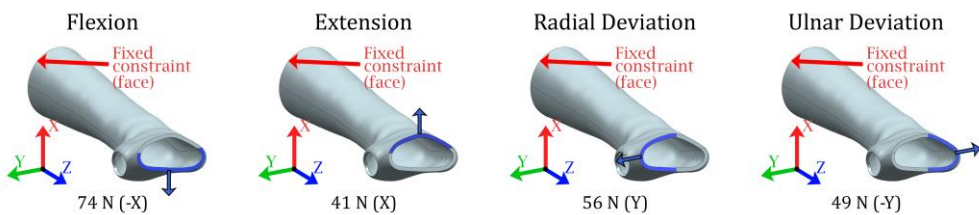
Figure 4-96 Loads configuration used in the study.
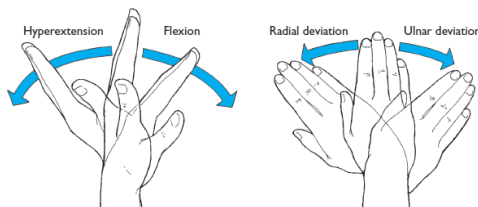
Figure 4-97 Wrist joint movements.

In all cases, the orthosis is constrained at the elbow with a fixed constraint essentially reproducing a clamped beam condition. All the choices were made trying to use a conservative approach: both the absence of the arm and the chosen constraints contribute to the definition of a condition more severe than the real one. The TO is performed with the two halves of the orthoses joined in the area where the zip ties are applied to reproduce the closing system; face-to-face contacts are considered on the other surfaces. The material used is ABS plastic. The analysis was carried out maximizing the stiffness/mass ratio of the object. The result obtained during this preliminary analysis is in Figure 4-98. The obtained pattern, although valid from a structural point of view, was subsequently manually edited to meet all the requirements discussed before. The result is visible in Figure 4-99. Since the reference pattern was obtained by adding material w.r.t. the model in Figure 4-98, its weight is obviously greater than the optimized one. On the other hand, the designed pattern assures full compliance with all the aspects imposed by the application.

Several differences can be observed comparing Figure 4-98 and Figure 4-99: evidently, the TO pattern has been heavily altered in order to consider all the previously described aspects (medical constraints, fabrication constraints, minimal level of regularity to assure its repeatability with an automatic procedure). The deviation from the orthosis model of Figure 4-98 is also justified by the philosophy followed in this study: the TO pattern is obtained studying a single, although representative, anatomy; its original efficacy and compliance to the structural needs of the device would still be hindered when applied on a different anatomy. As a result, the TO pattern of Figure 4-98 must be considered only as a general indication, i.e. a starting point.
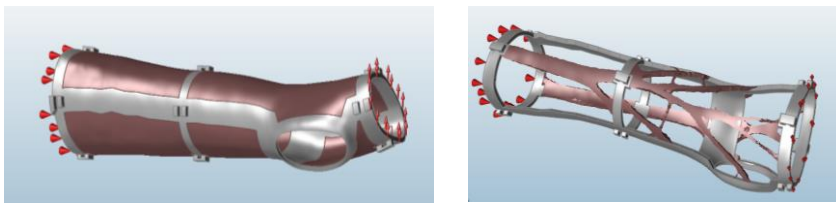
Figure 4-98 Topology Optimization procedure performed in Inspire Solidthinking; a) definition of the design space regions; b) final result obtained in one load configuration.

Figure 4-99 Final configuration of the reference pattern to be validated. The pattern is the result of manual modeling operations performed using the TO model as reference.

FE analyses

The reference pattern depicted in Figure 4-99 has been manually redrawn on two orthoses (named "Large" and "Small"), representative of the entire size spectrum of anatomies considered in this study. The Large orthosis is characterized by a length of ~400mm and a maximum diameter at the elbow region of ~90mm corresponding to a 95th percentile 14-

years-old male arm. The Small orthosis is ~195mm long and has a maximum diameter of ~65mm, taking the dimensions of a 5th percentile 5-years-old male arm as general reference [104]. On the two newly designed orthoses, FE simulations were carried out to test the mechanical validity of the generated geometries on both sides of the spectrum.

The results obtained are summarized in Table 4-15; the worst condition (Flexion load – Small orthosis) is depicted in Figure 4-100: a maximum von Mises stress value of 25.3 MPa is observed. Such value is compatible with the yield stress of 3D printed ABS (26 MPa along ZX axis of the FDM printer [106]). Displacement values are tolerable even in worst cases, especially considering that the simulated configuration is far from the real one on this specific aspect.

Table 4-15 Validation of the pattern - FE analyses results.

Load Configuration	Large Orthosis		Small Orthosis	
	Stress (Von Mises) [MPa]	Displacement [mm]	Stress (Von Mises) [MPa]	Displacement [mm]
Flexion	20.2	4.4	25.3	4.3
Radial Deviation	11.7	2.0	13.9	2.2
Ulnar Deviation	8.8	2.1	13.9	2.2
Extensions	7.5	1.6	11.6	1.8
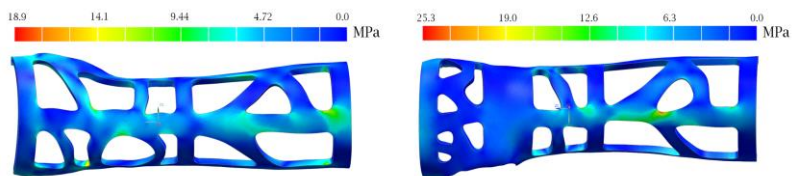
Figure 4-100 FE analysis (von Mises stress map) results for the Small orthosis, under the Flexion load (internal and external surface).

Adaptation Strategy

Once the structural and functional aspects of the ventilation pattern are outlined and its strength is tested, a strategy to automatically adapt it on any new orthosis has been developed.

After a preliminary phase of simplification of the reference orthosis holes pattern, the adaptation strategy consists of two phases: a) definition of a set of key points used to guide the creation of the holes, extracted from the scanning of the patient's arm; b) perforation of the CAD model using curves generated from the obtained key points. Both tasks (a) and (b) are completely automatized.

Pattern simplification

Before proceeding with the extraction of key points used to define the shape of the holes on a new orthosis, a simplification process of the hole pattern on the reference orthosis is required. The main aim of such a process is the generation of a simplified pattern that can be automatically scalable and replicable on each new case by modeling 3D polygons. Specifically, as visually described in Figure 4-101, the structure in Figure 4-99 is manually divided into 12 main zones (6 dorsal and 6 palmar). Subsequently, each zone undergoes a process of stylization of the holes, which are described by polygons rather that curves. The

vertices of such polygons (see Figure 4-101) are used as points to be automatically mapped to each individual case, as described in the next paragraph.

The simplified pattern of Figure 4-101 is the result of a series of attempts to identify a pattern based on the minimum number of highly reliable key points. In fact, the whole procedure needs to minimize error occurrences in the identification of key points on different anatomies. As a result, the simplification of the geometry is a tradeoff between the model described in Figure 4-99 and the need of a model less error-prone in term of model reconstruction. As previously stated, the need for an optimized structure is supplanted by safety and repeatability needs.
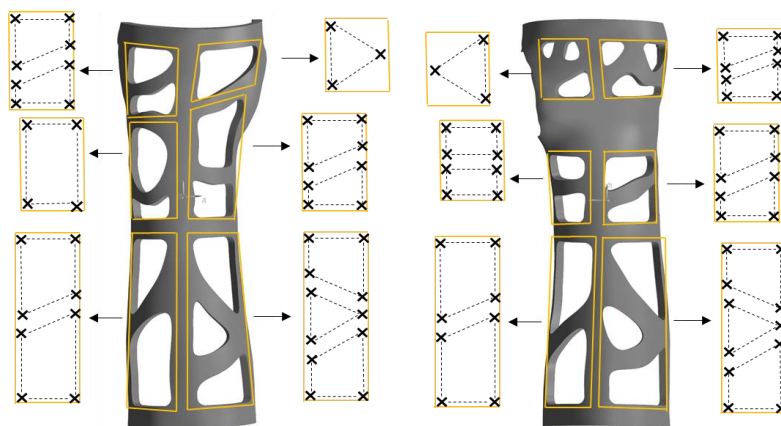
Figure 4-101 Simplification and stylization of the obtained pattern to ease the adaptation process. Points to be mapped on a new orthosis are cross-marked.

Key points extraction

As already mentioned, the development of an automatic procedure is supported by the availability of a number of repeatable references in the designed orthosis.

Specifically, the references provided to define the positions of the zip-ties housings and the opening lines of the orthosis are used, in addition two planes, parallel to the main sectioning direction, are extracted at a distance of +/- 10 mm from the intersection point between d1 and d2 (Figure 4-102a). These planes are used to delimit the area of the wrist to be preserved on the palmar half of the orthosis as this area is the most prone to impacts. For this area, a value of 20 mm along the Z direction was chosen; such a value assures a full protection to the wrist even in the worst case i.e. the orthosis of a male of 14 years old, at the 95th percentile.

Accordingly, with the above described features, it is possible to define on a new orthosis the same twelve zones (six palmar and six dorsal – yellow in Figure 4-102b) also defined for the reference pattern. As already said, such areas are used to map the reference simplified ventilation pattern, previously identified.

To this aim, a mapping grid is built within each zone in order to map the simplified reference hole pattern in each zone while keeping constant the proportions and shape of the polygonal holes. This is achieved by dividing the long side of each zone always by the same number of segments; for example, the side AB of zone 2 is divided into 9 segments (Figure 4-102c). In addition, the resulting segments are measured; if the distance between two

consecutive key points results less than 4 mm, distance is forced to assume such a value. The points obtained are finally stored in a text file and kept for reference for the generation of holes (phase b).

According to the way the key points are defined, they exactly lie on the internal profiles; consequently, they will not be in contact with the orthosis surface, which is generated through an offset of the scanned arm. Therefore, the patterns are subsequently extruded towards the target surface to intersect it, as discussed in the following paragraph.
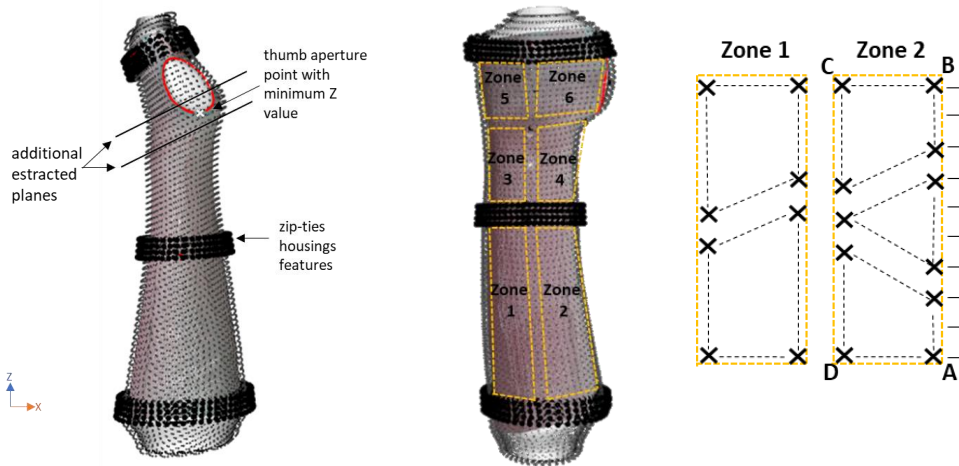
Figure 4-102 a) Extraction of the two planes defining the wrist area; b) the six zones of the dorsal pattern; c) template of the holes to be adapted for zone 1 and 2.

Holes opening in the CAD model
The second phase, i.e. the perforation of the CAD model, is carried out within Siemens NX® [107]. The main steps of the automatic procedure are reported in Table 4-16 with reference to the dorsal part of a given orthosis; the same procedure can be obviously applied on the ventral side.

Table 4-16 Phases of the CAD holes adaptation.

	The splines for the holes are created from the points saved in the text files. The splines are created of grade 1 to ensure that the shape is consistent with the template.
	The splines are projected onto the best-fit plane created on the curve itself.
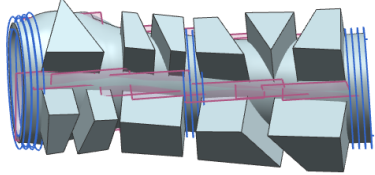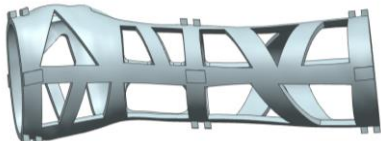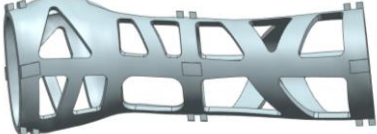
	The projected curves are extruded towards the shell to create solids. The automation of this step is not straightforward as the normal of the plane is not always directed outside or inside the orthosis. In fact, it was necessary to check the direction of the normals of each plane by making the scalar product with the X axis, to decide whether or not to reverse the direction of extrusion.
	The shell is perforated by subtracting the created solids.
	Fillets are generated on each internal edge with a radius of 5 mm to ensure easy construction of the device and patient comfort.

Figure 4-103 shows the result, on both sides, of the entire adaptation of the pattern and generation of holes. It is worth noting that on the dorsal side a larger opening is left in correspondence of the ulnar styloid process to prevent cutaneous lesions and to avoid discomfort.
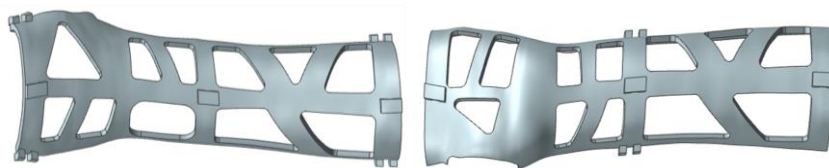
Figure 4-103 Final result of the CAD modelling and hole-generation procedure.

Mechanical Validation

The devised methodology was applied to five orthoses that are significantly different in size and local geometry from each other. The resulting pattern was approved from a medical perspective in all cases since all the medical requirements were satisfied. Mechanical performance of the orthoses was tested by means of FEA, performed following the indications of Figure 4-96. The most severe configuration was, as expected, due to the flexion load, which, in the worst case, caused a von Mises maximum stress equal to 24.8 MPa. The results for the five orthoses, in terms of maximum von Mises stress using the flexion load configuration, are reported in

Table 4-17. The worst condition was registered for the orthosis #1 and the resulting stress map is depicted in Figure 4-104. It is important to note that, according to the stress distribution map of Figure 4-104, most areas of the orthosis are subjected to stress values in

the 6-12 MPa range. Higher stress values, probably caused by stress concentrations factors and FE artefacts, are limited to small regions of the cast and therefore will not have any major impact on the strength of the whole device.

Table 4-17 Results of the FE analyses performed to validate the adaptation procedure.

Orthosis	Arm Length [mm]	Maximum Stress Value (Flexion Load Configuration) [MPa]
#1	~230	24.8
#2	~235	24.6
#3	~190	13.9
#4	~234	11.7
#5	~390	12.0
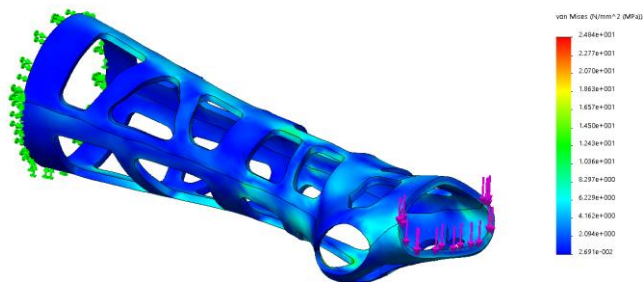
Figure 4-104 von Mises stress map on orthosis#1 under Flexion Load configuration.

Analyzing this third technique it is possible to conclude that:

1) It easily adapts to the flow of realization of the orthosis since it uses the scanner management software and Siemens NX. It is also completely transparent to the user and takes ~30 seconds longer to make the CAD model of the orthosis complete with ventilation holes.

2) This method allows to manage the positioning of the ventilation holes according to the patient's anatomy, to easily safeguard some areas and to manage the proportion of the holes in each area, keeping constant the proportions of the pattern that have been previously validated.

4.3. Clinical applications

4.3.1. Validation

After the complete installation of the arm scanner, tests have been carried out to verify the accuracy and repeatability of the measurements that can be obtained. The analysis is carried out through three different acquisitions of an object of known geometry (Table 4-18).

The acquisitions are compared in pairs to verify that the repeatability of the measurements is acceptable. Subsequently, an acquisition made with the scanner is compared with a reference acquisition for estimating the accuracy of the measurement.

The reference acquisition is obtained by the high precision laser scanner Romer Absolute Arm 7520 SI/SE (Hexagon Metrology S.p.A., Turin, Italy), which has a declared accuracy of ±0.063mm. The alignment and quantification of the deviation between the two meshes under examination is carried out with the Geomagic Studio software. The results are summarised below (Table 4-19).

Table 4-18 Characteristics of the reference object.

Reference Object	
Geometry	Full cylinder
Outside Diameter	30 mm
Length	350 mm

Table 4-19 Measurement of Mesh Deviations between different acquisitions and with respect to the reference acquisition.

Test: Repeatability of the Measure - Acquisitions: Acquisition 1 - Acquisition 2	
Measure	Mesh Deviations
	Statistical quantities
Mean	0.1282 mm
Standard Deviation s	0.3414 mm
Intervals s	**% points within the range**
±1σ	70.45%
±2σ	94.10%
±3σ	99.79%

Test: Repeatability of the Measure - Acquisitions: Acquisition 1 - Acquisition 3	
Measure	Mesh Deviations
	Grandezze Statistiche
Mean	0.0604 mm
Standard Deviation s	0.2949 mm
Intervals s	**% points within the range**
±1σ	78.61%
±2σ	94.46%
±3σ	97.88%

Test: Repeatability of the Measure - Acquisitions: Acquisition 2 - Acquisition 3	
Measure	Mesh Deviations
	Grandezze Statistiche
Mean	-0.0692 mm
Standard Deviation s	0.3768 mm
Intervals s	**% points within the range**
±1σ	70.97%
±2σ	94.96%
±3σ	99.31%

Test: Measurement Accuracy - Acquisitions: Acquisition 1 - Reference	
Measure	Mesh Deviations
	Grandezze Statistiche
Mean	0.2709 mm
Standard Deviation s	0.4233 mm
Intervals s	**% points within the range**
±1σ	71.99%
±2σ	94.64%
±3σ	99.10%

The tests carried out show an error between the mesh acquired with the scanner with respect to the reference always within the range defined in paragraph 6.2.2, with 99% of the points considered falling within a tolerance always less than ±1.5mm with respect to the reference.

The repeatability of the measurement is also acceptable, with an average error around ±0.1mm and with a variability that remains within the ±1mm range for 95% of the points.

4.3.2. Usability
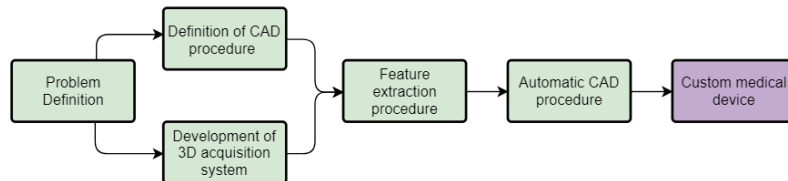
Figure 4-105 Diagram outlined to achieve the systematic realization of customized medical devices.

Once the system was developed, the software interface for scanner control and device modeling, explained in detail in the previous chapters, was tested for usability. The main steps to be performed by the users have been grouped in five tasks and are described in the following.
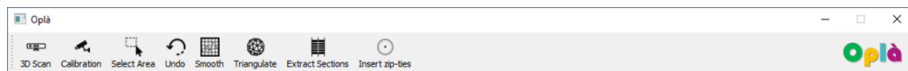
Figure 4-106 Toolbar of the devised control software

Task 1: Patient preparation and arm positioning

During this step the clinical professionals oversee the positioning of a white gauze on the patient's arm and the drawing of some visual references; specifically, they are asked to draw the knuckles line, the thumb finger base, the main orthosis boundaries, and the ulnar styloid process perimeter to next help the correct reconstruction of the orthosis model (Figure 4-107 on the left). Once ready, the patient is asked to place the arm into the 3D scanner and to assume the resting configuration (with the hand defining an angle of 10°-20° with the arm, Figure 4-107) and keep it during the scanning phase.

Figure 4-107 Example of landmarks drawn on the gauze (left); positioning of the arm into the acquisition system (right).

Task 2: 3D Scanning

Once the arm is positioned the clinical specialist is ready to press the 3D Scan button. The program launches a notification sound when the images are stored (within ~2.5 seconds), after which the patient can remove the arm from the scanner. In background the software processes the acquired raw data to obtain the point cloud of the wrist-hand-arm district.

Task 3: 3D Data selection and cut

When the 360° 3D image of the arm is ready the user must press the button Select Area to select and cut all those portions of points which will not be part of the orthosis (see Fig. 4-108). During this phase and the following, the user will take advantage from the lines previously drawn on the gauze. At the end of this step, the user must press the Smooth button to let the software perform the smoothing step in background.

Fig. 4-108. Workflow of the third task.

Task 4: Thumb finger overture

During this phase, the user must remove the thumb finger to create the right overture to allow the patient to freely move such finger. To perform this task, the user must navigate the 3D model to identify the right point of view to cut the thumb. Also, the user must select the area defining the opening space for the thumb finger. These operations are shown in Fig. 4-109.
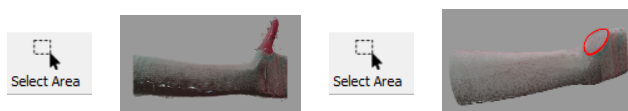
Fig. 4-109. Workflow of the fourth task.

Task 5: Zip ties positioning

The last task consists in pressing the button Triangulate to let the software perform in background the Poisson surface reconstruction which is a smooth and detailed mesh, and which automatically close the hole produced by removing the thumb finger.
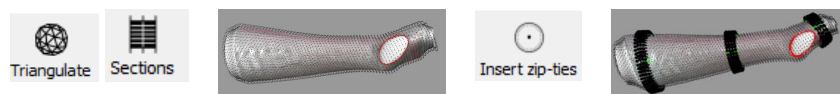
Fig. 4-110. Workflow of the fifth task.

Once the mesh has been computed the user has to press the button Sections: the program will automatically extract and visualize sectional profile of the mesh necessary to generate the final model of the orthosis in a CAD environment. Finally, after pressing the button Insert zip-ties the user defines the zip-ties housing locations.

Participants

Five participants have been chosen among the Meyer Chindren's Hospital orthopedic nurses, specifically orthopedic nurses have been chosen over doctors since they oversee the typical casting procedure for bone fractures. Despite the common practice to test the usability on five users [108], studies have demonstrated that the identification of flaws in the software remarkably increases with a higher number of participants [109]. However, five participants are considered to be enough for this preliminary study. The usability sessions have been conducted in a quiet and private room reserved for this task accommodating the scanning system. Institutional Review Board approval has been obtained from the study organization to conduct this research.

Methods

A preliminary meeting has been held to explain to participants each single task, and to give the possibility to familiarize with the procedure. After this preliminary phase, participants tests have been scheduled individually and the test has been performed by participants without any help by observers. The evaluation of each metric has been carried out as follow:

Effectiveness is calculated measuring the completion rate, by assigning a binary value of '1' if the test participant manages to complete a task and '0' otherwise.

$$Effectiveness = \frac{number\ of\ tasks\ completed\ successfully}{total\ number\ of\ tasks\ undertaken} \quad (16)$$

Efficiency is measured in terms of task time, i.e. the time spent by the users to achieve the goals

$$Time\ Based\ Efficiency = \frac{\sum_{j=1}^{R} \sum_{i=1}^{N} \frac{n_{ij}}{t_{ij}}}{NR} \quad (17)$$

$$Overall\ Relative\ Efficiency = \frac{\sum_{j=1}^{R} \sum_{i=1}^{N} n_{ij} * t_{ij}}{\sum_{j=1}^{R} \sum_{i=1}^{N} t_{ij}} \quad (18)$$

Where: N = total number of tasks, R = number of users, nij = result of task i by user j, tij = time spent by user j to complete task i.

Satisfaction is measured through standardized satisfaction questionnaires: the SEQ (Single Ease Question) questionnaire, which is reliable sensitive valid and easy to respond [110], has been administered after each task; the SUS (System Usability Scale) questionnaire [111], which has been found to give very accurate results, has been administered after the usability test session.

Results

The tables below illustrate the results of the usability metrics described above. On average the tests score is positive, highlighting both the general good impact of the software and some major flaws. As it can be noted from Table 4-20 all effectiveness scores are above average, i.e. they exceed the 78% [112].

Table 4-20. Effectiveness results scored by each user.

	User #1	User #2	User #3	User #4	User #5
Effectiveness	80%	100%	80%	100%	100%

Efficiency, which is the speed of work with the product, is typically compared with the Expert Efficiency, the highest theoretically possible speed of work. As it is shown in Table 4-21, the efficiency obtained with non-trained users (i.e. the first approach of participants to the software after the introductory presentation) is equal to ~.3 goal/min, and it is twice as the reported expert efficiency.

Table 4-21. Overall efficiency results.

Time-Based Efficiency	Expert Efficiency	Overall relative Efficiency
0.309 goal/min	0.6 goal/min	91.3 %

SEQ results are reported as the average SEQ value obtained by each user (see Table 4-22). Considering that satisfaction results typically range between 4.8 and 5.1 [113], Table 4-22 show a general high score of satisfaction by single users. Moreover, the most challenging task for users with no 3D modelling expertise has been task 4 (Thumb finger overture). Future work will be oriented to the simplification of this step to be performed within a medical facility.

Table 4-22. SEQ score averaged over each user.

	User #1	User #2	User #3	User #4	User #5
AVG SEQ score	5.6	6	3.6	5.4	5.2
Task with lower score	Task 4	Task 4	Task 4	Task 4	Task 4

As said, at the end of each session users were ask to compile the SUS questionnaire to measure their impression of the overall ease of use of the system. Results are reported in Fig. 4-111, where values below the red dashed line are to consider as strongly insufficient, the orange line states the sufficiency threshold, and results above the green line are considered optimal. The tested software obtained an average result of 85, and, in general all scores are above the sufficiency line, stating a general high level of satisfaction of the users.
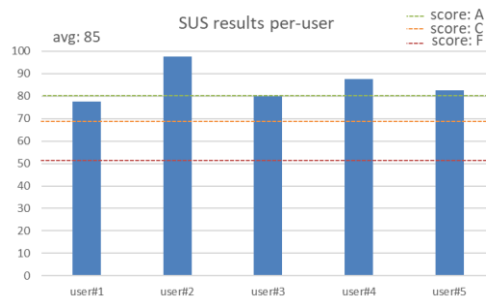
Fig. 4-111. SUS questionnaire results (in blue) and reference thresholds.

4.3.3. Clinical trial

The clinical trial was conducted at the Meyer Children's Hospital in Florence, Italy. Formal approval from the local Ethical Committee and from the Minister of Health was obtained. Between the 1st of October and the 18th of December 2018, ten consecutive children affected by a "buckle" fracture of the distal radius were enrolled. Inclusion criteria were: 1) the age range from 7 to 13 years; 2) isolated "buckle" fracture as diagnosed by the radiologist and confirmed by the orthopaedic consultant. Exclusion criteria were: 1) evidence of any other fracture pattern of the distal radius; 2) evidence of any other type of trauma; 3) history of acute or chronic illness; 4) presence of any skin affection equal or exceeding grade 1 according to the NPUAP/EPUAP classification; 5) history of any reaction or hypersensitivity that could be relatable to the material employed to produce the splint. Possible reasons for withdrawal from the clinical trial were: VAS>7 at any time; skin lesion >1 according to NPUAPA/EPUAP at any time; loss of immobilization, complete or incomplete, due to any observable evidence of device failure. To be enrolled, parents were informed on the purpose and the objectives of the study and had to agree to a specific consent. If the child arrived to the Accident & Emergency Department and was enrolled between 8 a.m. and 8 p.m., the scanning of the forearm was performed straight away. If the presentation occurred at night time, the forearm was provisionally immobilized in a volar plaster slab and arrangements were set to provide for the scanning within 24-36 hours.

In all the cases, the limbs were immobilized in volar plaster slabs after the scanning, while awaiting the 3D printed cast. Every patient was provided with an appointment within 24-48 hours after enrolment in the outpatient clinic to have their plaster splint removed and the 3D printed cast applied. The 3D scanning of the forearm was obtained with the HWA scanner presented above, considering that the digital cameras are CE certified for the acquisition of 3D images and approved by the FDA as Laser I products in conformance with EN/IEC 60825-1 2007 Safety of Laser products. As said, the 3D acquisition was obtained with the forearm positioned on a frame specially designed to hold the wrist in the neutral "thumb-up" position with the wrist in slight extension (10-15°). Before scanning, a Lohmann & Rauscher Tg® Soft stockinette was applied on the forearm and a point 3 to 5 cm distal to the elbow flexion crease, depending on the child size, the base of the thumb, the head of the metacarpals and the ulnar styloid positions marked. The orthosis CAD modelling procedure was carried out within Siemens NX modelling environment [89] as mentioned above. At the end of the modelling procedure the digital model was exported into two distinct STL files (one for each part of the device), ready to undergo construction in an additive manufacturing

process. As said, the cast was printed using the 3D Stratasys F370 printer in a laboratory located outside the hospital. The material chosen to construct the cast was acrylonitrile butadiene styrene (ABS), already approved by the FDA for a similar casting device known as ActivArmor® [114]. The 3D printed cast was made available within 24 hours from the scanning and was fitted to the patient at a prearranged outpatient clinic appointment.

After enrolment and application of the cast, patients were seen again after 3 (step 1), 7 (step 2) and 21 (step 3, end of treatment) days in the outpatient clinic. At each appointment, general comfort, as will be later described, was evaluated and recorded and a visual inspection of the cast undertaken and any possible structural anomaly described. The cast was always removed to enable visual inspection of the skin and then reapplied. At the latest evaluation at 21 days, in addition to what above mentioned, a final orthopaedic evaluation was performed.

The investigated primary outcomes were: general comfort; efficacy of contention; mechanical integrity. A secondary outcome was the practicability of the supply chain. The general comfort outcome was investigated as follows: possible pain during the treatment was measured using the Visual Analogue Scale (VAS) [115]; inspection for skin lesions was performed according to NPUAP/EPUAP classification [116]; general wellness was assessed with the Italian adaptation [117] of Positive affect-Negative affect Scale for Children (PANAS-C) [118] and the SelfAssessment Manikin (SAM) [119] clinical psychology tests. The PANAS-C consists of 30 items, 15 for "positive affect" reported as PA and 15 for "negative affect" reported as NA, so that the final result consists of two values. Ratings are made on a 5-point scale ranging from 1 (very slightly or not at all) to 5 (extremely). Children were asked to report the intensity (from very slightly or not at all to extremely) of their current affect, which is intended to assess state affect. Representative mean scores were extracted from available normative values [117]. The SAM is a nonverbal pictorial assessment technique that measures pleasure, arousal, and dominance associated with a person's affective reaction to a wide variety of stimuli, for children aged 3 to 16 years. Being based on figures rather than on words, it has proved to be a good language- culture-free tool for the measurement of emotions [119, 120]. Item scores range from 0 to 5 and are reversed so that a positive outcome should score high in the pleasure and dominance domains and low in the arousal domain [121].

In addition, other features related to general comfort were investigated by submitting to each child and to his/her parents a five item questionnaire constructed according to a Likert-type scale. In particular, the three questions related to the activity level were: 1. Have you been playing with your friends?; 2. Did you shower as usual?; 3. Did the cast limit your daily activities? To each of these questions an answer was accepted in a scale 1 to 5, being "1" the worst answer (never) and "5" the best one (as usual). One question related to the presence of itch (Did your arm itch?); again, the answer was collected on a scale from 1 to 5 being "1" no itch and "5" very itchy. Finally, a question related to the overall opinion on the cast. Answers, again, could range from "1" very poor, to "5" very good. This short questionnaire was administered to children and parents at each appointment. The clinical efficacy of contention was assessed at the time of 3D-printed cast application by inspection of the forearm-cast construct where the anatomic landmarks had to be respected and tolerance between the cast and the stockinette has not to exceed 3 mm. Moreover, as mentioned above, a standard clinical evaluation performed by and experienced orthopaedic surgeon (SL) was carried out at the end of treatment (step 3). It consisted in a general inspection of the limb, range of motion measurement after cast removal, tenderness evaluation over the fracture site or elsewhere, verification of the need for further treatment.

The mechanical integrity of the cast was assessed at the end of the treatment by performing a 3D scan on each single cast so as to compare the newly generated file with the

original orthosis file. An initial analysis of the supply chain was conducted with special consideration to the time interval between the transmission of the file with the desired cast and the availability of the cast for application. Reasons for delay in supply were recorded.

Results

Ten consecutive cases of "buckle" fracture of the distal wrist were enrolled between the 10th of October and the 17th of December 2018. All cases were admitted and screened for the fulfillment of inclusion criteria at the Emergency Department of the Meyer Children's Hospital in Florence. Mean age was 8.9 years (7-10 years) and there was an equal distribution between male and female (5:5). The right side was interested in 6 cases. Scanning of the forearm was carried out at the time of admission in eight cases. Two children admitted after 8 p.m. or over the week-end were immediately provided with a volar plaster slab and returned for scanning the first following working day. Pain was reported as follows: three cases at step 1, where two cases scored 2 on the VAS scale, with pain reported at the fracture site and one case scored 3, with pain reported at the ulnar styloid; pain was never reported at step 2; four cases at step 3, where one case scored 1, with pain reported at the proximal end of the cast, two cases scored 2, with pain reported at the base of the thumb and at the hypothenar eminence, one case scored 3 with pain reported at mid-forearm. No skin lesion was detected at any time according to the NPUAP/EPUAP classification. Two cases of mild irritation at the base of the thumb were noted (Figure 4-112).

Figure 4-112 A case with mild irritation at the base of the thumb.

The inconvenience disappeared after slight manual smoothening and padding of the cast. The PANAS-C scores for PA and NA were respectively 55.47±9.6 and 28±2.4 for girls and 45.64±10.5 and 23.19±5.2 for boys. The normative scores for PA and NA are respectively 42.99±8.1 and 27.38±8.2 for girls and 42.03±8.3 and 25.84±7.6 for boys. The mean SAM scores were 3.9±0.1 for pleasure, 1.65±0.2 for arousal and 3.6±0.2 for dominance. In relation to the evaluation questionnaire, the mean scores reported at each evaluation step for each item are reported in Table 4-23. All of the answers ranged in the positive positions, both in children as well as in parents and the median scores were generally overlapping. Interestingly, parents showed a higher overall opinion of the cast. Results on efficacy of contention showed fitting

within 3 mm tolerance in 7 cases, while in three case the tolerance measured between 3 and 5 mm. The clinical evaluation at the end of treatment (step 3) did never reveal a skin lesion, tenderness at the fracture site or elsewhere or limitation of the range of motion as evaluated several minutes after cast removal. Further treatment was never indicated.

Table 4-23 General comfort questionnaire: scores are reported as means at each follow-up visit.

	Step 1		Step 2		Step 3	
Items	Child	Parents	Child	Parents	Child	Parents
Have you been playing with your friends?	3.8	3.8	4.2	4	4.2	4
Did you shower as usual?	2.6	2.3	3.2	3.2	3.8	3.8
Did the cast limit your daily activities?	2.2	2.2	3.2	2.5	2.8	2.1
Did your arm itch?	1.7	1.3	2.6	1.6	2.1	1.6
Your opinion on the cast	3.9	4.8	4.3	4.73	4.5	4.6

Mechanical integrity

The 3D scanning of the used orthosis revealed that no permanent deformation can be measured. In fact, the averaged measured error between the original cast 3D file and the acquisition of the used 3D printed cast is 0.1 mm with a maximum error of 2 mm, that shows that the cast is unchanged after its usage. An example of the comparison between used and original orthosis 3D file is reported in Figure 4-113. The entire supply chain permitted for each clinical case, to have the final cast available for application within 24 hours from the 3D scanning.
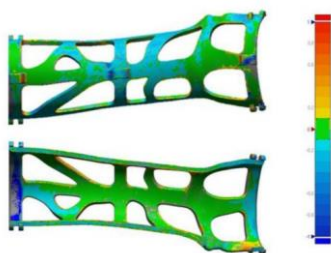
Figure 4-113 Result of the comparison between an orthosis with the related original 3D file.

Discussion

The trial provides Class IV evidence that a 3D printed orthosis can be effective, safe and well tolerated in treating "buckle" fracture of the distal radius in children. In this small, unblinded series with no concurrent control group, all the 10 children enrolled completed the treatment and no reasons to interrupt the study were met at any time. No skin lesions were reported at any time. Moreover, a positive response with regards to affect and emotional status was reported both from parents and children. "Buckle" fracture of the distal radius were chosen for this study because they are relatively frequent and carry virtually no risk of secondary displacement or of cosmetic or functional consequences [122, 123]. Limiting the application to this typology of fracture may be regarded as excessively prudent and restrictive, but due to the purpose of obtaining basic evaluation on patient comfort and satisfaction as well as on the practicability of the supply chain, it was felt that by eliminating more urgent treatment requirement, attention could be draw specifically to the wearability of the cast and its mechanical performance.

The general comfort displayed very low scores on the VAS scale that confirmed the uneventful course of the disease and that could be attributed to common clinical findings related to the injury sustained and to some very slight discomfort regularly associated with the use of any immobilization device.

No skin lesions according to NPUAP/EPUAP were reported at any time and the psychological test showed consistent results throughout the clinical course of the disease which appeared to be independent to the device but rather related to the imposed limitations to usual activity.

Conclusions on the PANAS-C and the SAM scores are difficult to define. The results obtained with both scales did not show negative responses compared to normal normative scores and allow to hypothesize that the experience with 3D device for wrist fractures of the participants was positive in terms of affect and emotional status. The questionnaire that was submitted to children and parents highlighted consistent results throughout the study (Table 4-23). The average result to each question was quite unvarying and always in the positive range at every step. The overall opinion on the cast was superior in the answers obtained from the parents. Possibly, this is due certainly to the fact that they were not personally injured and therefore limited, but it is likely that the positive acceptance of the orthosis came from the fact that they could compare it to traditional casts because of either direct or indirect experience.

The clinical efficacy was likewise confirmed: the fitting of the cast was always considered satisfying and deemed to offer adequate immobilization. In the two cases in which the cast displayed a wider tolerance to the metatarsal heads, it is thought that the problem arose from a not perfect fitting of the stockinette to the skin at the time of 3D-scanning. To avoid this problem, it is in the process of evaluation for the next case-series to directly mark bony-landmarks on the skin and then adjust the generated 3D cast model with the required tolerance.

The clinical evaluation performed at the end of the treatment (step 3) was uneventful, as expected for this type of fractures. The fitting of the cast, which can be considered a measure of the soundness of the product generation procedure, was of particular importance. The general positive results of this study have to be analyzed taking into account distinct limitations.

In this study, the definitive cast was printed in a facility outside the hospital and products were made available, as reported, in the required time-frame. Nevertheless, it is felt that the possibility to have a 3D printer on site would significantly streamline the procedure and would permit a more rapid availability of the cast and a straighter forward correction of the product if construction anomalies should be detected. In conclusion, the specifically designed scanner and software proved to be simple to use and accurate indicating that larger, randomized studies are recommended to confirm data emerging from this preliminary observation.

4.4. HWA scanner second version

Following the clinical application of the scanner for the fabrication of custom orthoses, its weaknesses and possible improvements were analyzed. The main factors on which this second version focuses are: 1) the acquisition time and the possibility to acquire the human anatomy without the need to use a gauze; 2) a further simplification of the use of the software following the usability tests.

This led to the identification of a new device, still belonging to the Intel RealSense family, which however reproduces depth with a different method of acquisition, as will be

explained below. The device was characterized as well, to verify its suitability. Subsequently, changes were made to the software as shown in the following paragraphs.

4.4.1. Choice of new acquisition sensor

Intel RealSense D415 Depth Camera

The Intel RealSense Depth Camera has been designed to equip devices with the ability to see, understand, interact with, and learn from their environment. The D415 features the Intel RealSense Vision D4 processor with a high-resolution depth (up to 1280×720 pixels at 30 frames per second), long-range capability (up to about 10 m), rolling shutter technology and, as noted, a narrow field of view ideal for precise measurements. The RealSense Vision D4 is a vision processor based on 28-nanometer (nm) process technology for real-time calculation of stereo depth data.

The device has a very compact depth camera (dimensions: $99 \times 20 \times 23$ mm3, weight: 72 g) that can either be integrated into computers and mobile devices or used as a self-standing device. Moreover, it comes with a color camera and a depth camera system, comprising two IR cameras and an IR projector (Figure 4-114).
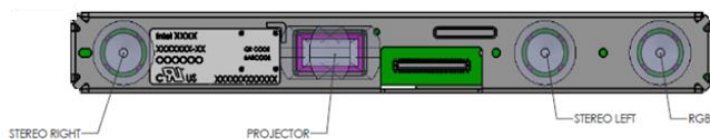
Figure 4-114 The component locations inside the RealSense D415 camera.

The infrared projector improves the ability of the stereo camera system to determine depth by projecting a static infrared pattern (Figure 4-115) on the scene to increase the texture of low-texture scenes. The left and right imagers capture the scene and send raw image data to the vision processor, which calculates depth values for each pixel in the image by correlating points on the left to those on the right image. The depth pixel values are processed to generate a depth frame. This active stereo depth computation makes this depth camera suitable for acquisitions both indoors and outdoors under reasonable illumination. To this purpose, the IR projector intensity can be tuned manually according to the environmental lighting conditions. The depth data generated with stereo vision uses the left image as the reference for stereo matching resulting in a non-overlapping region on the field of view of the left and right image. Therefore, there is no depth data at the left edge of the frame (Figure 4-115 in red). Closer scenes result in a wider invalid depth band than scenes at further distances.
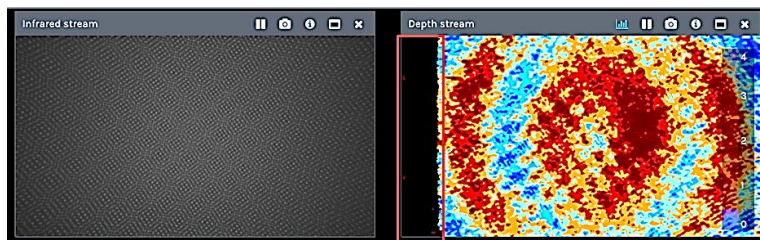
Figure 4-115 The static infrared dot pattern projected on a wall (left); highlighted in red is the non-overlapping region on the field of view of the left and right image (right).

The SR300 and the new D415 have different working principles for depth measurements (i.e., active stereo vs. structured light), which results in different performance as depicted in Figure 4-116. The figure shows a qualitative comparison of the two devices in representing a flat surface acquired at different camera distances. In grey are depicted the point clouds of a plane acquired at increasing distance using the SR300 model; the plane acquired with the D415 camera is instead described by the colored point clouds. It can be observed that the new device has a considerably lower error both in terms of planarity and of distance accuracy.
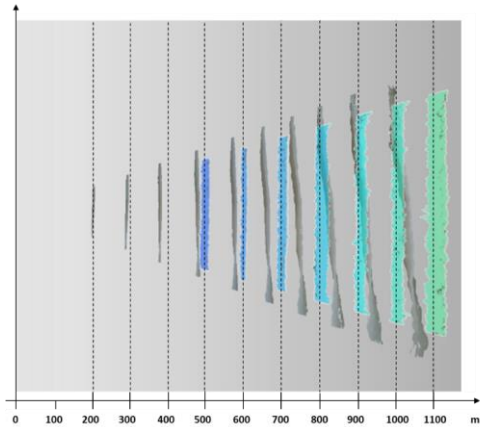

Figure 4-116 The qualitative evaluation of the error introduced in measuring a flat surface, and comparison between SR300 (grey point clouds) and D415 (colored point clouds) models.

The D415 has a narrow field of view solution using rolling shutter sensors; this means that very fast-moving objects or the fast movement of the device (such as quick horizontal panning) can result in slightly distorted images. The Intel RealSense D400 series is supported by the cross-platform and open source Intel RealSense SDK 2.0 [68], a library that allows the configuration of the camera with several internal settings (both for acquisition and post-processing). Furthermore, a set of visual pre-sets to improve performance is available. Such versatility allows users to arrange the best possible setup for the task under investigation.

The D415 is equipped with a color camera with a resolution up to 1920×1080 pixels, and provides texture information to be superposed on the depth data. The spatial resolution of the depth map of the Intel RealSense D415 is up to HD (1280×720 pixels), in a working depth range declared by the manufacturer equal to ~160–10,000 mm. The camera works at different pixel resolutions corresponding to different minimum depth values, point densities and framed areas. The specifications reported in Table 1 refer to the HD format. The declared horizontal field-of-view (FoV) (both for the depth and the RGB cameras) is approximately 69° and the vertical FoV is approximately 42°. The baseline between the two IR cameras is 55 mm. As can be seen from Table 4-24, which summarizes the technical characteristics of the device, horizontal and vertical FOVs are subject to an error of ±3 degrees. For this reason, the point density and framed area variations, evaluated by increasing the distance between the camera and the acquired scene are reported in Table 4-25,

Table **4-26** and Table 4-27.

Table 4-24 The technical specifications of Intel RealSense D415

Environment	Indoor and outdoor
Depth Technology	Active infrared (IR) stereo
Image Sensor Technology	Rolling shutter: 1.4 μm × 1.4 μm pixel size
Depth Field of View (FOV) (Horizontal × Vertical) for HD 16:9	69.4 × 42.5° (+/−3°)
Depth Stream Output Resolution	Up to 1280 × 720 pixels
Depth Stream Output Frame Rate	Up to 90 fps
Minimum Depth Distance (Min-Z)	0.16 m
Maximum Range	~10 m
RGB Sensor Resolution and Frame Rate	Up to 1920 × 1080 pixels at 30 fps
RGB Sensor FOV (Horizontal × Vertical)	69.4 × 42.5° (+/− 3°)
Camera Dimension (Length x Depth x Height)	99 mm × 20 mm × 23 mm
Connector	USB Type-C

Table 4-25 The point density and framed area variation at increasing camera–scene distance, computed using the FOV indicated in the Intel specifications (69.4 × 42.5°).

Distance (mm)	Scale factor	X (mm)	Y (mm)	Framed area (mm2)	Point density (point/mm2)
500	0.541	692.4	388.9	269,272.400	3.423
600	0.649	830.9	466.7	387,752.256	2.377
700	0.757	969.4	544.4	527,773.904	1.746
800	0.866	1107.9	622.2	689,337.344	1.337
900	0.974	1246.4	700.0	872,442.576	1.056
1000	1.082	1384.9	777.8	1,077,089.600	0.856
1250	1.352	1731.1	972.2	1,682,952.501	0.548
1500	1.623	2077.3	1166.6	2,423,451.601	0.380

Table 4-26 The point density and framed area variation at increasing camera–scene distance, computed using maximum and minimum FOV variations (69.4 × 42.5° +/- 3°).

Distance (mm)		FOV – 3°						FOV + 3°		
	Scale Factor	X (mm)	Y (mm)	Framed Area (mm2)	Point Density (point/mm2)	Scale Factor	X (mm)	Y (mm)	Framed Area (mm2)	Point Density (point/mm2)
500	0.874	745	419	312,607.4	0.98	0.748	638	359	229,168.6	1.34
600	1.048	895	503	450,154.7	0.68	0.898	766	431	330,002.8	0.93
700	1.223	1044	587	612,710.6	0.50	1.047	894	503	449,170.5	0.68
800	1.398	1193	671	800,275.0	0.38	1.197	1021	574	586,671.6	0.52
900	1.573	1342	755	1,012,848.1	0.30	1.346	1149	646	742,506.3	0.41
1000	1.747	1491	839	1,250,429.7	0.25	1.496	1277	718	916,674.4	0.34
1250	2.184	1864	1048	1,953,796.4	0.16	1.870	1596	898	1,432,303.8	0.21
1500	2.621	2236	1258	2,813,466.8	0.11	2.244	1915	1077	2,062,517.5	0.15

Table 4-27 The point density and framed area variation at increasing camera–scene distance, computed using the FOV of camera under investigation (67.24 × 41.01°).

Distance (mm)	Scale Factor	X (mm)	Y (mm)	Framed Area (mm2)	Point Density (point/mm2)
500	0.779	665	374	248,745.7	3.70
600	0.935	798	449	358,193.9	2.57
700	1.091	931	524	487,541.6	1.89
800	1.247	1064	599	636,789.1	1.45
900	1.403	1197	673	805,936.2	1.14
1000	1.559	1330	748	994,982.9	0.93
1250	1.714	1463	823	1,203,929.3	0.77
1500	1.870	1596	898	1,432,775.4	0.64

Point density variation is evaluated, respectively, for the FOV as indicated in the Intel specifications ($69.4 \times 42.5°$, Table 4-25), for the two FOV extrema (i.e., obtained by removing and adding $3°$, Table 4-26), and the actual FOV of the particular camera used to carry out the performance analysis ($67.24 \times 41.01°$, Table 4-27). The FOV of the experiment camera was evaluated on a depth frame with the get_stream_intrinsics function implemented in the librealsense SDK.

Materials and Methods

As mentioned above, the device under examination can work in different configurations. The camera software interface supports several predefined depth presets that can be selected according to the user's usage. Among the available presets, the Default configuration provides the best camera parameters to obtain the best visual appeal, clean edges, and to reduce point cloud spraying. With the aim of providing a comprehensive characterization of the camera and to enable a comparison with the other similar devices, while keeping the analysis as general as possible, in this work, the Default configuration was considered as the starting point from which to vary only a subset of critical parameters.

The characterization of the device was carried out by considering the maximum IR camera resolution (i.e., 1920×1080 pixels) and in a working range lower than 1 m (short range). Furthermore, tests were performed entirely by setting the depth unit (i.e., the depth step size) to its maximum value, equal to 100 µm, to obtain the best possible depth quantization. This limited the maximum range of the camera to circa 6.5 m. Lower depth unit values were not adopted to avoid quantization effects.

The critical parameters which were varied within the experiments are the disparity shift and the laser power, the former influencing the possible working distance and the latter influencing the depth sparsity.

The D415 system evaluates the depth as a proportional inverse of the pixel disparity from the right IR image to the left IR image, where the pixel disparity is evaluated along the rectified epipolar lines [124]. Such a depth, named the disparity shift, can be varied to modify the acquisition field.

For a given disparity shift, the maximum Z value ($MaxZ$) is given by the following formula:

$$MaxZ = focal\_length \ (pixels) \times baseline \ (mm)/disparity\_shift \qquad (19)$$

Where

$$focal\_length \ (pixels) = \frac{1}{2} \frac{Xres(pixels)}{\tan\left(\frac{HFOV}{2}\right)} \qquad (20)$$

The minimum Z value ($MinZ$) is defined by the following equation, taking into account that the camera searches in a disparity range of 126 bits:

$$MinZ = focal\_length \ (pixels) \times baseline \ (mm)/(disparity\_shift + 126) \quad (21)$$

By default, the disparity shift is set to 0 to cover the Z range from 435 mm to infinity. When the disparity shift is increased, the minimum acceptable Z value (i.e., the minimum camera–object distance) decreases, with the consequence of also reducing the maximum Z value. Figure 4-117 shows $MaxZ$ as a function of the disparity shift, calculated considering the horizontal field of view HFOV of the camera under investigation ($67.24°$). The yellow rectangle in the figure indicates the range of depth acquired based on the disparity value of the device, which is 126.
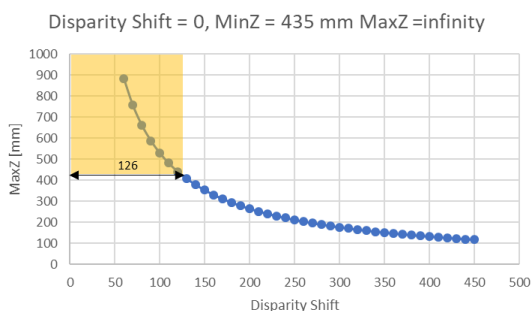
Figure 4-117 The graph shows the maximum acquirable depth as a function of the disparity shift, calculated considering the HFOV of the camera under investigation (67.24°).

As mentioned above, the second parameter used to carry out the sensor characterization consists of the laser power, i.e., the intensity of the infrared pattern projected on the scene to facilitate the search for matches between the left and right images. The depth data is, in fact, generated with stereo vision technology that is optionally assisted by an infrared laser projector. The value of this parameter can vary in the range of 0–360 mW and has a nominal value of 150 mW. If necessary, it can be increased or decreased from the nominal value for better results. For example, if the localized saturation of the laser point is noticed, the power can be reduced; to acquire distant objects, the power of the laser must be increased.

Under the premise of setting the device to its Default configuration and of using different values for disparity shift and laser power, the characterization is carried out by following the framework of Figure 4-118.
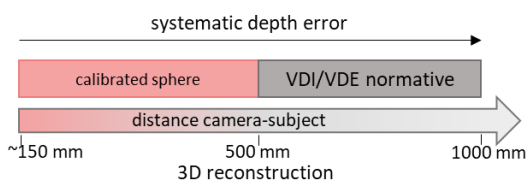
Figure 4-118 The proposed framework for the characterization of the device: a certified sphere is used in the very-close range (<500 mm); up to 1000 mm, the VDI/VDE 2634 Part 2 standard is applied; the systematic depth errors are evaluated on the entire range; and the 3D reconstruction of an object is tested for a camera–subject distance of 500 mm.

In detail, different tests are carried out based on the range under examination:

    a) From very-close object acquisition (150 mm) up to 500 mm, the characterization is assessed using a calibrated sphere positioned at progressive distances from the camera with a fixed pitch of 100 mm. As already mentioned, in this range, the disparity shift is required to be changed.

    b) From 500 mm to 1000 mm, the characterization is performed by following the guidelines of the VDI/VDE 2634 Part 2 standard.

    c) For the entire range, a planarity test is carried out to evaluate systematic depth errors.

d) With an object–camera distance equal to 500 mm, a test of the camera in allowing the three-dimensional reconstruction of objects with a multi-view acquisition is carried out. Such a reconstruction is made for two different artefacts.

Characterization in the Range 150–500 mm

In the short-range (i.e., from 150 to 500 mm) the VDI/VDE standard cannot be applied due to the fact that the change of the value of disparity shift does not allow the appreciation of the whole working volume required from the standard. In fact, a change in the disparity shift corresponds to a variation of the working volume (which becomes smaller as soon as the target nears the sensor).

Therefore, a different method has been conceived to characterize the device in such a range, inspired by Reference [125]. In particular, a calibrated sphere with a certified diameter of 25.4 mm was used to assess the camera's performance. The short-range was ideally divided into sub-regions with a 100 mm pitch (with the exception of the range 150–200 mm), thus defining 4 operative ranges where the acquisition is performed (see Table 4-28). Starting from a distance between the calibrated sphere and the sensor equal to 150 mm, the sphere is acquired at increasing distances. For each operative range, the disparity shift can be varied spanning from a given minimum and maximum value to obtain the correct acquisition of the sphere, as stated in Equations (1) and (3). This allows the definition of a disparity shift range for each operative range (see second column of Table 4-28).

The values shown in Table 4-28 specify the range of disparity shift that allows the acquisition in a selected depth window. The values have been calculated considering the two extremes of the HFOV as indicated in the specifics (i.e., $69.4° \pm 3°$). Figure 4-119 shows an example of the calculation of the disparity shift range when considering the sub-range of depth 200–300 mm.

(a)   (b)
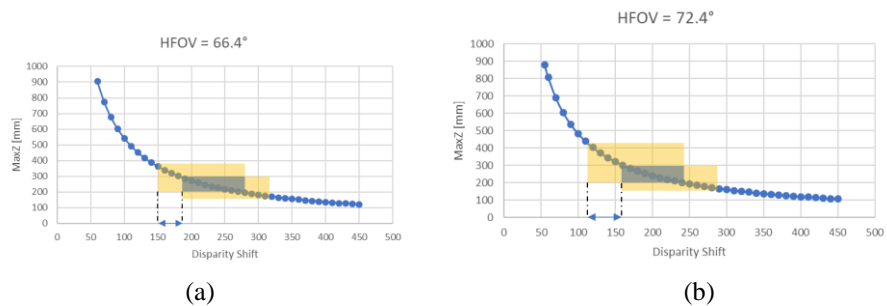
Figure 4-119 The graph shows the maximum acquirable depth as a function of the disparity shift, calculated considering HFOV = 69.4° ± 3°. The blue rectangle indicates the depth range 200–300 mm. The yellow rectangles are obtained computing the first and the last values of disparity shift that allow the acquisition of the whole sub-range, which are 150–180 when HFOV = 66.4°, and 114–160 when HFOV = 72.4°.

Figure 4-119a shows the case in which the HFOV is equal to 66.4°, in which the resulting range of the disparity shift is 150–180; if the HFOV is instead equal to 72.4° (Figure 4-119b), the resulting range of the disparity shift is 114–160. Consequently, if a disparity shift value between 150 and 160 is used, in both configurations, the entire sub-range can be acquired.

Any value for the disparity shift falling within the disparity shift range can be selected to perform the acquisition in a given sub-region. Therefore, the preferred values are the ones listed in third column of Table 4-28. Using this configuration, only the laser power remains as a changing parameter to test the device performance. In addition to the nominal value, the values 0, 250 and 360 mW were tested.

Table 4-28 The tested value of disparity shift and laser power for each sub-range.

Operative Range (mm)	Disparity Shift Range	Disparity Shift Value	Laser Power (mW)
150–200	234–240	235	0, 150, 250, 360
200–300	150–160	155	0, 150, 250, 360
300–400	49–125	50	0, 150, 250, 360
400–500	9–95	10	0, 150, 250, 360

To carry out the test, the camera was mounted on a stable tripod and the sphere was fixed on a sliding linear guide having a 4 mm pitch (see Figure 4-120).
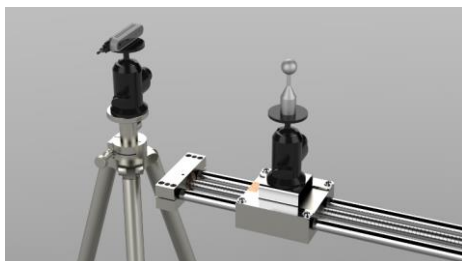
Figure 4-120 The acquisition setup for the very-close range evaluation test: the camera is mounted on a tripod facing the linear guide on which the sphere moves.

As noted, the calibrated sphere was scanned every 10 cm and, in each sub-region, 4 different laser power levels were tested (i.e., 0, 150, 250, and 360 mW). In Figure 4-121, 2 examples are reported out of the entire test set; respectively, Figure 4-121a shows the sphere acquired at increasing distance with the maximum laser power (360 mW), and Figure 4-121b shows the sphere acquired at increasing distance with a laser power equal to 250mW.

(a)

(b)

150–200mm   200–300mm   300–400mm   400–500mm

Figure 4-121(a) The point clouds of the sphere acquired at increasing distance with maximum laser power (360 mW); (b) the point clouds of the sphere acquired at increasing distance with a laser power of 250 mW.

Each acquisition was processed by extracting the best-fit sphere and comparing the obtained diameter (D) with the ground truth diameter (Dgt = 25.4 mm), thus defining the error E as follows:

$$E = \left|D_{gt} - D\right| \qquad (22)$$

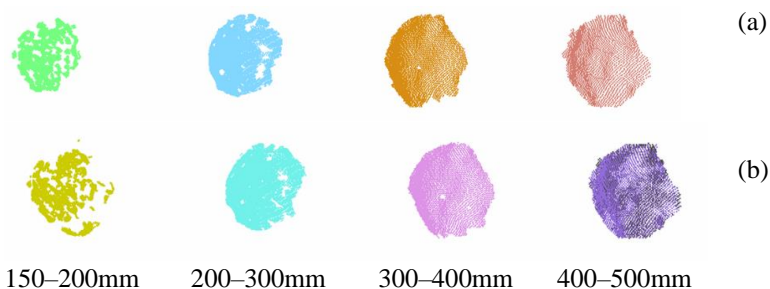Figure 4-122 shows the error value obtained for each sub-region with different values of the laser power parameter; such an error decreases as the laser power increases.
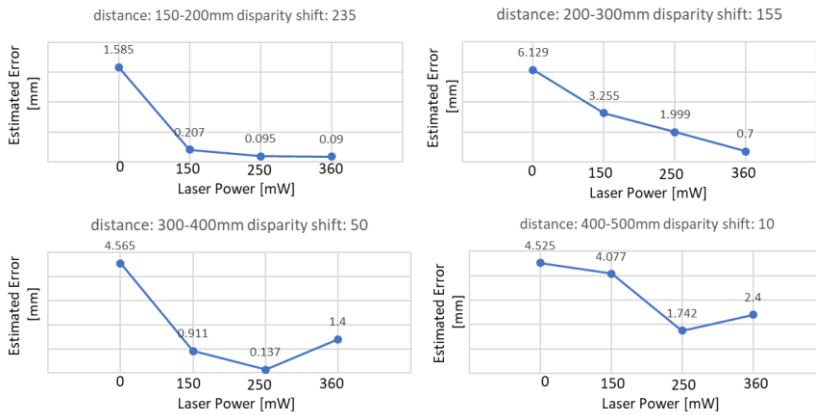

Figure 4-122 The errors in the estimation of the calibrated sphere for each sub-range from 150 to 500 mm, evaluated for increasing the value of the laser power (0 to 360 mW).

According to experimental results, in the very-close range of 150–500 mm, the biggest error corresponded to a laser power of 0. When the laser power used was the default (i.e., 150 mW), the errors obtained in the reproduction of the geometry of the sphere, intended as the difference between the actual diameter and the estimated diameter, ranged from approximately 0.2 mm to 4 mm, with an average error of 2.11 mm for the considered value of the disparity shift. As can be seen from the graphs shown in the figure, the error decreases if the laser power value does not exceed 250 mW and can be reduced by up to 20%. For higher values, the error behavior may vary, probably due to the laser-speckle effect, i.e., the coherent light interaction with the reference plane. In fact, scattering can create photometric inconsistencies producing matches where there are none [126]. From the results of the performed test, the scattering effect can be observed in the acquisition range of 300–500 mm when the laser power is equal to 360 mW. Globally, the average error obtained with a laser power equal to 250 mW was 0.99 mm, compared to an average error of 1.15 mm obtained with laser power equal to 360 mW.

Characterization in the Range 500–1000 mm: VDI/VDE Standard
The range of 500–1000 mm was characterized following the VDI/VDE 2634 Part 2 recommendations in order to provide a comparison with the previous Intel camera model (the Intel RealSense SR300) and other RGB-D devices, as mentioned above. In the first instance, the diagonal of the working volume L0 was determined; as mentioned above, this parameter is needed for sizing the spheres, the bar and the plane for the performance evaluation test. In

this regard, the truncated pyramid representing the working volume in the range of 500–1000 mm has a diagonal L0 equal to 1291.9 mm. According to the standard, the sphere used to characterize the probing error must have a diameter between 0.1 and 0.2 times L0. This translates into a diameter between 129.19 mm and 258.38 mm.

The distance between the centers of the two spheres of the ball-bar (to characterize the sphere-spacing error) is suggested to be greater than 0.3 times L0; accordingly, in the present test, such a distance is equal to 387.57 mm. Finally, the plane for the flatness error should be longer than 0.5 times L0., i.e., greater than 645.95 mm.

Starting from the values suggested by the standard, the artifacts chosen for carrying out the test had the following dimensions: the single sphere had a diameter of 143.15 mm, the distance between the centers of the two spheres of the ball-bar was 391.58 mm, and the plane for the flatness error was 646 mm long (Figure 4-123). These values were measured using a high precision scanner, the Romer Absolute Arm 7520 SI/SE (Hexagon Metrology S.p.A., Turin, Italy), which has an accuracy of ±0.063 mm, and therefore allowed for sufficiently reliable measurements for the purpose of this work.

(a)   (b)

(c)
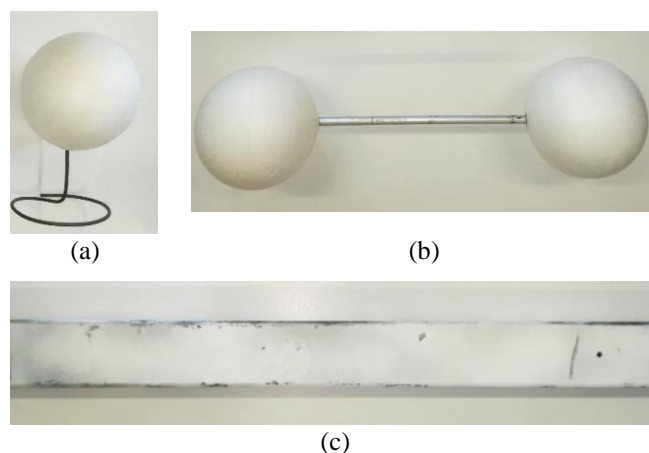
Figure 4-123 The artefacts proposed to measure the quality parameters inspired by the VDI/VDE standard: (a) single sphere having a diameter of 143.15 mm; (b) ball-bar composed of two spheres fixed at 391.58 mm from one another; and (c) iron bar of dimensions 50×646 mm2.

As mentioned in above, the following errors have to be measured to assess the accuracy of the imaging device.

The form probing error (PF) is defined as the absolute average value of the radial distances between the real measured points and a best-fit sphere evaluated according to the least-squares method, obtained for a number of acquisitions. The size probing error (PS) is the absolute average value of the differences between the estimated and the "true" diameter of the sphere, again obtained using several acquisitions. To perform the evaluation of both probing errors, the target sphere has been positioned in 10 sequential arbitrary locations (as indicated by the standard) within the working volume (Figure 4-124a), thus defining 10 different values for each error. Accordingly:

$$PF_i = |R_{imax} - R_{imin}| \qquad (23)$$

where PF_i is the error measurement for the ith acquisition, with $i = 1:10$ and R_{imax} and R_{imin} are, respectively, the maximal and minimal distances of the measured surface points of the ith sphere from the center of the compensating element. Therefore, the form probing error is given by

$$PF = \frac{\sum_{i=1}^{10} PF_i}{10} \qquad (24)$$

Additionally, for the size probing error, it is possible to define the ith measurement:

$$PS_i = |D_{mi} - Dc| \qquad (25)$$

where D_{mi} is the measured diameter of the sphere acquired at the ith position and Dc is the actual diameter of the calibrated sphere.

Therefore, it is possible to evaluate the size probing error according to the following equation:

$$PS = \frac{\sum_{i=1}^{10} PS_i}{10} \qquad (26)$$

The sphere spacing error (SS) is measured by using the ball-bar target. SS is the absolute average value of the differences between the acquired distance and the "true" distance (lk) between the centers of the two spheres (estimated from the point cloud data using a best-fit sphere fitting) for a number of different acquisitions. The target ball-bar was therefore positioned in 7 sequential arbitrary locations (as indicated by the standard) within the working volume (Figure 4-124b). For each acquisition it is possible to evaluate the jth error SS_j:

$$SS_j = |l_{mj} - lk| \qquad (27)$$

As a consequence:

$$SS = \frac{\sum_{j=1}^{7} SS_j}{7} \qquad (28)$$

According to the VDI/VDE standard, the flatness (or planarity) error (F), is computed as the average of the flatness F_k obtained for the acquisition of the iron bar positioned in 6 arbitrary positions within the working volume. In detail, F_k is defined as the distance between the two parallel planes enclosing the kth point cloud. Consequently:

$$F = \frac{\sum_{k=1}^{6} F_k}{6} \qquad (29)$$

(a)   (b)   (c)
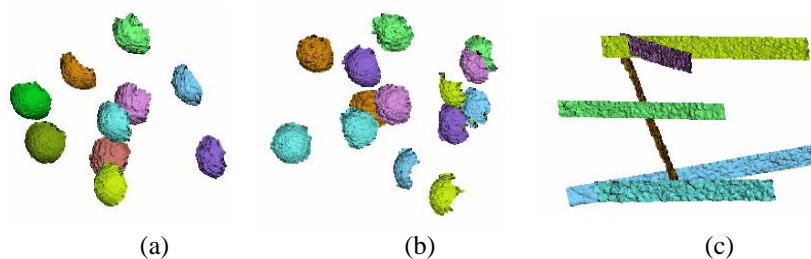
Figure 4-124 (a) The 3D recording of the single sphere captured in 10 arbitrary positions homogeneously distributed within the working volume. (b) 3D points of the ball-bar captured in 7 positions within the working volume (the same sphere color corresponds to the same bar). (c) 3D points of the plane captured in 6 positions within the working volume.

The values obtained by calculating the errors proposed by the standard are shown in Table 4-29, along with the results obtained with the Intel RealSense SR300, the Kinect v2 and the PrimeSense Carmine 1.09. Such results were obtained in Reference [127] by repeating the test setup provided by the standard for competitor cameras. As with the previous model, this experiment has been carried out on both raw and filtered data. To obtain the latter, the post-processing function of the SDK was activated, which by default applies decimation, spatial, time and edge-preserving filtering.

Table 4-29 The comparison between D415, SR300, Kinect v2 and PrimeSense Carmine 1.09 in terms of VDI/VDE error assessment.

Device	D415 (Raw Data)	D415 (Filtere Data)	SR300 (Filtered Data)	SR300 (Raw Data)	Kinect v2	Carmine 1.09
PF (mm)	13.83	8.42	8.30	15.43	20.13	9.32
PS (mm)	3.50	1.34	1.91	4.57	3.87	9.41
SS (mm)	4.99	5.03	6.05	5.11	19.7	26.08
F (mm)	15.36	9.45	6.88	19.33	12.58	6.71

Referring to the probing form error (PF), the new Intel device performances are comparable to the PrimeSense Carmine 1.09 and SR300, while Kinect v2 is characterized by a higher error. If the probing size error PS is considered, the Intel devices with filtered data prove to be the most effective, and the Kinect v2 performs analogously to the SR300 and D415 with raw data. The higher performance of both the D415 and SR300 Intel devices is even more evident when dealing with the sphere spacing error SS; in fact, the Δ_{SS} is considerably higher for tested competitor cameras. The performance in terms of flatness error F is almost the same for the SR300 and the D415 with filtered data and the PrimeSense Carmine 1.09. Interestingly, the behavior of the Kinect v2 in all tests is quite satisfying considering that this camera system is specifically designed to work in the medium to long range. It is interesting to note that the sphere spacing error measured for the SR300 and D415 using row data is almost the same assessed using optimized settings. This may be because the moderate smoothing effect obtained using the optimized setting does not have a particular effect on the position of the sphere's center when compared with the same position evaluated using raw data. When comparing the two RealSense models, it is noted that the results obtained are comparable: if

the raw data are considered, the new camera shows a slightly better performance for the whole test-set; on the other hand, the results obtained with filtered data are similar.

As reported in Reference [127], the discussion can be extended to other results from scientific literature. Reference [128] reports the results computed for the probing errors *PF* and *PS*) with several cameras, among them the Occipital Structure Sensor device, which is one of the most relevant competitors of Intel RealSense devices. This sensor scored an average value of ~10 mm for *PF* and ~2.2 mm for *PS*, while the values obtained with the latest Intel model for *PF* are 13.83 mm for raw data and 8.42 mm for filtered data, and for *PS*, 3.5 mm and 1.91 mm, respectively.

Regarding the flatness error, *F*, the performance of the D415 can be compared to the Occipital Structure Sensor device [128] with the result of reducing the error up to 50% when using D415 with filtered data.

The sphere spacing error, *SS*, can instead be compared to the results in Reference [74] obtained with the Asus Xtion Pro camera, whose results spanned from −8 to 2 mm compared to ~5 mm obtained with the D415 model.

Systematic Depth Errors in the Entire Range 150–1000 mm

As also reported in [127], one of the most common systematic errors for RGB-D devices is the so-called "inhomogeneous distance", i.e., the set of possible errors that may result from acquisitions at different distances from the sensor. To study these errors, the camera is required to be positioned perpendicularly to a surface plate and to acquisition at incremental distances (see Figure 4-125a) in the range 200–1000 mm with a pitch of 100 mm.

To this aim, the first step consists of positioning a linear guide perpendicular to the reference plane (see Figure 4-125a). In particular, the guide is iteratively positioned to (as closely as possible) reach the perpendicularity condition between the axis of one of the cylindrical rails and the reference plane. In the final orientation, the angle between the cylindrical rail and the reference plane, measured by using the Romer Absolute Arm 7520 SI/SE equipped with its contact probe, was 90.08°.

Once the correct positioning of the guide was assured, a dot IR reflective marker was physically placed on the reference plane. Subsequently, the camera was positioned so that the principal point of the left IR camera (which coincides with one on the depth map, plotted on the depth map image with a green cross) superimposed onto such a marker when the camera, mounted on the linear guide, moved away from the plane. In detail, the camera orientation was refined by assuring that for the two frames, acquired respectively at 200 mm and 1000 mm, the distance between the principal point and the acquired marker was lower than two pixels. The principal point was evaluated by performing an intrinsic calibration [129]. Although the depth map rotation around the optical axis of the left IR camera did not affect the metrological assessment of the systematic depth error, a rough alignment of the X and Y image axes with the horizontal and vertical directions was sought. Accordingly, two additional orthogonal lines were physically drawn on the reference plane (see Figure 4-125b) in the horizontal and vertical directions. Line orientation was checked by means of a laser level. The rough orientation of the camera was obtained by visually superimposing four additional crosses plotted on the left IR camera image on the drawn lines. Finally, the pitch of the linear guide, equal to 4 mm (therefore known a priori), assured the plane–camera distance.

The aim was to assess two types of errors: systematic non-planarity errors and offset errors on the depth. The first one was evaluated by referring to a ground truth plane (with a certified flatness of 50 μm), as in Reference [127], to verify the flatness of the obtained scan.

The latter was analyzed by studying the distance in Z between the obtained scan and the ground truth plane.
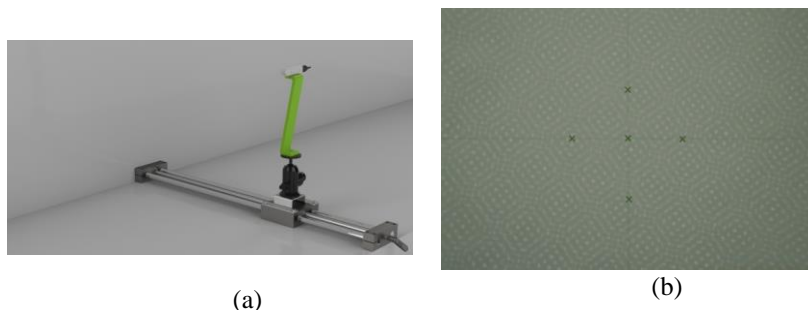

(a)

(b)

Figure 4-125 (a) The acquisition setup for systematic depth error evaluation test: the camera is mounted on a linear guide perpendicular to a planar surface. (b) Example of left camera frame acquisition of the reference plane with the physical marker.

Figure 4-126 shows the results obtained for the two tests. In detail, Figure 4-126a shows the error map between the scanned data and the best fitting planes built on such data, to highlight the non-planarity error that is introduced by the camera. The average deviation of the point clouds with respect to the ground truth planes ranges from 0.004 mm with a standard deviation of 0.345 mm at a distance of 200 mm from the plane, up to 0.237 mm with a standard deviation of 4.74 mm at a distance of 1 m. The maximum recorded error value spans from 1.6 mm to 26.5 mm, at 200 mm and 1000 mm distance, respectively. Figure 4-126b shows, instead, that nearly no error is present with regard to the depth offset, i.e., the point clouds are almost correctly positioned at a distance of 100 mm from each other. In fact, the best fitting planes evaluated for each point cloud using the Geomagic Design X® software package (3D Systems, Rock Hill, SC, USA) show a distance from the ground truth plane with a minimum value of 0.06 mm and a maximum value of 2.54 mm for the planes acquired at distances of 1000 mm and 900 mm, respectively.

The analysis of systematic depth errors led to interesting results, especially when compared to those obtained for the SR300. In the first instance, compared to the previous model, both the non-planarity of the single acquisitions and the depth offset have improved considerably. Specifically, as shown in Figure 4-126b, there is nearly no offset between the acquired data and the best fitting planes; moreover, the clouds do not have the "twist effect" that was noticed of the previous model. Noise tends to be distributed locally, leading to higher peaks than those reported by the previous sensor; a non-linearity, probably introduced by the lenses [125], can also be noted.
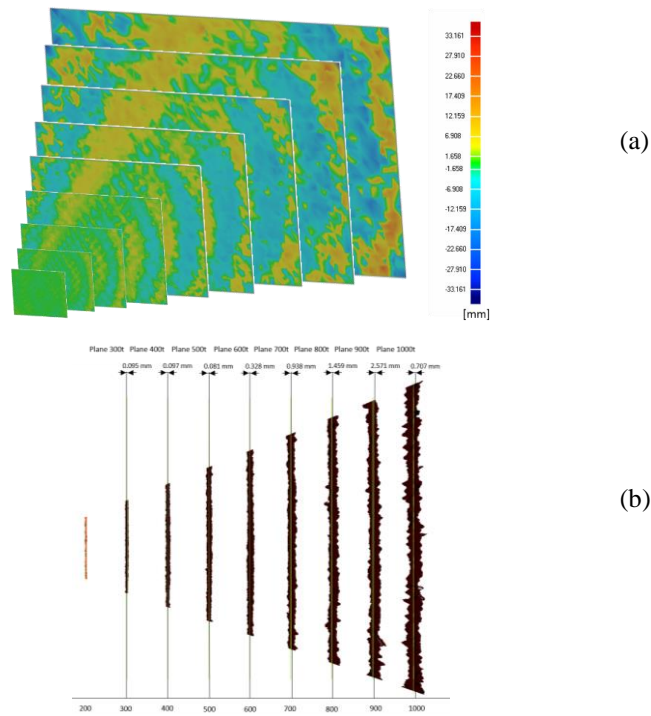
Figure 4-126 (a) The errror map between the target plane and the 9 point clouds acquired using the D415 device with increasing distance from the plane itself. (b) Evaluation of the depth-offset error for the 9 acquired planes.

3D Object Reconstruction

The last test carried out concerns the three-dimensional reconstruction of objects. Inspired by Part 3 of the VDI/VDE 2634 standard [130], which provides guidelines for the positioning of the camera around the artifact, the object under examination was rotated with respect to a stable camera.

It was decided to evaluate the accuracy of the reconstruction with the same two objects used to characterize the SR300 in [127]: a freeform smooth object (∼200 mm high and ∼70 mm wide) and a 3D tangram object (bounding box with dimensions of 150 mm high and 150 mm wide). Again, to provide an effective and easily replicable evaluation, the camera was used in the default configuration, with the only modified parameter being the depth unit, set to the best achievable resolution. To ensure the best performance, the camera–object distance was set to the smaller achievable value of approximately 500 mm. To obtain two reference models for assessing the device performances, the Romer Absolute Arm 7520 SI/SE was used (see Figure 4-127). The meshes, obtained using the Geomagic® Studio software package starting from the point cloud acquired with the D415 camera, and the reference 3D model were globally registered using the iterative closest point ICP algorithm [58]. To increase the quality of the mesh reconstruction, 5% of the borders were removed prior to performing the alignment.
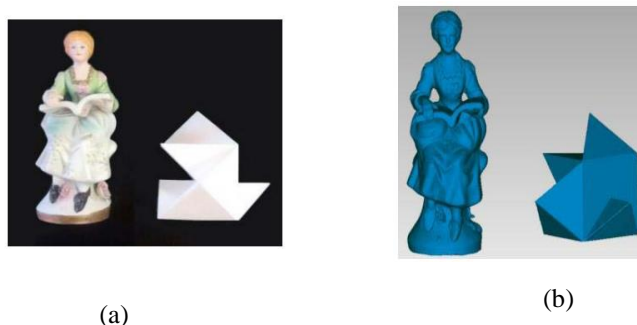
(a)

(b)

Figure 4-127 (a) The test objects for multiple-view reconstruction: a freeform statue and a 3D tangram; (b) reference 3D models for multiple-view reconstruction, obtained starting from the Romer Absolute Arm acquisition (an accuracy of ±0.063 mm).

Figure 4-128 shows the Euclidean distances between the acquired artifacts and the ground truth. The comparison between the ground truth and the acquired data is limited to the target portion obtained with the multiple-view acquisition; grey areas in Figures 15 are not, therefore, considered. As far as the tangram (Figure 4-128a) is concerned, an average deviation of 0.110 mm is obtained with a standard deviation of 0.902 mm; for the statue (Figure 4-128b), the average deviation obtained is −0.029 mm with a standard deviation of 1.856 mm.

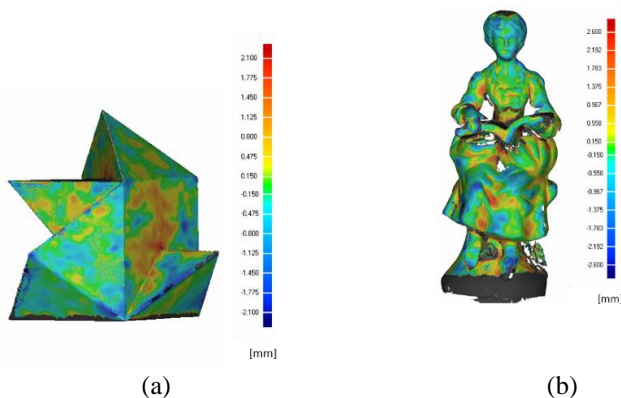(a)   (b)

Figure 4-128 (a) The 3D comparison between the tangram ground truth and the D415 acquired data. Errors are in mm. (b) The 3D comparison between the statue ground truth and the D415 acquired data. Errors are in mm.

The multi-view acquisition test for the full 3D reconstruction proves that both geometries are fairly measured, particularly if it is considered that for other RGB-D devices (e.g., the Microsoft Kinect) it has been evaluated that 3D reconstruction error can span an interval of 27 mm [53]. It can also be noted that there is no substantial difference with regard to the error assessed in the two reconstructions of the prismatic shape (tangram 3D) and the free form shape (statue), when the latest Intel model is used. Furthermore, the results shown here can be compared with the results obtained by scanning the same objects with the SR300 (Table 4-30). It can be noted that the results are fully comparable, with the main difference found in the

reconstruction of the statue which has, as noted, a free form shape: the new model performs with an average error of −0.029 mm against −0.2 mm obtained with the previous model.

Table 4-30 The average deviation (avg) and standard deviation (std) from the ground truth data obtained for the 3D reconstruction of the two artifacts for D415 and SR300 cameras.

	Reconstruction deviation from ground truth	
	Tangram	Statue
D415	avg: 0.11 mm, std:0.90 mm	avg: −0.029 mm, std:1.85 mm
SR300	avg: 0.10 mm, std: 0.4 mm	avg: −0.2 mm, std: 1.01 mm

Discussion and Conclusions

Given the growing popularity of RGB-D devices mainly due to their versatility and the interest that Intel RealSense devices have obtained in recent years for their accuracy, compactness and ease of use, in this work, a metrological evaluation of the latest model presented by Intel, the RealSense D415, was carried out. After investigating the operating principles of this device, a panel of tests was defined based on the distance between the camera and the examined scene. The main objective was, other than characterizing the new model, to compare this device with the previous model presented by Intel, the RealSense SR300 and, where possible, with other competitor RGB-D cameras.

In this work, the devices were compared through four types of tests: the error measured using a calibrated sphere at a very close range, the errors measured with the VDI/VDE 2634 Part 2 standard, the systematic depth errors extracted with the acquisition of a planar surface at increasing distances, and the 3D reconstruction of an object.

Tests have shown that the new D415 model is fully comparable to its predecessor model in terms of errors assessed through the VDI/VDE standard. The device is also in line with the results obtained with other devices in the scientific literature and exceeds their performance when considering the filtered data.

As for the 3D reconstruction, a comparison can be made with the previous Intel model, since both of them work in the close range with the result of a comparable deviation error.

The most interesting result is obtained from the estimation of the systematic depth errors: the D415, in fact, reports better results, both in terms of average flatness error and of displacement in Z from the real plane, with a maximum displacement from the ground truth plane of 2.52 mm.

In addition, the device is sufficiently accurate when acquiring very close distances (e.g., from 150 mm to 500 mm) as the reconstruction error in this range can be 0.99 mm on average when using a laser power equal to 250 mW.

As demonstrated by the experimental results of the characterization, it is possible to state that although the device is designed for addressing applications such as tracking, gaming or gesture recognition, it could also be satisfactorily employed as a 3D scanner, i.e., it could be used as a low-cost device for a number of 3D-scanning applications in a number of fields, including, among others, health, fashion, fitness and cultural heritage.

4.4.2. **Software update**

The new version of the software presented here maintains the main structure introduced above, but it has been developed using the QtQML libraries [131] thus changing, among other things, the way objects are rendered. The software has been updated by setting some

objectives. First of all it has been attempted to have an easier interaction of the user and to simplify the workflow. For this purpose, the functionalities have been grouped in two main Tabs, namely the functions that concern the acquisition of the arm and those that concern the modeling of the orthosis. The buttons to manage the 3D model have been moved to the 3D viewer (Figure 4-129).
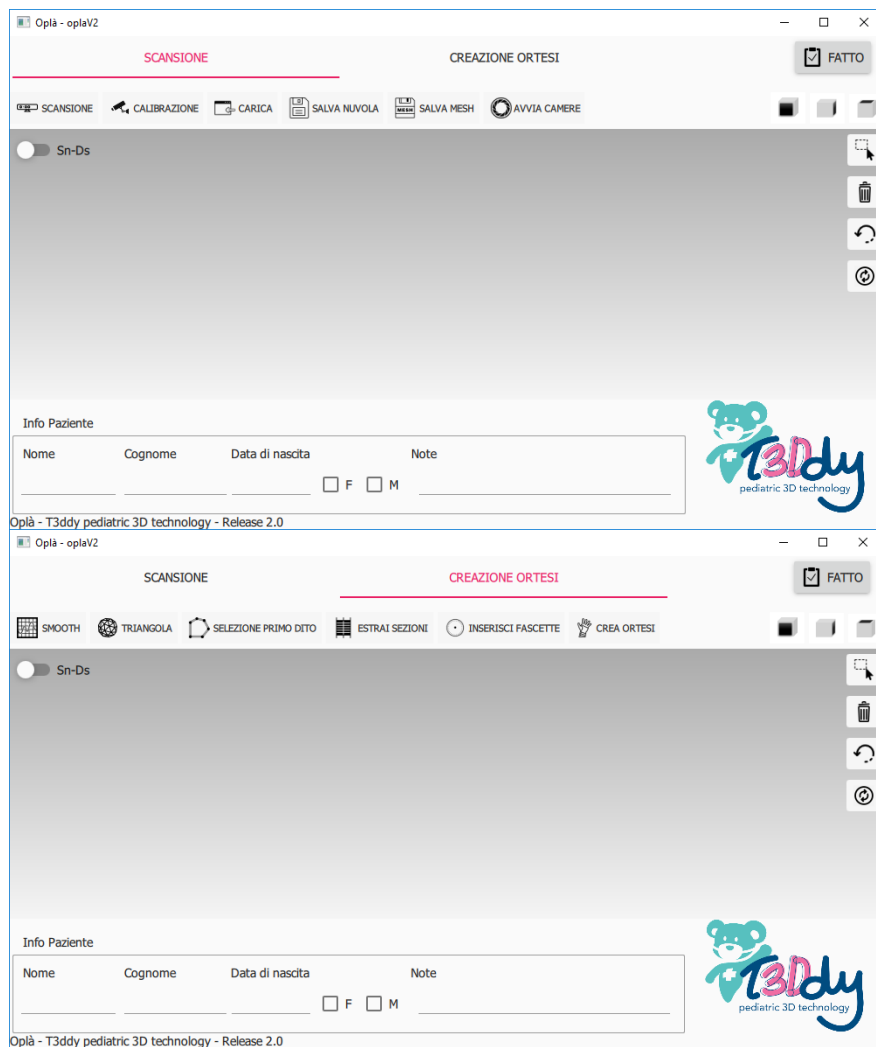

Figure 4-129 New Graphical User Interface.

Secondly, the program can be used to acquire two types of positions, shown in Figure 4-130, so there is a switch on the interface that indicates if it is acquiring the right or left arm of the patient, since it will no longer be identifiable by the position of the main lines as explained above.
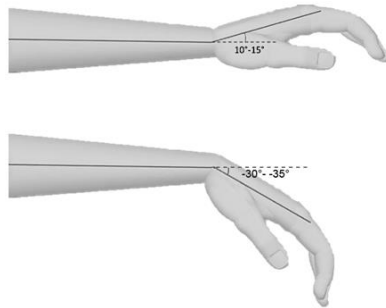
Figure 4-130 New position to be acquired by the hand-wrist-arm scanner.

An important adjustment is the selection of thumb opening points. Following the software's usability analysis, this point proved to be the most difficult to perform for an inexperienced user and was therefore simplified. The new selection mode allows to specify the points individually, these points will be imported directly into the NX procedure. Finally, a button has been inserted that directly invokes the execution of the NX procedure that will be carried out in the background, eliminating the need for the user to start the program and the procedure itself. We can see this button in Figure 4-129. The procedure is performed in the background using a utility provided by Siemens with NX called run_journal.exe that runs a journal and can be called by a script or other program. The run_journal utility starts an NX process in the background (without a graphical interface) and runs the specified journal.

With regard to scanning times, since the new device used, the IntelRealSense D415 camera, has an Active Stereo operating principle, it is possible to capture the scene from the 8 points of view simultaneously, without creating interference. Acquisition times are therefore reduced to about 0.1 seconds.

5. RE&AM methods and tools for thoracic malformations

The following are the implementation phases of the system for monitoring and treating thoracic malformations. It is necessary to draw attention to the fact that this second pilot case is composed of two distinct elements, dictated by clinical needs: i) the personalized medical device for the treatment of Pectus Excavatum (the Vacuum Bell); ii) the definition of severity indices for monitoring the progress of the two pathologies of Pectus Excavatum and Carinatum over time. Both elements will be implemented within the same acquisition system tool. The acquisition software will in fact allow both the creation of the personalized device and the calculation of the severity indices.

Given this double valence of the program, the feature extraction phase, which is the processing phase of the scanned model, is divided between 1) the creation of the surface that will represent the input of the CAD procedure, but also 2) the processing of the scan to extract some indices of severity. These and other steps will be explained in the following paragraphs.
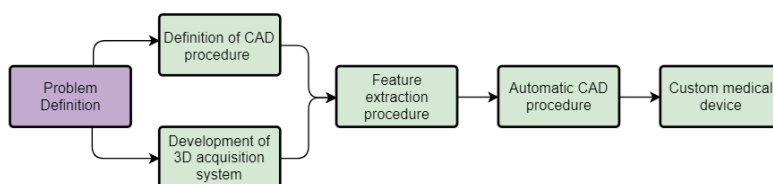
5.1. Clinical specifications

Figure 5-1 Diagram outlined to achieve the systematic realization of customized medical devices.

As mentioned, the two types of thoracic malformations considered are Pectus Excavatum and Pectus Carinatum, shown in Figure 5-2.
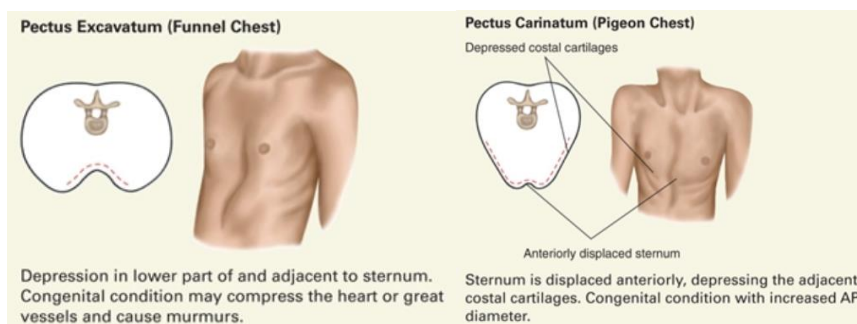

Figure 5-2 Pectus Excavatum (left) and Pectus Carinatum (right) description.

For the design of the scanner, no particularly restrictive constraints have been imposed on the total dimensions of the system, but simply objectives of realization dictated by the spaces in which it will be used. This pilot case does not require restrictive constraints because it was decided at this stage of defining the problem, that it is not necessary to scan the patient at 360° but a frontal scan of the chest is sufficient. In these terms, the scanner will be composed of a single device and it is only necessary to define the correct position of the camera with respect to the patient. It is also required that the scanner is easily movable and can, in case of need, acquire any anatomy, even patients with a great difference in age.

As far as the realization of the personalized Vacuum Bell is concerned, also in this case it is not necessary to impose restrictive constraints as the application has no contraindications.

The realization of the shape of the device will be entrusted to the doctor who, on the basis of considerations about the pathology of the individual patient, will have to indicate how the device will approach the area to be treated. On the basis of these indications, the system must create the device independently.

During this phase of problem definition, the need to monitor the progress of the disease over time has emerged. This need has been identified by doctors for several reasons including the definition of a proper use of the Vacuum Bell, but also the need to monitor over time the disease and possibly establish universal thresholds of severity. Another important reason is the psychological aspect of the patient, which in this way could have a quantitative comparison of the progress of the disease and find motivation.

It is necessary to define severity indices calculated on the external profile of the patient, both in case of Pectus Excavatum and Pectus Carinatum. The definition of these indices must therefore make it possible to measure the severity of the disease by preventing the patient from being exposed to radiation, as in the case of the indices most used in the literature.

5.2. Technical framework

For the realization of this second pilot case, steps similar to the previous case have been followed. In the first instance, among the low-cost devices available on the market, the one most suited to the needs of the specific case was chosen. The choice of device was supported by metrological characterization and performance evaluation of the device itself and comparison with other similar devices to validate its feasibility. The scanner's support structure was then created in accordance with medical specifications. The controlling software was developed to allow the creation of the 3D model of the thorax, which can be used to model the Vacuum Bell and to calculate the severity indices. The subsequent phase saw the development of a CAD procedure with robustness and repeatability features for the creation of the medical device. The software was then updated to extract the functionalities needed to automate the procedure, the execution of which is then made fully automatic in the CAD environment.

In the following paragraphs each step, which can be associated with a macroblock of the pipeline defined in 3.4, is described in detail.

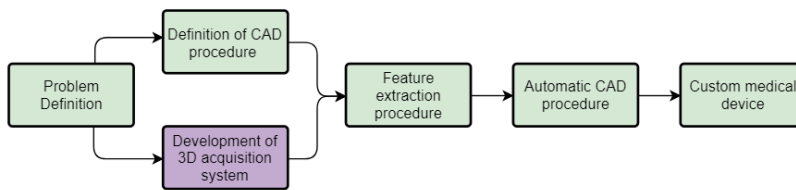### 5.2.1. Choice of 3D acquisition sensor and Hardware Setup

Figure 5-3 Diagram outlined to achieve the systematic realization of customized medical devices.

The choice of the scanning system is obviously a crucial step for the automatic creation of a personalized Vacuum Bell and to compute severity indices, since many factors depend on it: the precision of the final model, which given the field of application, should not be the best possible, the acquisition speed and the economic aspect. In this chapter it will be chosen, among some possible alternatives, the system that will be used to scan the patient chest.

The destination of use together with the fact that the scans will be made mainly to children, who hardly maintain a motionless position, suggest a type of low-cost scanner that allows to have short acquisition times, that is at least 30 frames per second.

Among the various acquisition systems that meet these requirements, three have been selected: Primesense Carmine, Microsoft Kinect v1 (K1) and Microsoft Kinect One or Kinect v2 (K2).

These scanning systems have significantly lower performances than, for example, professional scanners, but they have the advantage of being able to make many acquisitions in a short time, and their lower accuracy is not a problem for the case under examination. It is not necessary for the accuracy of the acquisition and therefore of the Vacuum Bell to be excessively high, as long as it remains in the order of 3-5 millimetres.

Table 5-1 shows the technical characteristics of the three selected devices. As can be seen from the table, the characteristics of Primesense and Kinect v1 are very similar and differ only in the focusing distance. In the case of Primesense the possibility to focus at 1.4 m allows the acquisition at a much closer distance than the other two devices.

What distinguishes Kinect v2 more than the other two is the type of scan; Primesense and Kinect v1 use an infrared pattern of structured lights (SL), while Kinect v2 uses time of flight technology (TOF).

In the following, the three scanning systems identified are compared experimentally in order to choose the one that best fits the application under consideration.

Table 5-1 Characteristics of Primesense Carmine, Microsoft Kinect 1 and Microsoft Kinect One.

	Carmine	Kinect 1	Kinect One
Color camera	640x480 @30fps	640x480 @30fps	1920x1080 @30fps
Depth camera	640x480	320x240	512x424
Max depth distance	1.4 m	4.5 m	4.5 m
Min depth distance	35 cm	40 cm near mode	50 cm
Horiz field of view	57.5 degrees	57 degrees	70 degrees
Vert field of view	45 degrees	43 degrees	60 degrees
Depth technology	structured-light	structured-light	Time of Flight

Comparison

Since the literature does not compare the three chosen acquisition systems, it was decided to make a characterization inspired by some techniques identified at the state of the art [61]. To evaluate the precision and accuracy, a structure was used with two 90 mm radius spheres connected by a wooden support that keeps the centres of the above mentioned spheres at a distance of 500 mm (Figure 5-4).

Figure 5-4 Designated artefact for device comparison.

The point clouds were obtained with the Kscan 3D software [132]. In Figure 5-5 it is possible to see the single point cloud obtained from Kinect v2.
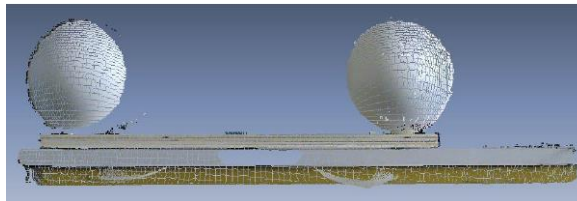

Figure 5-5 Example of obtained point cloud.

The creation of the meshes, and their subsequent processing, was performed with the Geomagic Studio software [133].

The angle of view of the Kinect v2 is greater and this means that to obtain the same framed area the scanner must be placed much closer to the object, thus improving in terms of resolution. However, this would give the scanner an advantage over the other two devices. It was therefore decided that, to objectively compare the scans of the 3 instruments, the Kinect v2 is used both at the same distance, and at a distance that displays the spheres in the same way, i.e. closer to the artifact. The latter mode, however, does not allow the two spheres to be fully focused, only a "circular crown" will be seen with a hole in the central area (where the scanner cannot focus since it is too close to the object).

In Figure 5-6 it can be immediately noticed that the meshes generated by the scans of the Primesense and the Kinect v1 are very similar, while those generated by the Kinect v2 are sensibly different: while in the first ones it is noticed the "scaling" along the z direction (due to the resolution of the structured light scanner) in the second ones this detail is not present, there is a smoothing effect, a better distribution of the points, because of the different type of scanner.
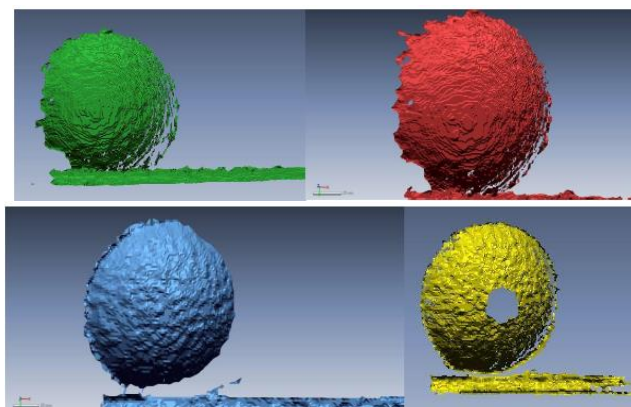
Figure 5-6 A detail of the mesh of the left sphere obtained with Primesense (green), Kinect 1 (red) and Kinect One from afar (blue) and Kinect One from near (yellow).

A numerical evaluation was then carried out to estimate how far the sphere of the mediated mesh, obtained from the three devices, deviates from the best fit sphere.

From this analysis it emerged that the best result is obtained by Kinect v2: in fact in both cases (far and near) the distribution of the error is less scattered than Kinect v1 and with less peaks than Primesense.

In order to estimate the precision and accuracy of the three scanners, the distance between the spheres and the measurement of the radius from the left sphere were evaluated (it was chosen to use only one of the two spheres as it was sufficient for the necessary evaluations). The measurements taken as a reference were calculated using the ROMER Absolute Arm 7520si scanner.

In particular, the reference values are: left sphere radius: 89.20 mm, distance between the centres of the spheres: 496.21 mm.
Table 5-2 shows the values resulting from the calculation of the distance between the centres of the spheres, carried out with Geomagic Studio.

Table 5-2 Values of the distances between the centres of the spheres obtained with the three scanners under examination.

	Estimated Value [mm]	Absolute error [mm]	Percentage error
Primesense	487.56	8.67	1.74 %
Kinect 1	506.66	10.45	2.10 %
Kinect v.2 vicina	497.80	1.59	0.32%
Kinect v.2 lontana	501.67	5.46	1.19%

From Table 5 2 it can be seen that the highest performance from this point of view is obtained with Kinect v2.

For the evaluation of the radius the best fit sphere is extracted from each acquisition followed by the measurement of its radius. Considering that the reference radius was 89.20 mm, the results obtained are depicted in Table 5-3.

Table 5-3 Values of the distances between the centres of the spheres obtained with the three scanners under examination.

	Measured radius [mm]	Absolute error [mm]	Percentage error
Primesense	87.83	1.37	1.54%
Kinect 1	88.61	0.59	0.66%
Kinect v.2 vicina	86.22	2.98	3.34%
Kinect v.2 lontana	86.65	2.55	2.85%

Table 5-3 shows that the best of the three scanners for measuring the sphere radius is Kinect v1.

In conclusion, the Kinect v2 is the best both for the deviation of the scan from an ideal sphere and for the measurement of the distance of the centers of the sphere, while it appears slightly lower than the Kinect v1 for the measurement of the radius. Therefore, the latest model from Microsoft is chosen for chest scanning, which also, being a TOF device, allows, if necessary, the simultaneous acquisition without interference of multiple devices.

For what concerns the pose of the patient for the 3D acquisition, the supine position is chosen to improve the steadiness of the measurement. This decision was taken following repeatability tests with standing and lying patients. More in detail, 10 patients aged between 7 and 17 years were selected for this preliminary study at the outpatient clinic dedicated to the treatment of chest malformations at the Meyer Children's Hospital. Each patient's chest was acquired 5 times from standing, and 5 times lying on a semi-rigid mattress placed on the ground. From these preliminary tests it emerged that the patient finds it much easier to maintain the position if lying down. The influence of the respiratory cycle on the repeatability of the measurements was then evaluated. According to the suggestions provided in [134, 135], the patient is asked to breath out and hold. This choice is mainly due to the fact that during exhalation the maximum range of Pectus Excavatum gravity is accentuated; but this type of procedure is also maintained for patients with Pectus Carinatum, where the respiratory phase does not affect the movement of the sternum, to maintain a fixed and easily repeatable procedure.

The 3D acquisition device is mounted on an appositely devised frame so as to acquire the patient chest frontally (see Figure 5-7). Such a frame is designed to allow vertical translation of the acquisition device; therefore, it can be adjusted to scan a wide range of patients from 2 to 17 years old while keeping a constant camera-chest distance (equal to approximately 100cm).

Figure 5-7 Sketch of the 3D chest scanner for the CI3D measurement.

System Calibration

Although the position of the camera in relation to the floor is kept constant, slight rotations may occur as a result of impacts or movements of the scanner, and in general it is not easy to calibrate its perpendicularity to the floor. For this reason, the acquired point cloud is processed to make the floor plane perpendicular to the Z axis.

The idea is to automatically locate the plane behind the patient and rotate the cloud to make the normal vector of the plane coincide with the Z axis.

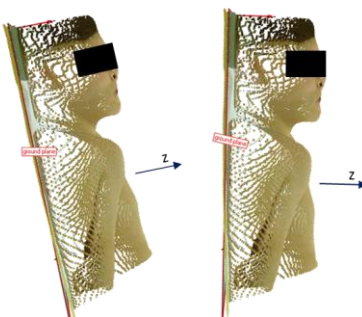The procedure is illustrated in Figure 5-8.

Figure 5-8 Example of point cloud rotation matching the normal of the floor with the z-axis.

In addition, the scan is rotated so that the line connecting the patient's armpits coincides to the X axis, so that it is consistent with the patient's body regardless of the pose taken during the scan (see Figure 5-9).
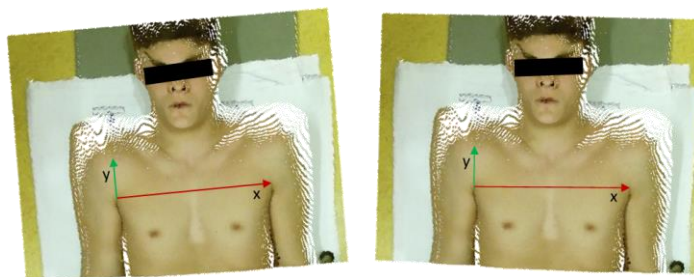

Figure 5-9 Example of point cloud rotation matching the x-axis with the line connecting the armpits.
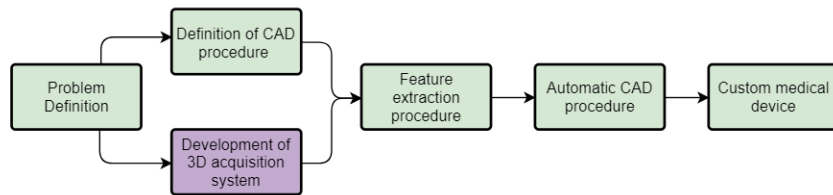
5.2.2. Initial Software Design

Figure 5-10 Diagram outlined to achieve the systematic realization of customized medical devices.

As in the previous case, the software is defined according to the requirements defined by the use cases.

In this chapter are shown the use cases related to the scanning of the chest and the calibration of the system; these use cases will be extended in the next chapters, introducing the features for the Vacuum Bell modelling and chest indices extraction.
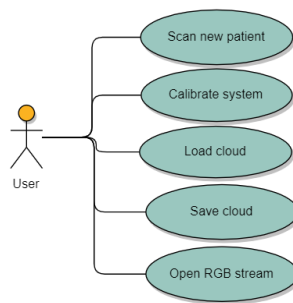

Figure 5-11 Initial use cases of the chest acquisition system.

Figure 5-11 shows the five initial use cases of the system: the actor must be able to calibrate the system, to capture the 3D anatomy of the patient, to store and load the 3D image and open the video stream to help the positioning of the patient.

As before, the software was designed accordingly, following the Model View Controller (MVC) design pattern.
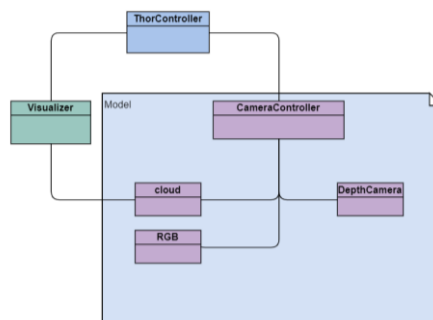

Figure 5-12 Class diagram of the control software.

Also in this case the structure of the classes (Figure 5-12) has been designed in such a way as to realize a modular structure. This means that each segment communicates with the others but remains, if necessary, replaceable.

In the following, it is shown how the single classes interact to realize the use cases.

Sequence diagrams and main steps

Each use case is now described in detail with a sequence diagram. As said a sequence diagram shows object interactions arranged in time sequence. It depicts the objects and classes involved in the scenario and the sequence of messages exchanged between the objects needed to carry out the functionality of the scenario.

For each use case, the sequence diagram is reported, and the main steps are described. In this work the user interface was handled using Qt framework [85], a free and open-source widget toolkit for creating graphical user interfaces and cross-platform applications. The management and processing of point clouds has been implemented for the most part through the open-source library PCL (Point Cloud Library) [86] and the open-source library VTK (VisualizationToolkit) [87] is used for mesh management. The interaction with the depth camera is managed by the libfreenect2 [73] library. The minimum requirements are: 6th generation Intel Core processor, 64-bit Windows 10 operating system, 8Gb disk memory, 4Gb RAM, x1 USB 3.0 ports. The times indicated are relative to a machine that mounts windows 10, Intel Core i7 processor, 16 GB of RAM.
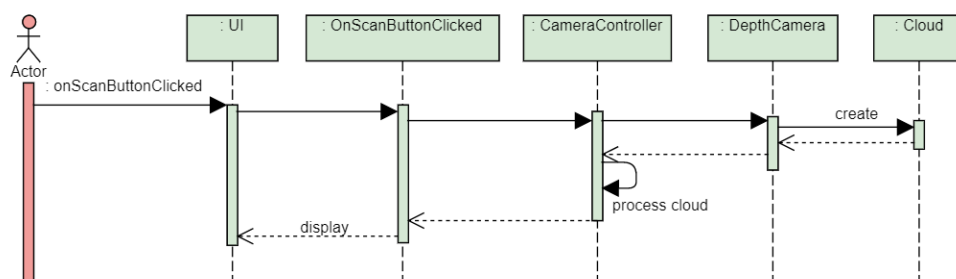
Scan new patient

Figure 5-13 Sequence diagram of the Scan new patient operation.

After the patient has laid down on the semi-rigid mattress, the "Scan" button is pressed to acquire the geometry.

Once saved, the cloud is cleaned with smoothing filter, spatial filtering and Statistical Outlier Removal to remove the noise. The parameters identified for these filters are: the smoothing radius is equal to 30 mm and the number of points for SOR analysis equal to 50 with standard deviation multiplier equal to 1.

The cloud is then processed to identify the floor plane and rotated to match the normal of this plane to the Z axis. This processing takes place in real time.
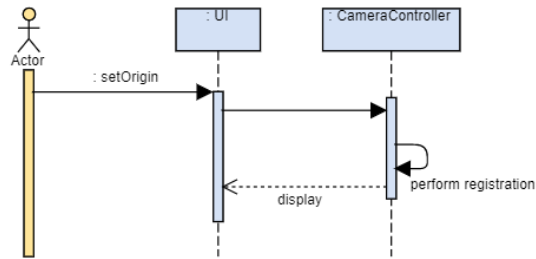
Calibrate system

Figure 5-14 Sequence diagram of the Calibrate system operation.

When the scan appears on the screen, it is possible to calibrate the position of the patient relative to the camera. The user manually selects, through the 3D viewer, the points in correspondence of the armpits and, by clicking on "setOrigin", the X axis rotates up to coincide with the direction that joins the two selected points. Then the centre of the system is brought to match the midpoint of the segment that joins the two points.
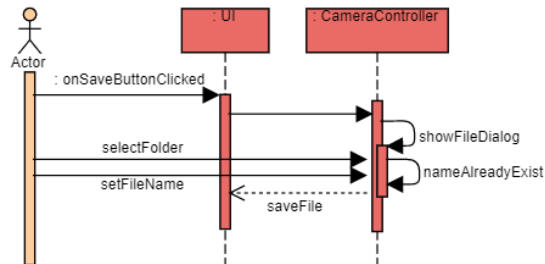
Save cloud

Figure 5-15 Sequence diagram of the Save scan operation.

When the user presses the "Save" button the program shows a dialog to choose location and file name, if the name is not already present in the selected folder the file is saved in ply format.
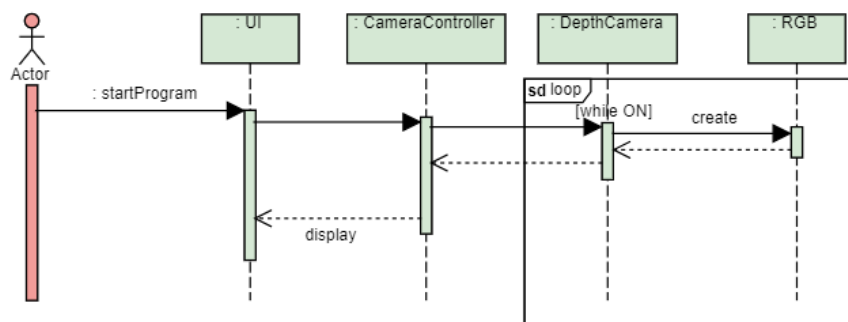
Open RGB stream

Figure 5-16 Sequence diagram of the Open RGB stream operation.

The RGB stream is shown on the screen when the program is started and remains open until the program is shut down.

The user interface programmed to provide the tasks described above is depicted in Figure 5-17. It is composed of a toolbar containing the described actions and a three-dimensional object viewer. In addition to these features, a form for saving patient information has been included.

Figure 5-17 Example of final result of chest acquisition.

5.2.3. CAD modelling
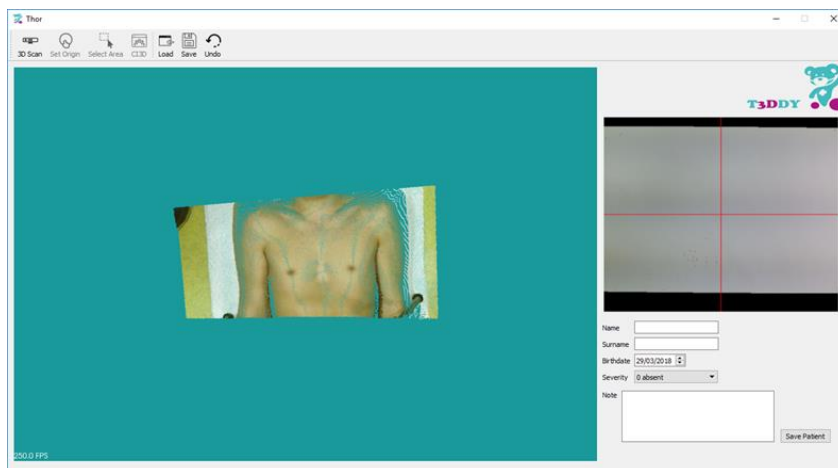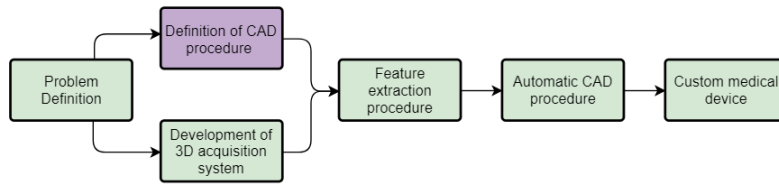

Figure 5-18 Diagram outlined to achieve the systematic realization of customized medical devices.

As specified in the introductory section, the final objective is to generate a semiautomatic methodology that physicians can use to create custom Vacuum Bell. The CAD modeling was therefore done in this perspective. The idea is to use as input the surface of the chest that is to be treated with this methodology (which changes from patient to patient and which will be obtained from the scan) and a curve that defines the area to be treated, which will vary from case to case and which will be chosen by the medical staff.

In the case used for this initial study, this curve was provided by the surgeon that created a drawing directly on his body, as visible in Figure 5-19.

Figure 5-19 Sketch of the back of the Vacuum Bell that will adhere to the patient's chest.

The creation of the customized Vacuum Bell CAD model is complicated by the need for this model to have the characteristic of updating according to changes made by the user, such as the modification of the starting curve or its positioning relative to the surface of the chest. It is therefore necessary to study a method of realization that takes this factor into account.

Several attempts have been made with different approaches and using different methods before finding the optimal one, which is presented below.
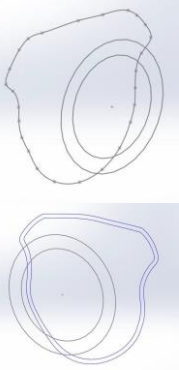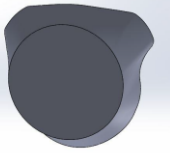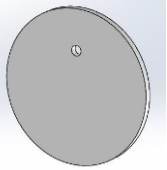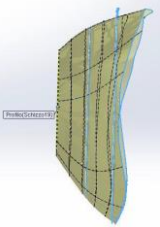
Before showing the final procedure, some problems encountered in the design phase that have become constraints for the final procedure are reported:

- the procedure must allow automatic updating if the spline representing the starting curve is changed;

- a shape that is too particular, not suitable for the practical realization of the piece, must not be generated. Specifically, the front part, i.e. the Plexiglas part, must always maintain the same shape;
- both for reasons of construction and ergonomics, the rear surface, the one in contact with the chest, must not be very deformed or not uniform.

The final procedure is explained in Table 5-4.

Table 5-4 Evolution phases of an applying example of the devised procedure.

	The procedure for the realization of the Vacuum Bell starts from two sketches. The first sketch is made by two circles; the second sketch is a 3D sketch of the projection of the 2D spline made by following the line indicated by the doctor (so that it is possible to bind his points to stay on the surface of the chest) and an offset of 3 mm (value taken from the original Vacuum Bell).
	Then a loft surface is executed between the outer circumference and the outer spline. The surface is then closed on both sides by two filling surfaces. The closed surface allows the creation of the solid.
	Then an extruded cut is made in the area where the Plexiglass part will be placed, which has been made separately and imported.
	The inner part is obtained through a loft cut starting from the inner surface of the plexiglass up to the projection on the chest of the offset of the starting spline. As in the case of the standard Vacuum Bell, an intermediate sketch is inserted in order to obtain a variable thickness. This sketch is made starting from a loft with only two sketches: finding the curve of intersection between the surface thus generated and the plane that is interested, it is possible to create a sketch that is a middle way between the circumference and the spline. Creating an offset of 3 mm it generates the intermediate sketch that is used for the loft.
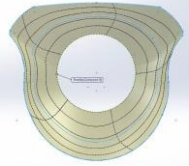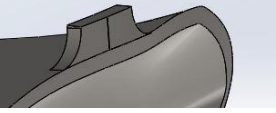
	Finally, the tab for detachment after use is made: it is also part of the contact area between Vacuum Bell and the patient's chest, so it must be projected onto the thoracic surface as done for the spline so that it is updated according to the changes. It has been realized through an extrusion.

Figure 5-20 shows the final CAD model.
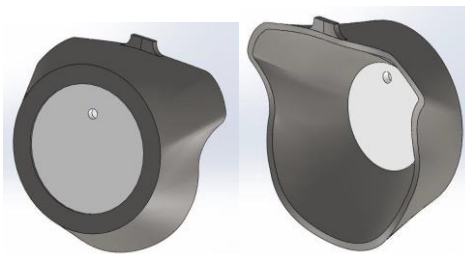
Figure 5-20 Final result of the Vacuum Bell modelling procedure.

Figure 5-21 shows the sections of the original Vacuum Bell and the personalized one in order to compare the thickness of the silicone part. The CAD model of the original Vacuum Bell was obtained by reverse engineering on the medical device. As it can be seen the thickness is very similar.
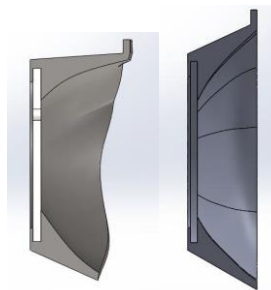
Figure 5-21 Thickness comparison between custom Vacuum Bell (left) and original Vacuum Bell (right).

In this case, as established, with only the input of the surface (resulting from the scanning of the chest) and the sketch of the spline (depicting the back of the Vacuum Bell) suitable for the case studied, by updating the model the Vacuum Bell lies on the chest of the patient following the pre-established sketch. To clarify this idea, Figure 5-22 and Figure 5-23 can be taken into consideration: they show the Vacuum Bell correctly positioned on the thoracic surface of the

patient deriving from the scan (Figure 5-22) and the sketch representing the part that will adhere to the thoracic wall (Figure 5-23).
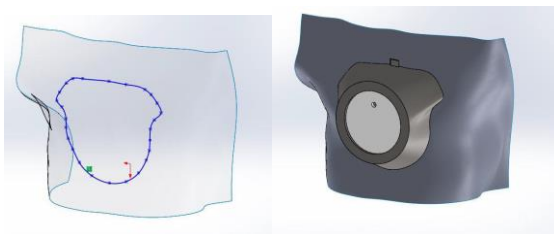
Figure 5-22 Spline obtained from the surgeon's drawing and projected onto the surface resulting from the scan (left). Vacuum Bell correctly positioned on the surface (right).

If necessary, it would be possible to translate the Vacuum Bell to modify its position with respect to the chest and updating the model would result in a modification of the final object (Figure 5-24).
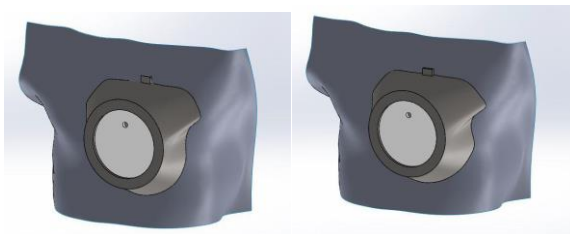
Figure 5-23 Translation of the Vacuum Bell on the thoracic surface (left) and consequent modification of the prototype (right).

If instead it is intended to modify the spline that represents the area on which the Vacuum Bell will operate, it would be sufficient to open the 2D sketch and move the points: once again, updating the model, the prototype would follow our corrections and would change accordingly (Figure 5-24).
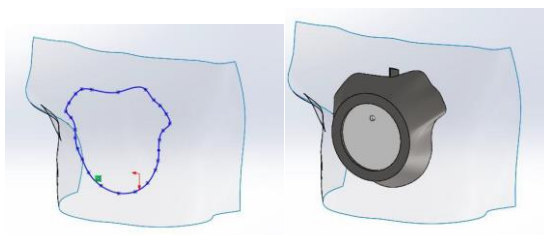
Figure 5-24 Modification of the spline (left) and consequent modification of the Vacuum Bell (right).

The latter CAD model therefore has all the required features.

5.2.1. **Surface Extraction**
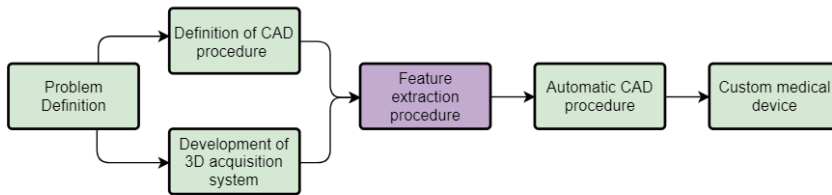
Figure 5-25 Diagram outlined to achieve the systematic realization of customized medical devices.

As explained in the previous chapter, the procedure to build a custom Vacuum Bell requires two inputs: the surface of the chest on which to lay the device and the curve that represents the profile of the custom device.

It is believed that drawing the curve, even in a CAD environment, can be an easy operation to carry out also for hospital staff and this step will be described in chapter 5.2.4 where the procedure is made semi-automatic.

The extraction of the surface is instead carried out inside the software that manages the scanner.

In detail, it is intended to create the surface starting from the manual selection of the area of the chest that contains the defect. The use cases in Figure 5-26 are then introduced.
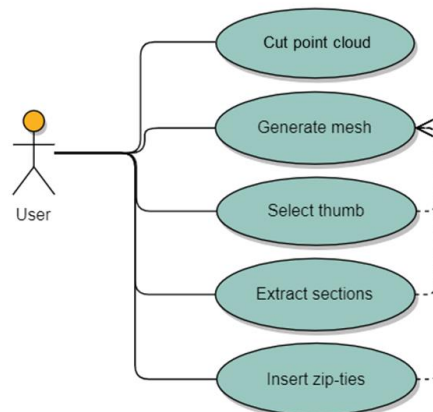
Figure 5-26 Additional use cases for feature extraction.

Select Area and Generate Surface

The modelling procedure of the Vacuum Bell foresees as input the surface corresponding to the area of the chest containing the defect. To create this surface, the program has been modified in such a way that the user is given the possibility of selecting, by clicking on the "Select Area" button, the area of interest on the original scan. Subsequently, if the "Generate Surface" button is pressed, the corresponding mesh is generated in the first instance. The generated mesh is sectioned with a parallel sheaf of planes, perpendicular to the Z axis, to extract subsequent sections. These sections are then given as input to a python routine that is

performed in the background, not visible to the user, created using the CAD library pythonOCC [102], which, through a loft operation, generates the surface and exports it in IGES format. Figure 5-27 shows these two steps.

Figure 5-27 Example of extracted sections (left) and computed surface (right).

5.2.2. PE chest indices
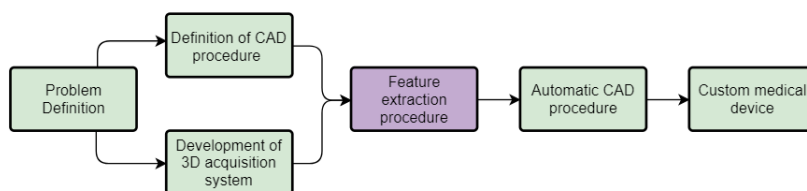
Figure 5-28 Diagram outlined to achieve the systematic realization of customized medical devices.

Many surgical correction techniques for severe PE deformities have been carried out in clinical practice [136, 137] all sharing the requirement for a preliminary pre-operative test and a fundamental role is played by pathology severity assessment. To qualify and/or quantify the anatomic defect, as said, several so called "thoracic indexes" have been therefore proposed, based on thoracic measurement which could be distinguished in five categories accordingly to [21]: clinical, chest-X-Ray, chest-CT-scan, chest and cardiac MRI and other indexes.

Referring to CT scan measurement-based methods [138], the Haller index (HI) stands out among the others. Defined as the ratio of the transverse diameter h1 (i.e. the horizontal distance of the inside of the ribcage) and the anteroposterior diameter h2 (i.e. the shortest distance between the vertebrae and sternum), the HI is traditionally used as the gold standard metric to evaluate the severity of pectus excavatum and to indicate the need for a surgical repair (see Figure 5-29).
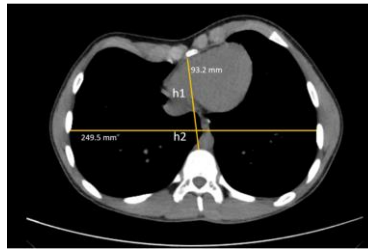
Figure 5-29 Measures acquired on a tomographic image to evaluate the Haller index; in this exemplificative case HI = 0.374.

Despite its wide use in the clinical practice, the HI (see Figure 5-29) presents several limitations; by way of example, in [139, 140] it is demonstrated that Haller index fails to correctly measure the whole population, by revealing a dramatic overlap between pectus excavatum patients and normal controls. The Haller index is, indeed, highly dependent on the patient chest width and for this reason it may fail in assessing the patient defect correctly. To overcome such a drawback, Peter et al. [139] proposed a new index, named Correction Index (CI) as an alternative to the HI. Based on the chest CT/MRI scan, such an index measures the percentage of PE depth that needs to be corrected by using the bar placement. In particular, as depicted in Figure 5-30, the CI is calculated on the CT/MRI scan according to:

$$CI = (A-B)/A \qquad (30)$$

Where A represents the maximum distance between the line L placed on the anterior spine and the inner margin of the most anterior portion of the chest (and it approximate the ideal chest length) and B is the minimum distance between the posterior sternum and the anterior spine.
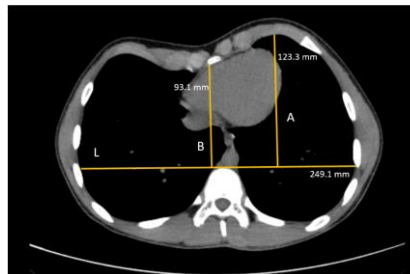
Figure 5-30 Measures acquired on a tomographic image to evaluate the Correction index; in this exemplificative case CI= 0.245.

Both A and B measures are evaluated on the slice that contains the greater sternal depression; such slice is manually selected by clinicians by scrolling all the tomographic images.

Both the abovementioned indexes (i.e. HI and CI) are computed on tomographic images, thus exposing the patient to ionizing radiation. Accordingly, the use of HI and CI to monitor the development of patient PE pathology is not recommended. On the other hand, a systematic PE evaluation, especially for young patients (2-17 years old), can play a fundamental role for a constant treatment follow up (e.g. vacuum bell or post-operative relapse).

With the aim of developing non-invasive chest indexes, some approaches have been proposed to assess the chest deformity based on optical 3D body scanners as a convincing radiation-free alternative to CT scan and MRI [21, 141, 142]. These techniques show promising results in assessing PE severity; however, they require human intervention in the measurement process or, most important, they require the patient to stand still for a considerable amount of time since even a minimum movement of the patient might invalidate the process (being this usually based on a 360° scan).

In view of that, has been devised a novel method for assessing the PE severity of patients with an appositely devised procedure to extract PE-related information.

Patients and Methods
Patients involved in experimentation are PE affected children from 2 to 17 years old with mild to severe diagnosis. Inform consent was obtained from each subject and if appropriate from parent or guardian.

3D body scan-based PE severity computation
The first step is to acquire the patient's chest as described above. The patient is asked to lie down on the semi-rigid mattress placed on the ground, the scanner is positioned with the optical center at the height of the point of maximum depression, with the help of the RGB stream that shows the real-time camera view, and the image is acquired in complete exhalation. Once the patient chest anatomy is acquired, thus resulting in a 3D model, it is possible to extract PE related information from such a model. In detail, a new index, named Correction Index 3D (CI3D) has been defined. Such a new index is inspired by the CI [142] but, differently from such widely known index, the proposed approach is based on the external surface of the chest. In particular, the new index CI3D is defined as follows:

$$CI3D = (C-D)/C = \Delta/C \qquad (31)$$

Where C and D are the vertical distances of, respectively, the maximum and minimum sternal depression from the reference plane (i.e. the semi-rigid mattress plane, depicted by the line K in Figure 5-31.
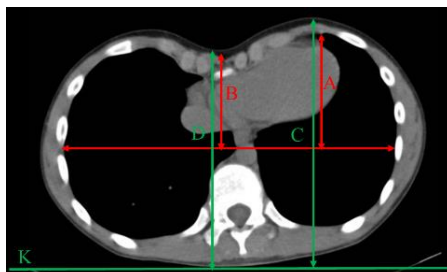
Figure 5-31 Example of CI calculation (red) and corresponding CI3D calculation (green).

To evaluate the CI3D index, the following procedure has been carried out. First, the reference plane (i.e. the floor) is automatically identified in the 3D model. Such a plane is considered as the XY plane of the global reference system where the 3D model is referred. Subsequently, a

number of equally spaced transverse planes (i.e. planes parallel to XZ with a plane-by-plane distance equal to 1 mm) are automatically drafted in the 3D model (see Figure 5-32).
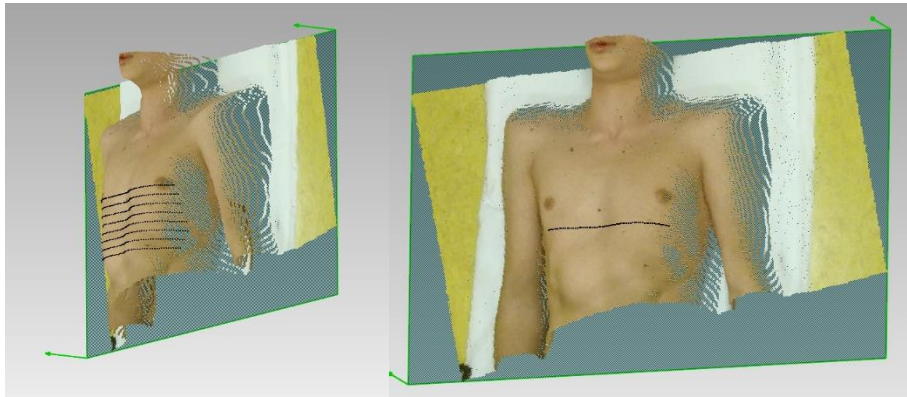
Figure 5-32 On the left, the sheaf of planes perpendicular to the ground cutting the chest. On the right, the slice containing the greater excursion automatically identified by the software.

The intersection of such planes with the 3D model of the chest allows determining, for each transversal plane, a different Δ value. Among all the Δ values measured on the set of transversal planes, the one considered as representative of the patient pathology is the maximum one. Such a value, in fact, is measured on the transversal plane where the greater chest depression is located. Finally, the CI3D index is computed with reference to such a plane (see Figure 5-33).
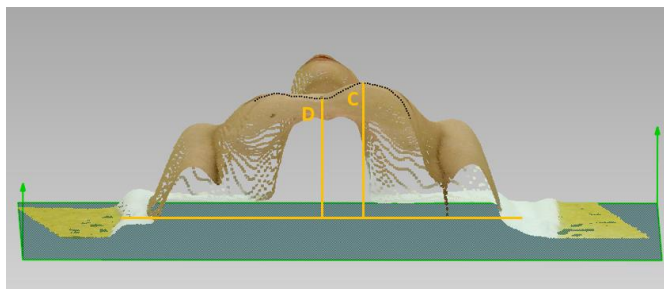
Figure 5-33 Computation of the distance C and D in the 3D model.

Data analysis

To prove the effectiveness of the proposed CI3D index, a statistical analysis has been carried out. In particular, a comparison between the CI3D index computed for a set of patients is compared with the traditional evaluation performed by doctors working in the field. To this purpose, the collected data (i.e. the CI3D values) were compared with the mean value of the blind severity assessment carried out by five different clinical professionals, which evaluated the severity of the defect for each patient. In other words, we considered as "ground truth" the mean value of the PE severity assigned by the doctors according to the levels listed in Table 5-5.

Table 5-5: Levels of PE severity.

0	Absent
1	Mild
2	Moderate
3	Moderate-to-severe
4	Severe
5	Highly Severe

With the aim to validate the proposed CI3D measure as an objective PE severity detector, also such an index is mapped in six levels of PE severity (as in Table 5-5) through the identification of a number of corresponding significant severity thresholds. To determine the severity classes boundaries, it has been chosen the Jenks Natural Breaks classification [143], an iterative clustering algorithm which computes the thresholds that better separate the data clusters. Aiming to define the precision of the classifier, an Attribute Agreement Analysis was performed (Kendall coefficient [144]) to assess the agreement between the rating of our system and the doctors' classification.

The statistical scatter plot and the Pearson correlation analysis between the computed CI3D values and the clinical evaluations of PE severity as well as the Cohen's Kappa statistics of the index classification were evaluated with the Minitab ® 18 software [145]. All statistics were considered significant if $p < 0.05$.

Results

51 patients (41 male and 10 female) with mild to highly severe PE diagnosis, aging from 2 to 17 years old were selected; 5 physicians were asked to assign a severity class to each patient, as reported in Table 5-5. The results of the corresponding CI3D values calculation are reported in Table 5-6. Figure 5-34 shows the histogram of the collected CI3D values and the line representing the mean clinical severity (MCS) on the same patients.

Table 5-6 CI3D values computed on 51 patients

P#	CI3D	P#	CI3D	P#	CI3D	P#	CI3D	P#	CI3D	P#	CI3D	P#	CI3D	P#	CI3D
1	12%	9	5%	17	10%	25	9%	33	11%	41	11%	49	16%		
2	23%	10	8%	18	16%	26	7%	34	9%	42	14%	50	17%		
3	5%	11	15%	19	5%	27	10%	35	25%	43	18%	51	7%		
4	23%	12	9%	20	5%	28	5%	36	8%	44	10%				
5	2%	13	10%	21	16%	29	10%	37	18%	45	15%				
6	17%	14	14%	22	5%	30	8%	38	9%	46	17%				
7	17%	15	11%	23	5%	31	5%	39	7%	47	7%				
8	14%	16	15%	24	13%	32	15%	40	14%	48	2%				
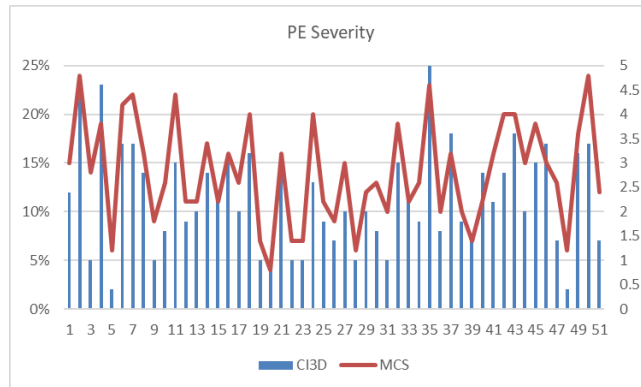
Figure 5-34 The Pectus Excavatum Severity according to the Mean Clinical Severity (MCS) as in Table 1, and the proposed Correction Index 3D (CI3D) on the 51 sampled patients.

Correlation between CI3D and MCS

To perform and present the correlation analysis the computed CI3D values are used as independent variables to be correlated with the mean clinical severity. A positive correlation between presented variables are depicted in Figure 5-35; the scatter plot shows a linear relationship between CI3D and the clinical assessments to a good accuracy; a least-squares regression line predicting the clinical diagnosis from the evaluated CI3D values is also reported in Figure 5-35.

Null hypothesis H0 was formulated as the lack of correlation between CI3D values and MCS values, and the correlation was tested with Pearson correlation coefficient at a significance level of α =0.05. As a result, a correlation coefficient of 0.87 is obtained and, due to lower p-value $\ll$ 0.05 the hypothesis of no-correlation was rejected thus indicating that CI3D is a right candidate to appropriately represent the PE severity.
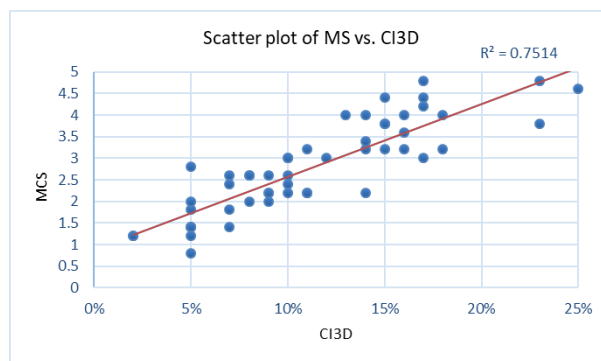
Figure 5-35: Scatter plot and regression line of the CI3D values and the Mean Clinical Severity (MCS)

Automatic thresholding and degree of agreement validation

The Jenks Natural Breaks (JNB) classification method is a data clustering method designed to determine the best arrangement of values into different classes by minimizing each class's average deviation from the class mean, while maximizing each class's deviation from the

means of the other groups. The five thresholds representing a map between six severity classes (absent to highly severe defect) and CI3D values are shown in Figure 5-36.
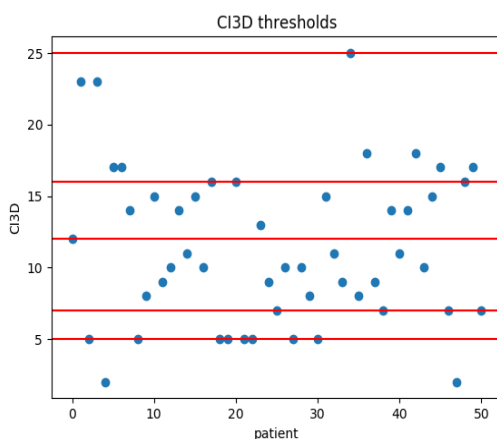
Figure 5-36: Blu dots are CI3D values of 51 patients and red lines represent the 5 thresholds produced by JNB classification

Once the thresholds have been identified and the CI3D values assigned to classes, the obtained classification has been compared to the MCS values to determine the strength of the CI3D when coupled with the chosen classifier. An attribute agreement analysis has been thus carried out to measures the percentage of the agreement between the appraisal (the CI3D values) and the standard (doctors' evaluation). In order to consider also the magnitude of agreement/disagreement the Kendall's correlation coefficient [144] is also computed; as a result, the percentage score is 64.71% while the Kendall's correlation coefficient is 80% with a p-value $\ll 0.05$, thus indicating that agreement exists among the appraisers and the standard.

CI3D as a quantitative sternal depression measurement
The proposed CI3D value together with the devised measuring protocol, can be thought also for monitoring the progression of the defect or evaluating if and how much a correction procedure is producing good results; for this purpose, as also proposed in [146], the proposed method has been tested to verify if the external measure can provide a uniform standardized measure of the pectus depression. With this aim, a preliminary test has been devised on three patients chosen to repeat the measurements before and after applying the Vacuum Bell for 20 minutes. The Vacuum Bell [147] is a widely used device for the treatment of asymptomatic PE patients, also referred to as treatment by cup suction.

Table 5-7: Comparison between CI3D values computed before and after 20 minutes of Vacuum Bell application

Patient	CI3D Pre-VB	CI3D Post-VB
P1	12%	9%
P2	8%	6%
P3	18%	15%

As shown in Table 5-7 all patients reported a significant improvement of the sternal depression after 20 minutes of device application thus indicating on one hand as expected the effectiveness (at least in the short time) of the treatment, and on the other hand the efficiency of CI3D index to measure the VB sternal correction.

> *CT/MRI scan 3D index to validate the scan*

In order to have a comparison and estimate the accuracy of the proposed 3D measuring system, CI3D values were calculated also on four available CT scans of a subset of the PE patients for which the 3D surface is obtained from the tomographic images; of course, we have to take into account that the position used for CT scan is different from the one chose in the proposed system, being supine with arms up, so the values would not be perfectly the same. Table 5-8 shows the results of CI3D values obtained on the four 3D reconstructions from CT scan compared with the proposed body scanner.

Table 5-8: Comparison between CI3D values computed on data acquired with the proposed body scanner and CI3D value computed on 3D reconstruction from CT scan

Patient	CI3D Scan	CI3D CT
P1	25%	24%
P2	10%	9%
P3	16%	15%
P4	19%	20%

> *Computation of other indices to improve accuracy*

The already introduced Three-Dimensional Correction Index (CI3D) represents the adaptation of the Correction Index (CI) to the outer perimeter of the chest, as shown in Figure 5-31.

As said, the CI assesses the percentage of chest depth, independently of the chest width, unlike the more common Haller Index [138].

Two deformity indices are calculated in addition to CI3D: Asymmetry (AI3D) and Eccentricity (EI3D). These two measures, introduced in the literature [21, 148, 149] and usually calculated on CT and MRI, have also been adapted to optical scanning by considering external rather than intercostal perimeters.

The selection of these deformity indices is based on the fact that some characteristics of the thorax can produce different impacts also with regard to the success of the correction procedure [150]. In fact, many of these characteristics cannot be evaluated with the most widely used methods, i.e. the Correction Index and the Haller Index, which only take into account the position on the sagittal plane of the point of maximum depression. The Asymmetry Index determines the ratio between the right and left prominence of the chest, measured by considering the maximum points with respect to the sagittal plane, calculated on the section containing the point of maximum depression (Figure 5-37).

Figure 5-37 Example of asymmetry index (AI) calculation (red) and corresponding asymmetry index three-dimensional (AI3D) calculation (green).

The Eccentricity Index represents the displacement, on the transversal plane, of the cavity and is calculated as the ratio between the two distances of the minimum point from the thoracic wall on the right and left sides (Figure 5-38).

$$AI3D = \frac{M1}{M2} \qquad (32)$$

$$EI3D = \frac{R}{L} \qquad (33)$$

Where $M1$ and $M2$ are left and right highest points on the section containing the maximum depression; R and L are the left and right distances of the point of maximum depression from the external thoracic wall.
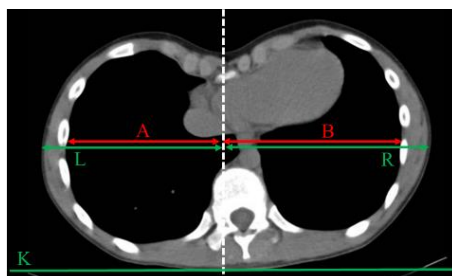
Figure 5-38 Example of eccentricity index (AI) calculation (red) and corresponding eccentricity index three-dimensional (EI3D) calculation (green).

Two further measures have been introduced to describe the thoracic malformation: Area and Width. The idea is to describe the extent and shape of the cavity, not only its depth. The Width is calculated as the Euclidean distance between left and right highest points, in correspondence of the section containing the point of maximum depression (see Figure 5-39). The Area is calculated by connecting the two highest points and approximating the area between the line thus obtained and the profile of the chest, always in correspondence of the section containing the minimum (yellow in Figure 5-39).
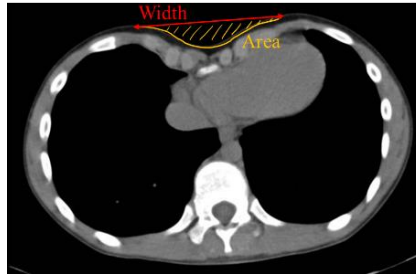
Figure 5-39 Example of Width and Area computation on the external profile of the chest.

The described values are calculated on the 3D model of the patient's chest and are, for explanatory purposes, depicted on the CT image, to have a visual comparison between the traditional indices and their adaptation to the 3D model, calculated considering external rather than intercostal perimeters.

In particular, for each of these values, the section containing the point of maximum depression is calculated automatically. In detail, the procedure is the same explained above, i.e., once the XY reference plane (i.e. the floor) is automatically identified in the 3D model, a number of transverse planes parallel to XZ with a reciprocal distance of 1 mm are automatically drawn (Figure 5-40). The intersection of these planes with the 3D model of the chest allows the determination of a different Δ value (corresponding to the local sagittal depression) for each transverse plane. Of all the Δ values measured in the transverse planes, the section which gives the maximum value is considered.
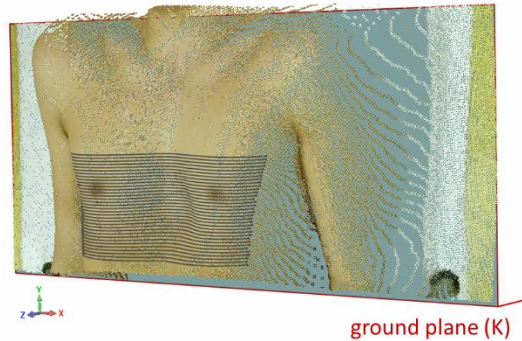
Figure 5-40 Sheaf of planes perpendicular to the ground plane cutting the chest for the automatic computation of the point of maximum depression.

Data analysis

With the aim of creating a diagnostic tool that can support the physician's judgment during the outpatient examination, it was decided to evaluate the parameters extracted by assigning a class of severity to each analyzed case. As in the previous case, a severity clinical score (SCS) was obtained by consulting five doctors, experts in the field of thoracic deformities, to independently assess the defect of each patient according to the classes listed in Table 5-5. To each clinical case is assigned the mean value of the five SCS (MSCS). The severity values

were mapped to six severity levels to allow a better discrimination of the different cases with respect to the basic severity levels (mild, moderate and severe).

50 new patients with mild (1) to extremely severe (5) diagnosis of PE were studied, aged between 2 and 17 years. For each patient the values of CI3D, Width, Area, AI3D and EI3D were extracted as described above and the MSCS was assigned.

The data were evaluated with Linear Discriminant Analysis (LDA), a very common technique used for supervised classification problems [151]. The objective of the LDA is to project characteristics of a larger space on a smaller space. This can be achieved in three steps: the first step is to calculate the separability between different classes (i.e. the distance between the mean of the different classes), also called as variance between classes. The second step is to calculate the distance between the mean and the samples of each class, which is called variance within the class. The third step is to construct the lower dimensional space that maximizes the variance between classes and minimizes the variance in the class.

In first instance, the Pearson correlation coefficient between each index and the MSCS was calculated (Table 5-9).

Table 5-9. Pearson correlation coefficient between each index and the MSCS.

CI3D	Width	Area	AI3D	EI3D
Corr: 0.87	Corr: 0.54	Corr: 0.80	Corr: -0.372	Corr: -0.154
p-value: 0.0005	p-value: 0.0005	p-value: 0.0005	p-value: 0.016	p-value: 0.336

As can be deduced from Table 5-9, among the selected values, the one that most describes the disease individually is the CI3D. Figure 5-41 shows the least-squares regression line predicting the clinical diagnosis from the evaluated CI3D values. The correlation was tested with the Pearson coefficient at a significance level of $\alpha = 0.05$. The null hypothesis was formulated as a lack of correlation between CI3D and MSCS values. As a result, a correlation coefficient of 0.87 was obtained and, due to a value of p lower than 0.005, the non-correlation hypothesis was rejected.
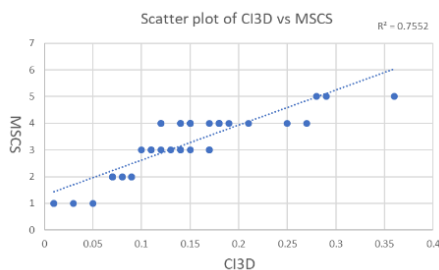
Figure 5-41 Scatter plot and regression line of CI3D values and MSCS values.

Furthermore, LDA analysis performed on CI3D values reached 70.7% of correspondence with clinical judgments.

To analyze which of the extracted parameters could improve the correspondences rate, a new LDA analysis was performed, with combination of inputs as described in Table 5-10.

According to the results presented in Table 5-10, the two most significant parameters are the Width, which, if combined with the CI3D allows to obtain a score of 87.8% (

Scatter plot and prediction model of CI3D vs Width
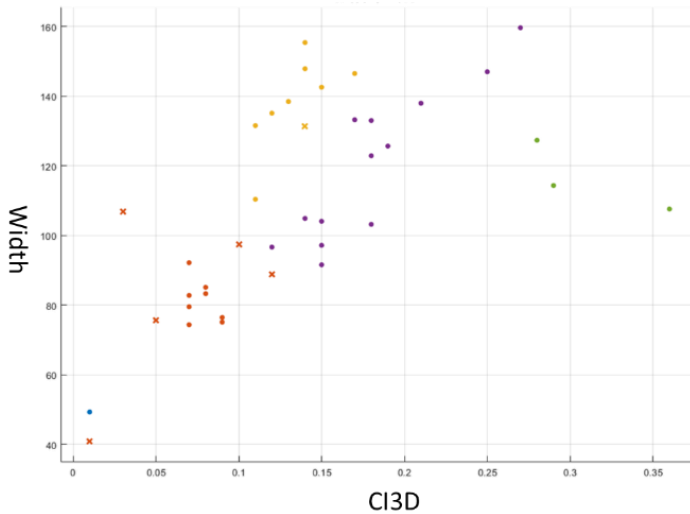
Figure **5-42**), followed by the Area.

Table 5-10 LDA analysis results with combined inputs.

CI3D	Width	Area	AI3D	EI3D
70.7%	56.1%	48.8%	46.3%	39.0%
	CI3D-Width	**CI3D-Area**	**CI3D-AI3D**	**CI3D-EI3D**
	87.8%	75.6%	73.2%	70.7%
		CI3D-Width-Area	**CI3D-Width-AI3D**	**CI3D-Width-EI3D**
		87.8%	85.2%	82.9%

The maximum percentage of precision achieved is of ~87%, which can be considered more than acceptable for the intended purpose. In addition, errors made by the classifier deviate from the assigned MSCS of only one class.

Scatter plot and prediction model of CI3D vs Width
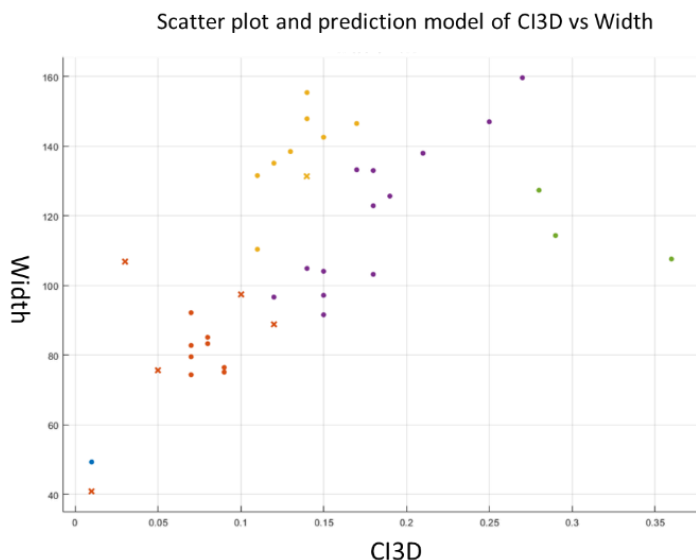
Figure 5-42 Scatter plot and LDA prediction results of CI3D vs Width: colors indicates the assigned class; dot values are correctly classified, "x" values are classification errors.

5.2.3. PC chest indices
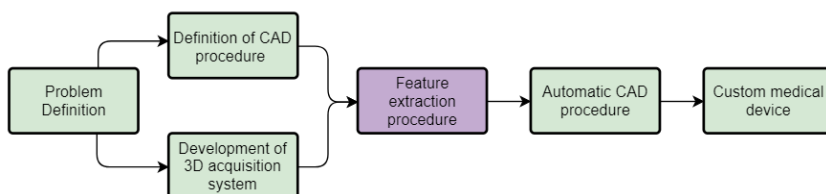
Figure 5-43 Diagram outlined to achieve the systematic realization of customized medical devices.

Inspired by the study of Ewert et al. [23] (mentioned in section 2) an External PC Index (EPCI), is here proposed. Such an index is computed on the chest surface as the perpendicular distance, on the sagittal plane, from the jugular notch to the point of maximum protrusion of the chest (JP), divided by the width of the chest area on the transversal plane (W). Accordingly (see Figure 5-44), the index is computed as follows:

$$EPCI = \frac{JP}{W} \qquad (34)$$

Figure 5-44 Indication of reference lengths and points for EPCI computation. In grey are depicted the parallel sections extracted to compute the chest's width (W).

The distance JP is normalized with the maximum chest's width W, since the chest excursion is naturally higher in adult patients, this value is normalized by the width of the patient, thus making the measure universal, in terms of patients age and size.

The measure is performed semi-automatically: the user only needs to define the position of the jugular notch, then a dedicated software automatically finds the point of maximum protrusion and compute the EI value. Only ~5% of PC patients are overweight [152], therefore the identification of the jugular notch on the 3D scan is usually done without difficulty. If this is not easily identifiable, however, the medical staff can, during the patient's visit, insert a visual reference, such as an adhesive or a hand-drawn marker, on the desired point, to make it easily recognizable.

In addition to the new index, the patients' chest scan was used to compute the Haller index adapted to Pectus Carinatum (as described in [153] and adapted to the external surfaces of the chest), to provide a comparison with the most widely used index. Since the acquisition system works with one camera facing the patient's chest, the point of maximum protrusion was considered with respect to the semi-rigid mattress plane upon which the patient is laying (P) (see Figure 5-45). The formula used to compute the adapted Haller index is:

$$HIpc = \frac{P}{W} \qquad (35)$$
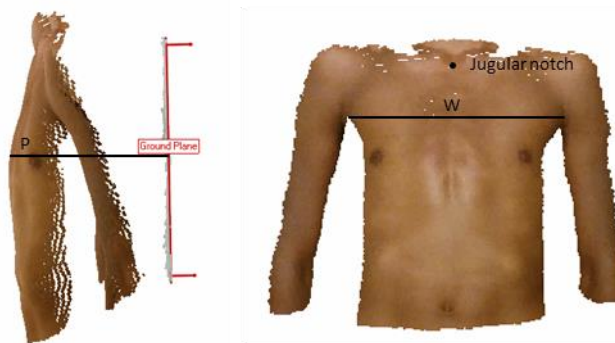
Figure 5-45 Indication of reference lengths and points for HIpc computation.

As mentioned, the system control software was used to acquire the patient's anatomy, and to compute the references necessary for the calculation of the indices. Specifically, the length W, corresponding to the maximum section of the chest, is calculated by sectioning the 3D data of the chest with a parallel sheaf of planes perpendicular to the direction of the semi-rigid mattress, 8 mm apart, and extracting the curve with the maximum length (see Figure 5-44 in grey). The length P corresponding to the highest point is instead obtained by extracting the point with maximum distance from the mattress. The only necessary input will be, as already said, the position of the jugular notch.

Patients
In collaboration with the Meyer Children's Hospital, 42 patients were collected: the 3D reconstruction of 21 normal controls (12 male, 9 female) were obtained from their CT scans and 21 3D scan of PC patients (16 male, 5 female) were collected using the described optical body scanner. Consent was obtained from all subjects involved and, when underage, consent was obtained from a parent or guardian. The overall age range varied between 6 to 60 years old. Nine additional patients (6 male, 3 female) were used to validate the proposed index. Among the pectus patients, 4 pediatric patients repeated the visit 3 times to study the progression of the deformation. The 4 patients selected for the pathology monitoring study are between 10 and 15 years old and all have started treatment with OCB (orthotic compression brace). For these patients, three visits were performed at a distance of about four months from each other.

Data Analysis
Figure 5-46 shows the results obtained computing the proposed EI index on both pectus patients and normal controls. A separation between the two classes has been found by means of a linear discriminant analysis [151], with an accuracy of the discrimination between PC patients and normal controls of 95.2%.

The method assumes that the conditional probability density functions are both normally distributed with mean and variance parameters $\mu_{control} = 0.14$, $\sigma_{control} = 0.03$ and $\mu_{pc} = 0.23$, $\sigma_{pc} = 0.035$ respectively. Under this assumption, the Bayes optimal

solution is to predict points as being from the second class if the log of the likelihood ratios is bigger than a threshold T, so that:

$$(\vec{x} - \overrightarrow{\mu_0})^T \Sigma_0^{-1}(\vec{x} - \overrightarrow{\mu_0}) + \ln|\Sigma_0| - (\vec{x} - \overrightarrow{\mu_1})^T \Sigma_1^{-1}(\vec{x} - \overrightarrow{\mu_1}) + \ln|\Sigma_1| > T \qquad (36)$$

As shown in Figure 5-46a the two datasets show a good separation, with a threshold between controls and PC patients set at a value of ~0.18.
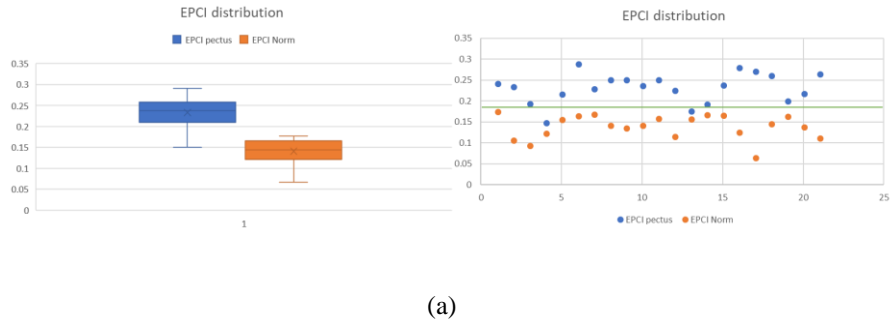
(a)
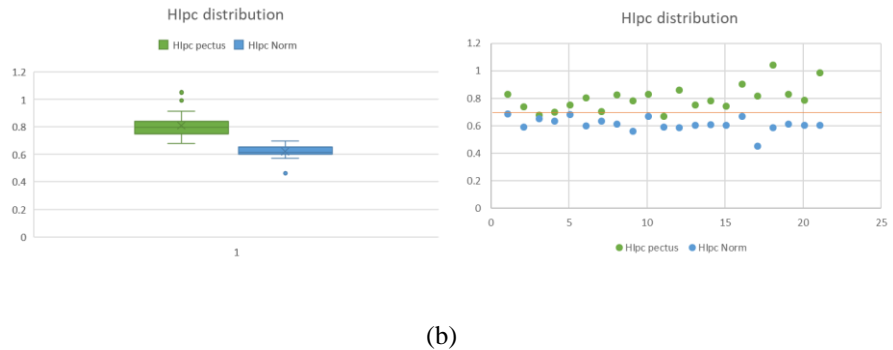
(b)

Figure 5-46 a) Distribution of obtained EPCI values with the corresponding threshold (in green) b) Distribution of obtained HIpc values with the corresponding threshold (in orange).

Furthermore, a 2-sample t-test was performed to compare the averages between the two groups and determine if there is a significant difference between them or if the observed difference is due instead to random chance. The t-test was computed with the Minitab software [145] and the null hypothesis (H0) of an equal distribution has been rejected with a p-value of 0.000, less than the α-level of 0.05, i.e. a 95% confidence interval.

The same test was conducted on the modified Haller index with $\mu_{control} = 0.62$ and $\sigma_{control} = 0.05$, for normal controls and $\mu_{pc} = 0.81$ and $\sigma_{pc} = 0.08$ for Pectus Carinatum patients. As shown in Fig. 4b the two datasets separate well, with a threshold between controls and PC patients set at a value of ~0.7.

This threshold value was also found by means of a linear discriminant analysis, and the accuracy of the discrimination between PC patients and normal controls is 92.9%.

Also, for the modified Haller index, the 2-sample t-test has brought to the rejection of the null hypothesis of an equal distribution with a p-value of 0.000.

The identified threshold on the proposed EPC Index was subsequently validated on nine additional patients. Figure 5-47 shows how these new cases are distributed compared to the previously found threshold.
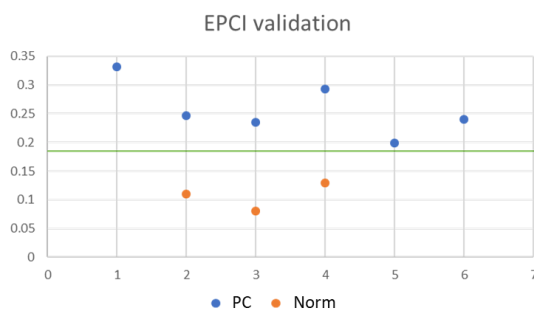
Figure 5-47 EPCI values of the 9 validation patients, compared with the previously found threshold (in green).

To verify that the two proposed indices are not two variations of the same measurement (if this were the case the introduction of EPCI would be a variation of HI) a linear correlation analysis was performed. With a value of $R^2 = 0.431$, a linear relationship between the two measurements was excluded, confirming that the proposed EPCI index assesses severity differently from the adapted HI index. Figure 5-48 reports the correlation between the values of the distances JP and P (values are expressed in mm), which are both divided by the length W for the computation of the two indices.
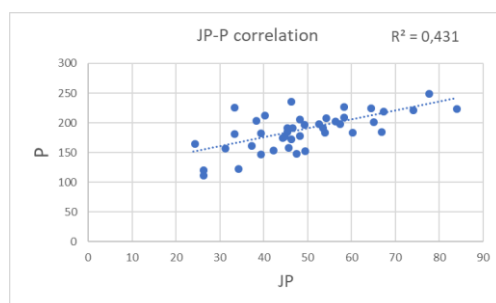
Figure 5-48 Scatter plot and regression line of P values (the distance point of maximum protrusion-mattress) and JP values (the distance jugular notch-point of maximum protrusion).

A second test was performed to assess the discriminatory capacity of the proposed index: four patients undergoing corrective treatment with OCB repeated the optical scan and EPCI measurements three times, at four months intervals. The data of the four patients relative to the three controls carried out in succession are reported in Table 5-11.

Table 5-11 Comparison between values of EPCI on four patients for progressive medical examination.

	EPCI at first visit	EPCI at second visit	EPCI at third visit
p1	0.23	0.18	0.16
p2	0.24	0.20	0.27
p3	0.18	0.18	0.16
p4	0.25	0.21	0.20

Patients 1 and 4 have made regular and continuous use of the orthosis and, in fact, show progressively decreasing values of EI. Patient 2 stopped treatment after the second check-up, showing a worsening of his condition and a consequent increase of EPCI at the next visit. Patient 3, on the other hand, began to diligently follow the corrective treatment from the second control onwards, significantly improving his situation and presenting dramatically lower EPCI values at the third assessment.

Finally, to validate the repeatability and stability of the EPCI calculation procedure, which involves the manual selection of the jugular notch by a user, a test was carried out by repeating the measurement three more times to validate if small variations of the distance JP leads to a stable value of EI. Figure 5-49 shows the distribution of PC patients and normal controls for the four measurements altogether.
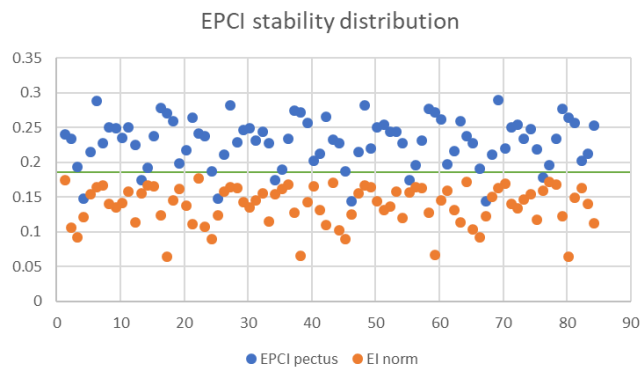
Figure 5-49 Scatter plot of EPCI values for repeatability test.

As a result, the accuracy score of the linear discriminant analysis remains rather stable with an accuracy value of 94.6%.

5.2.4. Automatic CAD procedure
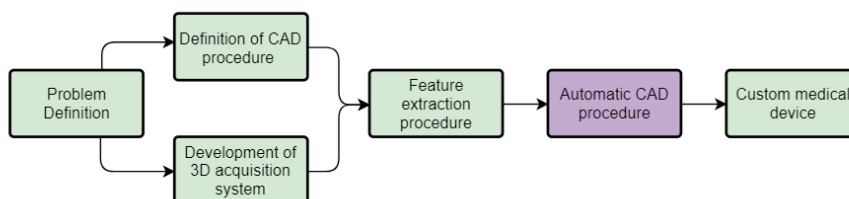
Figure 5-50 Diagram outlined to achieve the systematic realization of customized medical devices.

The main idea behind the semi-automatic generation of the personalized VB foresees the definition, directly by the medical staff, of the area to be treated (see Figure 5-51a). As already mentioned, the personalized VB may have dimensions and shape more suitable and comfortable for the patient; moreover, the VB will produce the required negative pressure, that lifts the sternum upwards, precisely in the caved-in area.

Obviously, to make the automatization possible, the area to be treated needs to be drawn directly in a CAD environment by using, for instance, a spline on the 3D chest geometry (see Figure 5-51b).

(a)   (b)

Figure 5-51 Area to be treated sketched on the chest by the medical staff (a) and the same area drew using a spline in a CAD environment (b).

In order to allow non-expert users (e.g. medical staff) to generate the personalized VB, a custom application (add-in) for Siemens® NX 11 CAD environment has been developed using Visual Basic programming language with NXOpen (a collection of API which allows through an open architecture the access to NX methods using well-known programming languages). The developed add-in is based on a procedural CAD modelling strategy and consists of the following 16 steps:

Step 1 -   (user guided) import the chest geometry (NURBS surfaces) obtained in the acquisition task. The geometry is properly oriented and the origin of the reference system is located in the deepest point of the pectus excavatum (with reference to the wall). This reference system is the one used for building the VB model;

Step 2 -   (automatic) a plane (Plane#1) parallel to the wall (W_Plane, corresponding to the xy plane in the global coordinate system) and passing through the point of the surface at the maximum distance from W_Plane is detected;

Step 3 -   (user guided) manually sketch a 2d spline (2Dspline) delimiting the area to be treated (see Figure 5-51b.) on Plane#1; an appositely developed GUI automatically opens the sketch using such a plane so as to avoid mistakes by the users on the correct positioning of the spline;

Step 4 -   (automatic) the spline defined in Step 3 is projected on the chest surface (3Dspline#1);

Step 5 -   (automatic) a plane (Plane#2) parallel to Plane#1 at a distance equal to $(1+\alpha)$ times the ratio between the area and the perimeter of the 3Dspline#1 is defined.

Step 6 -   (automatic) a circumference (Circ#1) on Plane#2, centered in the barycenter of the 2D spline and with a diameter so that its area is equal to β times the area defined by the 3Dspline#1 (see Figure 5-52a);

Step 7 -   (automatic) a volume loft (Loft#1) between 3Dspline#1 and Circ#1 (see Figure 5-52b) is built;

Step 8 -   (automatic) a plane (Plane#3) parallel to Plane#2 and placed at a distance equal to 8 mm, directed towards the chest is defined.

Step 9 -   (automatic) a circumference (Circ#2) on Plane#3 centered with Circ#1 and with a diameter equal to γ times the diameter of Circ#1 is drawn (see Figure 5-52c);

Step 10 -   (automatic) the external surface of the Loft#1 is offset to inside (5mm) thus defining a surface SLoft#1; The newly defined surface is then extended for 20mm in order to ensure it intersect with the chest geometry surface;

Step 11 -   (automatic) the intersection between SLoft#1 and the chest surface is evaluated so that to obtain a new 3D spline (3Dspline#2) (see Figure 5-52c);

Step 12 -   (automatic) a loft (Loft#2) between 3Dspline#2 and Circ#2 (see Figure 5-52c) is built;

Step 13 -   (automatic) the subtraction between Loft#1 and Loft#2 is carried out (see Figure 5-52d);

Step 14 -   (automatic) a circumference (Circ#3) on Plane#3 centered with Circ#1 and with a diameter equal to δ times the one defining Circ#1 is drawn (see Figure 5-52e);

Step 15 -   (automatic) a cut-extrusion of Circ#3 (6mm i.e. the thickness of the window that will be manufactured in transparent polycarbonate) is carried out;

Step 16 -   (automatic) a cut-extrusion of Circ#2 passing through the body is carried out (see Figure 5-52f).

(a)   (b)   (c)

(d)   (e)   (f)
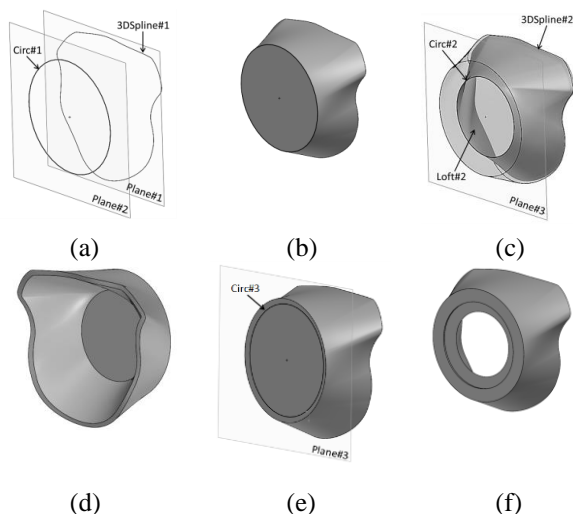
Figure 5-52 Some steps of the archetypal generation: (a) 3Dspline#1 obtained by projecting the 2D spline sketched by the medical staff onto the chest surface; (b) Loft#1 between 3Dspline#1 and Circ#1; (c) Loft#2 between 3Dspline#2 and Circ#2; (d) volume obtained by subtracting Loft#2 from Loft#1; (e) cut-extrusion using Circ#2 and Circ#3 and (f) final result.

The final result of the procedure described above consists of a 3D model of the "ring" that will be produced using silicone.

The procedural CAD modelling requires a number of parameters to be tuned (i.e. α, β, γ and δ) to work properly. On the basis of a trial and error approach by varying the chest surface and the 2Dspline, defined in Step 3, the optimal values of the parameter are listed in Table 5-12. Though appropriate for most of the case studies the procedure has been tested on, these tuned values may occasionally fail to produce correct geometries due to particular conformation of the patient's chest. Therefore, they may have to be manually adjusted in order to overcome the specific problem when it arises.

Table 5-12 Default parameters.

Parameter	Tuned Value
α	0.3
β	0.3
γ	0.7
δ	0.85

In order to finalize the personalized VB design, an additional part obtained by extruding Circ#3 (6mm) is performed so as to realize the inspection window. Obviously, in this step the new body has to be keep divided from the previously built one. Moreover, in such a body a small hole for a *G 1/8"* screw is also realized; the center position of the hole is located on a circumference whose diameter is equal to the half of the one of Circ#2. Such a hole is required in order to place the suction system.

The final model of the VB is shown in Figure 5-53.

Figure 5-53 Final result of the procedure.

Graphical User Interface

As mentioned above, one of the main aims of the devised procedure is to help medical staff in designing the personalized VB without the need of being aware on the procedural modelling strategy.

In other words, the medical staff is required only to choose the chest acquired with the Kinect and to sketch the 2D spline defining the contour of the area to be treated. Subsequently the devised application automatically builds the personalized VB. To this purpose a GUI, implemented as a new Tab of the Siemens NX 11 ribbon interface, has been developed (Figure 5-54). In detail the GUI is structured into a three-step procedure allowing to 1) import the chest surface, 2) draw the 2D spline) and 3) generate the personalized VB model.
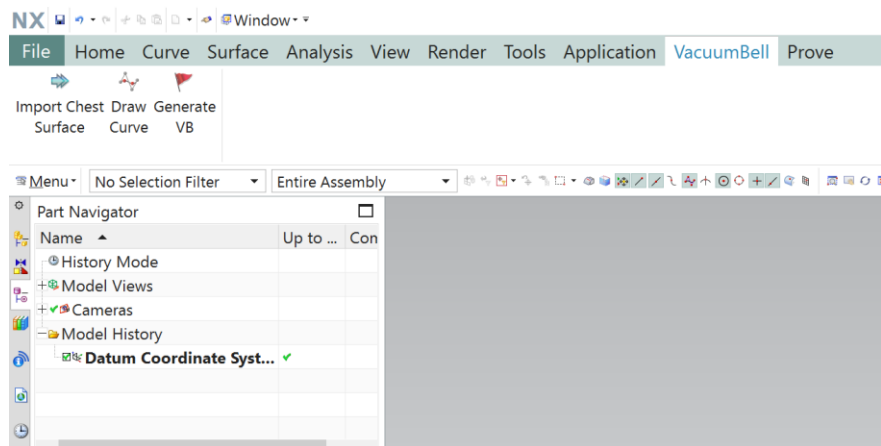
Figure 5-54 GUI implemented as a new Tab of the Siemens NX 11 ribbon interface.

The add-in is able to check and to prevent possible geometrical errors coming out during the generation of the VB model, with particular reference to the "hourglass effect" in loft generation (i.e. the erroneous loft reconstruction occurring when curves defining the loft are not consistently oriented). In fact, at the end of loft generation (e.g. Step 7) a pop-up window asks the user to confirm the correctness of the geometry (see Figure 5-55). In case the loft is not properly generated, the devised program automatically set the consistency of the two curves orientation.
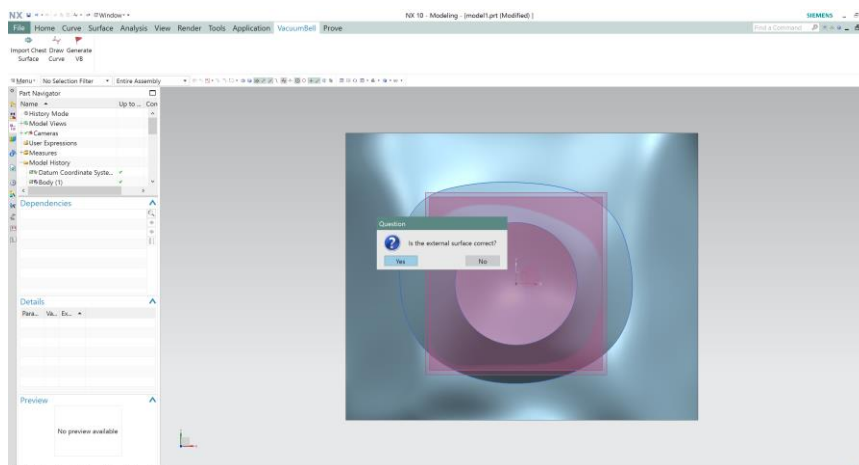
Figure 5-55 Pop-up window capable to correct possible "hourglass effect" in loft generation.

In the same way the user is asked to change parameters α, β, γ and δ, set to the default value of Table 5-12, if required. It has to be noticed that, while errors in loft generation are probable (but easy to be treated also by medical staff), the modification of α, β, γ and δ parameters is not straightforward for the medical staff. This is a drawback of the devised method. Fortunately in all the case studies the procedure has been tested on, no failure related to such parameters has been detected. It is however expected that in a real-life environment a few cases may occur. Therefore, a training for the medical staff will be required in the near future to confront with this issue.

Case Study

In order to verify the appropriateness of the developed procedure a number of case studies provided by the Children Meyer Hospital of Florence (Italy) have been analyzed. More in particular, a set of 30 different chest surfaces and different areas (i.e. splines) to be treated have been considered and personalized vacuum bells have been modelled. All subjects have been informed of the nature of the experimentation and written consent was obtained. The Ethical Guidelines of both the University of Florence and Italian law have been respected while performing the experimentation. Tests demonstrated the effectiveness of the method to adapt to different patients.

An exemplificative case study is discussed in this section to demonstrate the potential of the developed procedure. The case study refers to a patient (male, age 40 years) with a mild Pectus Excavatum to be treated with VB device. The entire reconstruction procedure was carried out by the medical staff without any help from the engineers. 3D acquisition of the patient chest has been performed in less than 1s and, using the developed interface the medical staff was able to process the point cloud in a few minutes. The CAD model of the personalized VB has been easily designed in less than 5 minutes. Finally, the CAD model has been exported in STL format to allow the manufacturing of a physical prototype using manufactured by casting the silicone into a mold (created starting from the STL file mentioned above) as shown in Figure 5-56.

Figure 5-56 Personalized VB.

5.3. Clinical application

Below are presented the methods of production and performance analysis of the system developed for the realization of the customized Vacuum Bell. It should be noted that the accuracy of the scanning system is not tested below, as this work uses a single camera to acquire the patient's chest and the used device, i.e. the Microsoft Kinect v2, has been widely characterized in the literature. In order to verify the validity of the clinical use of the proposed indexes, a data collection is planned. The collection is still ongoing and, given the size of the sample required, the analysis will end after the conclusion of this study.

5.3.1. Monitoring VB treatment
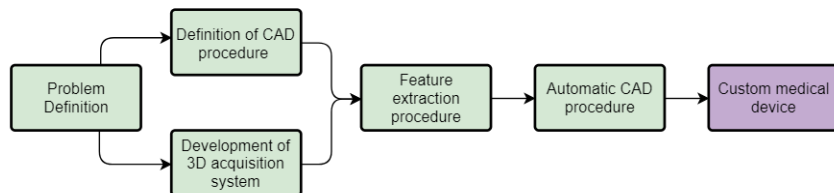
Figure 5-57 Diagram outlined to achieve the systematic realization of customized medical devices.

The conservative treatment through the application of a cup suction device, named vacuum bell (VB), is the only alternative nowadays to surgery for the correction of the Pectus Excavatum (PE). As said PE is the most frequent thoracic deformity with an incidence of 1 in 300-1000 births with a male/female ratio of about 4:1 [154–156] . The vacuum bell was initially introduced as a glass bell at the beginning of the last century [157] and was later replaced by a bowl-shaped device made of silicone, easier to apply and use, introduced by Ing. E. Klobe [158]. The VB body is made of a silicone ring and a transparent polycarbonate window (for inspection). Three different sizes (i.e. 16, 19 and 26 cm in diameter) as well as a model fitted for young women exist on the market. Inspired by Klobe's device, a number of alternatives have been proposed even tailored on the specific anatomy of a patient [159]. These devices achieve the elevation of the sternum by generating a negative pressure within them;

the short-term effects of this type of treatment have already been proved as promising [34, 160] especially when a precise medical guideline is followed by the patient.

Klobe, in the vacuum bell manual user, recommends patients to operate the device twice a day for 30 minutes for the first 4-6 weeks; later, the period of daily application of the VB can be varied according to the patient's outcomes at the discretion of the physician. Haecker et al. in [34, 160] carried out the measurement of the PE depth before and after the use of the VB by positioning the patient in a standardized supine position and by providing the depth using a designed scaled rod. Consequently, no real-time measurement during the treatment was encompassed. To overcome this limitation, Sesia et al. [161] proposed an electronic device for measuring the elevation of the sternum in relation to the depression within the VB (during the treatment). The device, called Distance and differential pressure measuring device (DPMD), allows to measure the negative differential pressure inside the VB and the relative elevation of the sternum during the application of the VB. The DPMD is placed on the upper part of the VB and does not alter its use. The device was designed to be compatible with the aforementioned different models of VB proposed by E. Klobe.

An alternative method for monitoring the chest elevation during the VB treatment is here presented. Unlike the work proposed by Sesia et al., chest uplift is here measured with an external optical device placed above the patient. Such a device can be used for any commercially available or self-produced vacuum bell under the only condition that the chest is visible through the transparent window. Moreover, the proposed system consists of a low-cost solution comprising a commercial RGB-D camera and an appositely devised user-friendly interface that can be exploited on any standard personal computer.

As mentioned above, the proposed method allows determining the elevation of the chest with respect to the pressure applied inside the vacuum bell.

In detail, the system encompasses two parallel modules providing a measurement of both pressure and elevation. To establish the pressure inside the suction device, a commercially available instrument was used, the PCE-P05 [162], which is linked to the pump tube by means of a junction (Figure 5-58). PCE-P05 is a portable digital pressure manometer for measuring the differential pressure in pneumatic systems, compressors, pumps, valves etc. Such a device visualizes the min, max and average values directly on a display and is supplied with real-time data recording capability with an adjustable interval from 1 second to 24 hours.

While the pressure values are recorded, the chest elevation is also registered. To calculate such an elevation, a dedicated software, that exploits a low-cost commercial depth sensor, has been developed. 3D laser scanners are not suitable for this application since it is needed a post processing step to add colors on the acquired 3D data [163]; on the contrary, the new generation consumer grade depth sensors are particularly suited to deal simultaneously with both 3D model and colors (needed to track the chest deepest point). In particular the Intel RealSense D415 [164] has been selected to acquire the depth elevation. As explained in section 4.4.1 the average error in depth evaluation at close distances (i.e. <500 mm), is equal to 2.11 mm that can be considered sufficient for this analysis. The device comprises both a color camera (RGB) and a depth camera system consisting of two infrared cameras and an infrared projector. The depth data are retrieved via active-stereo triangulation [54]. Moreover, the Intel RealSense D400 series is supported by the open-source multi-platform library, Intel RealSense SDK 2.0 [69], which allows the configuration of the camera with different internal settings (both for acquisition and post-processing), and in general facilitates the interface with the device.

To determine the sternum elevation, both RGB and depth streams are used. The point of maximum depression is automatically detected in the color image thanks to an appositely devised image-processing algorithm. At first a self-adhesive circular green-colored marker (Figure 5-59a) is manually applied to the patient chest at the point of maximum depression; then, the algorithm detects and tracks such marker using color separation: a green channel threshold is applied to the original image, thus obtaining a binary image in which the circle is identified through a Hough Transform which is a feature extraction algorithm widely used in digital image analysis [165]. It identifies objects with specified shapes by letting all edge pixels in the image "vote" and extract candidates with the highest votes. The classical Hough transform is associated with the identification of straight lines, but with some modification, the algorithm can be used to detect objects of arbitrary shapes (usually circles, ellipses) in an image. This detecting process allows to identify the pixels of the marker center within the RGB image.

Figure 5-58 Example of junction connecting PCE-P05 to vacuum bell.

The corresponding depth value (i.e. the 3D coordinates of the marker center) is then retrieved from the depth stream (Figure 5-59b). Since the RGB camera and the depth camera are intrinsically aligned in the D415 device, the pixel coordinates on the RGB image are directly related to the x,y and z values in the depth image.

As said, the aim is the estimation of the chest deepest point elevation during the VB treatment. Such an elevation value is assessed with respect to vertical direction which is orthogonal to the plane the patient is laid on. Therefore, it is necessary to assure the perpendicularity of the optical axis with respect to the mattress that will accommodate the patient. This is possible using the depth camera software [69] which provides the angle between the optical axis and a plane framed by the camera itself.

To perform the elevation measurement the camera is placed at an approximatively 300 mm distance from the patient's chest. This distance was chosen to obtain the necessary accuracy and to allow the algorithm to work on a small portion of the scene to make the marker search more robust. In this work, an appropriate support has been created to hold the camera at a fixed distance from the patient, mounted on the structure previously realized in [24] for the support of the chest severity measurement device.
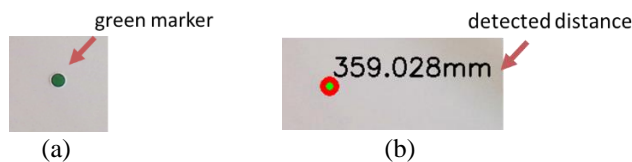
green marker   detected distance

(a)   (b)

Figure 5-59 Green colored marker (a), and output of the implemented algorithm (b).

The so-computed camera-marker distances are saved in a text file, in which the start time of the recording is also noted, to be subsequently aligned with the measured pressure values.

The system was, in the first instance, tested both on static and moving objects, as indicated below, then an initial analysis on 5 patients was carried out.

Preliminary accuracy tests

The first test conducted to evaluate the accuracy of the chest elevation measurement system examines a marker applied to a static calibrated object. After positioning the camera perpendicular to the plane containing the marker, the latter is progressively brought closer to the camera using calibrated blocks of 15 mm height. This allows to define a ground truth and then evaluate the difference between the real displacement of the marker and the one evaluated by the system. The test was repeated by placing the vacuum bell over the marker in order to test if the transparent window could cause alterations in the measurement (Figure 5-60).

300 mm
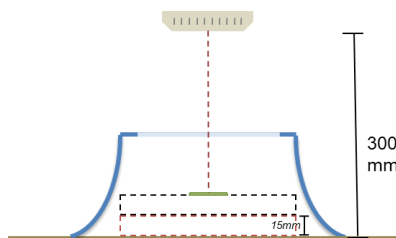
15mm

Figure 5-60 Acquisition setup for the first test: the marker is installed on a plane that is progressively brought closer to the camera by means of calibrated blocks with height 1.5 mm.

The graphs in Figure 5-61 show the trend of the absolute error with respect to the distance of the static object from the camera, defined as the absolute value of the difference between the real excursion and the one evaluated by the system, for the two cases, with (Figure 5-61a) and without vacuum bell (Figure 5-61b).

(a) (b)
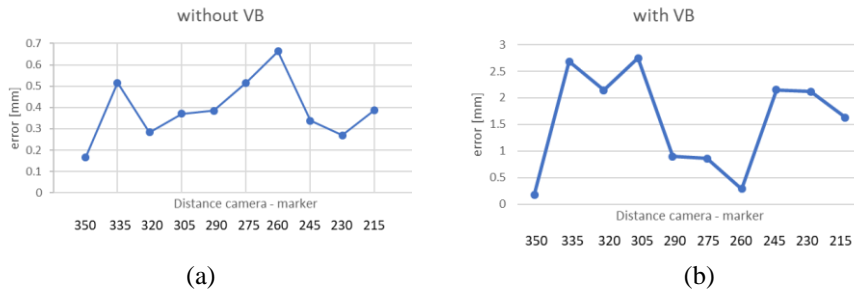
Figure 5-61 Results of static test computed as difference between real and measured marker excursion in absence of VB device (a) and with VB between the camera and the marker.

The average error evaluated without the VB device positioned between the marker and the camera is 0.38 mm with a standard deviation 0.14; the average error when the VB device is positioned between the marker and the camera is 1.56 mm with a standard deviation equal to 0.95. Both graphs show that the error does not depend on the camera-marker distance but oscillates around an average value. In addition, although the device's interference produces on average a higher deviation, a mean error of ~1 mm is considered more than acceptable for this application.

The second test studies the behavior of the measurement system in relation to an object in slow and continuous motion. To carry out this second experiment, the target is attached to an object positioned on a sliding linear guide (Figure 5-62). The object is progressively moved closer to the camera, to simulate the lifted chest, from a distance of 300 mm up to a distance of 200 mm. The entire shift takes place in one minute. Analogously to the first test, such a test was repeated by placing the vacuum bell between the camera and the marker.


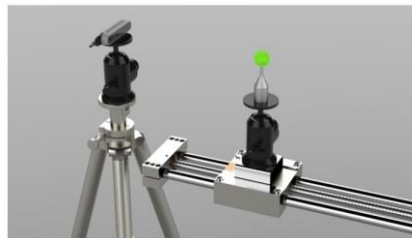**Figure 5-62 Acquisition setup for the second test: the marker is installed on a sliding linear guide and the camera is fixed frontally.**

The graphs in Figure 5-63 show the observed trend in blue and the linear continuous movement in orange. It is visible that the continuous movement of the marker is correctly recorded by the system, with few oscillations in case of the presence of the Vacuum Bell.
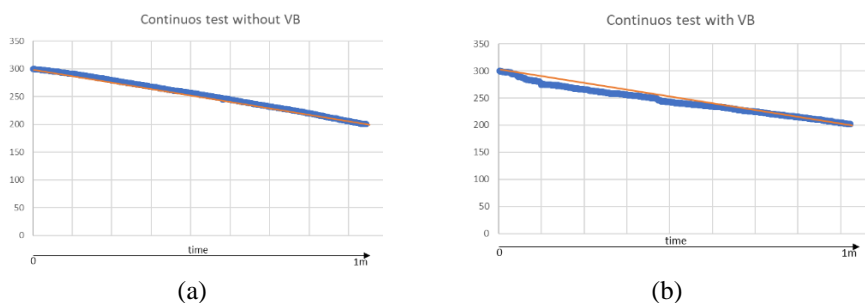
Figure 5-63 Results of dynamic test with and without VB between the marker and the camera (in blue). In orange the real movement of the marker on the linear guide.

Results

Five patients in pediatric age (patients' ages vary between 10 and 16 years old) have been selected, addressed by the specialized clinic for the deformations of the thoracic wall of the Meyer Children's Hospital.

The tests were carried out by placing the patient on a semi-rigid mattress and connecting the Vacuum Bell to the pressure monitoring device. The distance measuring system was then started, and the patient was asked to maintain the position for about 2 minutes. Figure 5-64 shows the placement and detection of the green marker during the experimental phase.
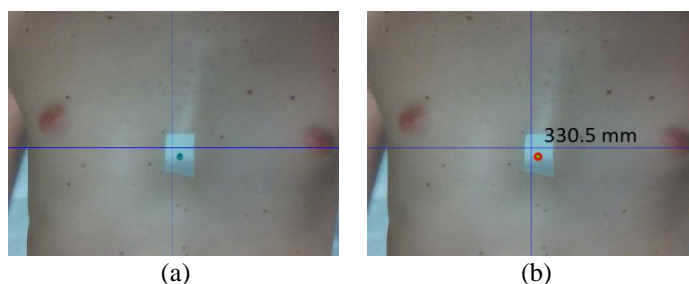
Figure 5-64 Example of placement (a) and automatic detection (b) of the green marker on patients during experimental phase.

The depression value inside the vacuum bell was set to a reference value defined by the clinician for each patient. It is important to notice that such a value is different for each patient and depends on age, cartilage strength, etc. During the recording time, when the pressure inside the device reached an excessively high value (e.g. -100 mbar), due to air leakage, it was brought back to the reference pressure. The pressure and distance values were then aligned accordingly to the recording start-time. Figure 5-65 shows the results obtained on two of the 5 patients which undergo the experimentation.
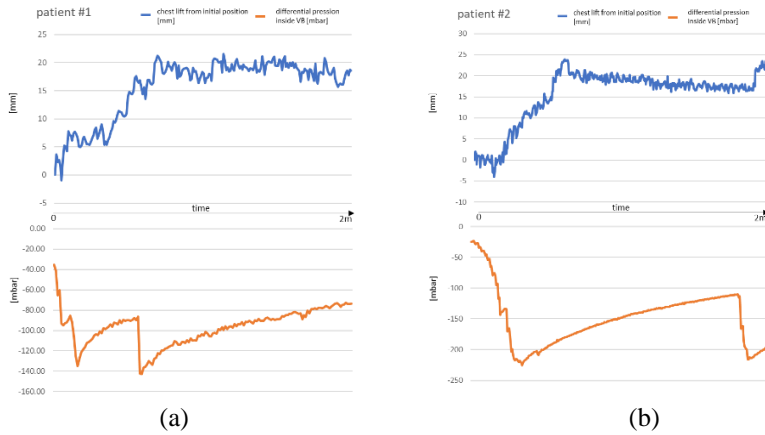
Figure 5-65 Results of the use of the proposed method on two patients. In blue the elevation of the chest, in orange the increasing negative pressure inside the VB.

In order to obtain a clear and comprehensible visualization of data, the first recorded depth value is considered as zero and the following values are reported in relation to it. In this way the graph shows how the chest is raised from a starting position.

The pressure values recorded for this first experimental test are consistent with the trial carried out in [161], for patients aged between 11 and 15 years.

5.3.2. Custom Vacuum Bell prototyping
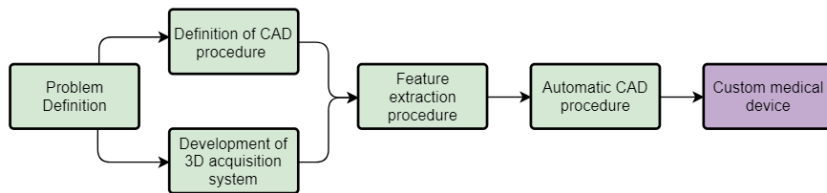
Figure 5-66 Diagram outlined to achieve the systematic realization of customized medical devices.

To test the creation of the Vacuum Bell physical model, once the Vacuum Bell 3D model has been designed, it was manufactured by pouring silicone into a properly created mould. The realization of the mould is detailed in the following.

Realization of the mould

To make the mould, a parallelepiped with dimensions equal to 205x205x107 was extruded to contain the Vacuum Bell completely and to leave enough material on the sides. From the solid thus obtained, the Vacuum Bell geometry was then subtracted. Subsequently, a division plane was determined to allow an easy draft and the parallelepiped was divided into two parts.

Silicone pouring is a rather complex process to be carried out without an autoclave; the risk is that the mould is not perfectly filled and imperfections such as air bubbles are formed. It was therefore decided to leave a part of the mould open (see Figure 5-67), to allow the

material to completely infiltrate even the most difficult parts. Four holes have also been created in the corners of the mould for centering the two halves.

The two parts thus generated are here called for simplicity, and to distinguish them, the full part (Figure 5-67 top) and the hollow part (Figure 5-67 bottom).

Figure 5-67 Full (top) and hollow (bottom) parts of the mould.

To keep the plexiglass in place and allow the silicone to fill the circular crown above it, a disc has been created to overlap the plexiglass during casting. The latter will be tightened by means of a threaded connection to the full part of the mould. The disc can be seen in Figure 5-68.
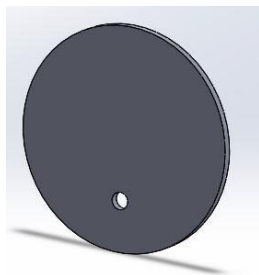
Figure 5-68 Disc that will be placed on top of the plexiglass during casting.

For a better understanding of the mould, exploded views and section views have been made (Figure 5-69).
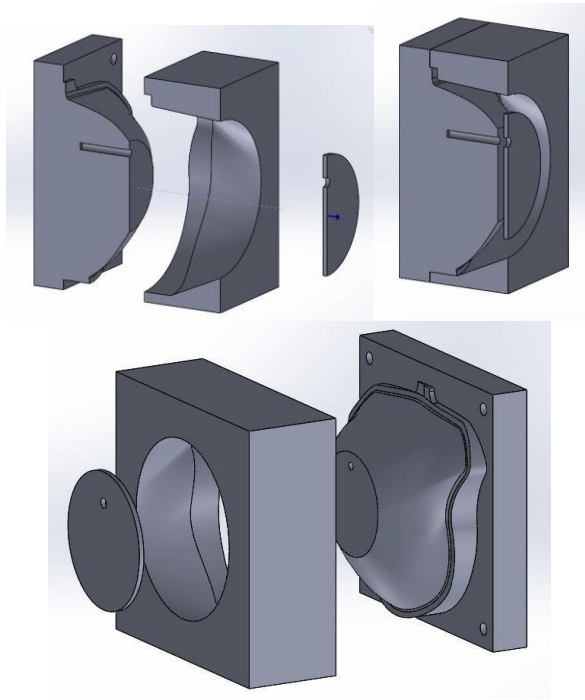
Figure 5-69 Sectional (top) and exploded (bottom) views of the complete mould.

The mould was made using two different production processes: the full half was created by additive production (EOS printer, Selective Laser Sintering), as well as the disc in Figure 5-68; the hollow half by milling a block of polyurethane. Figure 5-70 show the two machines used to create the mould: the 3D printer is an EOS Eosint P390, while the cutter is a Cielle Epsilon 100x200.

Figure 5-70 3D printer laser Eosint P390 (left); 3-axis milling cutter (right).

The decision to opt for two different types of production is due to several reasons. Laser sintering (3D printing) allows pieces to be made with even very complicated shapes and it is much less laborious for the operator to make the mould because it does not require the entire preparation phase of the tool path. It should be noted that, compared to the part of the mould made for additive production (Nylon powders), the part made by milling is much more rigid

because it is made of polyurethane, and thus allows a more robust product to be obtained. It would not be convenient, from an economic point of view, to create a completely full sintered model. In order to stiffen the structure, a series of ribs have been inserted as shown in Figure 5-71.
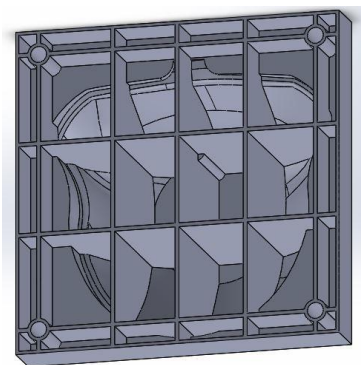
Figure 5-71 Nervations made in the full part of the model made in sintered.

The parts produced in additive production are also very porous because they are made from nylon powders. After having extracted and cleaned them of excess dust, it is necessary to use an epoxy resin to overcome the above problems. The resin, besides covering the porosity, further increases the stiffness of the piece. Figure 5-72 shows the full part of the mould and the disc made with a 3D printer on which the epoxy resin has been placed.

Figure 5-72 Sintered solid part (left) and disc (right) after epoxy resin coating.

It was also necessary to pass several coats of paint (in this case white) to cover the remaining porosity (few on the sintered pieces, many on the polyurethane piece) and to make the parts that will come into contact with the silicone as smooth as possible. Figure 5-73 shows the hollow part of the mould, made by milling, over which four coats of paint have been applied in order to cover the porosity of the polyurethane.

Figure 5-73 Hollow part in painted polyurethane.

As a last step it was necessary to apply about three coats of release agent on the parts that will come into contact with the silicone to facilitate the final detachment.

Once these operations have been completed, the mould is ready to accept the silicone. In Figure 5-74 on the left all the components of the mould are visible, while in Figure 5-74 right the mould is totally closed; it is possible to see that the plexiglass and the sintered disk have been fixed to the full part of the mould by means of a threaded connection.

Figure 5-74 Complete open mould (left) and complete closed mould (right).

Realization of Vacuum Bell

The main characteristic that silicone must have is its hardness, measured in Shore. This type of material can have different degrees of hardness to which correspond different densities: the greater the hardness, the greater the density. For silicones, increasing the density in turn reduces the elasticity of the material, which then deforms less. Stiffness and density are two important properties for Vacuum Bell because the second determines the weight (which must not be too high because the device must be worn for a few hours), while the first determines the deformability.

To choose the most suitable silicone, reference was made to the original Vacuum Bell, however, analyzing the description in the patent, is not indicated a single value but a range from 1 to 35 Shore A. Initially, a test specimen was made from 13 Shore A silicone, but this appeared to be less than that required for Vacuum Bell. The specimen is a bottom of a plastic glass and can be seen in Figure 5-75.

Figure 5-75 Test specimen made of 13 Shore A hardness silicone.

The characteristics of the silicone used are shown in Figure 5-76.

Figure 5-76 Characteristics of 13 Shore A hardness silicone.

The hardness was then increased to 22 Shore A (Figure 5-77).

Figure 5-77 Two-component silicone with a hardness of 22 Shore A.

It was therefore possible to perform the casting through the following steps:

1. initially the mould was closed by joining the two halves, while the two components of the silicone were mixed separately;

2. then the silicone was poured until the entire part of the Vacuum Bell underneath the plexiglass was filled;

3. then the plexiglass with the disc made in 3D print was inserted, tightening them to the full part by means of a screw;

4. finally, the remaining part of the silicone was poured;

5. the silicone was left to polymerize inside the mould for about 2 hours.

In Figure 5-78 the silicone is visible during the polymerization phase inside the mould.
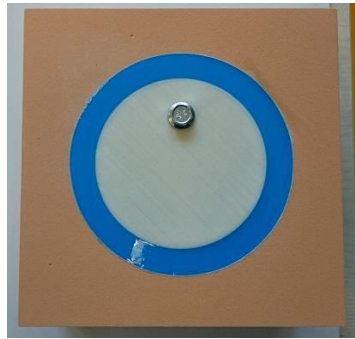
Figure 5-78 Silicone during polymerization inside the mould.

In Figure 5-79 it is possible to see the model realized; it is possible to notice, as hypothesized, the presence of air bubbles and some unavoidable imperfections in the absence of an autoclave.

Figure 5-79 Front and rear view of the Vacuum Bell made of 22 Shore A hardness silicone.

The result is an aesthetically good Vacuum Bell even if it appears stiffer and heavier than the reference one.

After consulting the doctors' opinion, it was therefore decided to make a test also with the 13 Shore A hardness silicone, which had initially been discarded.

The Vacuum Bell obtained in this way can be seen in Figure 5-80.

Figure 5-80 Front view of Vacuum Bell made of silicone with 22 Shore A.

This Vacuum Bell is more similar to the standard model in terms of stiffness and hardness than the first model made.

There are several air bubbles inside the piece, due to the fact that an autoclave was not used and that the area where the bubbles were released was rather small.

The surgeon on whom the vacuum bells were tested validated both devices created. Unfortunately, the problem of the biocompatibility of silicone remains open, a factor of considerable importance since the Vacuum Bell will have to be worn for a prolonged period of time. The silicone used in this work is not biocompatible; this choice is due to the fact that biocompatible silicones are more difficult to find and more expensive. It would therefore have been useless to use it in this first phase of experimentation.

Testing of Vacuum Bell prototypes

Once the prototypes of the Vacuum Bell have been produced, it is necessary to verify that they are working correctly and to evaluate their effectiveness with respect to the original one.

To verify the functioning of the Vacuum Bell, the plastic surgeon of Meyer was again used as patient, since the prototypes had been realized starting from a scan of his chest.

The Vacuum Bell used are 3: the original one, the prototype with silicone of hardness 13 Shore A (white) and the prototype with silicone of hardness 22 Shore A (blue).

First of all, it can be noted that the two personalized Vacuum Bell (identical in shape but composed of two different silicones) adhere perfectly to the chest, facilitating the adhesion of the instrument to the thoracic wall. Since this is an instrument that can be used for more than an hour and a half, it was decided not to use a standard fitting that connects the pump to the Plexiglass (as still happens in the original model), but a valve fitting, which allows the detachment of the pump with its tube (Figure 5-81b), facilitating its use. In Figure 5-81a it is possible to see the Vacuum Bell personalized with silicone with hardness 13 Shore A that acts on the surgeon's chest.

Figure 5-81 Vacuum Bell with 13 Shore A hardness silicone used by the surgeon with a valve connection that allows the tube to come off after generating the necessary depression.

The Konica Minolta Vivid scanner was used to analyze the changes in the thoracic surface.

The tests were carried out one week apart and without intermediate treatments, so as to ensure a return of the chest to its original condition.

With regard to the Vacuum Bell test with 22 Shore A hardness silicone, a leakage problem was found: during use, in fact, the depression created inside the instrument is not maintained due to a loss of air, making it impossible to achieve the suction effect necessary to improve the patient's chest.

This could be due to the fact that the Plexiglass is not bonded to silicone, as is the case of the standard Vacuum Bell. This did not happen with the other prototype of Vacuum Bell probably since it is made of a more flexible silicone and the part in contact with the plexiglass deforms as a result of the depression but without detaching itself from the body.

The tests were carried out as follows: the surgeon was scanned before the application of Vacuum Bell and 15 minutes after its use, both for the standard and for the customized one.

As an example, the images of the processing of the scan after the use of the Vacuum Bell with silicone of hardness 13 Shore A is shown.

Once the acquisition was carried out, the scans were processed to isolate the frontal area of the chest, where the Vacuum Bell is effective, as shown in Figure 5-82.
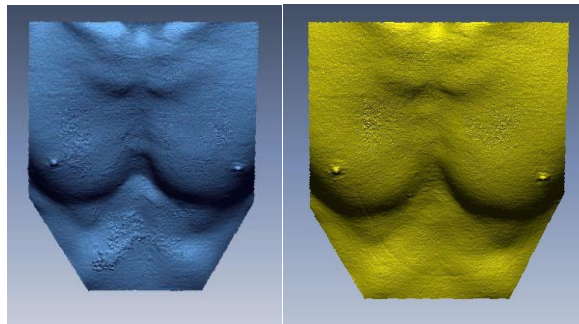
Figure 5-82 Isolation of the thoracic part of the scan carried out before (left, blue) and after (right, yellow) the use of Vacuum Bell with silicone of hardness 13 Shore A.

Subsequently it is performed a comparison between the scan before and after the use of the Vacuum Bell. In order to proceed, it was necessary first to align the two scans (Figure 5-83).
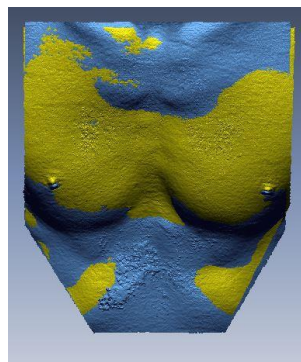
Figure 5-83 Alignment of the scan after use of the Vacuum Bell with 13 Shore A hardness silicone with the scan before application.

Once aligned it is possible to evaluate the difference introduced by the use of Vacuum Bell through the command Mesh Deviation: the software compares the two scans providing a visual map that reproduces the distance between them. In the following figure it is possible to see the result obtained for the standard Vacuum Bell and for the one with silicone of hardness 13 Shore A (Figure 5-84). The areas in red and dark blue are those with the greatest distance, positive and negative respectively.
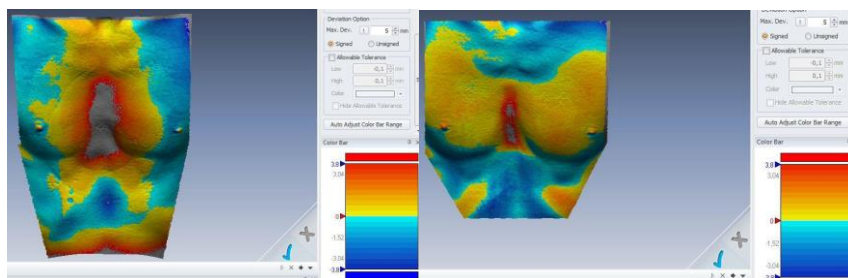
Figure 5-84 Comparison of the scan before and after 15 minutes of using the standard Vacuum Bell (left). Comparison of the scan before and after 15 minutes of using the Vacuum Bell with silicone of hardness 13 Shore A (right).

In both cases it is possible to notice a red area in the middle of the chest, where Vacuum Bell acts. The standard one has a greater effect, which can be due to many reasons, including a slight loss of air in the custom one, the different area on which the two instruments act, the different volume they occupy, the different stiffness of the material.

Beyond the experimental tests, however, it is important to evaluate the opinion of the specialist subjected to the treatment. The custom Vacuum Bels has been found to be well made and, above all, very comfortable to use: in fact, after 15 minutes (test time) the feeling was that the custom Vacuum Bells had a slightly weaker effect than the standard one, but a considerable advantage in terms of comfort.

6. Conclusions

In line with recent approaches to personalized medicine where 3D technologies are rapidly becoming a new concept of treatment based on the ability to model patient-specific devices, this work intended to analyze the life cycle of a customized device aiming at a systematized production of custom devices. The common approach for the realization of custom devices involves the digitization of the anatomy of interest, followed by the modeling of the device and the manufacture through additive techniques. This workflow can be difficult to follow for non-expert users in the field of CAD modeling and cannot be applied in common clinical practice, given the time and capabilities it requires.

With the idea of providing tools that can be introduced into clinical practice and used directly by hospital staff, the life cycle of the customized medical product has been analyzed, outlining a framework that defines the implementation phases of a customized treatment system. The phases described by the framework are: definition and analysis of the problem, definition of a robust and repeatable CAD procedure to realize the model of the customized device, development of a 3D acquisition system of the anatomy of interest, extraction of characteristics of each anatomy necessary to automate the procedure of realization of the customized CAD model, definition of an automatic or semi-automatic procedure of device modeling, production and validation of the device.

The framework has been tested on two pilot cases, identified in collaboration with the pediatric hospital Meyer medical staff within the T3Ddy joint laboratory: 1) the systematic production of orthotics for children for the treatment of bone fractures of the upper limbs; 2) the development of tools for the treatment of malformations of the thoracic cage.

It should be noted that the implementation of the two pilot cases was carried out following the steps described using common design and implementation tools.

As far as the first case is concerned, the work has been carried out following the described framework, therefore the first step has been the delineation of the characteristics of the system, intended both as an acquisition device and as a medical device. The anatomy of interest was then investigated to define the dimensions of the arm scanner and to define the characteristics of the orthosis (e.g. stiffness, shape, etc.). Subsequently, the phases of the scanner's design and the definition of the procedure for the realization of the orthosis, based on the acquired 3D data, were examined in depth. The final result was a scanner that uses eight low-cost depth sensors to create the 360° model of the arm. The scanner acquires the anatomy in about 2.5 seconds and is managed by a specially developed software. The procedure for the realization of the orthosis was defined and validated, before moving on to the study for automation, which led to the expansion of the functions of the scanner management software and the creation of an automatic CAD procedure. The time required by the semi-automatic feature extraction procedure is about 5 minutes and for the realization of the CAD model of the orthosis it is about 2 minutes in total.

The analysis and validation of the system for the modeling of custom orthoses has confirmed the adequacy of the product and has highlighted the main critical issues. Subsequently, the infrastructure was updated taking into account what emerged during the

validation phase. As a consequence, a new scanner was created that is able to acquire the anatomy in a fraction of a second and the interface with the acquisition software was improved, simplifying some critical aspects.

In conclusion, it can be said that a state of the art system has been created that allows to contemplate a new scenario in which, upon the arrival of a sick patient, the hospital staff is able to independently and quickly scan the anatomy to be treated and create the CAD model of the orthosis, then move on to printing and application of the corrective device.

The defined framework was also applied to the second pilot case, the treatment of thoracic malformations, following in order the identified phases. In the first phase, the characteristics of the acquisition system and the device were outlined, which were much less restrictive than in the previous case, mainly due to the fact that it is not necessary to acquire the 360° thorax anatomy in order to achieve the pre-established objectives. Following some experiments about the best position of the patient to obtain repeatable measurements, the acquisition scanner was created using a single commercial optical device placed in front of the patient's chest, coupled also in this case by a specifically developed management software. The acquisition takes place in a fraction of a second. At the same time, a procedure has been defined for the creation of personalized Vacuum Bell for the treatment of the Pectus Excavatum. An important step was the update of the software such to extract some severity indices from the scan chest. These indices are fundamental to follow the progression of the pathology over time, therefore to be able to ascertain the functioning of the therapy and give the patient a quantitative feedback. The extracted indices have been validated with respect to the opinion of the specialized physician. From the processing of the scan are also extracted the information used by the semi-automatic CAD procedure for the realization of Vacuum Bell.

In the final phase, a prototype of Vacuum Bell and a chest lift monitoring system were created, which can be used to clinically test the device.

Also in this second case it can be said that a state of the art system has been realized that allows to have an easy to use outpatient aid that allows the hospital staff to make new (non-invasive) measurements and to produce a personalized medical device without the external intervention of experts.

Acknowledgements

Bibliography

1. Javaid, M., Haleem, A.: Additive manufacturing applications in medical cases: A literature based review. Alexandria J. Med. 54, 411–422 (2018). https://doi.org/10.1016/j.ajme.2017.09.003.
2. Hazeveld, A., Huddleston Slater, J.J.R., Ren, Y.: Accuracy and reproducibility of dental replica models reconstructed by different rapid prototyping techniques. Am. J. Orthod. Dentofacial Orthop. 145, 108–15 (2014). https://doi.org/10.1016/j.ajodo.2013.05.011.
3. D'Urso, P.S., Barker, T.M., Earwaker, W.J., Bruce, L.J., Atkinson, R.L., Lanigan, M.W., Arvier, J.E., Effeney, D.J.: Stereolithographic biomodelling in cranio-maxillofacial surgery: A prospective trial. J. Cranio-Maxillo-Facial Surg. 27, 30–37 (1999). https://doi.org/10.1016/S1010-5182(99)80007-9.
4. Zopf, D.A., Hollister, S.J., Nelson, M.E., Ohye, R.G., Green, G.E.: Bioresorbable airway splint created with a three-dimensional printer. N. Engl. J. Med. 368, 2043–5 (2013). https://doi.org/10.1056/NEJMc1206319.
5. Schievano, S., Migliavacca, F., Coats, L., Khambadkone, S., Carminati, M., Wilson, N., Deanfield, J.E., Bonhoeffer, P., Taylor, A.M.: Percutaneous pulmonary valve implantation based on rapid prototyping of right ventricular outflow tract and pulmonary trunk from MR data. Radiology. 242, 490–7 (2007). https://doi.org/10.1148/radiol.2422051994.
6. Kim, M.S., Hansgen, A.R., Carroll, J.D.: Use of rapid prototyping in the care of patients with structural heart disease. Trends Cardiovasc. Med. 18, 210–6 (2008). https://doi.org/10.1016/j.tcm.2008.11.001.
7. Kim, M.S., Hansgen, A.R., Wink, O., Quaife, R.A., Carroll, J.D.: Rapid prototyping: a new tool in understanding and treating structural heart disease. Circulation. 117, 2388–94 (2008). https://doi.org/10.1161/CIRCULATIONAHA.107.740977.
8. Ebert, L.C., Thali, M.J., Ross, S.: Getting in touch--3D printing in forensic imaging. Forensic Sci. Int. 211, e1-6 (2011). https://doi.org/10.1016/j.forsciint.2011.04.022.
9. Werner, H., dos Santos, J.R.L., Fontes, R., Daltro, P., Gasparetto, E., Marchiori, E., Campbell, S.: Additive manufacturing models of fetuses built from three-dimensional ultrasound, magnetic resonance imaging and computed tomography scan data. Ultrasound Obstet. Gynecol. 36, 355–61 (2010). https://doi.org/10.1002/uog.7619.
10. Schievano, S., Sebire, N.J., Robertson, N.J., Taylor, A.M., Thayyil, S.: Reconstruction of fetal and infant anatomy using rapid prototyping of post-mortem MR images. Insights Imaging. 1, 281–286 (2010). https://doi.org/10.1007/s13244-010-0028-5.
11. Structure Sensor - 3D scanning, augmented reality, and more for mobile devices, https://structure.io/, last accessed 2018/12/18.

12. Holey, realizzazione di tutori ortopedici per i vostri pazienti, https://holey.it/, last accessed 2018/05/04.

13. Professional 3D Scanners | Artec 3D | Best 3D Scanning Solutions, https://www.artec3d.com, last accessed 2018/05/04.

14. Evill, J.: Cortex - Evill, http://www.evilldesign.com/cortex, last accessed 2018/05/04.

15. Osteoid, http://www.osteoid.com/, last accessed 2018/05/04.

16. Lin, H., Shi, L., Wang, D.: A rapid and intelligent designing technique for patient-specific and 3D-printed orthopedic cast. 3D Print. Med. 2, 4 (2015). https://doi.org/10.1186/s41205-016-0007-7.

17. Kim, H., Jeong, S.: Case study: Hybrid model for the customized wrist orthosis using 3D printing. J. Mech. Sci. Technol. 29, 5151–5156 (2015). https://doi.org/10.1007/s12206-015-1115-9.

18. Palousek, D., Rosicky, J., Koutny, D., Stoklásek, P., Navrat, T.: Pilot study of the wrist orthosis design process. Rapid Prototyp. J. 20, 27–32 (2014). https://doi.org/10.1108/RPJ-03-2012-0027.

19. Chen, Y.-J., Lin, H., Zhang, X., Huang, W., Shi, L., Wang, D.: Application of 3D–printed and patient-specific cast for the treatment of distal radius fractures: initial experience. 3D Print. Med. 3, 11 (2017). https://doi.org/10.1186/s41205-017-0019-y.

20. Li, J., Tanaka, H.: Rapid customization system for 3D-printed splint using programmable modeling technique - a practical approach. 3D Print. Med. 4, 5 (2018). https://doi.org/10.1186/s41205-018-0027-6.

21. Martinez-Ferro, M.: Indexes for Pectus Deformities. In: Chest Wall Deformities and Corrective Procedures. pp. 35–60. Springer International Publishing, Cham (2016). https://doi.org/10.1007/978-3-319-23968-2_7.

22. Sujka, J.A., St. Peter, S.D.: Quantification of pectus excavatum: Anatomic indices. Semin. Pediatr. Surg. 27, 122–126 (2018). https://doi.org/10.1053/j.sempedsurg.2018.05.006.

23. Ewert, F., Syed, J., Wagner, S., Besendoerfer, M., Carbon, R.T., Schulz-Drost, S.: Does an external chest wall measurement correlate with a CT-based measurement in patients with chest wall deformities? J. Pediatr. Surg. 52, 1583–1590 (2017). https://doi.org/10.1016/j.jpedsurg.2017.04.011.

24. Uccheddu, F., Ghionzoli, M., Volpe, Y., Servi, M., Furferi, R., Governi, L., Facchini, F., Lo Piccolo, R., McGreevy, K.S., Martin, A., Carfagni, M., Messineo, A.: A Novel Objective Approach to the External Measurement of Pectus Excavatum Severity by Means of an Optical Device. Ann. Thorac. Surg. (2018). https://doi.org/10.1016/J.ATHORACSUR.2018.02.024.

25. Bliss, D.P., Vaughan, N.A., Walk, R.M., Naiditch, J.A., Kane, A.A., Hallac, R.R.: Non-Radiographic Severity Measurement of Pectus Excavatum. J. Surg. Res. 233, 376–380 (2019). https://doi.org/10.1016/j.jss.2018.08.017.

26. Sarwar, Z.U., DeFlorio, R., O'Connor, S.C.: Pectus Excavatum: Current Imaging Techniques and Opportunities for Dose Reduction. Semin. Ultrasound, CT MRI. 35, 374–381 (2014). https://doi.org/10.1053/j.sult.2014.05.003.

27. Lain, A., Garcia, L., Gine, C., Tiffet, O., Lopez, M.: New Methods for Imaging Evaluation of Chest Wall Deformities. Front. Pediatr. 5, 257 (2017). https://doi.org/10.3389/fped.2017.00257.

28. Poncet, P., Kravarusic, D., Richart, T., Evison, R., Ronsky, J.L., Alassiri, A., Sigalet, D.: Clinical impact of optical imaging with 3-D reconstruction of torso topography in common anterior chest wall anomalies. J. Pediatr. Surg. 42, 898–903 (2007).

https://doi.org/10.1016/j.jpedsurg.2006.12.070.

29. Szafer, D., Taylor, J.S., Pei, A., de Ruijter, V., Hosseini, H., Chao, S., Wall, J.: A Simplified Method for Three-Dimensional Optical Imaging and Measurement of Patients with Chest Wall Deformities. J. Laparoendosc. Adv. Surg. Tech. A. 29, 267–271 (2019). https://doi.org/10.1089/lap.2018.0191.

30. Taylor, J.S., Madhavan, S., Szafer, D., Pei, A., Koppolu, R., Barnaby, K., Wall, J.K., Chao, S.D.: Three-Dimensional Optical Imaging for Pectus Excavatum Assessment. Ann. Thorac. Surg. 108, 1065–1071 (2019). https://doi.org/10.1016/j.athoracsur.2019.04.074.

31. Boyd, A.S., Benjamin, H.J., Asplund, C.: Principles of casting and splinting. Am. Fam. Physician. 79, 16–22 (2009).

32. Chudnofsky CR, B.S.: Splinting techniques. Roberts JR, Hedges JR, Chanmugam AS, eds. Clin. Proced. Emerg. Med. 4th ed. Ph, 989 (2004).

33. Jung, J., Chung, S.H., Cho, J.K., Park, S.J., Choi, H., Lee, S.: Brace compression for treatment of pectus carinatum. Korean J. Thorac. Cardiovasc. Surg. 45, 395–400 (2012). https://doi.org/10.5090/kjtcs.2012.45.6.396.

34. Haecker, F.-M., Sesia, S.: Vacuum bell therapy. Ann. Cardiothorac. Surg. 5, 440–449 (2016). https://doi.org/10.3978/11506.

35. Fried, S.: Splint and or Method of Making Same. (2007).

36. Ootsubo, K., Kobayashi, K.G., Yamaguchi, K.: A Development of Tailor-Made Design System for Arm Brace. Comput. Aided. Des. Appl. 11, 526–532 (2014). https://doi.org/10.1080/16864360.2014.902682.

37. Lochner, S.J., Huissoon, J.P., Bedi, S.S.: Parametric design of Custom foot orthotic model. Comput. Aided. Des. Appl. 9, 1–11 (2012). https://doi.org/10.3722/cadaps.2012.1-11.

38. Abran, A., Khelifi, A., Suryn, W., Seffah, A.: Usability meanings and interpretations in ISO standards. In: Software Quality Journal. pp. 325–338. Kluwer Academic Publishers (2003). https://doi.org/10.1023/A:1025869312943.

39. Jokela, T., Iivari, N., Matero, J., Karukka, M.: The standard of user-centered design and the standard definition of usability. Presented at the (2003). https://doi.org/10.1145/944520.944525.

40. Gordon, C.: Anthropometric data, http://www.theergonomicscenter.com/graphics/Workstation Design/Tables.pdf, last accessed 2018/05/04.

41. Kinect - Windows app development, https://developer.microsoft.com/en-us/windows/kinect, last accessed 2019/06/17.

42. Intel® RealSense™ Technology, http://www.intel.com/content/www/us/en/architecture-and-technology/realsense-overview.html, last accessed 2018/05/04.

43. Chen, C., Liu, K., Kehtarnavaz, N.: Real-time human action recognition based on depth motion maps. J. Real-Time Image Process. 12, 155–163 (2016). https://doi.org/10.1007/s11554-013-0370-1.

44. Wang, R., Choi, J., Medioni, G.: Accurate full body scanning from a single fixed 3D camera. In: Proceedings - 2nd Joint 3DIM/3DPVT Conference: 3D Imaging, Modeling, Processing, Visualization and Transmission, 3DIMPVT 2012. pp. 432–439 (2012). https://doi.org/10.1109/3DIMPVT.2012.57.

45. Tong, J., Zhou, J., Liu, L., Pan, Z., Yan, H.: Scanning 3D full human bodies using kinects. IEEE Trans. Vis. Comput. Graph. 18, 643–650 (2012).

https://doi.org/10.1109/TVCG.2012.56.

46.   Furferi, R., Governi, L., Uccheddu, F., Volpe, Y.: A RGB-D based instant body-scanning solution for compact box installation. Lect. Notes Mech. Eng. 819–828 (2017). https://doi.org/10.1007/978-3-319-45781-9_82.

47.   ROMER Absolute Arm | Hexagon Manufacturing Intelligence, https://www.hexagonmi.com/products/portable-measuring-arms/romer-absolute-arm, last accessed 2019/10/26.

48.   Konica Minolta Range 7 3D Scanner | NeoMetrix, http://3dscanningservices.net/konica-minolta-3d-digitizers/konica-minolta-range-7-3d-scanner/, last accessed 2019/10/26.

49.   AICON 3D Systems | Hexagon Manufacturing Intelligence, https://www.hexagonmi.com/it-IT/about-us/about-hexagon-manufacturing-intelligence/our-history/aicon-3d-systems-history, last accessed 2019/10/26.

50.   Oikonomidis, I., Kyriazis, N., Argyros, A.A.: Efficient Model-based 3D Tracking of Hand Articulations using Kinect.

51.   Cai, Q., Gallup, D., Zhang, C., Zhang, Z.: 3D deformable face tracking with a commodity depth camera. In: Lecture Notes in Computer Science (including subseries Lecture Notes in Artificial Intelligence and Lecture Notes in Bioinformatics). pp. 229–242 (2010). https://doi.org/10.1007/978-3-642-15558-1_17.

52.   Silberman, N., Fergus, R.: Indoor scene segmentation using a structured light sensor. In: Proceedings of the IEEE International Conference on Computer Vision. pp. 601–608 (2011). https://doi.org/10.1109/ICCVW.2011.6130298.

53.   Lachat, E., Macher, H., Landes, T., Grussenmeyer, P.: Assessment and Calibration of a RGB-D Camera (Kinect v2 Sensor) Towards a Potential Use for Close-Range 3D Modeling. Remote Sens. 7, 13070–13097 (2015). https://doi.org/10.3390/rs71013070.

54.   Zanuttigh, P., Marin, G., Dal Mutto, C., Dominio, F., Minto, L., Cortelazzo, G.M.: Operating Principles of Structured Light Depth Cameras. In: Time-of-Flight and Structured Light Depth Cameras. pp. 43–79. Springer International Publishing, Cham (2016). https://doi.org/10.1007/978-3-319-30973-6_2.

55.   Micro-mirrors from STMicroelectronics Provide Precision in Perceptual Computing, https://www.st.com/content/st_com/en/about/media-center/press-item.html/p3657.html, last accessed 2019/10/26.

56.   Beraldin, J.-A., Mackinnon, D., Cournoyer, L.: Metrological characterization of 3D imaging systems: progress report on standards developments. https://doi.org/10.1051/metrology/20150013003.

57.   VDI/VDE 2634-1 BLATT1 : 2002 | OPTICAL 3D MEASURING SY... | SAI Global, https://infostore.saiglobal.com/en-gb/standards/vdi-vde-2634-1-2002-1115310_SAIG_VDI_VDI_2590578/, last accessed 2019/10/26.

58.   Zhang, Z.: Iterative Point Matching for Registration of Free-Form Curves and Surfaces. (1994).

59.   Gonzalez-Jorge, H., Rodríguez-Gonzálvez, P., Martínez-Sánchez, J., González-Aguilera, D., Arias, P., Gesto, M., Díaz-Vilariño, L.: Metrological comparison between Kinect I and Kinect II sensors. Measurement. 70, 21–26 (2015). https://doi.org/10.1016/J.MEASUREMENT.2015.03.042.

60.   Wasenmüller, O., Stricker, D.: Comparison of kinect v1 and v2 depth images in terms of accuracy and precision. In: Lecture Notes in Computer Science (including subseries Lecture Notes in Artificial Intelligence and Lecture Notes in Bioinformatics). pp. 34–45. Springer Verlag (2017). https://doi.org/10.1007/978-3-319-54427-4_3.

61. Zennaro, S., Munaro, M., Milani, S., Zanuttigh, P., Bernardi, A., Ghidoni, S., Menegatti, E.: Performance evaluation of the 1st and 2nd generation Kinect for multimedia applications. In: Proceedings - IEEE International Conference on Multimedia and Expo. IEEE Computer Society (2015). https://doi.org/10.1109/ICME.2015.7177380.

62. Khoshelham, K., Elberink, S.O., Khoshelham, K., Elberink, S.O.: Accuracy and Resolution of Kinect Depth Data for Indoor Mapping Applications. Sensors. 12, 1437–1454 (2012). https://doi.org/10.3390/s120201437.

63. Dutta, T.: Evaluation of the Kinect^{TM} sensor for 3-D kinematic measurement in the workplace. Appl. Ergon. 43, 645–9 (2012). https://doi.org/10.1016/j.apergo.2011.09.011.

64. Menna, F., Remondino, F., Battisti, R., Nocerino, E.: Geometric investigation of a gaming active device. Presented at the June 9 (2011). https://doi.org/10.1117/12.890070.

65. Lachat, E., Macher, H., Landes, T., Grussenmeyer, P.: Assessment of the accuracy of 3D models obtained with DSLR camera and Kinect v2. Presented at the June 21 (2015). https://doi.org/10.1117/12.2184866.

66. Breuer, T., Bodensteiner, C., Arens, M.: Low-cost commodity depth sensor comparison and accuracy analysis. In: Electro-Optical Remote Sensing, Photonic Technologies, and Applications VIII; and Military Applications in Hyperspectral Imaging and High Spatial Resolution Sensing II. p. 92500G. SPIE (2014). https://doi.org/10.1117/12.2067155.

67. Guidi, G., Gonizzi, S., Micoli, L.: 3D capturing performances of low-cost range sensors for mass-market applications. ISPRS - Int. Arch. Photogramm. Remote Sens. Spat. Inf. Sci. XLI-B5, 33–40 (2016). https://doi.org/10.5194/isprsarchives-XLI-B5-33-2016.

68. Intel® RealSense^{TM} Cross Platform API (librealsense): Main Page, https://software.intel.com/sites/products/realsense/camera/, last accessed 2018/11/27.

69. Intel RealSense SDK 2.0 - Intel RealSense Depth & Tracking Cameras, https://realsense.intel.com/sdk-2/, last accessed 2019/02/14.

70. Chiabrando, F., Chiabrando, R., Piatti, D., Rinaudo, F., Chiabrando, F., Chiabrando, R., Piatti, D., Rinaudo, F.: Sensors for 3D Imaging: Metric Evaluation and Calibration of a CCD/CMOS Time-of-Flight Camera. Sensors. 9, 10080–10096 (2009). https://doi.org/10.3390/s91210080.

71. Davis, J., Nehab, D., Ramamoorthi, R., Rusinkiewicz, S.: Spacetime Stereo: A Unifying Framework for Depth from Triangulation.

72. OpenNI 2 Downloads and Documentation | The Structure Sensor, https://structure.io/openni, last accessed 2019/10/26.

73. Open source drivers for the kinect for windows v2 device, https://github.com/OpenKinect/libfreenect2, last accessed 2018/06/19.

74. Boehm, J.: Accuracy Investigation for Structured-light Based Consumer 3D Sensors. Photogramm. - Fernerkundung - Geoinf. 2014, 117–127 (2014). https://doi.org/10.1127/1432-8364/2014/0214.

75. Kersten, T.P., Lindstaedt, M., Starosta, D.: Comparative geometrical accuracy investigations of Hand-Held 3D scanning systems - An update. In: International Archives of the Photogrammetry, Remote Sensing and Spatial Information Sciences - ISPRS Archives. pp. 487–494. International Society for Photogrammetry and Remote Sensing (2018). https://doi.org/10.5194/isprs-archives-XLII-2-487-2018.

76. blender.org - Home of the Blender project - Free and Open 3D Creation Software, https://www.blender.org/, last accessed 2019/10/26.

77. Garrido-Jurado, S., Muñoz-Salinas, R., Madrid-Cuevas, F.J., Marín-Jiménez, M.J.: Automatic generation and detection of highly reliable fiducial markers under occlusion. Pattern Recognit. 47, 2280–2292 (2014). https://doi.org/10.1016/J.PATCOG.2014.01.005.

78. Crivellaro, A., Rad, M., Verdie, Y., Yi, K.M., Fua, P., Lepetit, V.: A Novel Representation of Parts for Accurate 3D Object Detection and Tracking in Monocular Images. In: 2015 IEEE International Conference on Computer Vision (ICCV). pp. 4391–4399. IEEE (2015). https://doi.org/10.1109/ICCV.2015.499.

79. Sesia, S.B., Heitzelmann, M., Schaedelin, S., Magerkurth, O., Kocher, G.J., Schmid, R.A., Haecker, F.-M.: Standardized Haller and Asymmetry Index Combined for a More Accurate Assessment of Pectus Excavatum. Ann. Thorac. Surg. 107, 271–276 (2019). https://doi.org/10.1016/j.athoracsur.2018.07.086.

80. López-Fernández, D., Madrid-Cuevas, F.J., Carmona-Poyato, A., Muñoz-Salinas, R., Medina-Carnicer, R.: A new approach for multi-view gait recognition on unconstrained paths. J. Vis. Commun. Image Represent. 38, 396–406 (2016). https://doi.org/10.1016/J.JVCIR.2016.03.020.

81. Dhall, A., Chelani, K., Radhakrishnan, V., Krishna, K.M.: LiDAR-Camera Calibration using 3D-3D Point correspondences. (2017).

82. Munoz-Salinas, R.: ARUCO: a minimal library for Augmented Reality applications based on OpenCv., (2012).

83. The DCI Architecture: A New Vision of Object-Oriented Programming, https://web.archive.org/web/20090323032904/https://www.artima.com/articles/dci_vision.html, last accessed 2019/10/26.

84. How to use Model-View-Controller (MVC), https://web.archive.org/web/20120729161926/http://st-www.cs.illinois.edu/users/smarch/st-docs/mvc.html, last accessed 2019/10/26.

85. Qt Company: Qt for developers by developers | Cross-platform development, https://www.qt.io/developers/, last accessed 2018/05/04.

86. Rusu, R.B., Cousins, S.: 3D is here: Point Cloud Library (PCL). In: 2011 IEEE International Conference on Robotics and Automation. pp. 1–4. IEEE (2011). https://doi.org/10.1109/ICRA.2011.5980567.

87. Schroeder, W., Martin, K., Lorensen, B., Kitware, I.: The visualization toolkit : an object-oriented approach to 3D graphics. Kitware (2006).

88. OpenCV, https://opencv.org/, last accessed 2019/10/26.

89. Siemens Product Lifecycle Management Software Inc.: Siemens NX, https://www.plm.automation.siemens.com/en/products/nx/, last accessed 2018/05/04.

90. F123 Series Printers | Stratasys, http://www.stratasys.com/3d-printers/f123, last accessed 2018/05/04.

91. Ata, S.T.R.: ABS-M30, The 3D printing solution company, http://global72.stratasys.com/~/media/Main/Files/Material_Spec_Sheets/MSS_FDM_ABSM30_0517a_Web.pdf, last accessed 2018/05/04.

92. Nellans, K.W., Kowalski, E., Chung, K.C.: The Epidemiology of Distal Radius Fractures, (2012). https://doi.org/10.1016/j.hcl.2012.02.001.

93. Douglas, D.H., Peucker, T.K.: Algorithms for the Reduction of the Number of Points Required to Represent a Digitized Line or its Caricature. In: Classics in Cartography. pp. 15–28. John Wiley & Sons, Ltd, Chichester, UK (2011).

https://doi.org/10.1002/9780470669488.ch2.

94. Boyd, A.S., Benjamin, H.J., Asplund, C.: Principles of casting and splinting, (2009).

95. Kazhdan Michael, Bolitho Matthew, Hoppe Hugues: Poisson surface reconstruction. In: Proceedings of the fourth Eurographics symposium on Geometry processing. pp. 61--70. Eurographics Association, Cagliari, Sardinia, Italy (2006).

96. Documentazione di Siemens: Overview of Programmer's Guide, https://docs.plm.automation.siemens.com/tdoc/nx/10/nx_api#uid:index_nxopen_prog_guide:id1142156:purpose, last accessed 2018/05/04.

97. Morhart, M., Tredget, E.E., Jarman, A.T.A., Ghahary, A.: Wrist Fractures and Dislocations: Background, Epidemiology, Etiology, http://emedicine.medscape.com/article/1285825-overview#a5, last accessed 2018/05/04.

98. Davidson, S.: Grasshopper (Algorithmic modeling for Rhino), http://www.grasshopper3d.com/, last accessed 2018/05/04.

99. Brackett, D., Ashcroft, I., Hague, R.: Topology optimization for additive manufacturing. Presented at the (2011).

100. Powerful and Easy-to-use FEA and Optimization for Design Engineers | solidThinking Inspire 2018, https://solidthinking.com/inspire2018.html, last accessed 2018/05/04.

101. Heckbert, P.S.: Survey of texture mapping. In: Proceedings - Graphics Interface. pp. 207–212. Canadian Information Processing Soc (1986). https://doi.org/10.1109/MCG.1986.276672.

102. pythonOCC, 3D CAD/CAE/PLM development framework for the Python programming language, http://www.pythonocc.org/, last accessed 2019/10/26.

103. Buonamici, F., Furferi, R., Governi, L., Lazzeri, S., McGreevy, K.S., Servi, M., Talanti, E., Uccheddu, F., Volpe, Y., Buonamici, F.; Furferi, R.; Governi, L.; Lazzeri, S.; Mc Greevy, K. S.; Servi, M.; Talanti, E.; Uccheddu, F.; Volpe, Y.: A Practical Methodology for Computer Aided Design of Custom 3D Printable Casts for Wrist Fractures. Vis. Comput. 1–16 (2019). https://doi.org/10.1007/s00371-018-01624-z.

104. Zivicnjak, M., Narancić, N.S., Szirovicza, L., Franke, D., Hrenović, J., Bisof, V.: Gender-specific growth patterns for stature, sitting height and limbs length in Croatian children and youth (3 to 18 years of age). Coll. Antropol. 27, 321–34 (2003).

105. Cazon, A., Kelly, S., Paterson, A.M., Bibb, R.J., Campbell, R.I.: Analysis and comparison of wrist splint designs using the finite element method : Multi-material three-dimensional printing compared to typical existing practice with thermoplastics. 231, 881–897 (2017). https://doi.org/10.1177/0954411917718221.

106. ABS-M30: A High Strength 3D Printing Material | Stratasys.

107. Siemens PLM Software Inc: NX: Siemens PLM Software.

108. Nielsen, J., Landauer, T.K.: Mathematical model of the finding of usability problems. In: Conference on Human Factors in Computing Systems - Proceedings. pp. 206–213. Publ by ACM (1993). https://doi.org/10.1145/169059.169166.

109. Faulkner, L.: Beyond the five-user assumption: Benefits of increased sample sizes in usability testing. In: Behavior Research Methods, Instruments, and Computers. pp. 379–383. Psychonomic Society Inc. (2003). https://doi.org/10.3758/BF03195514.

110. Sauro, J., Lewis, J.R.: Quantifying the User Experience. Elsevier Inc. (2012). https://doi.org/10.1016/C2010-0-65192-3.

111. Affairs, A.S. for P.: System Usability Scale (SUS). (2013).

112. MeasuringU: What Is A Good Task-Completion Rate?, https://measuringu.com/task-completion/, last accessed 2019/10/26.

113.   MeasuringU: 10 Things To Know About The Single Ease Question (SEQ), https://measuringu.com/seq10/, last accessed 2019/10/26.

114.   ActivArmor | Custom 3D-Printed Casts and Splints, https://activarmor.com/, last accessed 2019/10/26.

115.   Streiner, D.L., Norman, G.R., Cairney, J.: Health Measurement Scales. Oxford University Press (2015). https://doi.org/10.1093/med/9780199685219.001.0001.

116.   Prevention and Treatment of Pressure Ulcers/Injuries: Clinical Practice Guideline, https://internationalguideline.com/, last accessed 2019/10/26.

117.   Ciucci, E., Baroncelli, A., Tambasco, G., Laurent, J., Catanzaro, S.J., Joiner, T.E.: Measuring Positive Affect, Negative Affect, and Physiological Hyperarousal among Italian Youth: Translations of the PANAS-C and PH-C. J. Psychopathol. Behav. Assess. 39, 373–382 (2017). https://doi.org/10.1007/s10862-017-9596-8.

118.   Laurent, J., Catanzaro, S.J., Rudolph, K.D., Joiner, T.E., Potter, K.I., Lambert, S., Osborne, L., Gathright, T.: A measure of positive and negative affect for children: Scale development and preliminary validation. Psychol. Assess. 11, 326–338 (1999). https://doi.org/10.1037/1040-3590.11.3.326.

119.   Bradley, M.M., Lang, P.J.: Measuring emotion: The self-assessment manikin and the semantic differential. J. Behav. Ther. Exp. Psychiatry. 25, 49–59 (1994). https://doi.org/10.1016/0005-7916(94)90063-9.

120.   Observations: SAM: The self-assessment manikin: An efficient cross-cultural measurement of emotional response. - PsycNET, https://psycnet.apa.org/record/1996-00218-005, last accessed 2019/10/26.

121.   Behavioral treatment and bio-behavioral assessment: Computer applications | BibSonomy, https://www.bibsonomy.org/bibtex/272693fa11a4aa5f447d91e385f2e5444/schultem, last accessed 2019/10/26.

122.   Ben-Yakov, M., Boutis, K.: Buckle fractures of the distal radius in children. CMAJ. 188, 527 (2016). https://doi.org/10.1503/cmaj.151239.

123.   Handoll, H.H.G., Elliott, J., Iheozor-Ejiofor, Z., Hunter, J., Karantana, A.: Interventions for treating wrist fractures in children, (2018). https://doi.org/10.1002/14651858.CD012470.pub2.

124.   Morgan, G.L.K., Liu, J.G., Yan, H.: Precise Subpixel Disparity Measurement From Very Narrow Baseline Stereo. IEEE Trans. Geosci. Remote Sens. 48, 3424–3433 (2010). https://doi.org/10.1109/TGRS.2010.2046672.

125.   Giancola, S., Valenti, M., Sala, R.: A Survey on 3D Cameras: Metrological Comparison of Time-of-Flight, Structured-Light and Active Stereoscopy Technologies.

126.   Keselman, L., Woodfill, J.I., Grunnet-Jepsen, A., Bhowmik, A.: Intel R RealSense TM Stereoscopic Depth Cameras.

127.   Carfagni, M., Furferi, R., Governi, L., Servi, M., Uccheddu, F., Volpe, Y.: On the Performance of the Intel SR300 Depth Camera: Metrological and Critical Characterization. IEEE Sens. J. 17, 4508–4519 (2017). https://doi.org/10.1109/JSEN.2017.2703829.

128.   Kersten, T.P., Lindstaedt, M., Starosta, D.: Comparative geometrical accuracy investigations of hand-held 3D scanning systems - an update. ISPRS - Int. Arch. Photogramm. Remote Sens. Spat. Inf. Sci. XLII–2, 487–494 (2018). https://doi.org/10.5194/isprs-archives-XLII-2-487-2018.

129.   Herrera, D., Kannala, J., Heikkilä, J.: Joint depth and color camera calibration with

distortion correction. IEEE Trans. Pattern Anal. Mach. Intell. 34, 2058–2064 (2012).

130. | VDI/VDE 2634 Blatt 3, https://www.vdi.eu/guidelines/vdivde_2634_blatt_3-optische_3_d_messsysteme_bildgebende_systeme_mit_flaechenhafter_antastung/, last accessed 2018/11/28.

131.   Qt QML 5.13.1, https://doc.qt.io/qt-5/qtqml-index.html, last accessed 2019/10/26.

132.   KScan Redirect LP | LMI3D, https://lmi3d.com/kscan3d-software, last accessed 2019/10/26.

133.   Geomagic Studio 12 offers fastest way to convert 3D scans of physical objects into parametric models for direct exchange with PTC® Pro/ENGINEER® | 3D Systems, https://www.3dsystems.com/press-releases/geomagic/studio-12-offers-fastest-way-to-convert-3d-scans-of-phy, last accessed 2019/11/11.

134.   Birkemeier, K.L., Podberesky, D.J., Salisbury, S., Serai, S.: Breathe In... Breathe Out... Stop Breathing: Does Phase of Respiration Affect the Haller Index in Patients With Pectus Excavatum? Am. J. Roentgenol. 197, W934–W939 (2011). https://doi.org/10.2214/AJR.11.6430.

135.   Raichura, N., Entwisle, J., Leverment, J., Beardsmore, C.S.: Breath-hold MRI in evaluating patients with pectus excavatum. Br. J. Radiol. 74, 701–708 (2001). https://doi.org/10.1259/bjr.74.884.740701.

136.   Ravitch, M.M.: The operative treatment of Pectus Excavatum. Ann. Surg. 129, 429–444 (1949). https://doi.org/10.1097/00000658-194904000-00002.

137.   Nuss, D., Kelly, R.E., Croitoru, D.P., Katz, M.E.: A 10-year review of a minimally invasive technique for the correction of pectus excavatum, (1998). https://doi.org/10.1016/S0022-3468(98)90314-1.

138.   Jaroszewski, D., Notrica, D., McMahon, L., Steidley, D.E., Deschamps, C.: Current Management of Pectus Excavatum: A Review and Update of Therapy and Treatment Recommendations. J. Am. Board Fam. Med. 23, 230–239 (2010). https://doi.org/10.3122/jabfm.2010.02.090234.

139.   St. Peter, S.D., Juang, D., Garey, C.L., Laituri, C.A., Ostlie, D.J., Sharp, R.J., Snyder, C.L.: A novel measure for pectus excavatum: the correction index. J. Pediatr. Surg. 46, 2270–2273 (2011). https://doi.org/10.1016/j.jpedsurg.2011.09.009.

140.   Poston, P.M., Patel, S.S., Rajput, M., Rossi, N.O., Ghanamah, M.S., Davis, J.E., Turek, J.W.: The correction index: setting the standard for recommending operative repair of pectus excavatum. Ann. Thorac. Surg. 97, 1176–9; discussion 1179-80 (2014). https://doi.org/10.1016/j.athoracsur.2013.12.050.

141.   Poncet, P., Kravarusic, D., Richart, T., Evison, R., Ronsky, J.L., Alassiri, A., Sigalet, D.: Clinical impact of optical imaging with 3-D reconstruction of torso topography in common anterior chest wall anomalies. J. Pediatr. Surg. 42, 898–903 (2007). https://doi.org/10.1016/j.jpedsurg.2006.12.070.

142.   Gomes-Fonseca, J., Vilaça, J.L., Henriques-Coelho, T., Direito-Santos, B., Pinho, A.C.M., Fonseca, J.C., Correia-Pinto, J.: A new methodology for assessment of pectus excavatum correction after bar removal in Nuss procedure: Preliminary study. J. Pediatr. Surg. 52, 1089–1097 (2017). https://doi.org/10.1016/j.jpedsurg.2016.12.029.

143.   JENKS, F., G.: The Data Model Concept in Statistical Mapping. Int. Yearb. Cartogr. 7, 186–190 (1967).

144.   Stuart, A.: Rank Correlation Methods. By M. G. Kendall, 2nd edition. Br. J. Stat. Psychol. 9, 68–68 (1956). https://doi.org/10.1111/j.2044-8317.1956.tb00172.x.

145.   Minitab, http://www.minitab.com/en-us/, last accessed 2019/01/14.

146.   Obcid, M.F., Obermever, R., Kidane, N., Kelly, R.E., MeKenzie, F.D.: Investigating

the fidelity of an improvement-Assessment tool after one vacuum bell treatment session. In: Simulation Series. pp. 476–479. The Society for Modeling and Simulation International (2016). https://doi.org/10.22360/summersim.2016.scsc.099.

147.   Haecker, F.-M., Sesia, S.: Vacuum bell therapy. Ann. Cardiothorac. Surg. 5, 440–449 (2016). https://doi.org/10.3978/11506.

148.   Cartoski, M.J., Nuss, D., Goretsky, M.J., Proud, V.K., Croitoru, D.P., Gustin, T., Mitchell, K., Vasser, E., Kelly, R.E.: Classification of the dysmorphology of pectus excavatum. J. Pediatr. Surg. 41, 1573–1581 (2006). https://doi.org/10.1016/J.JPEDSURG.2006.05.055.

149.   Kim, H.C., Choi, H., Jin, S.O., Lee, J.J., Nam, K.-W., Kim, I.-Y., Nam, K.C., Park, H.J., Lee, K.H., Kim, M.G.: New Computerized Indices for Quantitative Evaluation of Depression and Asymmetry in Patients With Chest Wall Deformities. Artif. Organs. 37, 712–718 (2013). https://doi.org/10.1111/aor.12085.

150.   Sesia, S.B., Heitzelmann, M., Schaedelin, S., Magerkurth, O., Kocher, G.J., Schmid, R.A., Haecker, F.-M.: Standardized Haller and Asymmetry Index Combined for a More Accurate Assessment of Pectus Excavatum. Ann. Thorac. Surg. 107, 271–276 (2019). https://doi.org/10.1016/j.athoracsur.2018.07.086.

151.   Izenman, A.J.: Linear Discriminant Analysis. Presented at the (2013). https://doi.org/10.1007/978-0-387-78189-1_8.

152.   Kuru, P., Cakiroglu, A., Er, A., Ozbakir, H., Cinel, A.E., Cangut, B., Iris, M., Canbaz, B., Pıçak, E., Yuksel, M.: Pectus Excavatum and Pectus Carinatum: Associated Conditions, Family History, and Postoperative Patient Satisfaction. Korean J. Thorac. Cardiovasc. Surg. 49, 29–34 (2016). https://doi.org/10.5090/kjtcs.2016.49.1.29.

153.   Glinkowski, W., Sitnik, R., Witkowski, M., Kocoń, H., Bolewicki, P., Górecki, A.: Method of pectus excavatum measurement based on structured light technique. J. Biomed. Opt. 14, 044041 (2009). https://doi.org/10.1117/1.3210782.

154.   Cobben, J.M., Oostra, R.-J., van Dijk, F.S.: Pectus excavatum and carinatum. Eur. J. Med. Genet. 57, 414–417 (2014). https://doi.org/10.1016/j.ejmg.2014.04.017.

155.   Sarwar, Z.U., DeFlorio, R., O′Connor, S.C.: Pectus Excavatum: Current Imaging Techniques and Opportunities for Dose Reduction. Semin. Ultrasound, CT MRI. 35, 374–381 (2014). https://doi.org/10.1053/j.sult.2014.05.003.

156.   Tocchioni, F., Ghionzoli, M., Messineo, A., Romagnoli, P.: Pectus excavatum and heritable disorders of the connective tissue. Pediatr. Rep. 5, e15 (2013). https://doi.org/10.4081/pr.2013.e15.

157.   Lange F. Thoraxdeformitäten: Chirurgie und Orthopädie im Kindesalter. Pfaundler M, Schlossmann A, Ed. Handb. der Kinderheilkd. V, 157 (1910).

158.   Schier, F., Bahr, M., Klobe, E.: The vacuum chest wall lifter: an innovative, nonsurgical addition to the management of pectus excavatum. J. Pediatr. Surg. 40, 496–500 (2005). https://doi.org/10.1016/j.jpedsurg.2004.11.033.

159.   Carfagni, M., Facchini, F., Furferi, R., Ghionzoli, M., Governi, L., Messineo, A., Servi, M., Uccheddu, F., Volpe, Y.: A semi-automatic computer-aided method for personalized Vacuum Bell design. Comput. Aided. Des. Appl. 15, 247–255 (2018). https://doi.org/10.1080/16864360.2017.1375676.

160.   Haecker, F.-M., Mayr, J.: The vacuum bell for treatment of pectus excavatum: an alternative to surgical correction? Eur. J. Cardio-Thoracic Surg. 29, 557–561 (2006). https://doi.org/10.1016/j.ejcts.2006.01.025.

161.   Sesia, S.B., Hradetzky, D., Haecker, F.-M.: Monitoring the effectiveness of the vacuum bell during pectus excavatum treatment: Technical innovation. J. Pediatr.

Surg. 53, 411–417 (2017). https://doi.org/10.1016/j.jpedsurg.2017.05.023.

162. Differential Pressure Manometer PCE-P05 | PCE Instruments, https://www.pce-instruments.com/english/measuring-instruments/test-meters/manometer-pce-instruments-differential-pressure-manometer-pce-p05-det_61709.htm, last accessed 2019/02/14.

163. Uccheddu, F., Del Mastio, A., Remondino, F., Pelagotti, A., Cappellini, V.: Texture mapping of flat-like 3D models. In: 2009 16th International Conference on Digital Signal Processing. pp. 1–6. IEEE (2009). https://doi.org/10.1109/ICDSP.2009.5201210.

164. Intel® RealSense™ Technology, https://www.intel.com/content/www/us/en/architecture-and-technology/realsense-overview.html, last accessed 2018/11/27.

165. Yuen, H.K., Princen, J., Illingworth, J., Kittler, J.: A comparative study of Hough transform methods for circle finding. https://doi.org/10.5244/C.3.29.